


<b>Title</b>	Development of large-scale colloidal crystallisation methods for the production of photonic crystals
<b>Author(s)</b>	McGrath, Joseph
<b>Publication date</b>	2014
<b>Original citation</b>	McGrath, J. 2014. Development of large-scale colloidal crystallisation methods for the production of photonic crystals. PhD Thesis, University College Cork.
<b>Type of publication</b>	Doctoral thesis
<b>Rights</b>	<p>© 2014, Joseph McGrath</p> <p><a href="http://creativecommons.org/licenses/by-nc-nd/3.0/">http://creativecommons.org/licenses/by-nc-nd/3.0/</a></p> 
<b>Embargo information</b>	No embargo required
<b>Item downloaded from</b>	<a href="http://hdl.handle.net/10468/2010">http://hdl.handle.net/10468/2010</a>

Downloaded on 2017-02-12T09:41:10Z

# Development of Large-Scale Colloidal Crystallisation Methods for the Production of Photonic Crystals.



A thesis submitted for the degree of

**Doctor of Philosophy**

to the

Department of Chemistry  
National University of Ireland, Cork

**Joseph McGrath.**

**2014**

Supervisor: **Professor Martyn Pemble**

Head of Department: **Professor Martyn Pemble**



Advanced Materials and Surfaces Group  
(AMSG)  
Tyndall National Institute  
University College Cork (UCC)  
Lee Maltings, Prospect Row, Cork, Ireland.

# TABLE OF CONTENTS

## ABSTRACT

### 1. CHAPTER 1: INTRODUCTION.

1.1	COLLOIDS	10
1.2	COLLOIDAL MOTION	12
1.3	SELF ASSEMBLY	13
1.4	OPTICAL PROPERTIES OF PHOTONIC CRYSTALS	18
1.4.1	THE BRAGG-SNELL LAW	22
1.4.2	THE PHOTONIC BAND GAP	30
1.5	PHOTONIC CRYSTALS AND SELF ASSEMBLY	31
1.6	COLLOIDAL PHOTONIC CRYSTAL PRODUCTION METHODS	36
1.7	INTRODUCTION TO SELF ASSEMBLY METHODS	41
1.7.1	RING FORMATION	41
1.7.2	GRAVITATIONAL SEDIMENTATION	42
1.7.3	CONTROLLED EVAPORATION	43
1.7.4	SOLVENT EFFECTS ON CONTROLLED EVAPORATION	45
1.7.5	SILICA BONDING IN CONTROLLED EVAPORATION	47
1.7.6	DIP COATING	47
1.7.7	THE LANGMUIR-BLODGETT METHOD	48
1.7.8	UNDER OIL CRYSTALLISATION	49
1.7.9	SHEAR INDUCED MECHANISMS	50
1.7.10	FLUID AND REDUCED FRICTION SUBSTRATES	51
1.7.11	VIBRATION ASSISTED DEPOSITION	52
1.7.12	INKJET PRINTING	54
1.7.13	SPIN COATING	55
1.7.14	TEMPLATE ASSISTED DEPOSITION	56
1.8	OTHER LARGE AREA / CRACK FREE METHODS	57
1.9	ASSESSMENT OF COLLOIDAL CRYSTAL FILM QUALITY	62
1.9.1	EFFECTS ON OPTICAL QUALITY	63
1.9.2	THE FULL WIDTH AT HALF MAXIMUM (FWHM)	65
1.9.3	THE USE OF FABRY-PEROT FRINGES	67
1.9.4	FAST FOURIER TRANSFORM IMAGES	70
1.9.5	AIMS OF THE PRESENT WORK	72
	REFERENCES	75

2.	<b><u>CHAPTER 2: EXPERIMENTAL DETAILS</u></b>	
2.1	CHEMICALS AND MATERIALS	90
2.2	UNDER OIL DEPOSITION	93
2.3	ULTRASONIC DEPOSITION	96
2.4	EVAPORATION DEPOSITION	99
2.5	OPTICAL CHARACTERISATION	103
2.6	PHYSICAL CHARACTERISATION	104
2.6.1	OPTICAL MICROSCOPY	104
2.6.2	SCANNING ELECTRON MICROSCOPY	104
	REFERENCES	105
3.	<b><u>CHAPTER 3: DEVELOPMENT OF AN IMPROVED METHOD FOR THE SYNTHESIS OF SILICA PARTICLES</u></b>	
3.1	INTRODUCTION	107
3.2	PARTICLE SYNTHESIS	108
3.3	RESULTS AND DISCUSSION	111
3.3.1	SILICA SYNTHESIS	111
3.3.2	SYNTHESIS OF LARGER PARTICLES (>600nm)	113
3.4	CONCLUSIONS & FURTHER WORK	116
	REFERENCES	118
4.	<b><u>CHAPTER 4: IMPROVED SONICATION-ASSISTED FILM GROWTH</u></b>	
4.1	EXPERIMENTAL	121
4.2	RESULTS AND DISCUSSION	122
4.3	DISCUSSION	127
4.4	CONCLUSIONS & FURTHER WORK	132
	REFERENCES	133



5.	<b><u>CHAPTER 5: CRACK-FREE OPAL FILMS BY UNDER OIL CO-CRYSTALLISATION</u></b>	
5.1	INTRODUCTION AND AIMS	135
5.2	EXPERIMENTAL	137
5.2.1	INFILLING SILICA PARTICLE FLEXIBLE FILMS	138
5.2.2	INFILLING POLYSTYRENE PARTICLE FLEXIBLE FILMS	139
5.2.3	UNDER OIL CO-CRYSTALLISATION DEPOSITION	140
5.3	RESULTS	141
5.3.1	UNDER OIL CRYSTALLISATION ON GLASS SUBSTRATES	141
5.3.2	INFILLING OF SILICA PARTICLES ON RUBBER SUBSTRATES	143
5.3.3	RESULTS OF UNDER OIL CO-CRYSTALLISATION DEPOSITION	145
5.3.4	OTHER UNDER OIL CRYSTALLISATION INFILTRATION	
	METHODS	157
5.4	DISCUSSION	159
5.4.1	SILICA INFILLING BY UNDER OIL CO-CRYSTALLISATION	159
5.5	CONCLUSION AND FURTHER WORK	160
	REFERENCES	162
6.	<b><u>CHAPTER 6: POLYMER ADDITION DURING EVAPORATION DEPOSITION</u></b>	
6.1	INTRODUCTION	163
6.2	EXPERIMENTAL	164
6.3	RESULTS - ADDITION OF A REDISPERSIBLE POLYMER	165
6.4	DISCUSSION – REDISPERSIBLE POLYMER	173
6.5	RESULTS – ADDITION OF UV CURING FLEXIBLE ADHESIVE	174
6.6	DISCUSSION – UV CURING FLEXIBLE ADHESIVE	176
6.7	RESULTS - ADDITION OF MMA MONOMER	179
6.8	DISCUSSION - ADDITION OF MMA MONOMER	182
6.9	RESULTS - ADDITION OF PVA WATER SOLUBLE ADHESIVE	183
6.10	DISCUSSION OF POLYMER ADDITIONS DURING EVAPORATION DEPOSITION	185
6.11	CONCLUSIONS AND FURTHER WORK	187
	REFERENCES	188

7.	<b><u>CHAPTER 7: EVAPORATION DEPOSITION USING MIXED SOLVENTS</u></b>	
7.1	INTRODUCTION	189
7.2	EXPERIMENTAL	191
7.3	RESULTS	192
7.4	DISCUSSION	198
7.5	CONCLUSIONS & FURTHER WORK	205
	REFERENCES	207
8.	<b><u>CHAPTER 8: FAST FOURIER TRANSFORMS AND SURFACE QUALITY ASSESSMENT</u></b>	
8.1	INTRODUCTION	210
8.2	RESULTS & DISCUSSION	214
8.3	CONCLUSIONS	221
	REFERENCES	222
	<b><u>CONCLUSIONS</u></b>	223
	<b><u>APPENDIX A.</u></b>	
	CRACK FREE ETHANOLIC FILMS BY CONTROLLED EVAPORATION	226
	REFERENCES	239
	<b><u>APPENDIX B.</u></b>	
	CERTIFICATE FOR NIMS INTERNSHIP	240
	<b><u>APPENDIX C.</u></b>	
	PAPERS: PRESENTATIONS: POSTER PRESENTATIONS	241

## **Acknowledgements**

I would like to thank Professor Martyn Pemble for the opportunity to undertake this research for PhD, and his help and support throughout. I would also like to thank all my co-workers in the Advanced Materials and Surfaces Group (AMSG), Tyndall, especially Dr Maria Bardosova, Dr Sibu Padmanabhan, John Kinsella and Syara Kassim.

I would also like to thank Dr Hiroshi Fudouzi for his support during my internship in Japan at the National Institute of Materials Science, (NIMS) Tsukuba, Japan, during some difficult times.

Most of all, I would like to thank my wife, Elaine, for giving me constant love, support and encouragement; and my children, Thomas, Maya & Odhran, for putting up with me working away from home for 2 years.

This work is supported by SFI PI Grant No. 07/NI.1/I787, and the Higher Education Authority of Ireland PRTL Project INSPIRE

## **Declaration**

I hereby declare that I have written this thesis independently, but with help from my supervisors and colleagues, and permitted aids only. There has not been any assistance from any prohibited means.

I declare that all parts of this thesis which have been taken from published and unpublished sources, documents, talks and presentations which have been reproduced here, have been mentioned as such at the corresponding places in the thesis by citation, where the extents of the original quotes are indicated.



Joseph McGrath

September 2013

# **ABSTRACT:**

Photonic crystals are being studied for a variety of potential applications for the manipulation of light including the fabrication of more efficient lasers and LEDs, the development of improved optical sensors, the development of optical interconnects and the fabrication of photovoltaic devices having improved efficiencies via light trapping and reduced reflection.

Colloidal photonic crystallisation, using a “bottom-up” self-assembly approach, of sub-micron particles, offers the opportunity to produce large scale photonic crystal films for these applications more cost effectively than micro-fabrication methods (“top-down” lithography and etching etc.). However, the lack of long range order in these films resulting from the natural formation of defects is perceived to be a major roadblock towards their routine incorporation into device fabrication technologies.

The work presented in this thesis provides new insight into how these defects arise, advances in the methods used to characterise and quantify these defects and potential solutions designed to overcome defect formation on a scale comparable to a 4-inch wafer.

A range of methods for the production of ‘large-area’ colloidal photonic crystals have been investigated including sonication, under oil co-crystallization and controlled

evaporation, with a view to their exploitation and further development in order to reduce cracking and other defect formation.

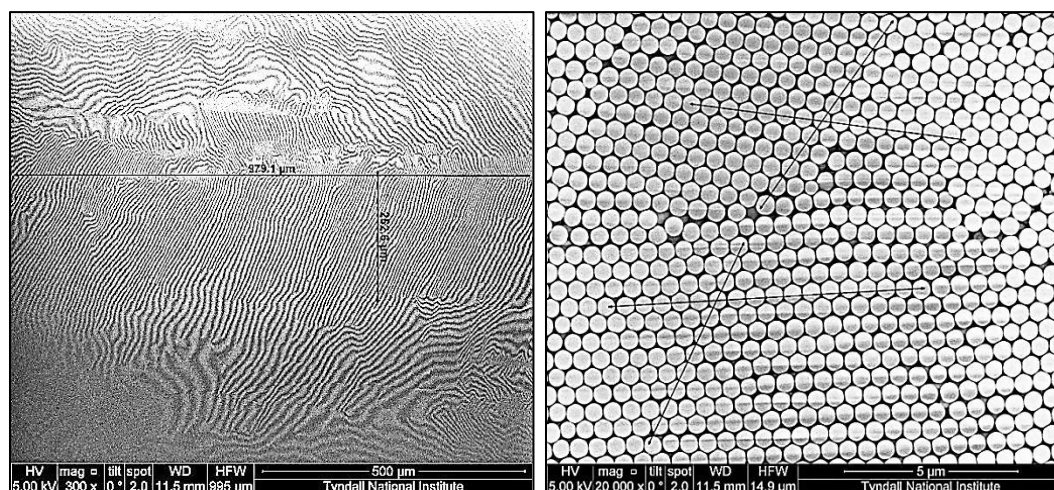
By way of a starting point for these studies the issue of particle synthesis was addressed since conventional methods were deemed to fall short of the required particle size distributions needed for the fabrication of high-quality photonic crystals. A simple yet completely monotonic method has been developed in order to produce silica particles in the range of 80 to 600nm in a single step.

In order to evaluate the quality of the films a number of approaches were investigated. An analytical method to assess the surface quality of produced films was developed which assesses the surface particle ordering in the films in a semi-quantitative manner. Using the fast Fourier transform (FFT) spot intensities, an area method of grey scale symmetry, has been used to quantify the FFT profiles.

An ‘under oil co-crystallisation’ method was devised which results in the particles being bound together at the same time as forming the film. It is demonstrated that while this method has the potential to form very large areas, the method needs further refinement in order to be established as a production technique. Achieving high quality photonic crystals using relatively low concentrations (<5%) of polymeric adhesives in order to provide adhesion yet still maintain refractive index contrast, proved difficult and degraded the uniformity of the films. Adding ultrasonic vibrations

during film formation demonstrated that large area films could be assembled rapidly, however film ordering suffered as a result.

It is further demonstrated that a controlled evaporation method, using a mixed solvent suspension, presents the most promising method to produce high quality films over large areas, 75mm x 25mm. By using this mixed solvent approach, the film is kept in the wet state longer, thus reducing cracks developing during the drying stage. These films are crack-free up to a critical thickness, and show very large domains. These large domains are visible in low magnification SEM images as Moiré fringe patterns. Higher magnification reveals the separation between alternate fringe patterns are domain boundaries between individual crystalline growth fronts, see below.



**SEM images of a colloidal crystal film surface: (left) low magnification image showing large Moiré fringe patterns (>1000μm x 200μm), and (right) higher magnification image of the particle packing either side of a domain boundary.**

# CHAPTER 1.

## INTRODUCTION

### 1.1 COLLOIDS.

A colloid is defined as a system of minute particles dispersed throughout another substance or medium. Familiar colloids include fog, smoke, homogenized milk, and ruby-coloured glass. This categorization includes the whole range of materials; including polymers, ceramics, and biological materials. Colloidal particles are larger than molecules but are generally too small to be observed directly with an optical microscope. By contrast in a true solution particles of a dissolved substance are of molecular size, and in a coarse mixture (e.g. suspension) the particles are much larger than colloidal particles. Although there are no precise boundaries of size between the particles in colloids, solutions, or suspensions, colloidal particles are usually on the order of 10nm to 1000nm in size. Table 1.1 shows the classification of colloidal particles and dispersing media, with some examples. [1]

**Table 1.1. Classification and examples of colloids [1].**

		Dispersed substance		
		Gas	Liquid	Solid
<b>Continuous medium</b>	<b>Gas</b>	None	Liquid aerosol (e.g., fog, mist, clouds)	Solid aerosol (e.g., smoke)
	<b>Liquid</b>	Foam (e.g., whipped cream)	Emulsion (e.g., milk, mayonnaise)	Sol (e.g., pigmented ink)
	<b>Solid</b>	Solid foam (e.g., aerogel, styrofoam)	Gel (e.g., jelly, gelatin, cheese, <b>opal</b> )	Solid sol (e.g., cranberry glass)



One property of colloid systems that distinguishes them from true solutions is that colloidal particles scatter light. If a beam of light passes through a colloid, the light is reflected (scattered) by the colloidal particles and the path of the light can be observed. When a beam of light passes through a true solution (e.g., salt in water) there is little or no scattering and the path of the light cannot be seen. The scattering of light by colloids, known as the Tyndall effect, was first explained by the physicist John Tyndall. Under a microscope, larger colloidal particles can be seen as tiny dots in constant motion, Brownian motion, which keeps the particles in suspension, figures 1.1(a&b)

Colloidal dispersions in a fluid phase solvent, like those shown in figure 1.1, are fundamental to a wide variety of systems with scientific and technological importance, including paints, ceramics, cosmetics, biological cells, photonic crystals, etc.

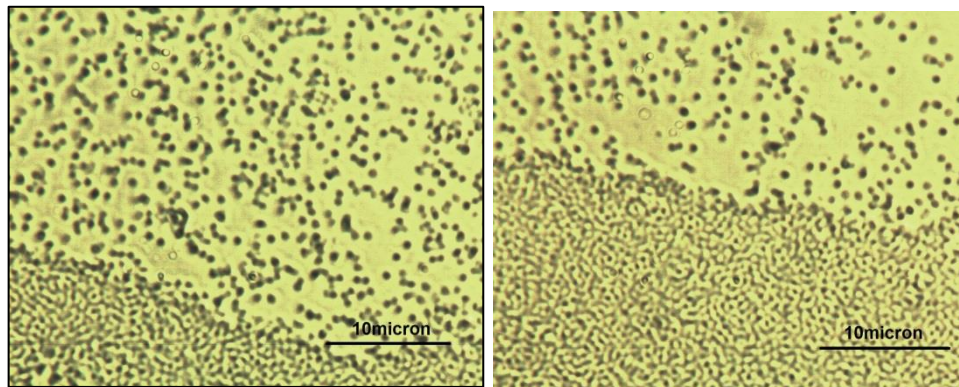


**Figure 1.1(a&b).** Optical microscope images of colloidal particles (approx. 800nm diameter) in random Brownian motion, coming to rest towards bottom left of the images, as the suspension dries.

## 1.2 COLLOIDAL MOTION

Colloidal particles collide with each other due to Brownian motion, convection, gravity and other forces. As colloidal particles approach each other, they will attract by van der Waals forces. If there are no counteracting forces, particles will aggregate and the colloidal system becomes destabilized. However there are many forces surrounding colloidal particles in a suspension including: van der Waals, electrostatic, depletion, biological, solvophobic (e.g. hydrophobic), solvation, and steric, as shown in Figure 1.2 below. The total potential energy from all these forces is usually written as:

$$\phi = \phi_{vdw} + \phi_{electrostatic} + \phi_{depletion} + \phi_{biological} + \phi_{solvophobic} + \phi_{solvation} + \phi_{steric} \quad [2]$$

where  $\phi$  = total potential energy (& energy relating to each force)

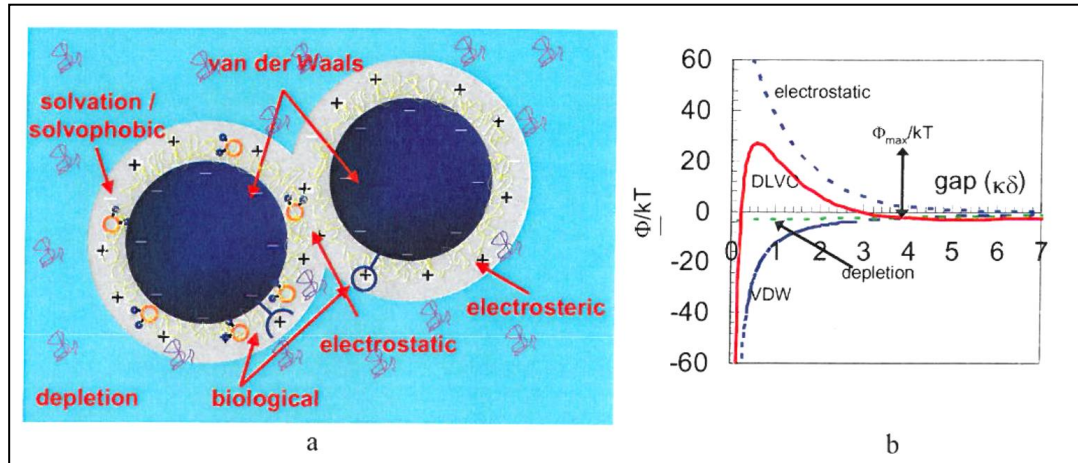


**Figure 1.2. Colloidal forces between two particles. (a) Many types of forces exist. All of these forces are available for colloidal fabrication, (b) The force profile considers three of the forces (electrostatic, van der Waals, and depletion), [2]**

Therefore, the colloidal stability of nanoparticles strongly depends on the repulsive and attractive forces acting on colloidal particles as a function of temperature (Brownian motion), and the interaction of nanoparticles in a colloidal suspension greatly influences the self-assembly process. Other key issues of self-assembly are the nucleation process, and controlled placement using an appropriate solvent during assembling process. [3]

### **1.3 SELF ASSEMBLY**

Self-assembly is common in nature, and can happen to particles of all sizes, including atomic, nano-, meso- and macroparticles. What is self-assembly? Different disciplines have had varying definitions, however a general definition is: “self-assembly is the autonomous organization of components into patterns or structures without human intervention” [4]. Or “self-assembly is a spontaneous process by which molecules to macroscopic entities assemble into one-, two- and three-dimensional ordered arrays” [3], in other words a structure that builds itself.

Whitesides and Boncheva [5] state that self-assembly is scientifically and technologically important for at least four reasons. The first is that it is centrally important in life; living cells contain a range of complex structures that form by self-assembly. The second is it provides a route to a range of materials with regular structures. Third, self-assembly of components larger than molecules, provides great

potential for use in materials science. Fourth, self-assembly offers a general strategy for generating nanostructures. Thus self-assembly has become important in a range of fields: chemistry, physics, biology, materials science, nano-science, and manufacturing. The potential of self-assembly as a strategy for forming interesting structures now extends beyond molecules, and provides a way of assembling electrically or optically functional components, photonic crystals, 3D microelectronic systems, displays, and sensors.

Jiang et al. [4] state that an assembly of particles is actually a packing of particles, and in general, there are three categories: ordered, disordered and partially ordered. Clearly, to produce a regular pattern, a self-assembled structure of particles must give an ordered structure. Particles, as building blocks, must therefore be properly formed in shape to allow structured self-assembly to occur, otherwise it would be difficult to yield ordered structures. Chemical technology is able to produce nanoparticles of different shapes, some of which are shown in figure 1.3.

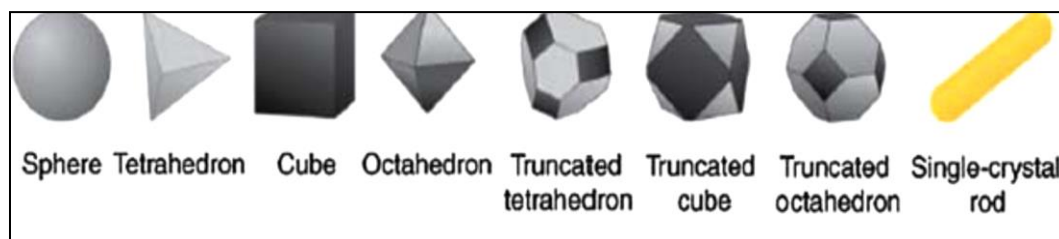


Fig. 1.3 Schematic illustrations of the diversity and complexity of nanostructure shapes [4].

In a self-assembly process, particles must be able to move around and interact with surrounding particles, and to occupy the correct positions required in order to form regular patterns. Particles of simple, uniform geometry, e.g. spheres, cubes, discs and

rods, can produce self-assembled structures relatively easily. However, non-spherical particles, and those with complicated shapes, are more difficult to self-assemble into ordered structures. Mixed particles of different shapes and sizes, are also much more difficult to self-assemble. Various forces may act as the controlling, or driving forces, in forming a particle assembly. The relative importance of these forces often varies with particle size (diameter or aspect ratio) [4].

While human intervention is nominally excluded in self-assembly processes, control over the assembly environment (e.g. temperature, and humidity) is required, so that the particles can assemble themselves. The environment is therefore very broad, and also includes the surrounding medium (e.g., gas and/or liquid), external forces (e.g. gravitational, electric, or magnetic field), and boundary constraints such as templates. Use of the surfactants can lead to different hydrophobic or hydrophilic forces between particles, and therefore can also be regarded as a chemical control in the environment for self-assembly. Therefore, in addition to particle–particle forces, particle–environment forces, (e.g. viscosity, buoyancy, and drag), also play a significant role in self-assembly of colloidal particles. The control of the particle–particle and particle–environment interactions is therefore multi-faceted. In many applications, there is more than one driving force, and their simultaneous control is difficult.

Different self-assembly techniques have been used, and their success usually comes from one major mechanism: the control of the dominant or driving forces. Some successful examples are given in Table 1.2. Existing wet self-assembly or “bottom up”

methods commonly begin with the deposition or adsorption of particles from the solution to the substrates. The adhered particles then self-assemble into ordered arrays with the help of solvents. “Bottom-up” self-assembly has the advantage over mechanically directed assembly in that it is simple and requires no machinery to move and locate particles, letting random, Brownian motion and other previously mentioned forces do the job instead.

**Table 1.2. Some typical self-assembly methods, their features and controlling forces [4].**

<b>Self-assembly techniques</b>	<b>Main features</b>	<b>Controlling forces or mechanisms</b>
<i>Top-down approach</i> <b>Photolithography</b> <b>Ink-jet printing</b>	Physical constraints for particle positioning, useful for making microelectronic devices, but limited to a few nanometres in resolution.	Template and boundary constraints
<i>Bottom-up approach</i> <b>Dip-coating or convective deposition</b>	Rapid and dynamic self-assembly process; and conducted in a steep concentration gradient assisted by substrates	Capillary forces and gravitational forces mainly drive the SA of particles
<b>Gravity sedimentation</b>	Close-packed planes perpendicular to gravity	Gravitational and capillary forces
<b>Dewetting/evaporation</b>	Irreversible evaporation of the solvent; and the high degree of convection-induced monolayer assembly	Capillary force
<b>Layer-by-layer assembly</b>	Precise control of deposition density, thickness and step growth; and versatile and simple in control of assembly	Capillary and gravitational forces
<b>Electrodeposition</b>	Electrochemical deposition of colloids on the conducting surface of template	Electric field force
<b>Spin-coating</b>	Simple but difficult to obtain ordered patterns or structures	Mechanical and friction forces
<b>Langmuir–Blodgett</b>	Large-area monolayer of particles with different morphologies (spheres, rods)	Mechanical forces and capillary forces dominate the SA process
<b>Fluid–fluid interface assembly</b>	Hydrodynamic flow directing the assembly of colloids, and avoiding steric and electrostatic repulsions	Hydrodynamic and capillary forces

Self-assembly on the sub-micron scale occurs in nature e.g. precious opals are made from self-assembled sub-micron silica particles, and some butterfly wings have

grown repeating structures on the same scale. Natural opals are an example of a colloidal crystal with photonic properties. Self-assembled natural opals have ordered arrays of silica colloidal particles that produce a beautiful “play of colours” based on Bragg diffraction [6, 7].

Self-assembly is now a method used to construct at the nano- and micrometre scale. An example is the formation of two- and three- dimensional lattices composed orderly arrangements of monodisperse spheres. Starting from a suspension of the colloidal spheres, if the solvent is allowed to evaporate under suitable conditions, capillary interactions drive the particles into an ordered structure, often referred to as an artificial opal.

Some of the first colloidal devices were conceived of in the 1980s by Yablonovitch [8] and John [9] for photonic applications [10] to critically affect the propagation of light. These researchers evaluated how materials with periodic dielectric properties could give a localization of photons, or a photonic band gap. Materials with a photonic band gap could, for instance, pass one wavelength of light, but block another. The first artificial device using colloidal crystals as a photonic manipulator was patented by Sandy Asher [11]. He used a colloidal particle film to control the propagation of photons using polystyrene particles to filter narrowband radiation. Since many factors determine the nature of the stop band and therefore the colour properties of photonic crystals, much research is being done on crystal systems that change colour in response to a particular stimulus. For example, crystals can be mechanically deformed to change

the distances between the spheres. Polymers have been used to infill between the spheres in a photonic crystal can be swollen with solvents, forcing the spheres apart. These stimulus responsive systems are being explored as sensors and for display technology, for example photonic paper [12], humidity sensors [13], and integration of colloidal films for miniaturised spectrometers [14]. Since their first use nearly 30 years ago, many advances have been made, notably the “champion” diamond photonic band-gap structure [15, 16], cloaking [17], and negatively-refracting meta-materials [18, 19].

#### **1.4 OPTICAL PROPERTIES OF PHOTONIC CRYSTALS**

Photonics is the investigation of light, its transmission, emission, amplification and detection. Light can be transmitted through any transparent medium, in optical communications optical fibres allow for transmission over hundreds of kilometers. Photonic crystals are fabricated structures with engineered optical properties. A photonic crystal is defined as “a periodic dielectric structure with an index of refraction periodicity of the order of the wavelength of light” and hence may be able to affect the motion of photons in a similar manner that semiconductor crystals affect the motion of electrons [20]. These structures were first investigated in the 1980s, and have since been researched for their potential applications, which may include electro-optic components, ultra-small lasers and optical fibres, telecommunications, information processing, illumination, spectroscopy, medicine, and military technology.



Photonic crystal properties are determined by the periodicity of the index of refraction, which can be scaled from submicron dimensions to control UV/Visible/IR light. Since the wavelengths being controlled are typically of the order of hundreds of nanometers, photonic crystals need to be scaled at this level, i.e. ~200nm (giving a response in the blue region) to ~400nm (giving a response in the red region).

Photonic crystals contain regularly repeating regions of high and low dielectric constant which exhibit diffraction-based phenomena called stop bands. According to conventional optics, when an electromagnetic plane wave crosses the boundary between two media, refraction and reflection occur at the interface between these two media. In a photonic crystal, which consists of periodic arrays of boundaries between components of high and low dielectric constant, the scattered waves at these boundaries can either interfere constructively or destructively. If the periodicity of the variation is comparable to the wavelength of light, photons may or may not propagate through this structure depending on their wavelength. Wavelengths of light that are allowed to travel are known as modes, and groups of allowed modes form bands. Disallowed bands of wavelengths are called photonic band gaps, i.e. ranges in the electromagnetic spectrum in which electromagnetic waves are prevented by destructive interference from passing through the crystal in specific directions. Consequently, the interference gives rise to the opening of so-called photonic band gaps (PBGs), which are analogous to forbidden zones in the electronic energy band structure of solids. The term “Photonic Crystal” is therefore used to signify the similarity between photonic crystals which act upon photons and atomic crystals acting on electrons. The photonic band gap can therefore

provide a means to control optical emissions. To obtain a photonic band gap for optical frequencies, it is essential to fabricate structures that are 3-dimensionally periodic on an optical scale and composed of a solid with a high refractive index ( $n$ ). An image of a typical colloidal photonic crystal structure is given in Figure 1.4 below.

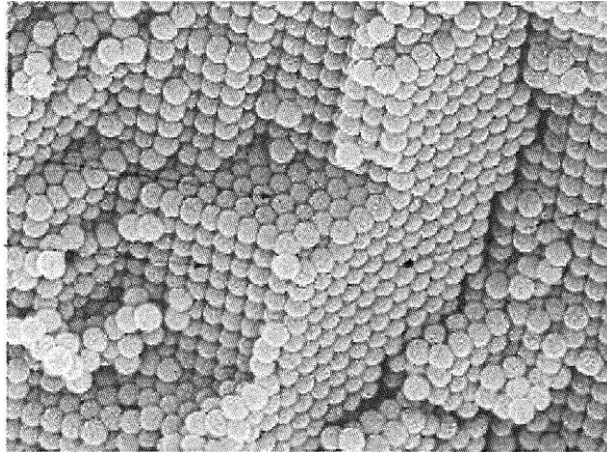


**Figure 1.4. SEM image of a typical colloidal photonic crystal structure [22].**

Most materials derive their colour by the absorption of visible light. When a substance absorbs certain wavelengths of visible light, its colour is determined by the wavelengths of visible light that remain. The substance exhibits the colour that it reflects, which is complementary to the colour of light that it absorbs. Photonic crystals, on the other hand, appear coloured, not due to absorption of light, but due to diffraction of light from the crystalline arrangement of their mono-dispersed particles. A consequence of this difference in the origin of colour is the ability to observe two components of the light instead of one. Photonic crystals do not absorb the complementary colour; this colour is instead transmitted through the opal (Figure 1.5). At a particular particle size, a sample can look green when observed in reflection, and red when observed in transmission. This is often referred to as structural colour.

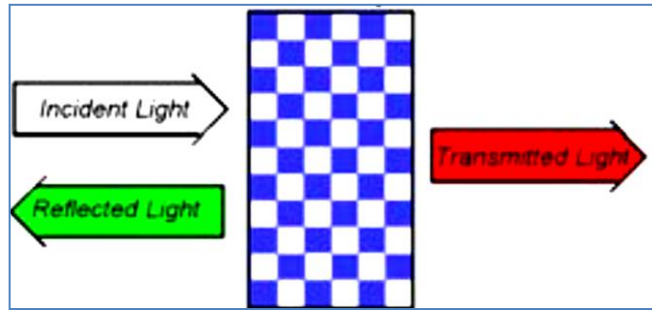


Figure 1.5. Observed behaviour of the interaction of incident white light with photonic crystals. When white light strikes the sample, it is separated into two components: light of one colour is reflected from the surface of the opal, while light of the complementary colour is transmitted through the opal, (adapted from [21]).

Colloidal photonic crystal films tend to grow in face centered cubic (fcc) crystal-like structures with the (111) planes of the crystals oriented parallel to a flat substrate [22-24], so that the (111) plane is most usually seen in the upper surface of the films, shown in figure 1.6 & 1.7. Measurements of the stop bands of these photonic crystal films can be most easily made by observing the spectroscopic behaviour of the films in a direction perpendicular to the sample surface (and hence the (111) planes). (The (111) refers to a type of notation referred to as Miller indices and will not be described further). One of the simplest ways to probe the structural and optical quality of colloidal crystals is by observation of their reflectance and transmission spectra as shown in figure 1.6. One then observes the first stop band described by a combination of the diffraction Bragg law, and refraction, Snell's law.

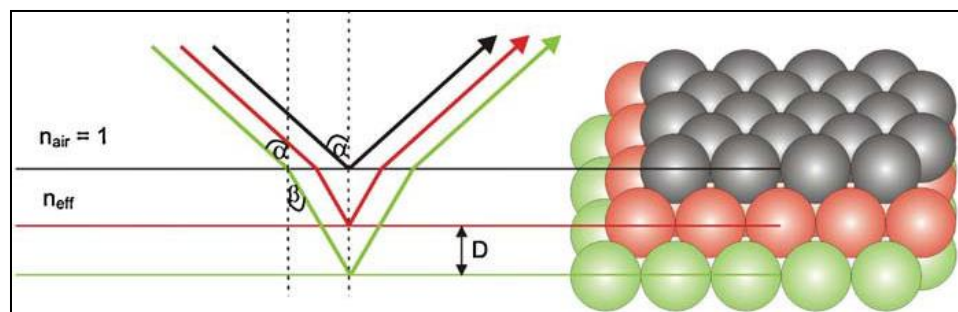
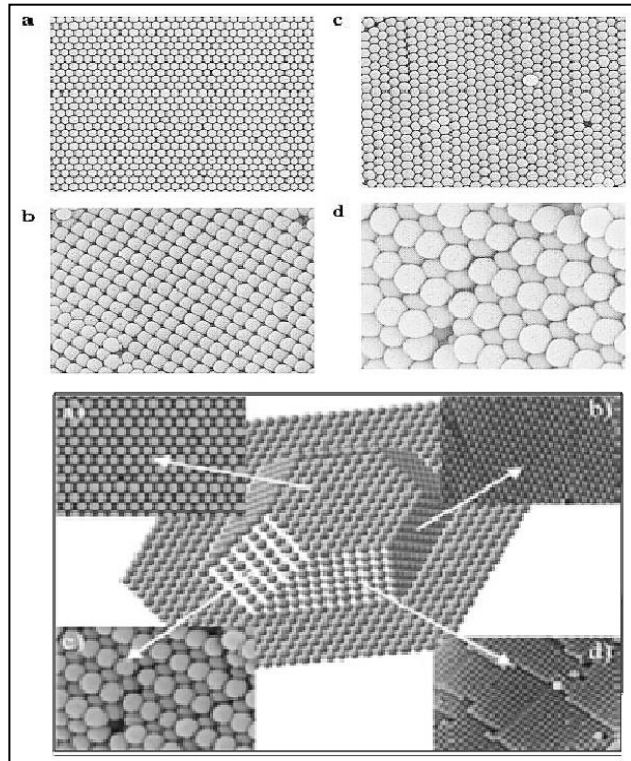


Figure 1.6. Scheme of the optical path of incident light in an opal. [25]



**Figure 1.7. Upper (a-d): SEM micrographs of: top surface (a); and 3 different lateral surfaces observed in cleaved edges (b-d) of a colloidal crystal film. The hexagonal arrangement observed in the top surface (a) could correspond to a number of the possible stacking sequences of sphere layers, the square, triangular, and rectangular arrangements observed in the cleaved edges (shown in b, c, and d, respectively) are only compatible with fcc packing (adapted from [22]). Lower: SEM images of four facets in a real opal compared with a model crystal (centre). (a) Outer (111); (b) inner (111); (c) inner (110); (d) inner (100). (adapted from Ref.[26])**

#### **1.4.1 THE BRAGG-SNELL LAW**

Crystals can diffract electromagnetic waves that have approximately the same wavelength as the scale of their repeating patterns; therefore in order to measure the distances between atoms in crystals (typically less than a nanometre), short wavelength electromagnetic waves such as X-rays are used. Specifically, X-rays are thought of as being “reflected” by planes of atoms in crystals. Whether the reflected X-rays interfere

constructively or destructively depends on a number of factors; the conditions for constructive interference can be summarized by Bragg's law of diffraction:

$$m\lambda = 2d\sin\theta_{in} \quad (1)$$

Where:

- $m$  = the diffraction order (usually, but not always 1)
- $\lambda$  = the wavelength of the diffracted light at the centre of the stop band (or, the wavelength of the Bragg reflected peak)
- $d$  = the layer spacing between the planes of the crystal
- $\theta$  = the angle between the incident X-rays and the normal to the planes of the crystal.

The inter-planar, or layer spacing for an fcc crystal,  $d_{111}$ , is given by:

$$d_{(111)} = (2/3)^{1/2}D \quad (\text{or} = 0.816D) \quad (2)$$

Where:

$D$  = the centre-to-centre distance of the nano-particles, or equivalent to the mean diameter of the particles.

By the same considerations, the lattice constant of the photonic crystal must be comparable to the wavelength of light, in order to satisfy the Bragg equation. Bragg scattered waves interfere constructively resulting in a high reflection (or low transmission) band of wavelengths. Unlike the electronic band gap in semiconductors

leading to absorption, the photonic band gap corresponds to the range of wavelengths that is not allowed to propagate through the structure resulting in reflection [27].

A representative transmission and reflectance spectra for a photonic crystal film is shown in figure 1.8. The major reflection around 600nm (in this case) corresponds to the stop band of the photonic crystal film.

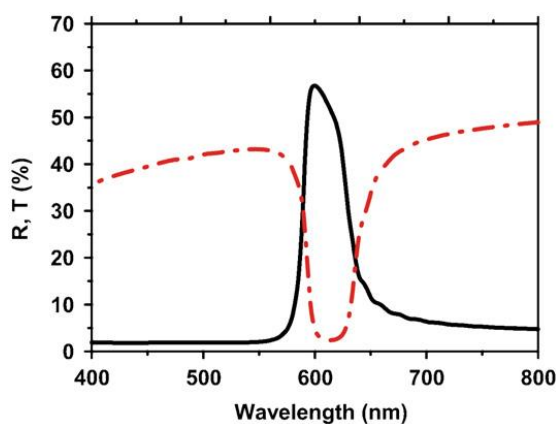


**Figure 1.8.** Reflection (R, solid line) and transmission (T, red dashed line) spectra for a self-assembled photonic crystal with a stop band around 600nm (corresponding to a particle size of approximately 280nm) [44].

The colour of light reflected from the photonic crystal film corresponds to the wavelength of the centre of the stop band, which ultimately depends on the diameter of the spheres; therefore this wavelength can be used to calculate the diameter of the spheres in the photonic crystal. This colour is approximately complementary to the colour of the light transmitted through the film, (Figures 1.8 & 1.9).

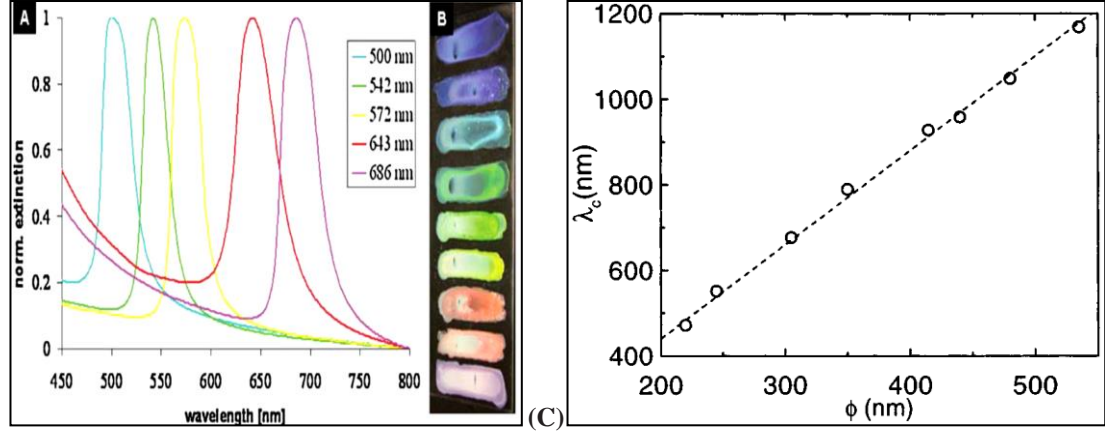


Figure 1.9. (A) Reflection spectra showing the Bragg peaks of some polymer colloidal photonic crystal films, which consist of different sphere sizes and (B) corresponding photographs. (C) The Bragg reflection maximum wavelength ( $\lambda$ ) plotted against the sphere size, and fitted to Bragg's law (dashed line). [25]

However, since light can also be refracted by photonic crystals, this must be accounted for in the equation, resulting in a combination of the diffraction Bragg law, and refraction, Snell's law:

$$\eta_1 \sin \theta_1 = \eta_2 \sin \theta_2 \quad (3)$$

Where:

- $\eta_1$  = refractive index of medium 1 (from the incoming medium)
- $\sin \theta_1$  = incidence angle
- $\eta_2$  = refractive index of medium 2
- $\sin \theta_2$  = angle of refraction

Combining equations (1), (2) and (3) gives a master equation, often referred to as a modified Bragg (or Bragg-Snell) equation:

$$m\lambda = 2d(n_{\text{eff}}^2 - \sin^2 \theta)^{1/2} \quad (4)$$

Where:

- $m$  is the diffraction order
- $\lambda$  is the wavelength of the diffracted light at the centre of the stop band
- $\theta$  is the angle between the incident light and the normal to the planes of spheres in the crystal. For a beam of incident light striking perpendicular to a set of planes,  $\theta$  would be  $0^\circ$ .
- $d$  is the spacing between the planes of spheres in the crystal. For the face centered cubic structure, the spacing between the (111) planes of spheres is  $(2/3)^{1/2}$  times the mean diameter of the spheres.
- $n_{\text{eff}}$  is the effective refractive index of the crystal (calculated as a weighted average of the materials present)

In accordance with this modified Bragg law, the minimum in the transmission spectrum (or peak reflectance) moves to shorter wavelengths with increasing angle of incidence,  $\sin \theta$ , as shown in Figure 1.10.



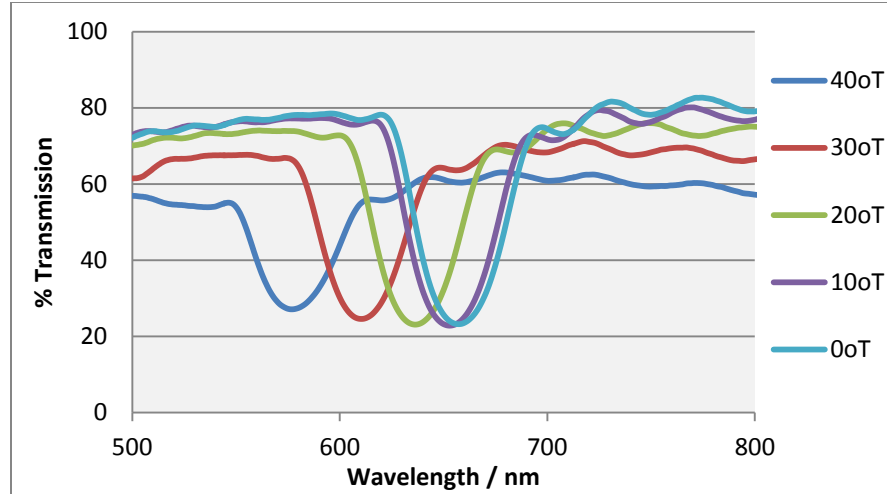


**Figure 1.10.** Typical transmission spectra for different incidence angles,  $\theta$ , in a sample made from 280nm diameter silica particle spheres (taken from a sample prepared in this study).

Also within the Bragg equation, increasing the lattice spacing,  $d$ , will cause the transmission dip to move to longer wavelengths. This can be done by increasing the separation between the colloidal spheres, or by stretching or swelling the lattice structure, as shown in Figure 1.11 [28], and by changing the lattice structure from a fcc structure to another lattice structure, Figure 1.12. The lattice parameter is a fundamental distance which is used to characterize the separation between the basic building blocks of this material.

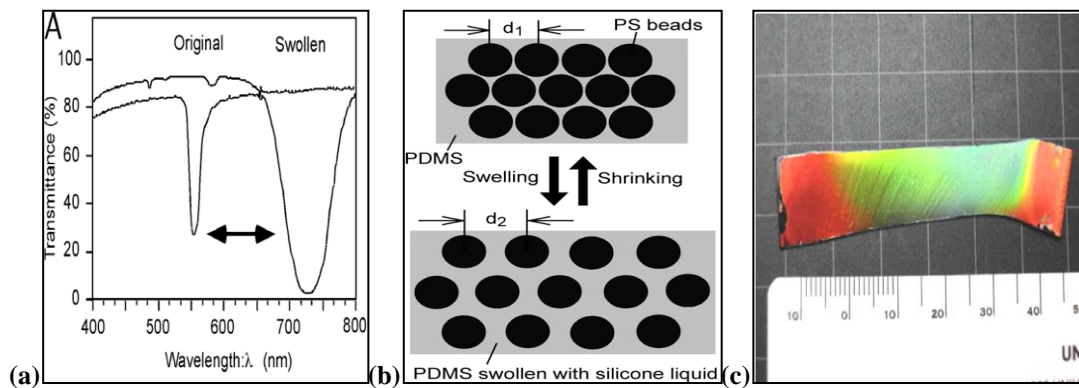


**Figure 1.11.** Expanding lattice distances of fcc (111) planes by swelling. (a) Change of the wavelength of Bragg diffraction. (b) Colloidal crystal material within a PDMS elastomer. The lattice distance of colloidal crystal enables reversible change by swelling and shrinking of PDMS elastomer. (c) Plastic deformation imaged as change of structural colour [28].

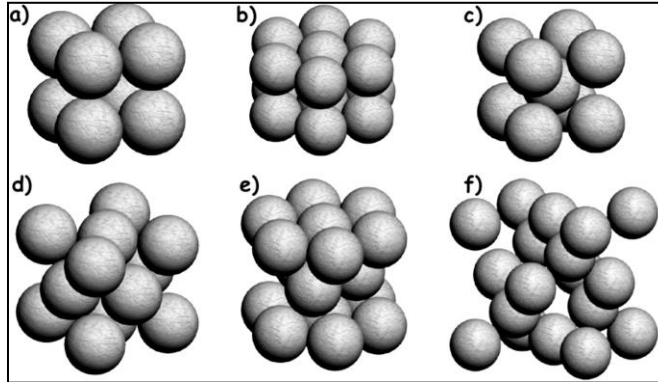


**Figure 1.12: Different lattice structures effect d, a) simple cubic, b) hexagonal, c) body centred cubic, d) face centred cubic, e) hexagonal close packed, and f) diamond lattice.**

Refraction is the bending of a wave when it passes from one medium to another. The amount of bending depends on the refractive indices of the two media, and is an indication of how much a material can bend light. The refractive index of a material is defined as the speed of light in a vacuum divided by the speed of light in the material, and is also described by Snell's Law (Eq. 3). The mean effective refractive index of a colloidal photonic crystal takes into account the fact that the spheres must have a different refractive index than the surrounding medium in order to behave as a photonic crystal. The effective refractive index is calculated using equation 5:

$$n_{\text{eff}}^2 = (V_s n_s^2) + (V_m n_m^2) \quad (5)$$

where:

- $n_{\text{eff}}$  is the mean effective refractive index of the crystal
- $V_s$  and  $V_m$  are the volume fractions of the spheres and medium. For a face centered cubic structure, these values are 0.74 and 0.26, respectively.
- $n_s$  and  $n_m$  are the refractive indices of the spheres and medium, respectively

As can be seen from the modified Bragg equation, the Bragg reflectance peak wavelength (or transmission dip) can be changed by varying one of a number of factors, either:

- 1 D, the particle size: reflectance peak will shift to longer wavelengths with increasing particle size
- 2  $\theta$ , “reflective” angle: reflectance peak will shift to shorter wavelengths with increasing angle
- 3 d, lattice spacing: the Bragg peak can be changed by changing the lattice structure from fcc to another, e.g. bcc, diamond structure, etc;  
or by stretching/compressing the lattice structure
- 4  $\eta_{\text{eff}}$ , effective refractive index: the Bragg peak can be changed by changing the construction materials of the photonic crystal

Figure 1.13, therefore illustrates each of the parameters which can have an effect on the optical properties of photonic crystals.

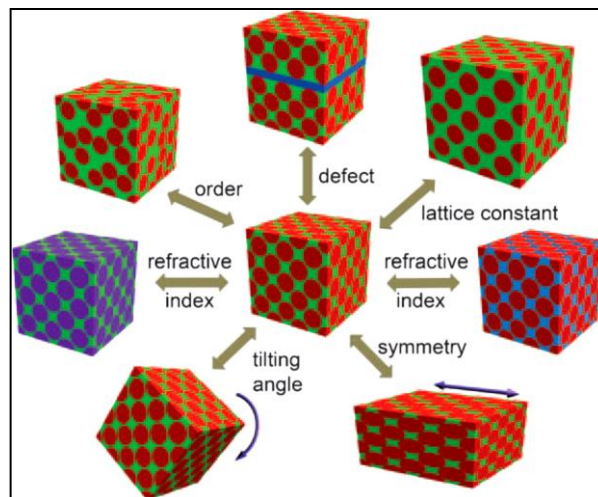


**Figure 1.13. Schematic illustration of the parameters that can be tuned in a 3D responsive photonic crystal structure [29]**

### 1.4.2 THE PHOTONIC BAND GAP

In addition to the effects described above, multiple scattering becomes an important factor and higher order reflections are no longer described by the Bragg equation, especially for the case of large refractive index contrast between spheres and interstitial voids. In this scenario the so-called full band-gap may evolve (Figure 1.14) [8, 9]. The opening of a photonic band gap is determined by the refractive index contrast between the particles and the voids. However, in self-assembled opal films (dielectric spheres and air voids), no matter how high the RI contrast is, no complete photonic band gap can be achieved, owing to the intrinsic structural properties of the FCC lattice, (the photonic band gap (PBG) is closed along  $\Gamma$ -W direction in the Brillouin zone for any value of RI contrast). However, dielectric spheres arranged in a diamond structure are theoretically proven to exhibit a complete PBG which extends throughout the Brillouin zone [30], but colloidal crystallization cannot easily be used to form a diamond structure, (the fcc structure being predominant, as discussed earlier). Experimentally opal films must be infiltrated with a material with a sufficiently large refractive index, and the spheres subsequently removed by etching or other techniques. The resulting structure is usually referred to as an inverse opal, and a full band-gap has been predicted if the infill has  $n > 2.85$ . As a result of the full band-gap, photons of this frequency cannot propagate in any direction inside the photonic crystal (PC). Thus the crystal becomes a perfect mirror for light, and light may be localized inside [8-10].

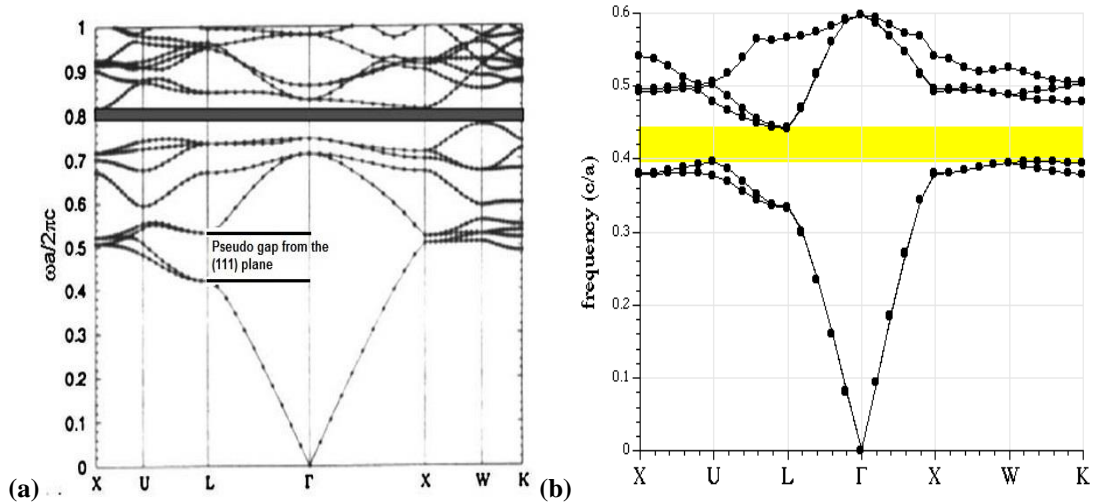


**Figure. 1.14.** Calculated optical band structures of a 3D Photonic Crystal having (a) fcc structure of air holes in a silicon matrix, and (b) diamond lattice. The dark grey and yellow bars indicate the full band gap. [25]

## 1.5 PHOTONIC CRYSTALS AND SELF ASSEMBLY

Photonic crystal structures occur naturally e.g. in opal gemstones, where spheres of silica form a close-packed periodic structure, giving rise to the typical “play of colour” or opalescence of these gems. Structural colour is also a significant feature in some insects, most notably butterfly wings, and certain beetles [31, 32].



**Figure 1.15.** Images of naturally occurring photonic structures (peacock feathers, opals, butterfly wings, and beetle skeleton) (Images taken from [32]).

It is possible to create photonic crystals by assembling colloidal silica or polymeric particles into regular crystalline arrays. One approach is to allow the particles to self-assemble, for which there are a large variety of experimental methods. Submicron silica or polymeric spherical particles with low size dispersity, (i.e. mono-disperse to <5% [33]), can be induced to organise into thin crystalline films, sometimes referred to as synthetic opals. Photonic crystals comprised of these colloid sized particles, are usually fabricated by drying a suspension of the colloidal spheres, as the suspension dries, the spheres pack together into face-centered cubic (fcc) structures [22, 23], shown in figure 1.7.

Self-assembly is considered to be a cost effective method, in comparison to “top down” fabrication methods, such as lithographic and other mechanised techniques designed to make 3D ordered photonic crystals. The first 3-dimensional photonic structure was produced by Yablonovitch et al. (1991) [34] who constructed a fcc lattice by drilling or etching through a slab of “material”. Later lithographic methods were designed by Noda et al. [35] and Lin et al. [36, 37] and used for making 3D photonic crystals, often referred to as woodpile or layer-by-layer structures. Other techniques that have been used are micromanipulation (2002) [38], and a holographic technique (2000) [39, 40] (Figure 1.16). As can be seen, these “top down” processes are generally complex, multi-step methods which are therefore relatively expensive. By contrast, the self-assembly of mono-disperse submicron silica or polymer spheres into colloidal crystals provides a simple, fast, and cheap materials chemistry approach to producing photonic crystals [41].

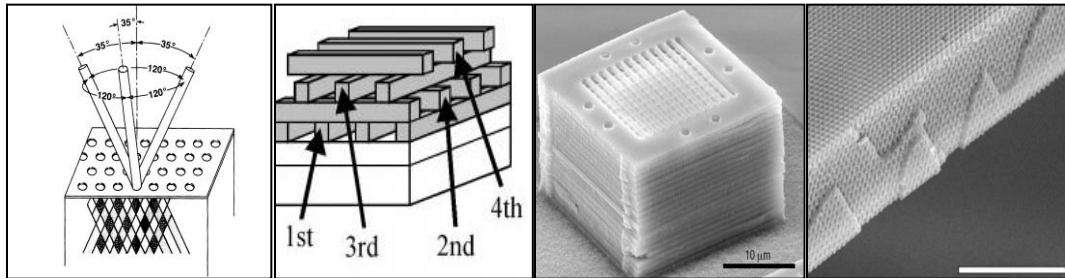


**Figure 1.16.** “top down” photonic crystal assembly methods; (a) drilling [34] (b) wafer etching woodpile [35-37] (c) micromanipulation [38] (d) holography [39, 40]

The first deliberate attempt to make an artificial opal was by Philipse (1989) [42] which possessed highly ordered silica spheres. Davis et al. (1991) [43] produced artificial opal films by sedimentation. Subsequently, similar close packed structures have been fabricated using silica or polymer colloidal suspensions, in a variety of self-assembly methods (which will be reviewed in the next section) including gravitational sedimentation, evaporation deposition, dip coating, under oil crystallisation, Langmuir-Blodgett film formation, sonication, and many others.

All self-assembly methods have certain advantages and disadvantages. While they are generally inexpensive, and most methods do not require sophisticated laboratory equipment, there are drawbacks associated with the self-assembling routes, such as the difficulty in getting crystalline structures other than fcc, and the inability to control the number of defects in the crystals, such as point defects (interstitial particles, vacancies), stacking faults, dislocations and micro-cracks [44].

The strategy behind the colloidal assembly approach is to exploit the self-assembly of mono-disperse sub-micrometre spheres to create a synthetic opal film, which can act as a template into which a semiconductor (or other material) is infiltrated.

Subsequent removal of the template leads to a three-dimensional (3D) photonic crystal inverse opal that has periodic air-spheres embedded inside the semiconductor skeletal framework. If the refractive index of the semiconductor is sufficiently high ( $>2.85$ ), such a structure should exhibit a complete band-gap [45]. However, while self-assembly can yield high quality films, defects will always appear in the crystal lattice. These manifest themselves in the optical spectra, as a broadening of the peaks, diffuse scattering and a decrease in reflectance (increase in transmission) at the gap wavelength [26] which can easily close the gap by filling it with localized photonic states. Renarajan et al. [33] suggest the primary source of scattering is point defects, i.e., structures similar in size to the spheres such as vacancies, while Galisteo-Lopez et al. [46] state that stacking faults along the (111) direction, are not known to affect the optical properties of the crystal, but greater polydispersity ( $>5\%$ ), will broaden the width of the Bragg peak [47].

The other dominant type of defect in colloidal crystal films is cracking. Cracks may be observed using an optical microscope at magnifications as low as 40x. Micro-cracks can range from very fine - a fraction of the diameter of the particles themselves - to much greater than a sphere diameter. Micro-cracks are considered to be largely unavoidable for colloidal crystal films of silica spheres. When a colloidal dispersion is applied to a rigid substrate and allowed to dry, its volume decreases due to evaporation of the solvent. The silica particles have a water and alcohol solvation layer surrounding them. After they self-assemble into a closely packed array, the loss of the solvation layer causes a decrease in the “apparent” sphere size, forcing the closely packed array to shrink. Constrained by the rigid substrate, this volume reduction generates various



stresses in the drying film, and if these stresses exceed the strength of the film, they will release in the form of cracks [1, 48]. Typical crack densities are about one per hundred to several hundred spheres, with the highest quality films having the smallest number of cracks. But since the solvation layer does not change proportionally with the size of the spheres, films formed from smaller particles will naturally exhibit more cracks [48].

Adjacent crystal domains often fit like pieces of a jigsaw puzzle, the registry of the fcc packing being preserved across the cracks, indicating that the cracks were formed after the spheres had self-assembled into the crystalline structure. Hartsuiker and Vos [49] show that for photonic crystals, with domains that are required to be as large as possible, combined with controlled thickness, the possible combinations are limited, because the ratio of the thickness and domain size is fixed. This means that the density of grain boundaries (cracks) is related to the opal thickness. Given that grain boundaries contribute to the scattering of light, and if the ratio of the thickness and domain size is fixed, then the extinction due to scattering from grain boundaries is therefore fixed for each thickness. This means that there is an upper limit to the reflectivity measured in the Bragg peak if the focus of the light beam is larger than a crystal domain. This in turn means that there is a lower limit to the range of thicknesses for which the scattering from grain boundaries can be reduced to zero, given a certain focus size of the light beam.

Wong, Kitaev, and Ozin [48] state that cracks do not appreciably affect the order parameter and optical properties for relatively large-area silica colloidal crystal films, since the portion of the surface occupied with cracks is minor (<1%) and their

influence tends to average out. However, cracks can pose problems for miniature optical devices relying upon light interactions with very small, well-defined areas within a colloidal crystal film [48]. Often there is a perceived problem with a material displaying such defects; however the presence of cracks may not be detrimental in the application of the final product.

## **1.6 COLLOIDAL PHOTONIC CRYSTAL PRODUCTION METHODS**

Colloidal crystallisation (known as a bottom up self –assembly approach) of silica nanoparticles offers the opportunity to produce large scale photonic crystals more cost effectively than top down micro-fabrication methods (e.g. lithography and etching etc). A current perceived “roadblock” for the colloidal crystallisation approach is cracking of the formed crystal films due to shrinkage during drying from the colloidal solution. Self-assembly of colloidal crystals can be achieved through a variety of methods, including gravitational sedimentation, evaporation deposition, dip coating, spin-coating, Langmuir-Blodgett layering and under oil crystallisation, (some of which are discussed in more detail in below). A number of methods are shown schematically in Figure 1.17 below. Also within this review section large area production methods that have been developed which reduce and/or avoid the issue of cracking in these films are described.

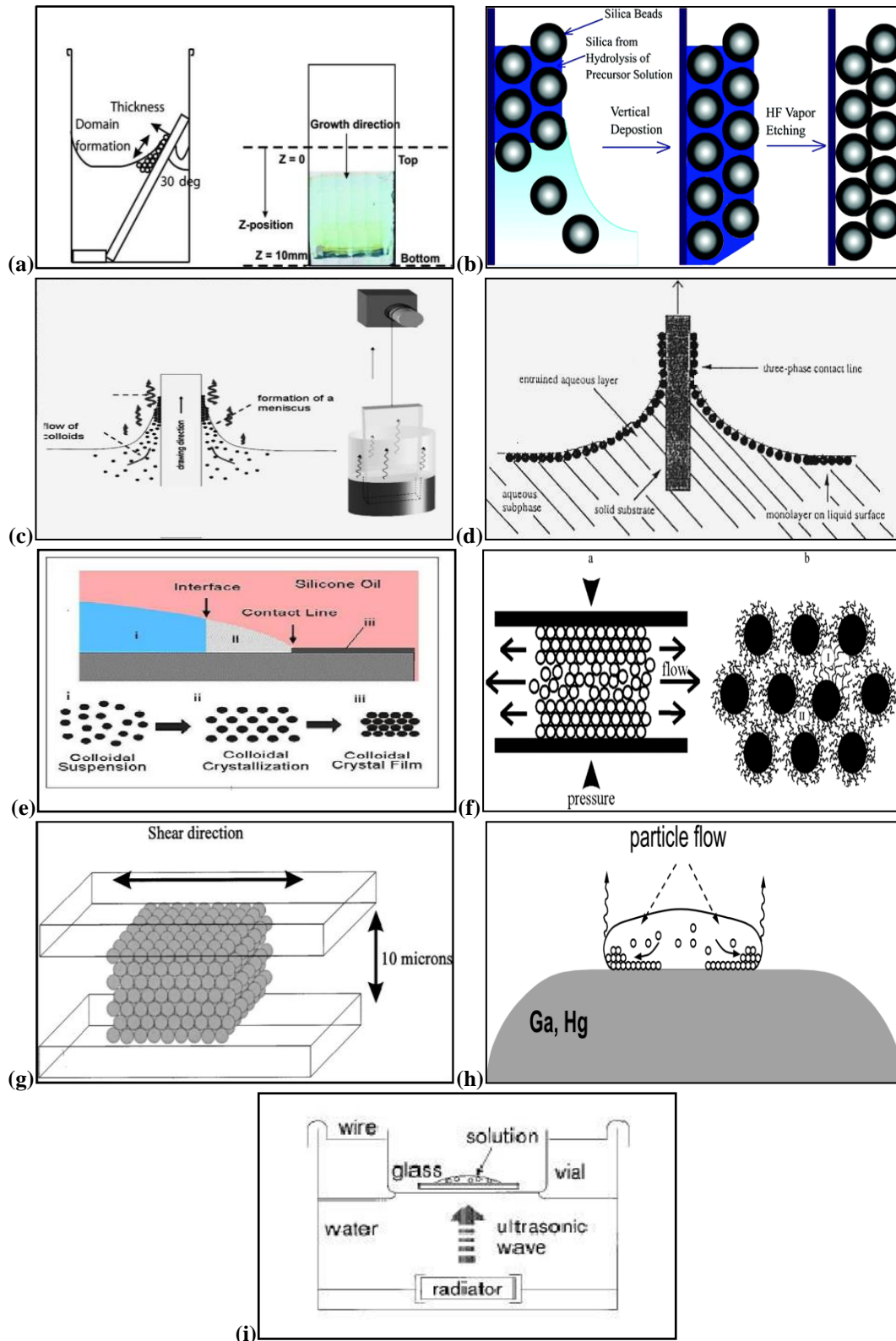


Figure 1.17(a-i). (a) Controlled Evaporation deposition [49]; (b) Silica infilled evaporation deposition [50]; (c) Vertical dip coating [51]; (d) Langmuir-Blodgett [52]; (e) Under oil crystallisation [53]; (f & g) Shear induced mechanisms [54, 55]; (h) Crystallisation on fluid substrates [56]; (i) Sonication [57].

Of concern is that during the crystal growth process defects such as vacancies, stacking faults, dislocations, and grain boundaries, will influence the photonic band gap and, depending on the type of defect, may make it unsuitable for certain applications. Therefore photonic crystals require well-ordered domains that are large as possible, with minimal localized defects.

However, the dominant defects in colloidal crystal films are micro-cracks, which could pose a problem for miniature optical devices relying upon light interaction with small well-defined areas in the colloidal crystals. Unwanted light scattering due to cracks would be reduced in large crystalline domains.

Thin opaline films on glass substrates give large (cm) well-ordered structures in which the fcc (111) plane is parallel to the plane of the glass slide. The individual crystals are, however, separated by cracks, which appear due to shrinkage at a late stage of drying, as the volume density of the of the colloidal crystal approaches 74%. The cracking due to drying can make for serious technological consequences because they can destroy the efficacy of coatings, and controlling these drying induced cracks is very important in areas such as paints, paper coatings and ceramic films [58].

The essential issue here is that when a thin film of a colloidal dispersion is applied to a nonporous rigid substrate and allowed to dry, its volume decreases due to evaporation of the solvent. Constrained by the rigid substrate, this volume reduction generates various stresses in the drying film. If these stresses exceed the strength of the

material, they will release in the form of cracks [1]. In colloidal photonic crystal self-assembly, “depending on the crystallisation conditions and particle size, these cracks separate to crystallites of 40µm (quickly dried) and 250µm (very slow drying, 1 week). .... since a high refractive index contrast is desired, it is not acceptable to fill the voids [56]. Another factor affecting the stresses in the drying film is the drying of the water/alcohol solvation layer (or liquid bridge) surrounding the spheres after self-assembly, which may cause a decrease in individual sphere sizes, forcing the closely packed array to shrink and give rise to cracks. [48]

Whilst a large variety of self-assembly production methods have been investigated, many researchers have not investigated the major issue of cracking in the final film. For the production of large-scale photonic crystals, large area methods need to be developed (with the need to have reproducible, high quality films in a relatively short time period), therefore the two main causes of cracking, are the constraints induced by the rigid substrate, and stresses exceeding the strength of the material, need to be overcome.

The thermodynamic factors which drive cracking were considered by Griffith in his energy balance concept. According to this concept, cracking will only occur as the film thickness exceeds a critical value [1, 59]. The critical film thickness can be expressed as:

$$H_c = 2G_c E^* / (Z\sigma^2) \quad (\text{Eq. 6})$$

Where:

$G_c$  = the critical strain energy release rate (a measure of fracture toughness)

$E^* = E/(1-\nu)$ , where  $E$  is Young's modulus

$\nu$  = Poisson's ratio,

$\sigma$  = the biaxial tensile stress,

$Z$  = a parameter whose value depends on the geometry of the crack tip and is the order of 2.

Hence, cracking can be avoided either by keeping the stress low, which means slow drying or reducing the surface tension of the liquid, or by increasing the mechanical properties of the drying powder compact. Although decreasing the drying rate should theoretically allow for the preparation of crack-free films, Juillerat et al. [60] calculated that by decreasing the stress down to 1kPa would require a drying time of more than 8 months, which is clearly impractical.

In order to control the formation and quality of colloidal crystals, various self-assembly conditions and parameters have been studied, including modification of the drying conditions, temperature, colloidal solvent, humidity, suspension / air / substrate contact line and meniscus forces etc, and controlling the suspension chemistry, including modifying the particle chemistry, and controlling the substrate chemistry. Some or all of these factors may be used to control and avoid crack formation during the colloidal film drying process.

## **1.7 INTRODUCTION TO SELF ASSEMBLY METHODS**

### **1.7.1 RING FORMATION**

When a particle loaded droplet dries the residue left is typically thickest, and hence most concentrated, along the edge of the stain giving the deposit a ring like appearance. Since the suspension was uniformly distributed in the liquid prior to drying, this type of segregation at the edge is at first surprising, and is often referred to as a “coffee ring” deposit. Figure 1.18(a), shows how the probability of escape of an evaporating molecule is affected by its point of departure. A random walk initiated at the centre of the drop results in the molecule being reabsorbed (dashed line). However, the same random walk initiated from the edge allows the evaporating molecule to escape. This demonstrates why the evaporation rate is larger at the edge [61]. Figure 1.18 (b) shows a typical “coffee ring” formation resulting from a dried colloidal deposit. Hence, colloidal particles accumulate at the contact line. Often the contact line undergoes a sequence of stick-slip, or pinning-depinning, events with particles accumulating whenever the contact line is pinned. The pinning-depinning process may then lead to multiple ring formation [62] (Figure 1.18 (c)).

Controlling the distribution of solute during drying is therefore vital in many industrial and scientific processes, e.g. paint manufacturers use additives to ensure that the pigment is evenly dispersed and remains so during drying. Ring formation and segregation effects are undesirable in many cases, and this is also the case in this study

where self-assembly is being used to produce the required uniform colloidal films necessary to produce the photonic band gap effects, discussed earlier.

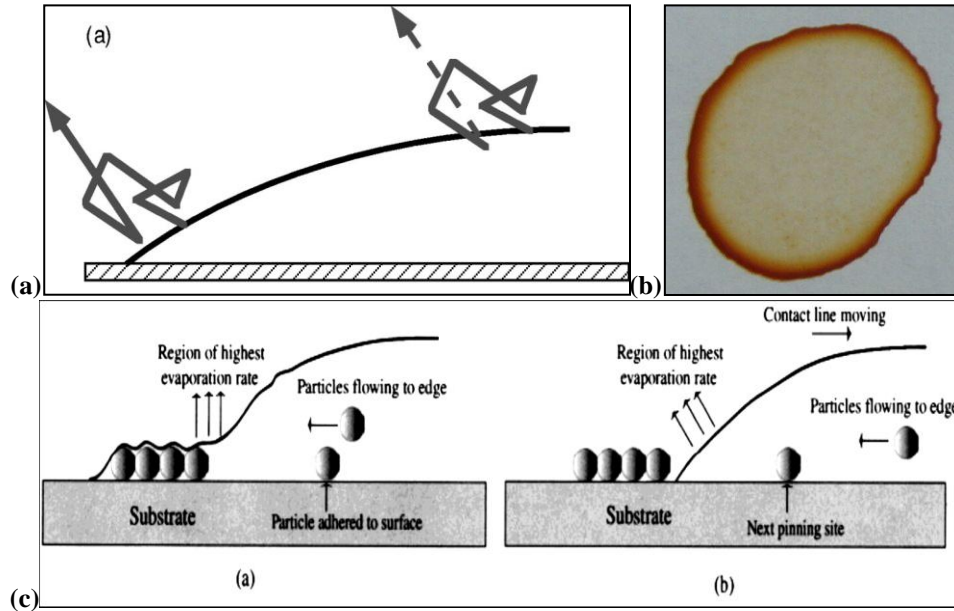


**Figure 1.18.** Upper (a) shows how the probability of escape of an evaporating molecule is affected by its point of departure. [61]. Upper (b) shows a typical “coffee ring” formation from a dried colloidal deposit. Lower (a) A schematic of a pinned contact line. Evaporating water at the contact line induces a flow of particles toward the edge. However, some particles are pinned to the substrate. (b) Once the contact line “slips”, it keeps moving until it runs into a fixed particle, at which point it may become pinned again [62], resulting in multiple ring formations.

## 1.7.2 GRAVITATIONAL SEDIMENTATION

One of the first and simplest methods described to produce colloidal photonic crystals was gravitational sedimentation. When gravitational sedimentation was used to concentrate dispersions of colloidal silica, Davis et al. (1989) noted that with sufficiently small particles, slow sedimentation permitted the rearrangement into iridescent ordered structures [63]. Although the sedimentation method is simple, requiring little operator involvement, Salvarezza et al. (1996) [64] noted there are difficulties in controlling the morphology of the top surface and the number of layers of the 3D ordered arrays. Also



film formation timescales are of the order of weeks to months, for the sub micrometre particles to be completely settled.

### **1.7.3 CONTROLLED EVAPORATION (Figure 1.17(a))**

One of the most researched methods to produce colloidal crystals is the controlled evaporation vertical deposition method of Jiang, et al. (1999) [65]. Compared to sedimentation, controlled evaporation, driven by capillary forces, produces superior quality colloidal crystals, having fewer defects and controlled evaporation films are generally not polycrystalline due to directional crystallization in the meniscus. Capillary forces at the lowering meniscus assemble the particles as a result of evaporation of the solvent. The thickness of the fabricated films is controlled by the concentration of particles. Whereas initial findings suggested that film thicknesses obtained by this method were uniform, in reality sample thicknesses were found to increase from the top to the bottom of the substrate [49], because the concentration of the particles increases during evaporation, due to evaporation of the solvent. This concentration change therefore has an effect on film thickness over the time of deposition, usually 2-3 days. The optical properties, such as the stop-band width, and reflectance peak (transmission dip) are dependent on the film thickness [66]. However, film thickness can also be controlled to some extent by tilting the substrate at an angle [67].

Controlled evaporation has two limitations: first, the long times for evaporation; and second, deposition is limited to smaller colloidal spheres that sediment slower than the solvent evaporates. For silica particles sedimenting away from the meniscus, (thus terminating the deposition process), formation of continuous large-area colloidal crystal films from spheres larger than approximately 500nm is unlikely. To minimize sedimentation and provide a continuous flow of particles toward the meniscus region, Norris et al. [45] reported the addition of a convective flow, by heating a vial of a suspension of large (855nm) silica particles from the bottom. While demonstrating the preparation of very high quality films, their SEM images indicated defect densities were much lower than for sedimented opals. However, it has been reported that their convective procedure is difficult to reproduce [48].

In evaporation deposition and similar methods, evaporation induced self-assembly is driven by capillary forces at the meniscus. Maintaining an optimum rate of evaporation is crucial to achieving high quality colloidal crystals. Excessively high or low rates of solvent evaporation can induce stacking faults and micro-cracking. Temperature is the key parameter for solvent evaporation, and thus directly affects the assembly of the particles [48]. A high temperature will increase the kinetic energy of the particles, and result in a poorly ordered film. While low temperatures will prolong the assembly, and be costly in terms of time.

It is possible to increase the processing rate by elevating the evaporation temperature, but this can result in the deposition of less-ordered crystals. However,

increased quality colloidal crystals can be obtained in a controlled high humidity system, resulting from the existence of enhanced capillary forces between particles. Kuai et al. [68] discussed the effect of humidity on the quality of colloidal crystals. They compared the morphology of polystyrene (PS) (300nm) colloidal crystals obtained at elevated temperatures, with constant humidity (84%RH). High-quality crystals were fabricated at 60°C and 84%RH in 24 hours, while only poorly ordered structures were obtained at higher temperatures. However, at 60°C, if the humidity is reduced to 65%RH, the quality of colloidal crystals decreases. Therefore humidity is also a key factor for controlling the quality of colloidal crystals.

In their review of the growth parameters affecting the quality of colloidal crystals via controlled evaporation of 260nm PS particles in aqueous suspensions, Liu, Wang and Ji [69] found 35°C, 70%RH, and 6.0kPa, to be the conditions to obtain the highest quality colloidal crystals. (Note: in this paper, they added a pressure variable in the experiments, not normally used in many other controlled evaporation papers. Here pressure was controlled via a valved pump connected to a vacuum oven).

#### **1.7.4 SOLVENT EFFECTS IN CONTROLLED EVAPORATION**

Solvent also plays an important role in the self-assembly of colloidal crystals. Li and Marlow [70] investigated the effects of solvent in the deposition of colloidal crystals from colloidal suspensions of PS microspheres. Since ethanol and water are used as the solvents in most self-assembly processes studied to date, mixtures of these solvents at

varying ratios were used to tune properties, such as surface tension, viscosity, and volatility. They found that both the surface morphology (crack distribution and film thickness) and the structure (ordering of the microspheres) of the colloidal crystal films were influenced significantly by the solvent.

Wang et al. [71] also used an ethanol and water mixed solvent to deposit silica particles up to 600nm diameter. Here they used 10% ethanol in their aqueous ethanol mixture at 55°C to obtain their best films (whereas Li and Marlow used a 20% ethanol). Yoldi et al. [72] suggested their best films (largest domain sizes) were achieved using 50% ethanol at 70°C in their mixed aqueous solution. Yoldi et al. also increased their domain sizes fivefold, and hence reduced cracking within their films, by adding small amounts (0.5 – 1.0volume%) of co-solvents such as glycerol. As the co-solvent is non-volatile at room temperature, it remains between the particles, slowing down or avoiding complete drying. Hence the number of defects could be reduced and domain sizes increased.

Wang and co-workers [73] also used a mixed solvent suspension, 30% particles, 50% ethanol and 20% water by volume in their developed “room temperature floating self-assembly” method for the rapid fabricating relatively large colloidal crystal films of either silica or PS particles. Essentially they used fast dipping followed by horizontal drying at room temperature, with a mixed solvent suspension of particles, to produce uniform films over 10cm<sup>2</sup> in very short timescales, typically 10 minutes. They claim that a high solvent evaporation rate is crucial for the crystallisation at the air-liquid interface

in their method. They were also able to produce hetero-structures [74], and deposit onto porous substrates by this mixed solvent method [75].

#### **1.7.5 SILICA BONDING IN CONTROLLED EVAPORATION (Figure 1.17(b))**

Wang and Zhao added a silica precursor solution (containing TEOS) [50] to a solution of colloidal silica particles in a controlled evaporation crystal growth method to achieve a crack-free film. During the assembly process, additional silica is produced from hydrolysis of the precursor solution, filling the voids between the silica spheres and forming a crack-free film. The filling can then be removed using hydrofluoric acid, leaving a crack-free, but non-close packed crystal behind. Likewise, Hatton et al. [76] were able to co-assemble PMMA spheres and infilling material by controlled evaporation, the PMMA being easily removed to leave a crack free inverse opal structure. However, they noted that cracking did begin to occur in these structures at approximately 20 layers thickness.

#### **1.7.6 DIP COATING (Figure 1.17(c))**

Gu et al. [77] used a dipping method for the fabrication photonic crystals from polystyrene particles, the film thickness being controlled by either the particle concentration or the lifting speed.

Ye et al. [51] adapted the method from Gu to allow for the fabrication of opaline photonic crystals from large silica spheres (890nm diameter) using a combination of “lifting and stirring” (where evaporation has only a minor influence on the speed of the moving meniscus). Khunsin et al. alternatively maintained 398nm PMMA particles in suspension using noise vibrations, the acoustic vibration apparently giving the spheres a chance to move along the substrate and equalise the stress over the lattice, producing larger crystalline domain sizes [78].

#### **1.7.7 THE LANGMUIR-BLODGETT METHOD (Figure 1.17(d))**

Silica particles floated on a water surface can be deposited onto a cleaned substrate using a Langmuir-Blodgett trough. On compression of a colloidal silica particle monolayer on the surface of a water sub-phase, the upstroke of the Langmuir-Blodgett trough transfers the monolayer onto the substrate. By repeating the process a layer-by-layer colloidal film can be achieved with precisely known layer thickness.

Gil et al. [79] reported crack-free films from 455nm silica particle by the Langmuir-Blodgett (L-B) technique. By functionalising these particles with N-trimethoxysilylpropyl-N,N,N-trimethylammonium chloride (TMS) the silica particles were found to possess the right hydrophobic-hydrophilic balance to allow them to be spread at the air/water interface, (avoiding gravitational sedimentation) and for them to be transferred onto a glass substrate using a vertical dipping technique. However, the L-B approach is not able to tune the particle packing structure between each layer, and as

such a fully 3-D structure is unlikely, rather 2D+1D layers are more likely [80]. Here the first layer deposited consists of highly ordered domains, which make good contact with one another. With deposition of further layers the domain structure gradually disappears due to layer misalignments, but these layers still have a good degree of order, hence a (2+1)D structure is proposed [80]. Bardosova et al. [81] found that it may be unnecessary to functionalise silica particles up to 360nm to deposit repeated monolayers onto glass substrates by the L-B method

#### **1.7.8 UNDER OIL CRYSTALLISATION (Figure 1.17(e))**

Fudouzi [82] [83] uses a horizontal crystallisation technique which involves covering a polystyrene colloidal suspension with silicone oil. The opal film then forms by drying on a hydrophilic solid substrate. In the conventional method, a ring-shaped film usually forms at the edge (contact line) of the suspension on the substrate, as described previously. Drying under oil improves the process by drying the colloidal suspension such that it occurs without ring formation. The driving force of ring formation is based on capillary flow in the suspension from inside to outside because of the higher evaporation rate at the contact line. To prevent this capillary flow, the contact line of the suspension is covered with hydrophobic silicone liquid. As a result ring formation is suppressed and flat opal films with uniform structure formed. This method can be scaled up to coat large areas, 70cm<sup>2</sup>, with areas between cracks on average being approximately 50 x 200µm [82].

### 1.7.9 SHEAR INDUCED MECHANISMS (Figure 1.17(f & g))

Amos et al. [55] applied a lateral shear force (Figure 1.17(f)) across a prepared PMMA colloidal crystal, and from initial small domain sizes of approximately 100 $\mu\text{m}$ , were able to produce a single crystal region spanning the entire cell ( $\sim 2\text{cm}^2$ ). This shearing process could potentially be used to reduce the formation of cracks in thin films, and also to convert structures from (2+1)D type into a full 3D fcc structure, i.e. from “post deposition processing” of Langmuir-Blodgett films [84].

Ruhl, Pursiainen and others [54, 85-87] have used hard-core soft-shell particles to form crystalline structures over large areas with no cracking. The hard cores form the crystalline lattice, while the soft shells form a matrix around them, there being no free space between the spheres. Shear flow under uniaxial compression (Figure 1.17(g)) in melts of these particles rapidly leads to the formation of large area colloidal fcc crystals without cracks. Both inorganic (silica) and organic (polystyrene) core particles have been used in this method. This melt flow compression technique can produce very large areas in short timescales, with domain sizes of ca. 10s of square centimetres. However, local crystalline order is not as good in these films as that achieved through drying suspensions. Nevertheless films are macroscopically orientated and consist of large crystalline mono-domains. One drawback to this melt flow technique is that the films contain disordered, non-crystalline, layers between the outer crystalline layers.



#### **1.7.10 FLUID AND REDUCED FRICTION SUBSTRATES (Figure 1.17(h))**

As highlighted earlier, in the work of Xu et al. [1] the issue of cracks is believed to arise for two main reasons: the film is constrained by a rigid substrate, and drying stresses exceed the strength of the material. Lazarov et al. [88] suggest that there are shortcomings in depositing onto solid substrates, in that the surface has an inherent roughness, and “irreversible” sticking of the particles to the substrate may occur before their incorporation into the ordered array. They used a fluid substrate to reduce the effects of lateral sticking at the substrate surface, and were able to deposit crack-free ordered arrays of latex particles.

To overcome this “irreversible sticking”, Dimitrov et al. [89] and Grieseböck [56] used mercury and Lazarov et al. [88] worked with perfluorinated oil (F-oil) as a liquid substrate. Interfaces between fluids have been shown to be ideal for the assembly of colloidal particles. At the interface, the particles are highly mobile and rapidly achieve an equilibrium assembly [90].

In their experiments, Lazarov et al. [88] showed that 2D latex arrays can be formed over an F-oil substrate. They also proved that if the groups of particles are not completely dry, they can merge upon collision to form larger domains. The ordering process on F-oil showed many similarities with that on a glass substrate, however, they state there are several differences between the two cases, which are connected mainly with the ‘softness’ (vertical flexibility) of the surface of the F-oil substrate. Finally, the

formed arrays could be transferred onto solid substrates, without damage, after complete evaporation of the F-oil.

Griesebock et al. [56] used fluid substrates of mercury and gallium, to eliminate lateral sticking during crystallisation of colloidal PMMA particles, and successfully obtained high quality films over large areas, greater than  $2\text{mm}^2$  in size, with low defect densities. However, due to the nature of their substrate it proved difficult to transfer the crystals to a suitable substrate without breaking the film.

Sadhukhan et al. [91] proposed a spring model to simulate the crack formation on two different surfaces, glass and polypropylene (PP), and showed that the increased smoothness of the glass surface was also a factor in reducing the crack formation by allowing some slip of the particles across the smoother glass surface. Groisman and Kaplan [92] demonstrated that in many cases, cracking is due to friction between the substrate and suspension.

#### **1.7.11 VIBRATION ASSISTED DEPOSITION (Figure 1.17(i))**

Sasaki and Hane [57] used ultrasonic vibrations during the evaporation deposition of a colloidal solution of PS particles, in order to improve the quality and ordering of monolayers of colloidal particles. They suggest that sonication induces forces which may overcome the relatively weak interactions, both particle to particle and

particle to substrate, and therefore rearrange the particles in the film enlarging the ordered areas and reducing voids.

Járai-Szabó et al. [93] used a computer model based on a spring-block stick-slip model to simulate a 2-D monolayer sonication-assisted colloidal film forming method, and confirmed that random shaking during the drying process would produce more ordered structures. They also found that increasing the intensity of the random, ultrasonic force up to the limit of the pinning (or friction) forces acting on the nanoparticles is beneficial to film formation and could eliminate most of the defects.

Li et al. [94] also used a sonicated-assisted method to form highly ordered 3D polystyrene particle films, from various sphere sizes, up to 1053nm diameter. The thickness of their 3D films was adjusted up to 30 layers by changing the concentration of the initial particle suspensions. They concluded that, unlike with gravitational sedimentation and vertical deposition, there is no limit to the diameter of PS spheres for obtaining ordered films, and hence the photonic stop band is adjustable from the visible to near infra-red simply by adjusting the sphere size.

Vickreva et al. [95] and Zhang et al. [96] both used piezoelectric devices to obtain an “oscillatory shear” across their polystyrene particles, and found the optimised or “resonance” conditions required for particles to be assembled into the highest quality films possible.

### 1.7.12 INKJET PRINTING

Park and Moon [97] investigated the use of picolitre-sized water based droplets of 700nm silica spheres, also containing either formamide or diethylene glycol during an inkjet printing method. Whereas a water based ink produced a ring like deposit, 2D monolayers with well-ordered structures were obtained from the mixed solvent inks. Variations in the deposited patterns are explained by the so called “tears of wine”, or Marangoni effect, which is a description of the mass transfer in a liquid mix due to surface tension differences. Since a liquid with a high surface tension pulls more strongly on the surrounding liquid than one with a low surface tension, the presence of a gradient in surface tension will cause the liquid to flow away from regions of low surface tension, thus creating a flow within the colloidal solution. This flow can be made to oppose the evaporation flux to the edge of a droplet under single solvent conditions.

Cui et al. [98] used ethylene glycol as less hazardous alternative to formamide, in their inkjet printing experiments. Using a printing speed of  $2\text{cm}^2/\text{s}$ , they produced a flower pattern which was the “first demonstration of macroscale patterned photonic crystals with different stop bands fabricated by inkjet printing”, with a thickness of approximately  $7\mu\text{m}$ , and reflectivity of nearly 50%, over cm scale areas.

### 1.7.13 SPIN COATING

Jiang and McFarland [99] suggest that many self-assembly techniques are unfavourable for scaling-up to industrial-scale mass-production, due to their use of slow fabrication methods and their general incompatibility with wafer-scale micro-fabrication methods widely used by the semiconductor industry. In addition, many methods lead to either non-uniform or non-controllable crystalline thickness over large-areas. Using an alternative approach they spin coated silica colloids dispersed in ethoxylated trimethylolpropane triacrylate (ETPTA) monomer, and were able to produce large area, (4-inch wafers) 3D colloidal crystal structures with controllable thickness in a short time frame, although the final crystals were found to be non-close-packed, upon removal of the polymer. However, spin coating is a rapid process compatible with contemporary micro-fabrication, with the ability to use a wide particle diameter range, typically 100nm to 2 $\mu$ m.

Mihi et al. [100] used a mixture of solvents as the dispersion media (in place of the monomer solution of Jiang and McFarland above), and were able to spin coat both silica and latex particles into ordered arrays, without any further processing, with large crystalline domains of 100 $\mu$ m x 100 $\mu$ m. They were also able to control the crystal orientation by use of different solvent mixtures. Wang et al. [74] were able to manufacture colloidal photonic crystals involving a hetero-structure composed of two opalline films of silica spheres with different diameters, using a 2-step spin-coating method. Liu et al. [101] have also reported a colloidal silica spin-coating approach, on

silicon wafers, for the potential fabrication of surface-enhanced Raman scattering devices.

#### **1.7.14 TEMPLATE ASSISTED DEPOSITION**

Jin et al. [102] present a method for the formation of high-quality (100) oriented fcc PS colloidal crystal films using a template-assisted self-assembly method. Using electron beam lithography, they fabricated periodic pillars arranged in a square lattice on silicon wafers, which were then used as a template to direct colloidal crystal self-assembly. The spheres in the bottom layer were restricted to initial positions dictated by the pillars when the crystal dries out, i.e. the template negates the drying stresses by not allowing movement of the particles during drying, resulting in a crack-free structure, with small regular arrays of gaps between the spheres. The authors state that a position deviation of 1.5% does not seriously affect the band-gap of the opal. The colloidal crystal films were shown to be free of cracks over a large area,  $800 \times 800 \mu\text{m}^2$ .

Hur and Won [103] present a template assisted method using the Langmuir-Blodgett deposition method. By using a substrate containing micro-fabricated cylindrically depressed holes, large single crystal monolayer (2D) domains, over a hundred micrometres, could be fabricated.

Khanh and Yoon [104] reported a dry template crack free assembly method (Figure 1.19(f)), whereby rubbing dry spherical colloidal particles into patterned nano-

well arrays leads to fast organisation of the particles into large (centimetre scale), perfect 1D and 2D arrays. Multilayer assembly on the same scale ( $\text{cm}^2$ ) was also achieved, although with more difficulty. The authors also state that the forces applied during the dry rubbing induces deformation of the nano-wells and particles, and thus even a 10% particle size variation can be tolerated, demonstrating that this technique has a higher tolerance to monodispersity over wet self-assembly techniques.

## **1.8 OTHER LARGE AREA / CRACK-FREE METHODS**

Four papers prepared by Sawada et al. (National Institute of Materials Science, NIMS, Tsukuba, Japan) involving air pulse assembly, assembly by the addition of a base, thermally driven assembly, and hydrogel immobilisation assembly, have been published, all with the theme of pursuing the fabrication of large area crack free films, within production timescales.

In 2005, Kanai and Sawada [105] used short air pulses (figure 1.19(a)) to drive polystyrene colloidal particles into a flat capillary cell (0.1 x 9 x 70mm). Above a critical pressure, the cell is filled with a uniform high quality photonic crystal, which yielded a transmission spectrum having sharp dips due to the stop-band. Being a fast automated process, the authors claim this air pulse method has potential as a mass production method for colloidal photonic crystals.

Wakabayashi, Sawada et al. [106] were able to produce 3D centimetre size single crystals in a 1 x 1 x 4.5cm PMMA cell, by the addition of sodium hydroxide (NaOH) base into an aqueous dispersion of colloidal silica particles. Crystallisation was driven long range electrostatic interactions between the particles. Interestingly a body centred cubic (bcc) orientated crystal was achieved by this base addition method.

Toyotama, Sawada et al. developed a thermally driven method [107] (figure 1.19(b)) to fabricate large well orientated (1mm x 10mm x 30mm) single domain crystals in a short time scale (<10 minutes), using colloidal silica in the presence of pyridine, a heated copper block, and a horizontal quartz cell. Again a bcc structure was formed by this method.

Kanai and Sawada [108] prepared crack free colloidal crystals by immobilising a loosely packed crystal in a hydrogel, (figure 1.19(d)) which was subsequently homogeneously shrunk and dried, producing a crack free opal film. Unlike in conventional opal films, in this example the Bragg wavelength can be adjusted by varying the amount of gelation reagent, without changing particle diameter.

Cai et al. [109] were able to grow crack free silica opal films on patterned silicon substrates (periodicity of patterning was 10 $\mu$ m) (figure 1.19(e)), using the controlled evaporation method of Jiang and Colvin [65]. The authors suggest that the patterning not only guided the growth of the colloidal crystals, but also restricted the alignment of the silica particles. It is also possible that the patterning is acting in a similar manner to



expansion joints found in roads and bridges etc, and that shrinkage of the film is reduced to near zero, thus reducing cracking in the films to zero. The authors suggest that patterned silicon substrates could be used as back reflectors in thin film solar cells to improve light absorption and hence enhance the light to energy/electricity conversion.

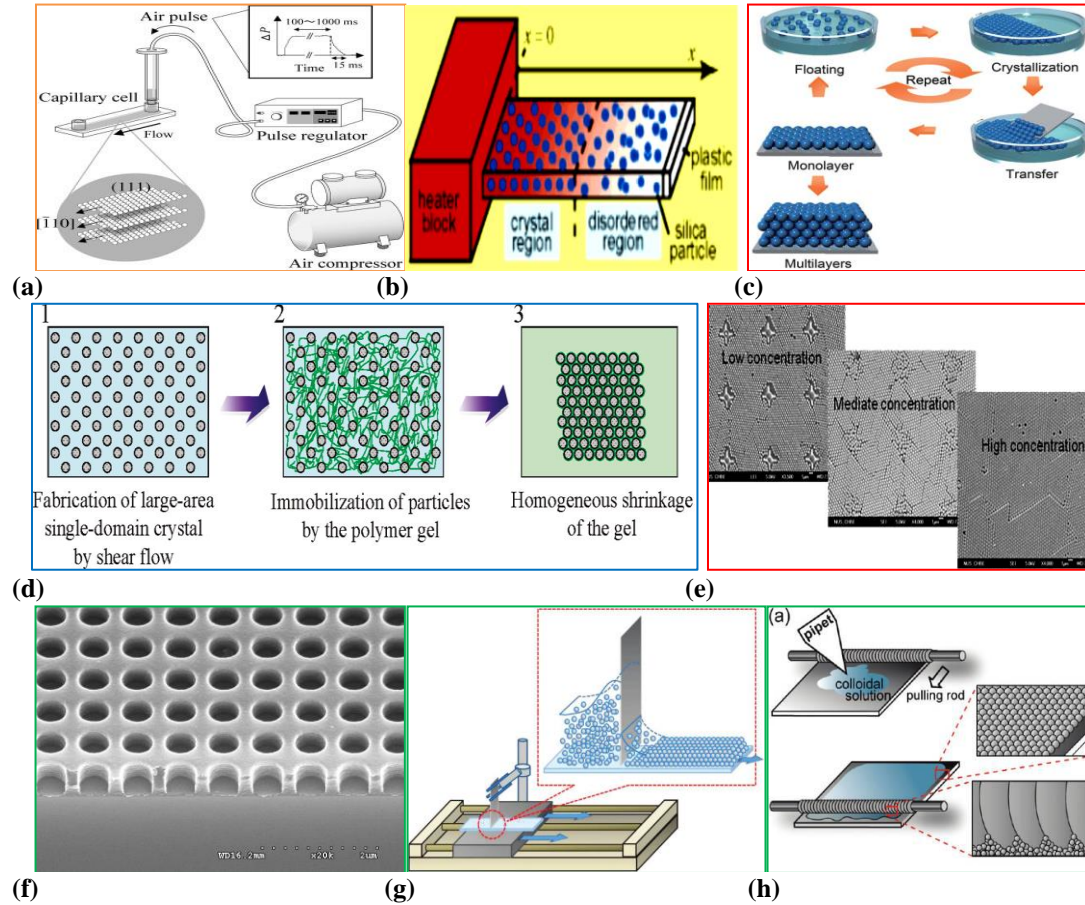


**Figure 19(a-h).** (a) Air pulse assembly [105]; (b) Thermally driven assembly [107]; (c) Scooping [110]; (d) Hydrogel immobilisation [108]; (e) Patterned silicon substrates [109]; (f) Dry assembly [104]; (g) Doctor blade [111]; (h) Wire-wound rod coating method [112].

Oh et al. [110] reported assembling crack free polystyrene colloidal crystals over a 4 inch wafer, using a method similar to that of L-B. Here, floating monolayers of PS particles were transferred onto a silicon wafer by a “scooping” method (figure 1.19(c)).

This layer-by layer approach is able to achieve crack free films by keeping the critical film thickness (see equation 6) below its critical value at each layer. After each layer has dried out, the next layer is added, again, at a thickness below the critical level. Large crack free areas have also been reported by Gil et al. [79] using the L-B method. Here, Oh and co-workers were able to float PS particles from 250nm to 850nm, which means that the formed film can perform across the visible and IR regions of the spectrum.

Yang and Jiang [111] used a doctor blade coating process (figure 1.19(g)) to achieve colloidal crystals by a method capable of industrial roll-to-roll scale up. Monodisperse silica particles were redispersed in ethoxylated trimethylolpropane triacrylate monomer (ETPTA), to which Darocur 1173 (2-hydroxy-2-methyl-1-phenyl-1-propanone) was added as the photoinitiator. The substrate was moved at controlled speed, and the doctor blade spread the colloidal suspension uniformly across the substrate. The ETPTA monomer is finally photopolymerized by exposure to ultraviolet radiation to form a 3D highly ordered colloidal crystal-polymer nanocomposite. Monolayer to 10+ layers were fabricated by this method, and crystalline films achieved through the removal of the silica particles, leaving an inverse polymeric opal structure (macroporous polymer membrane), or removal of the ETPTA matrix, to leave a silica colloidal crystal. The authors experimentally proved the use of a doctor blade made film as a microporous filtration membrane.

Jeong et al. [112] likewise describe a large area, industrial scalable roll-to-roll method of producing colloidal crystal films, using a wire wound rod coating method

(figure 1.19(h)). The authors demonstrated their large area method could be useful on substrates for improved of light absorption in solar thin films.

A brief review of some self-assembly methods are given in Tables 1.3a & b, (taken from the works of Galisteo-Lopez et al. [113] and Velev & Gupta [114].

**Table 1.3a. Summary of some common self-assembly techniques and their limitations [113].**

Assembly method	Thickness	Area	Time	Optical Quality	Issues
Sedimentation	mm	mm <sup>2</sup>	weeks	poor	fragile, material waste
Cell confinement	few to tens of monolayers	mm <sup>2</sup>	1–2 days	good	opening the cell
Controlled evaporation	1 to tens of monolayers	mm <sup>2</sup>	1–2 days	excellent	large beads plummet
Langmuir-Blodgett	1 to several monolayers	10 x cm <sup>2</sup>	hours	poor	sequential
Shear induced	mm	10 x cm <sup>2</sup>	minutes	poor	polycrystalline, high amount needed
Motor drawing	1 to tens of monolayers	mm <sup>2</sup>	hours	good	high concentrations needed
Air-water interface	few to tens of monolayers	mm <sup>2</sup>	minutes	fair	indetermined orientation, substrate detached
Spin coating	1 to tens of monolayers	wafer size	minutes	fair	polycrystalline
Wedge cell	1 monolayer	cm <sup>2</sup>	hours	excellent	only 2D

**Table 1.3b. Summary of some common self-assembly techniques and their limitations [114].**

Type	Thickness	Scalability	Complexity/Cost
Sedimentation	3D	yes	small
Controlled evaporation	2D, 3D	yes	Small
Adsorption / LbL	2D, 3D	Yes	Small
External force field	1D, 2D, 3D	Limited	Medium
Bio-specific	1D, 2D, 3D	Limited	High
Templated on surfaces	1D, 2D, 3D	Limited	Very high
Templated on droplets	Supra	yes	medium

## **1.9 ASSESSMENT OF COLLOIDAL CRYSTAL FILM QUALITY**

Researchers have used a variety of methods to assess the quality of colloidal crystal films. Optical spectroscopy [68, 115, 116], domain size [117, 118] and qualitative inspection of scanning electron micrographs (SEM) [48, 115] have all been recorded in the literature. Indeed, Ozin and co-workers [48] systematically investigated the relationship between the microscopic order and optical properties of the colloidal crystals using SEM and UV-vis-NIR spectroscopy. Their findings were that the highest structural quality of the colloidal crystal films, observed by SEM, is always translated to the highest quality optical spectra for samples of more than five layers thick. They state that their observations suggest two conclusions: that SEM is the best and most revealing method for evaluation of colloidal crystal perfection; and that the optical properties of colloidal crystals are quite tolerant of dislocation defects and stacking faults. Such findings they suggest open up the possibility of self-assembled colloidal crystal films being successfully implemented into practical devices.

Li and co-workers [119] also state that long range ordering is visible as Moiré patterns in low magnification SEM images from their layer by layer approach.

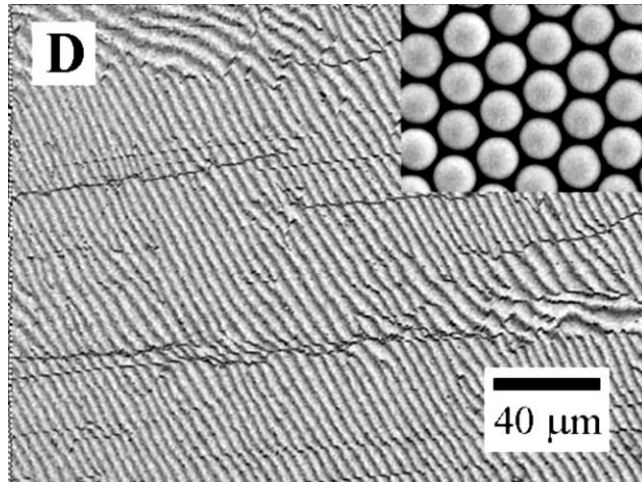


**Figure 1.20.** Low magnification SEM image of a colloidal crystal surface, showing Moiré patterning [119]

### 1.9.1 EFFECTS ON OPTICAL QUALITY (defects etc)

Recent studies have revealed that crystal imperfections, such as site vacancies, dislocations, stacking faults, size, shape, positional disorder and fracture lines in a photonic lattice, strongly affect the optical properties. With the presence of these defects and disorder, the transmission dip stop band will become shallower, give a broadening of the gap, decreasing the transmission in the pass-bands [115]. In addition, calculations have shown that poly dispersity (sphere size distribution) greater than 2-5% is sufficient to degrade or close the complete photonic band-gap [41]. Here, the sphere size distribution is defined as the ratio of the standard deviation of the sphere diameters to the mean diameter.

In order to improve the quality of the 3D colloidal crystal films, Li and co-workers [120] developed a particle selection technique, separating single spheres from

aggregated spheres to improve their monodispersity, and hence were able to make higher quality SiO<sub>2</sub> opals by gravity sedimentation. The photonic band-gap structure of the opals was measured in transmission, and the value of  $I_{\max}/I_{\min}$  in the spectra was used to represent the quality of the structures. Figure 1.21 shows that the value of  $I_{\max}/I_{\min}$  increased from 17.5 to 61.0 by using their selection technique, also resulting in an increase in the domain sizes of the opals.

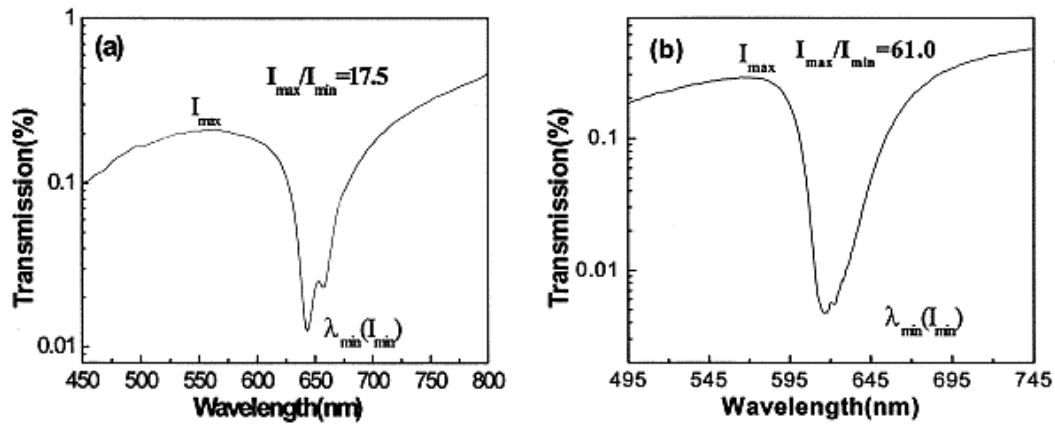
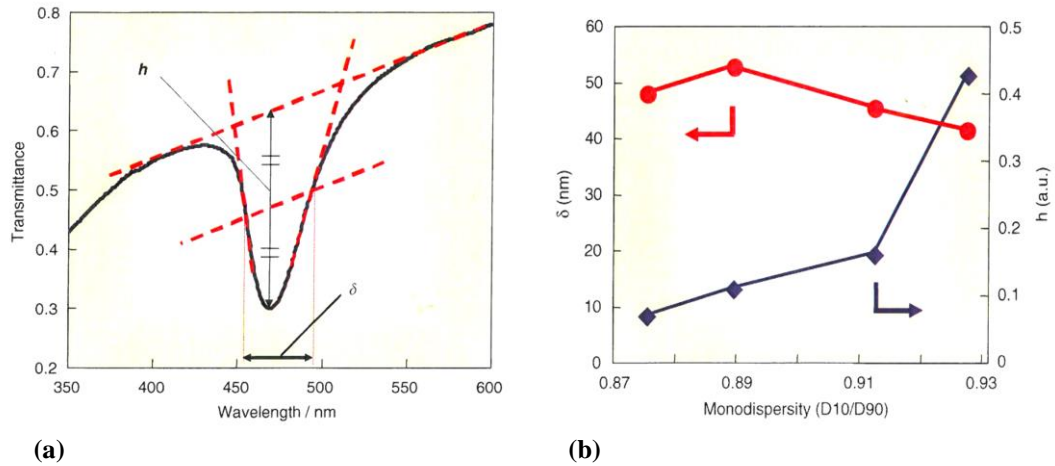


Figure 1.21. Transmission spectra of 2 silica opals (a) without selection procedure of spheres; (b) with the selection procedure of spheres [120].

Likewise, Li et al. [121] used their qualitative  $I_{\max}/I_{\min}$  assessment in controlled drying experiments on samples prepared by natural sedimentation, and achieved a maximum attenuation of the gaps ( $I_{\max}/I_{\min}$ ) in the transmission spectra of the colloidal crystals dried at 50°C was 109.6.

Enomoto et al. [122] also established a method to assess the quality of their films, via the study of the impact of increasing monodispersity on the quality of their films. By carefully controlling the monodispersity of their prepared particles they made a number of films and used the transmission spectra (figure 1.22(a)) to assess the film quality. The depth ( $h$ ) and the width ( $\delta$ ) of the dip were used to evaluate the colloidal

crystallinity. It can be seen in figure 1.22(b) that the depth ( $h$ ) increases with increasing monodispersity, and the width ( $\delta$ ) generally decreases with increasing monodispersity, in opal films prepared by varying the addition of small amounts of the 294nm spheres into 304nm spheres. They introduced a new parameter,  $h/\delta$ , which they suggested represents the colloidal crystallinity of the opal film.



**Figure 1.22.** (a) Typical transmission spectrum for an opal film. Depth ( $h$ ) and width ( $\delta$ ) of the absorption dip were measured and their ratio ( $h/\delta$ ) was noted as an index of crystallinity for the film. (b) Depth ( $h$ ) and width ( $\delta$ ) of the dip in the transmission spectra of the opal film prepared by adding different amounts of the 294nm spheres into 304nm spheres [122].

### 1.9.2 THE FULL WIDTH HALF MAXIMUM (FWHM)

Piret and Su [123] state that a peak broadening effect observed in the reflectance spectra can be attributed to disorder within the structure, and that this effect can be quantified by the fractional bandwidth ( $\Delta\lambda/\lambda$ ), where  $\Delta\lambda$  is the full width at half maximum (FWHM) and  $\lambda$  the position of the maximum reflectance of the peak. The fractional bandwidth is dependent only on the crystal structure, and hence is an ideal

parameter for comparing the quality of different samples. Ko and Shin [124] produced colloidal crystals films by dip coating with a FWHM ( $\Delta\lambda/\lambda$ ) of approximately 7%, and stating this value approximately agrees with the theoretical calculation result for a fcc crystal.

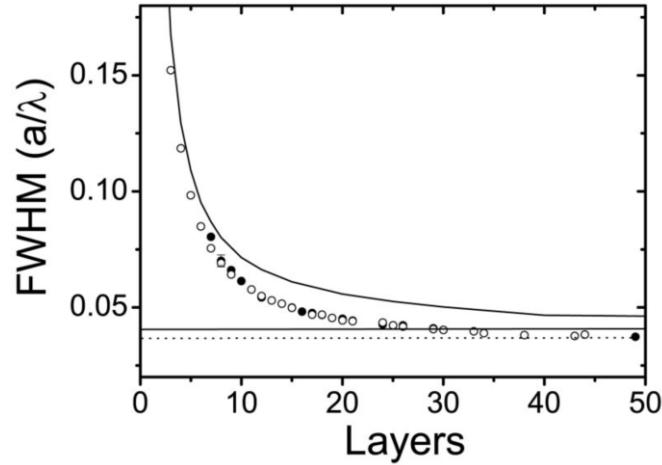


**Figure 1.23. FWHM of reflectivity peaks for samples grown on silicon and glass substrates, as a function of the sample thickness. Theoretical (lines) and experimental data (dots) are presented [46], (where  $a$  is the lattice parameter of the fcc structure)**

Figure 1.23 [46] represents experimental results and theoretical predictions of the FWHM of samples grown on glass and silicon substrates. It can be seen that the results from both substrates coincide, indicating that the FWHM of the Bragg peak is an intrinsic signature of the photonic crystal, and independent of the substrate used. The experimental FWHM of the Bragg peak is seen to decrease as the number of lattice planes increases, until it reaches a finite value, practically the same as the predicted results.

Colvin et al. [66] noted that the stop band narrows to a certain critical width with increasing film thickness. Further increases in film thickness did not result in narrower



band widths. They calculated that for crystals of high dielectric contrast, diffraction is very strong, and the amplitude of the radiation attenuates rapidly with propagation distance into the crystal. As a result, most of the incident radiation interacts only with the first few lattice planes, near the surface. Hence the measured bandwidth is determined largely by these interactions near the surface, and not by the further propagation through the medium. Thus, increasing the thickness of the crystal above a certain critical thickness,  $N_c$ , has little effect on the bandwidth. For close-packed spheres of silica /air films,  $N_c = 13$  layers, and for an air/polymer film made with poly(alkyl methacrylate) PAMA ( $n = 1.64$ ),  $N_c = 6$  layers.

Li and Han [125] grew thickness graded colloidal crystals, with increasing numbers of layers along the surface of a substrate. They calculated the FWHM of the Bragg peak and also found it presented an exponential decay with increasing layer thickness, the narrowing of the FWHM reaching a minimum of 28 nm above a certain critical thickness, which was calculated to be 13 layers for silica particles.

### **1.9.3 THE USE OF FABRY-PEROT FRINGES**

Oscillations in transmission and reflectance spectra (figure 1.24) either side of the stop band can be understood as Fabry-Perot fringes that occur because of interference of light reflected by the opposite surfaces of the opal film. The fringes become smaller and more closely spaced as film thickness increases. In the case of thin

colloidal films, the fringes are an indication of the high quality of crystals [125]. These fringes also indicate the uniformity of the thickness and the similarity of orientation of the colloidal crystal films, which can be confirmed by SEM. If the thickness of the sample varies by more than 10%, then these well-defined maxima and minima will not be observed. However, for opals which are too thick, these fringes form a continuous background and are therefore again difficult to observe [71].

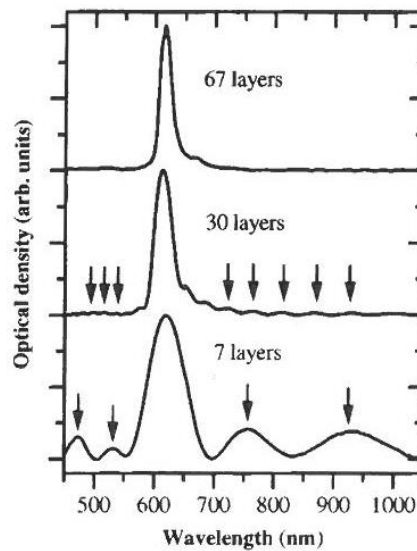


**Figure 1.24.** Normal incidence transmission spectra (optical density) of three samples with increasing film thickness, (curves offset for clarity). Thicker samples exhibit more closely spaced (and smaller) Fabry-Perot fringes. The arrows indicate local maxima,  $\lambda_p$ , used for thickness analysis, with the longest wavelength as  $p = 0$ . [65]

As previously discussed, the number of layers, and therefore the thickness, of the sample is important when studying the optical properties of the thin opal film. While the use of SEM can provide an accurate measure of thickness/number of layers, it is a destructive method. However, the number of layers can also be calculated from the spectral separation of the F-P fringes.

At normal incidence, one particular F-P minimum occurs at a longest wavelength,  $\lambda_0$  given by:

$$p_0 \lambda_0 = 2n_{\text{eff}}T \quad (\text{Eq. 7})$$

Where:  $p_0$  is an interger;  $n_{\text{eff}}$  is the effective refractive index of the film; and  $T$  is the film thickness.

Subsequent minima appear at shorter wavelength:

$$(p+p_0) \lambda_p = 2n_{\text{eff}}T \quad (\text{Eq. 8})$$

Here  $p$  is a positive integer numbering consecutive minima from the fringe  $p_0$ .

Combining Snell's law and Bragg's law, we obtain the Bragg diffraction wavelength,  $\lambda_c$  at normal incidence:

$$\lambda_c = 2n_{\text{eff}}d_{\text{hkl}}, \quad (\text{Eq. 9})$$

Where:  $d_{\text{hkl}}$  is the distance between two adjacent diffracting lattice planes.

Rearranging Eqs.(7), (8) & (9) gives the number of layers,  $L$ :

$$L = T/d_{hkl} = (p \lambda_p \lambda_0) / (\lambda_c (\lambda_0 - \lambda_p)) \quad (\text{Eq. 10})$$

Using the above equation, (10), we can obtain the number of layers from diffraction spectra independently, (assuming films are regularly ordered in the vertical direction).

The calculated film thickness from the optical Fabry-Perot fringes is found to agree with film thicknesses found from SEM cross sectional images [65].

#### **1.9.4 FAST FOURIER TRANSFORM (FFT) IMAGES**

Several researchers have illustrated colloidal crystal order / quality by showing FFT [126] images taken from an original SEM image of ordered particles. The original SEM images usually show a relatively large area top surface image of particle ordering, and the dot patterns of the FFT images are often described as “illustrating the long range order of the crystal” [66], or “these regular microstructures were also assessed by Fourier transform analysis of the corresponding SEM images and the sharp peaks confirm the presence of long-range crystalline order” [98].

To assess the sample ordering over long ranges, centimetres, Colvin et al. [65] compared SEM micrographs of  $40\mu\text{m}^2$  areas collected as a sequence over their samples. They suggested that if the FFT registry were aligned between these images, then this

would show single domain structures over these length scales. Also FFT images could be used to confirm poor quality structures e.g. reduced particle monodispersity. In two samples with differing size distributions, the sample with a narrow size distribution showed sharp peaks in the FFT image, while the polydisperse sample, having only short range order, showed rings in the FFT image.

Khunsin and co-workers [127] characterized the ordering of spheres in the (111) lattice of the growth plane using the magnitudes of harmonics in the FT pattern from top surface SEM images. The FT pattern points represent harmonics of the periodic structure in the SEM image. They compared the magnitude of the 1st harmonic in the FT pattern to estimate the regularity of the sphere spacing, and the rate of decrease in the magnitudes of the 2<sup>nd</sup> and 3<sup>rd</sup> harmonics, taken from a line drawn across the pattern points (Figure 1.25a). By comparing the magnitudes of the 1<sup>st</sup>, 2<sup>nd</sup> and 3<sup>rd</sup> harmonics of different FT patterns it is possible to judge which lattice is more ordered. A quantitative comparison of different samples becomes possible assuming the same brightness and contrast of the images and taking into account the areas contain an equal number of the particles in the sampled area, i.e., this approach remains a local one. Nevertheless, it provides guidelines for experimental work on optimization of crystallization conditions. They also noted that cracks in the opal film do not strongly affect the lattice spacing, but lead to a decrease in magnitude of the higher harmonics in the FT pattern.

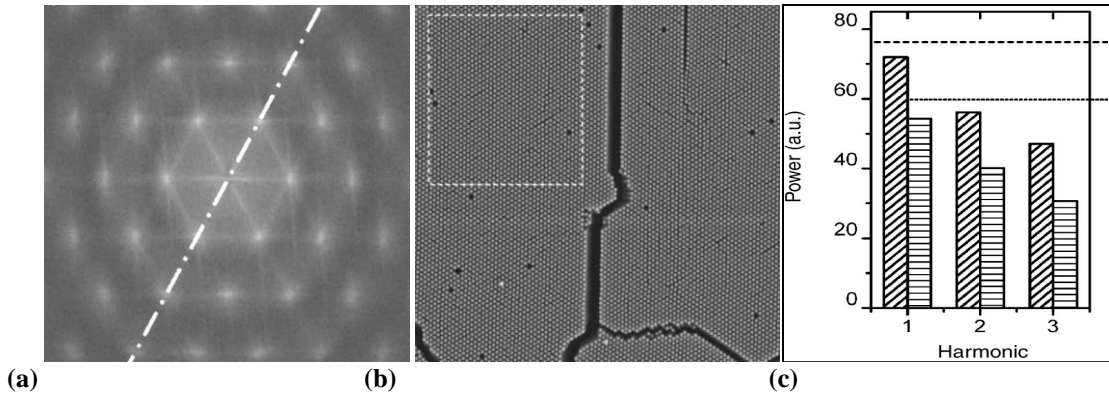


**Figure 1.25.** (a) FFT pattern of the area enclosed by the dashed lines in the SEM image in (b). (c) Shows the magnitudes of the first three harmonics in the FFT pattern shown in (a) diagonal lines = “with noise”, horizontal lines = “without noise” in their experiments, (adapted from [127]).

### 1.9.5 AIMS OF THE PRESENT WORK.

The ideal assembly method would aim to produce large single crystals, with controlled orientation, achieved in the shortest times, using a reproducible and scalable method, while minimizing residual disorder. Obviously disorder is never fully eliminated and partial disorder is always present [113].

Therefore, the aim of this project was to optimize film growth conditions to obtain a high quality crystal over a large scale area (4inch wafer). Added to this is the requirement to have minimal defects, of which cracking within the films in particular is seen as the major roadblock for the formation of these crystalline films over large areas.

A further requirement is to have films of a given thickness. In the case of silica particle films, a minimum of approximately 15 layers is required, and to have as even as possible a thickness over the whole area of the film. For this to be achievable layer by

layer techniques would appear to offer the most viable solutions (L-B, scooping, etc), although these methods offer reduced particle ordering in the vertical plane. A number of horizontal methods claim uniform layering of the particles, e.g. under oil crystallisation, shear induced methods, spin coating, sonication etc, and vertical methods are also able to achieve relatively uniform layering over relatively large areas, e.g. controlled evaporation, dip coating, etc.

This work set out to take as a baseline, some of the more promising methods described for the production of large-scale, defect free, colloidal photonic crystals, and to develop these further together with some new approaches, in an attempt to overcome the major perceived roadblock for the utilisation of these materials in a range of applications. Necessarily this work also addresses the methods by which the quality of colloidal photonic crystals may be reliably assessed.

The remainder of this thesis is set out as follows: Chapter 2 deals with the materials and experimental methods employed; Chapter 3 then describes the development of an improved method for the targeted production of silica particles of specified diameters; Chapter 4 describes the development of an improved colloidal photonic crystal film growth method via sonication; Chapter 5 describes a collaborative project with the National Institute of Materials Science (NIMS), Tsukuba, Japan, the primary aim of which was to prepare mechanically strengthened opal films by co-crystallisation using the under oil crystallisation method developed at NIMS; Chapter 6 describes the investigation of a number of polymeric additives used to strengthen

colloidal photonic crystal film; Chapter 7 describes the development of large area crack-free films by produced controlled evaporation deposition using a mixed solvent approach; Chapter 8 describes an analytical method to assess the quality of produced films via the assessment of their FFT profiles.



## REFERENCES:

1. Xu, P., A.S. Mujumdar, and B. Yu, *Drying-Induced Cracks in Thin Film Fabricated from Colloidal Dispersions*. Drying Technology, 2009. **27**(5): p. 636-652.
2. Velegol, D., *Assembling colloidal devices by controlling interparticle forces*. Journal of Nanophotonics, 2007. **1**.
3. Barick, K.C. and D. Bahadur, *Self-Assembly of Colloidal Nanoscale Particles: Fabrication, Properties and Applications*. Journal of Nanoscience and Nanotechnology. **10**(2): p. 668-689.
4. Jiang, X.C., et al., *Self-assembly of particles: some thoughts and comments*. Journal of Materials Chemistry, 2011. **21**(42): p. 16797-16805.
5. Whitesides, G.M. and M. Boncheva, *Beyond molecules: Self-assembly of mesoscopic and macroscopic components*. Proceedings of the National Academy of Sciences of the United States of America, 2002. **99**(8): p. 4769-4774.
6. Vukusic, P. and J.R. Sambles, *Photonic structures in biology*. Nature, 2003. **424**(6950): p. 852-855.
7. Sanders, J.V., *Colour Of Precious Opal*. Nature, 1964. **204**(496): p. 1151-&.
8. Yablonovitch, E., *Inhibited Spontaneous Emission In Solid-State Physics And Electronics*. Physical Review Letters, 1987. **58**(20): p. 2059-2062.
9. John, S., *Strong Localization Of Photons In Certain Disordered Dielectric Superlattices*. Physical Review Letters, 1987. **58**(23): p. 2486-2489.
10. Joannopoulos, J.D., P.R. Villeneuve, and S.H. Fan, *Photonic crystals: Putting a new twist on light*. Nature, 1997. **386**(6621): p. 143-149.

11. S.A. Asher, "Crystalline colloidal narrow band radiation filter," U.S. Patent number 4,627,689 (filed 8 Dec 1983, issued 9 Dec 1986).
12. Fudouzi, H. and Y.N. Xia, *Colloidal crystals with tunable colors and their use as photonic papers*. Langmuir, 2003. **19**(23): p. 9653-9660.
13. Hawkeye, M.M. and M.J. Brett, *Optimized Colorimetric Photonic-Crystal Humidity Sensor Fabricated Using Glancing Angle Deposition*. Advanced Functional Materials, 2011. **21**(19): p. 3652-3658.
14. Kim, S.H., et al., *Integration of Colloidal Photonic Crystals toward Miniaturized Spectrometers*. Advanced Materials, 2010. **22**(9): p. 946-+.
15. Maldovan, M. and E.L. Thomas, *Diamond-structured photonic crystals*. Nature Materials, 2004. **3**(9): p. 593-600.
16. Norris, D.J., *A view of the future*. Nature Materials, 2007. **6**(3): p. 177-178.
17. Pendry, J.B., D. Schurig, and D.R. Smith, *Controlling electromagnetic fields*. Science, 2006. **312**(5781): p. 1780-1782.
18. Soukoulis, C.M., S. Linden, and M. Wegener, *Negative refractive index at optical wavelengths*. Science, 2007. **315**(5808): p. 47-49.
19. Soukoulis, C.M., M. Kafesaki, and E.N. Economou, *Negative-index materials: New frontiers in optics*. Advanced Materials, 2006. **18**(15): p. 1941-1952.
20. Lipson, R.H. and C. Lu, *Photonic crystals: a unique partnership between light and matter*. European Journal of Physics, 2009. **30**(4): p. S33-S48.
21. "Inverse Opal Photonic Crystals: A Laboratory Guide" R. C. Schroden, N. Balakrishnan, University of Minnesota, Materials Research Science and Engineering Center

22. Miguez, H., et al., *Evidence of FCC crystallization of SiO<sub>2</sub> nanospheres*. Langmuir, 1997. **13**(23): p. 6009-6011.
23. Brewer, D.D., et al., *Mechanistic Principles of Colloidal Crystal Growth by Evaporation-Induced Convective Steering*. Langmuir, 2008. **24**(23): p. 13683-13693.
24. Norris, D.J., et al., *Opaline photonic crystals: How does self-assembly work?* Advanced Materials, 2004. **16**(16): p. 1393-1399.
25. Lange, B., F. Fleischhaker, and R. Zentel, *Chemical approach to functional artificial opals*. Macromolecular Rapid Communications, 2007. **28**(12): p. 1291-1311.
26. Lopez, C., *Materials aspects of photonic crystals*. Advanced Materials, 2003. **15**(20): p. 1679-1704.
27. Nair, R.V. and R. Vijaya, *Structural and optical characterization of photonic crystals synthesized using the inward growing self-assembling method*. Applied Physics a-Materials Science & Processing, 2008. **90**(3): p. 559-563.
28. Fudouzi, H., *Optical properties caused by periodical array structure with colloidal particles and their applications*. Advanced Powder Technology, 2009. **20**(5): p. 502-508.
29. Ge, J. and Y. Yin, *Responsive Photonic Crystals*. Angewandte Chemie International Edition, 2011. **50**(7): p. 1492-1522.
30. Ho, K.M., C.T. Chan, and C.M. Soukoulis, *Existence Of A Photonic Gap In Periodic Dielectric Structures*. Physical Review Letters, 1990. **65**(25): p. 3152-3155.

31. Large, M.C.J., et al., *Insights from nature: Optical biomimetics*. Physica B-Condensed Matter, 2007. **394**(2): p. 229-232.
32. Zhao, Y., X. Zhao, and Z. Gu, *Photonic Crystals in Bioassays*. Advanced Functional Materials, 2010. **20**(18): p. 2970-2988.
33. Rengarajan, R., et al., *Effect of disorder on the optical properties of colloidal crystals*. Physical Review E, 2005. **71**(1).
34. Yablonovitch, E., T.J. Gmitter, and K.M. Leung, *Photonic Band-Structure - The Face-Centered-Cubic Case Employing Nonspherical Atoms*. Physical Review Letters, 1991. **67**(17): p. 2295-2298.
35. Noda, S., et al., *Full three-dimensional photonic bandgap crystals at near-infrared wavelengths*. Science, 2000. **289**(5479): p. 604-606.
36. Lin, S.Y., et al., *A three-dimensional photonic crystal operating at infrared wavelengths*. Nature, 1998. **394**(6690): p. 251-253.
37. Fleming, J.G. and S.Y. Lin, *Three-dimensional photonic crystal with a stop band from 1.35 to 1.95  $\mu$  m*. Optics Letters, 1999. **24**(1): p. 49-51.
38. Aoki, K., et al., *Three-dimensional photonic crystals for optical wavelengths assembled by micromanipulation*. Applied Physics Letters, 2002. **81**(17): p. 3122-3124.
39. Campbell, M., et al., *Fabrication of photonic crystals for the visible spectrum by holographic lithography*. Nature, 2000. **404**(6773): p. 53-56.
40. Sharp, D.N., et al., *Photonic crystals for the visible spectrum by holographic lithography*. Optical and Quantum Electronics, 2002. **34**(1-3): p. 3-12.

41. Ozin, G.A. and S.M. Yang, *The race for the photonic chip: Colloidal crystal assembly in silicon wafers*. Advanced Functional Materials, 2001. **11**(2): p. 95-104.
42. Philipse, A.P., *Solid Opaline Packings Of Colloidal Silica Spheres*. Journal of Materials Science Letters, 1989. **8**(12): p. 1371-1373.
43. Davis, K.E., W.B. Russel, and W.J. Glantschnig, *Settling Suspensions Of Colloidal Silica - Observations And X-Ray Measurements*. Journal of the Chemical Society-Faraday Transactions, 1991. **87**(3): p. 411-424.
44. Nair, R.V. and R. Vijaya, *Photonic crystal sensors: An overview*. Progress in Quantum Electronics, 2010. **34**(3): p. 89-134.
45. Vlasov, Y.A., et al., *On-chip natural assembly of silicon photonic bandgap crystals*. Nature, 2001. **414**(6861): p. 289-293.
46. Galisteo-Lopez, J.F., et al., *Optical study of the pseudogap in thickness and orientation controlled artificial opals*. Physical Review B, 2003. **68**(11).
47. Allard, M. and E.H. Sargent, *Impact of polydispersity on light propagation in colloidal photonic crystals*. Applied Physics Letters, 2004. **85**(24): p. 5887-5889.
48. Wong, S., V. Kitaev, and G.A. Ozin, *Colloidal crystal films: Advances in universality and perfection*. Journal of the American Chemical Society, 2003. **125**(50): p. 15589-15598.
49. Hartsuiker, A. and W.L. Vos, *Structural properties of opals grown with vertical controlled drying*. Langmuir, 2008. **24**(9): p. 4670-4675.

50. Wang, L.K. and X.S. Zhao, *Fabrication of crack-free colloidal crystals using a modified vertical deposition method*. Journal of Physical Chemistry C, 2007. **111**(24): p. 8538-8542.
51. Ye, J.H., et al., *Integration of self-assembled three-dimensional photonic crystals onto structured silicon wafers*. Langmuir, 2006. **22**(17): p. 7378-7383.
52. Image taken from a Google search of "Langmuir Blodgett images"
53. Fudouzi, H., *Novel coating method for artificial opal films and its process analysis*. Colloids and Surfaces a-Physicochemical and Engineering Aspects, 2007. **311**(1-3): p. 11-15.
54. Ruhl, T., P. Spahn, and G.P. Hellmann, *Artificial opals prepared by melt compression*. Polymer, 2003. **44**(25): p. 7625-7634.
55. Amos, R.M., et al., *Fabrication of large-area face-centered-cubic hard-sphere colloidal crystals by shear alignment*. Physical Review E, 2000. **61**(3): p. 2929-2935.
56. Grieseböck, B., M. Egen, and R. Zentel, *Large photonic films by crystallization on fluid substrates*. Chemistry of Materials, 2002. **14**(10): p. 4023-+.
57. Sasaki, M. and K. Hane, *Ultrasonically facilitated two-dimensional crystallization of colloid particles*. Journal of Applied Physics, 1996. **80**(9): p. 5427-5431.
58. Carreras, E.S., et al., *Avoiding "mud" cracks during drying of thin films from aqueous colloidal suspensions*. Journal of Colloid and Interface Science, 2007. **313**(1): p. 160-168.

59. Singh, K.B. and M.S. Tirumkudulu, *Cracking in drying colloidal films*. Physical Review Letters, 2007. **98**(21).
60. Juillerat, F., P. Bowen, and H. Hofmann, *Formation and drying of colloidal crystals using nanosized silica particles*. Langmuir, 2006. **22**(5): p. 2249-2257.
61. Deegan, R.D., et al., *Contact line deposits in an evaporating drop*. Physical Review E, 2000. **62**(1): p. 756-765.
62. Shmuylovich, L., A.Q. Shen, and H.A. Stone, *Surface morphology of drying latex films: Multiple ring formation*. Langmuir, 2002. **18**(9): p. 3441-3445.
63. Davis, K.E., W.B. Russel, and W.J. Glantschnig, *Disorder-To-Order Transition In Settling Suspensions Of Colloidal Silica - X-Ray Measurements*. Science, 1989. **245**(4917): p. 507-510.
64. Salvarezza, R.C., et al., *Edward-Wilkinson behavior of crystal surfaces grown by sedimentation of SiO<sub>2</sub> nanospheres*. Physical Review Letters, 1996. **77**(22): p. 4572-4575.
65. Jiang, P., et al., *Single-crystal colloidal multilayers of controlled thickness*. Chemistry of Materials, 1999. **11**(8): p. 2132-2140.
66. Bertone, J.F., et al., *Thickness dependence of the optical properties of ordered silica-air and air-polymer photonic crystals*. Physical Review Letters, 1999. **83**(2): p. 300-303.
67. Im, S.H., M.H. Kim, and O.O. Park, *Thickness control of colloidal crystals with a substrate dipped at a tilted angle into a colloidal suspension*. Chemistry of Materials, 2003. **15**(9): p. 1797-1802.

68. Kuai, S.L., et al., *High-quality colloidal photonic crystals obtained by optimizing growth parameters in a vertical deposition technique*. Journal of Crystal Growth, 2004. **267**(1-2): p. 317-324.
69. Liu, G.Q., Z.S. Wang, and Y.H. Ji, *Influence of growth parameters on the fabrication of high-quality colloidal crystals via a controlled evaporation self-assembly method*. Thin Solid Films, 2010. **518**(18): p. 5083-5090.
70. Li, H.L. and F. Marlow, *Solvent effects in colloidal crystal deposition*. Chemistry of Materials, 2006. **18**(7): p. 1803-1810.
71. Wang, J., C.W. Yuan, and F.Q. Tang, *Self-assembling three-dimensional colloidal photonic crystal multilayers from aqueous ethanol mixture solutions*. Chinese Physics, 2005. **14**(8): p. 1581-1584.
72. Yoldi, M., et al., *On the parameters influencing the deposition of polystyrene colloidal crystals*. Materials Science & Engineering C-Biomimetic and Supramolecular Systems, 2008. **28**(7): p. 1038-1043.
73. Wang, A., S.-L. Chen, and P. Dong, *Rapid fabrication of a large-area 3D silica colloidal crystal thin film by a room temperature floating self-assembly method*. Materials Letters, 2009. **63**(18-19): p. 1586-1589.
74. Wang, A.J., et al., *Fabrication of Colloidal Photonic Crystals with Heterostructure by Spin-Coating Method*. Chinese Physics Letters, 2009. **26**(2).
75. Wang, A.J., et al., *Fabrication of large-area and high-quality colloidal crystal films on nanocrystalline porous substrates by a room temperature floating self-assembly method*. Thin Solid Films, 2011. **519**(6): p. 1798-1802.



76. Hatton, B., et al., *Assembly of large-area, highly ordered, crack-free inverse opal films*. Proceedings of the National Academy of Sciences of the United States of America, 2010. **107**(23): p. 10354-10359.
77. Gu, Z.Z., A. Fujishima, and O. Sato, *Fabrication of high-quality opal films with controllable thickness*. Chemistry of Materials, 2002. **14**(2): p. 760-765.
78. "Improving the opal-based photonic crystals by noise-assisted crystallization" W. Khunsin, G. Kocher, S. G. Romanov, C. M. Sotomayor Torres International Workshop and Conference on Photonics and Nanotechnology 2007, Proc. of SPIE Vol. 6793, 67930B, (2008)
79. Gil, A., et al., *Stress-free production and effective medium model of colloidal crystals*. Journal of Materials Chemistry, 2007. **17**(23): p. 2434-2439.
80. Romanov, S.G., et al., *(2+1)-dimensional photonic crystals from Langmuir-Blodgett colloidal multilayers*. Applied Physics Letters, 2006. **89**(4).
81. Bardosova, M., et al., *Langmuir-Blodgett assembly of colloidal photonic crystals using silica particles prepared without the use of surfactant molecules*. Journal of Colloid and Interface Science, 2009. **333**(2): p. 816-819.
82. Fudouzi, H., *Fabricating high-quality opal films with uniform structure over a large area*. Journal of Colloid and Interface Science, 2004. **275**(1): p. 277-283.
83. Fudouzi, H. *Novel coating method for artificial opal films and its process analysis*. in *14th International Seminar on Nisshin Engineering Particle Technology*. 2005. Hakone, JAPAN: Elsevier Science Bv.
84. SFI Application

85. Ruhl, T., et al., *Large area monodomain order in colloidal crystals*. Macromolecular Chemistry and Physics, 2004. **205**(10): p. 1385-1393.
86. Pursiainen, O.L.J., et al., *Nanoparticle-tuned structural color from polymer opals*. Optics Express, 2007. **15**(15): p. 9553-9561.
87. Pursiainen, O.L.J., et al., *Shear-induced organization in flexible polymer opals*. Advanced Materials, 2008. **20**(8): p. 1484-+.
88. Lazarov, G.S., et al., *Formation Of 2-Dimensional Structures From Colloidal Particles On Fluorinated Oil Substrate*. Journal of the Chemical Society-Faraday Transactions, 1994. **90**(14): p. 2077-2083.
89. Dimitrov, A.S., et al., *Observations Of Latex Particle 2-Dimensional-Crystal Nucleation In Wetting Films On Mercury, Glass, And Mica*. Langmuir, 1994. **10**(2): p. 432-440.
90. Takeda, S. and P. Wiltzius, *Growth of highly ordered colloidal crystals using self-assembly at liquid-liquid interfaces*. Chemistry of Materials, 2006. **18**(24): p. 5643-5645.
91. Sadhukhan, S., et al., *Desiccation cracks on different substrates: simulation by a spring network model*. Journal of Physics-Condensed Matter, 2007. **19**.
92. Groisman, A. and E. Kaplan, *An Experimental-Study Of Cracking Induced By Desiccation*. Europhysics Letters, 1994. **25**(6): p. 415-420.
93. Jarai-Szabo, F., et al., *Shake-induced order in nanosphere systems*. European Physical Journal E, 2007. **23**(2): p. 153-159.

94. Li, Y.Z., T. Kunitake, and S. Fujikawa, *Efficient fabrication of large, robust films of 3D-ordered polystyrene latex*. Colloids and Surfaces a-Physicochemical and Engineering Aspects, 2006. **275**(1-3): p. 209-217.
95. Vickreva, O., O. Kalinina, and E. Kumacheva, *Colloid crystal growth under oscillatory shear*. Advanced Materials, 2000. **12**(2): p. 110-112.
96. Zhang, J., et al., *Fabrication of high-quality colloidal crystal films by vertical deposition method integrated with a piezoelectric actuator*. Thin Solid Films, 2010. **518**(18): p. 5204-5208.
97. Park, J. and J. Moon, *Control of colloidal particle deposit patterns within picoliter droplets ejected by ink-jet printing*. Langmuir, 2006. **22**(8): p. 3506-3513.
98. Cui, L., et al., *Fabrication of large-area patterned photonic crystals by ink-jet printing*. Journal of Materials Chemistry, 2009. **19**(31): p. 5499-5502.
99. Jiang, P. and M.J. McFarland, *Large-scale fabrication of wafer-size colloidal crystals, macroporous polymers and nanocomposites by spin-coating*. Journal of the American Chemical Society, 2004. **126**(42): p. 13778-13786.
100. Mihi, A., M. Ocana, and H. Miguez, *Oriented colloidal-crystal thin films by spin-coating microspheres dispersed in volatile media*. Advanced Materials, 2006. **18**(17): p. 2244-+.
101. Liu, X.F., et al., *Wafer-Scale Surface-Enhanced Raman Scattering Substrates with Highly Reproducible Enhancement*. Journal of Physical Chemistry C, 2009. **113**(33): p. 14804-14811.

102. Jin, C.J., et al., *Template-assisted growth of nominally cubic (100)-oriented three-dimensional crack-free photonic crystals*. Nano Letters, 2005. **5**(12): p. 2646-2650.
103. Hur, J. and Y.Y. Won, *Fabrication of high-quality non-close-packed 2D colloid crystals by template-guided Langmuir-Blodgett particle deposition*. Soft Matter, 2008. **4**(6): p. 1261-1269.
104. Khanh, N.N. and K.B. Yoon, *Facile Organization of Colloidal Particles into Large, Perfect One- and Two-Dimensional Arrays by Dry Manual Assembly on Patterned Substrates*. Journal of the American Chemical Society, 2009. **131**(40): p. 14228-+.
105. Kanai, T., et al., *Air-pulse-drive fabrication of photonic crystal films of colloids with high spectral quality*. Advanced Functional Materials, 2005. **15**(1): p. 25-29.
106. Wakabayashi, N., et al., *Three-dimensional centimeter-sized colloidal silica crystals formed by addition of base*. Langmuir, 2006. **22**(18): p. 7936-7941.
107. Toyotama, A., et al., *Thermally driven unidirectional crystallization of charged colloidal silica*. Journal of the American Chemical Society, 2007. **129**(11): p. 3044-+.
108. Kanai, T. and T. Sawada, *New Route to Produce Dry Colloidal Crystals without Cracks*. Langmuir, 2009. **25**(23): p. 13315-13317.
109. Cai, Z.Y., et al., *Self-Assembly of Crack-Free Silica Colloidal Crystals on Patterned Silicon Substrates*. Journal of Physical Chemistry C, 2011. **115**(20): p. 9970-9976.

110. Oh, J.R., et al., *Fabrication of wafer-scale polystyrene photonic crystal multilayers via the layer-by-layer scooping transfer technique*. Journal of Materials Chemistry, 2011. **21**(37): p. 14167-14172.
111. Yang, H. and P. Jiang, *Large-Scale Colloidal Self-Assembly by Doctor Blade Coating*. Langmuir, 2010. **26**(16): p. 13173-13182.
112. Jeong, S., et al., *Fast and Scalable Printing of Large Area Monolayer Nanoparticles for Nanotexturing Applications*. Nano Letters, 2010. **10**(8): p. 2989-2994.
113. Galisteo-Lopez, J.F., et al., *Self-Assembled Photonic Structures*. Advanced Materials, 2011. **23**(1): p. 30-69.
114. Velev, O.D. and S. Gupta, *Materials Fabricated by Micro- and Nanoparticle Assembly - The Challenging Path from Science to Engineering*. Advanced Materials, 2009. **21**(19): p. 1897-1905.
115. Ye, Y.H., et al., *Self-assembling three-dimensional colloidal photonic crystal structure with high crystalline quality*. Applied Physics Letters, 2001. **78**(1): p. 52-54.
116. Shimmin, R.G., A.J. DiMauro, and P.V. Braun, *Slow vertical deposition of colloidal crystals: A Langmuir-Blodgett process?* Langmuir, 2006. **22**(15): p. 6507-6513.
117. McLachlan, M.A., et al., *Thin film photonic crystals: synthesis and characterisation*. Journal of Materials Chemistry, 2004. **14**(2): p. 144-150.
118. McLachlan, M.A., et al., *Domain size and thickness control of thin film photonic crystals*. Journal of Materials Chemistry, 2005. **15**(3): p. 369-371.

119. Li, W., B. Yang, and D. Wang, *Fabrication of Colloidal Crystals with Defined and Complex Structures via Layer-by-Layer Transfer*. Langmuir, 2008. **24**(23): p. 13772-13775.
120. Li, Q.Y., et al., *Preparation of higher-quality SiO<sub>2</sub> opals using a new submicrospheres selection technique*. Colloids and Surfaces a-Physicochemical and Engineering Aspects, 2003. **216**(1-3): p. 123-128.
121. Li, Q.T., Y.F. Chen, and P. Dong, *Improvement of the quality of silica colloidal crystals by controlling drying*. Materials Letters, 2005. **59**(27): p. 3521-3524.
122. Enomoto, N., et al., *Novel processing for improving monodispersity of ceramic spheres and colloidal crystallinity*. Science and Technology of Advanced Materials, 2006. **7**(7): p. 662-666.
123. Piret, F. and B.L. Su, *High quality photonic opaline structure in one night and their optical reflectance*. Chemical Physics Letters, 2008. **454**(4-6): p. 318-322.
124. Ko, Y.G. and D.H. Shin, *Effects of liquid bridge between colloidal spheres and evaporation temperature on fabrication of colloidal multilayers*. Journal of Physical Chemistry B, 2007. **111**(7): p. 1545-1551.
125. Li, J.A. and Y.C. Han, *Optical intensity gradient by colloidal photonic crystals with a graded thickness distribution*. Langmuir, 2006. **22**(4): p. 1885-1890.
126. A fast Fourier transform (FFT) is an efficient algorithm to compute the discrete Fourier transform (DFT) and its inverse. A DFT decomposes a sequence of values into components of different frequencies. An FFT is a way to compute the same result more quickly

127. Khunsin, W., et al., *Quantitative analysis of lattice ordering in thin film opal-based photonic crystals*. Advanced Functional Materials, 2008. **18**(17): p. 2471-2479.

# **CHAPTER 2.**

## **EXPERIMENTAL DETAILS**

In this chapter the experimental techniques used in this research are introduced, including materials, chemicals, and equipment. The chapter is divided into 3 areas: firstly the chemicals and other materials used in each opal film manufacturing method are described; secondly, a description of the opal film manufacturing methods, including a brief description of each method of crystallisation is given; thirdly, the optical and physical characterisation of those films with respect to the overall requirements of this study is described, used to assess each method in terms of the benefits and drawbacks to production of high quality, large area films.

### **2.1 CHEMICALS AND MATERIALS**

Silica particles were synthesised using a modified Stöber synthesis [1] involving the hydrolysis of tetraethyl orthosilicate (TEOS) in the presence of ethanol and ammonium hydroxide as a catalyst. Each preparation was performed at room temperature under constant magnetic stirring for 24 hours, followed by removal of unreacted TEOS and ammonia by repeated centrifuging, washing-sonication cycles in ultrapure water and ethanol. Tetraethyl orthosilicate (TEOS), ammonium hydroxide (25%) and ethanol 100 were purchased from Sigma-Aldrich, and used as received without further purification. Ethanol was filtered through Whatmann filter papers before



use to remove any particulate impurities. Ultrapure water (18.2M $\Omega$ cm) was used directly from a Millipore water system.

Bulk silica particle samples at 210nm (KEW20) and two samples at 250nm and 280nm (KEW30) were also purchased from Seahostar, Nippon Shokubai, Japan. These were received at approximately 20wt% in pure water, and reduced to the required concentration during film growth experiments using pure water and/or ethanol (the details of which are given in the experimental chapters)

Standard glass microscope slides and silicon wafers were cut to required sizes and used as substrates for film growth. Both types of substrates were made hydrophilic in either Piranha solution (3:1 mixture of sulphuric acid and hydrogen peroxide), or by sonicating in a mixture of pure water, hydrogen peroxide and ammonium hydroxide at a ratio of 5:1:1. Sulphuric acid (95-98%), ammonium hydroxide (25%), hydrogen peroxide (30%), were purchased from Sigma-Aldrich, and used as received without further purification. Prior to being rendered hydrophilic, both substrates were ultrasonically cleaned in ethanol for 5 minutes, which also helped remove particulates.

Fluoride silicone rubber substrates were rendered hydrophilic by first sonicating in a detergent solution for 5 minutes, before rinsing in pure water, drying with nitrogen, and then placing in oxygen plasma (Harrick plasma cleaner, PDC-002), or Ion Bombardment chamber (PRI-10), for 5 minutes.

Under oil crystallisation experiments used silicone oil (Dow Corning Poly (Dimethylsiloxane) 200 fluid, 10cSt, or Xiameter PMX200 10cSt) to cover the silica suspension during film formation, and a volatile 0.65cSt silicone oil (Dow Corning Dimethylsiloxane, DMS 200 fluid, 0.65cSt, or Xiameter PMX200, 0.65cSt), for rinsing and drying the film after the process was complete.

During the sonication film growth 2 solvents were added to standard silica suspensions; formamide (Sigma-Aldrich) and glycerol (Sigma-Aldrich). Both solvents were used as received from the manufacturer.

During the evaporation deposition experiments several polymers were investigated, including a redispersible polymer (Elotex FX2700, a redispersible binder based on a copolymer of vinyl acetate and ethylene) [2], poly vinyl alcohol (PVA), polymethyl methacrylate (PMMA) monomer (99% Sigma-Aldrich), and a high refractive index ( $\eta=1.54$ ) adhesive, Norland Optical Adhesive 68 (NOA68). All polymers / adhesives were added to the colloidal suspension, pre dispersed in an ultrapure water solution at low concentrations, with the exception of NOA68 which was pre dissolved in ethanol prior to adding to the silica suspensions.

## 2.2 UNDER OIL DEPOSITION

One of the simplest and most convenient methods of forming an opal film is by drying a colloidal suspension on a solid substrate. However, with this simple method it is difficult to form a uniform opal film. On a hydrophilic substrate, the colloidal particles accumulate at the edge of the droplet due to pinning at the contact line. As a result, a “coffee ring” shaped opal is formed at the contact line, often with a much thinner central area. This phenomenon is explained on the basis of capillary flow causing ring formation (Chapter 1, figure 1.18). Reducing capillary flow in a colloidal suspension can depress ring formation as the suspension dries.

The Under Oil Crystallisation (UOC) method covers the suspension with a hydrophobic silicone liquid. The cover layer of silicone oil reduces evaporation of water at the contact line of the suspension, suppressing capillary flow, and thus enables the fabrication of a uniform, flat opal film over a large area on a hydrophilic solid substrate [3]. The silicone oil (specific gravity, 0.97g/mL) is less dense than water and thus sits on top of the colloidal suspension. In this work a hydrophilic substrate was placed in a flat bottomed dish on a levelled stage in an oven at 50°C. 0.5ml of an aqueous silica suspension at a given percent by weight was placed onto the substrate using a pipette. The suspension spread across the surface of the substrate to form a liquid droplet film. Silicone oil was then slowly added to the dish and to cover the colloidal suspension. After 2-3 days the water of the suspension had evaporated through the oil layer leaving an oil-filled crystalline film on the substrate. The surface of the colloidal suspension was completely

covered with the hydrophobic silicone oil, (figure 2.1a(A)) thus, the rate of the evaporation of water was greater at the centre than that at the contact line. As the water in the suspension decreased, silica particles crystallized due to electrostatic interactions. The crystallization starts from near the contact line of the suspension and spreads inwards to the centre. Once crystallisation is complete, the silicone oil was removed using a syringe, and the film was rinsed with a volatile silicone oil (Dow Corning Dimethylsiloxane, DMS 200 fluid, 0.65cSt, or Xiameter PMX200, 0.65cSt), and allowed to dry.

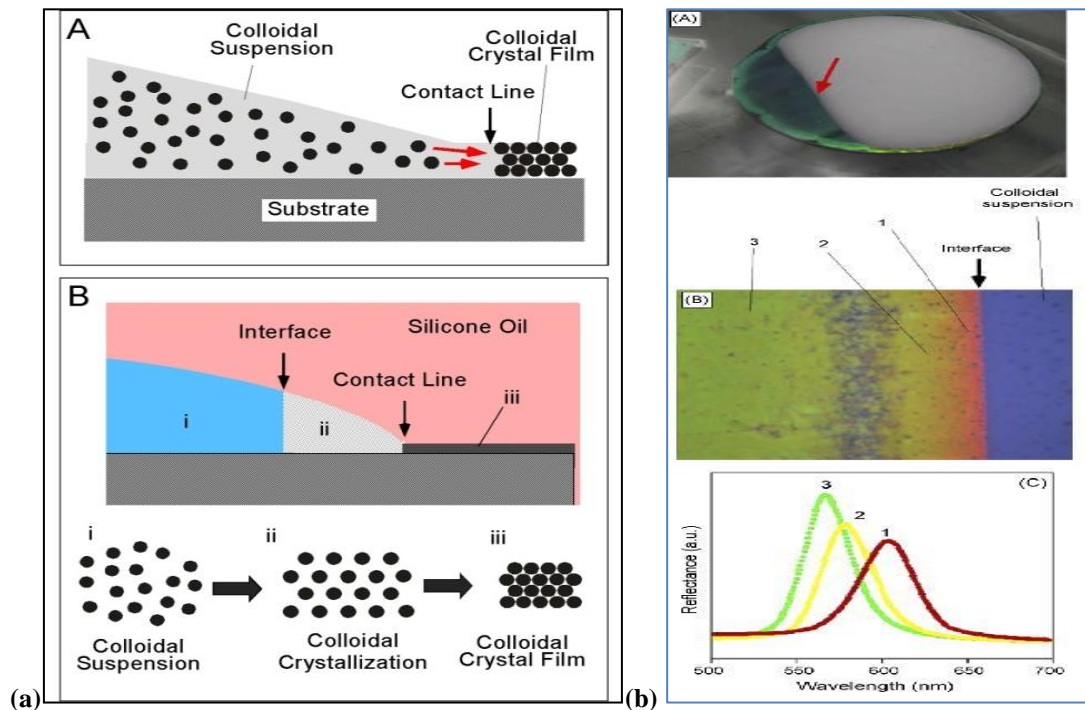


**Figure 2.1 (a).** Comparison of the packing models: (A) Crystallization in the conventional method by capillary flow; (B) Under Oil Crystallization method, illustrating the three stages: (i) colloidal suspension; (ii) non-close packed colloidal crystal; (iii) closely packed colloidal crystal; these stages represent the corresponding regions indicated in (b). (b) Observations of the crystallization process. (A) Image from a CCD camera during the process. (B) Optical microscope image near the interface. (C) Spots near 1, 2, and 3 in image B were measured by using a fibre optic spectrometer. (Figures taken from reference [4])

Figure 2.1a(B), shows a schematic diagram of the growth process of an opal film grown under a silicone oil layer employed in this present work. Region (i) shows the colloidal suspension in Brownian motion. In front of the advancing colloidal crystal a non-close-packed ordered colloidal crystal forms at the location labelled as the “interface”, region (ii). In region (ii) the distance between the colloidal particles in the non-close-packed ordered colloidal crystal decreases as the water continues to evaporate. Here the lattice spacing,  $d$ , is larger than the diameter of the silica microspheres; thus the stop band position is located at longer wavelengths (figure 2.1b(C)). With further evaporation of water from the colloidal suspension,  $d$  decreases and the film colour gradually changes from red to green (figure 2.1b(B)). Finally a close-packed colloidal crystal opal structure filled with silicone liquid is formed on the glass substrate, at the location labelled “contact line” in region (iii). This crystallization process is different from that of conventional convective self-assembly processes because, here, the colloidal crystal grows from the contact line at the outer edge of the suspension due to the loss of the liquid from the suspension through the silicone oil. Fudouzi suggests that the role of the silicone oil is to slow down the self-assembly process. Within the close-packed region the silicone oil replaces the water so that there will be a water-silicone oil interface within the close packed crystal as well.

Figure 2.1b(A), shows a digital camera image of the typical crystal growth during UOC. The milky white area is the wet colloidal suspension film on a silicon wafer. In contrast, a crystalline opal film has formed in the green area. The interface between the milky white and green regions is the boundary between the order-disorder

states of a silica colloidal suspension. An optical microscope image reveals the region in the vicinity of this interface.

Thus, drying the suspension under silicone oil leads to the formation of an opal film with a uniform surface. In addition the areas between cracks of opal films made by UOC are larger than those made by conventional methods, some of these areas being as large as 1mm. During crystallization, the water is replaced with silicone liquid. The silicone liquid may reduce the hydrostatic tension at the final stage of shrinking of the wet opal film, and as a result, the domains grown by the UOC method are larger. Fudouzi states that the UOC method is easy to scale up and has no theoretical size limit [3]. Using this method, flat and uniform opal films of areas  $>100\text{cm}^2$  have been produced. However, the opal films produced are not a single crystal but rather are separated into many domains separated by cracks.

## **2.3 ULTRASONIC DEPOSITION**

A second method designed to overcome the pinning of the contact line of a droplet on a horizontally placed hydrophilic substrate uses small vibrations from an ultrasonic bath. In this method the suspension is kept homogeneous by application of the ultrasound agitation, thus avoiding the formation of a lateral deposition front [5]. Marlow et al. [5] suggest that evaporation leads to a gradient, but that this is now perpendicular to the film. Consequently, the opal formation front will also move perpendicular to the film; that is, only over a very short distance which means that films

can be formed much faster. They also note that this method may enable the production of large-area films in much shorter timescales, and with reduced cracking. The sonication forces therefore may be able to overcome the relatively weak interactions of both particle-to-particle and particle-to-substrate, rearranging the particles in the film into large ordered areas with reduced voids [6].

Figure 1.17(i) (Chapter 1) shows a schematic of the set up used in these experiments, and figure 2.2 shows a digital camera image of the set-up of the film fabrication method before drying. A glass substrate was placed centrally in a polycarbonate petri dish, which was floated on the surface of a water filled ultrasonic bath (Bandelin, Sonorex Digital 10P, 35kHz). A given amount of silica colloid suspension (0.5ml on a 25mm x 25mm substrate) was placed onto the glass substrate using a pipette, and spread uniformly across the hydrophilic surface. Then the ultrasonic bath was switched on, with a predetermined power setting, and the suspension water was allowed to evaporate during sonication. The time to form a crystalline thin film was generally less than 1 hour at 35-45°C. A number of control films were prepared under the same conditions but without sonication. In order to establish a Marangoni flow during film formation during sonication, 2 solvents were added to a standard aqueous suspension, and sonicated as described previously.

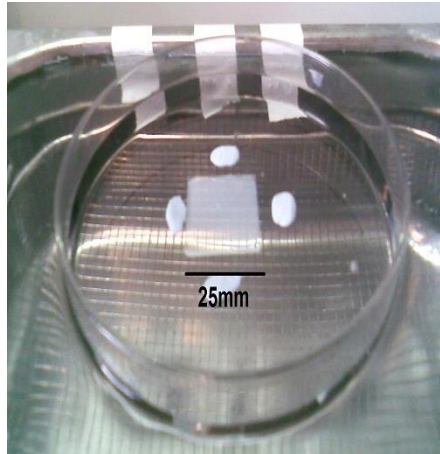


**Figure 2.2. Silica colloidal suspension on glass substrate floated at the surface of the ultrasonic bath before drying.**

Sasaki and Hane [7] used ultrasonic radiation during the evaporation of colloidal solutions of PS particles to improve the quality and ordering of monolayers of colloidal particles. Li et al. [8] also used a sonicated-assisted method to form highly ordered 3-D PS particle films, from various sphere sizes, up to 1053nm diameter. The thickness of their 3D films being adjusted, up to 30 layers, by changing the concentration of the initial particle suspension. Both Vickreva [9] and Zhang [10] suggest that “resonance conditions” (optimised vibration conditions), are required for particles to be manufactured into the highest quality film possible.

By using a mixed solvent approach, Park and Moon [11] showed that the initial evaporation develops a concentration gradient along the droplet surface, while edge evaporation is slowed down, and a concentration gradient occurs within the droplet. A Marangoni flow is established from regions with low surface tension to regions with high surface tension. They used formamide, a high boiling point solvent compared to water with a lower surface tension (58.2mN/m compared to 72.8mN/m), to create their



edge to centre circulation flow, which prevented the particles from concentrating at the contact line during drying. In combination with sonication, these 2 effects would therefore suppress ring formation, and promote the formation of a uniform, flat crystalline opal film. In this present work small quantities of formamide and glycerol were added to standard suspensions, and stirred for 10 minutes before placing them onto the substrate for sonication.

## **2.4 EVAPORATION DEPOSITION**

Since its introduction in 1999 by Jiang et al. [12] the evaporation deposition (or vertical deposition) method has become the most widespread self-assembly technique used to fabricate opalline 3D photonic crystals, and is based on the convective self-assembly of colloids on a substrate by the action of a moving meniscus.

In a typical experimental set up a cleaned, hydrophilic, flat substrate is placed into a vial containing a known concentration of colloidal suspension, nominally from 0.1 to 2vol.% silica spheres in ethanol or ethanol / water mixes. The colloidal suspension wets the substrate and a meniscus is formed at the substrate, air and suspension interface (Figure 2.3). Crystal growth initiates at the point of the meniscus where its thickness is below the diameter of the sphere [13]. Menisci are formed between the spheres, which are pulled towards the substrate and to each other, due to capillary forces as the particle-particle distances become smaller, which tends to order them into a close packed array.

Solvent flow towards the meniscus region due to evaporation (which is highest in the meniscus region), drags spheres from the suspension and these are incorporated into an ordered fcc structure [14, 15].

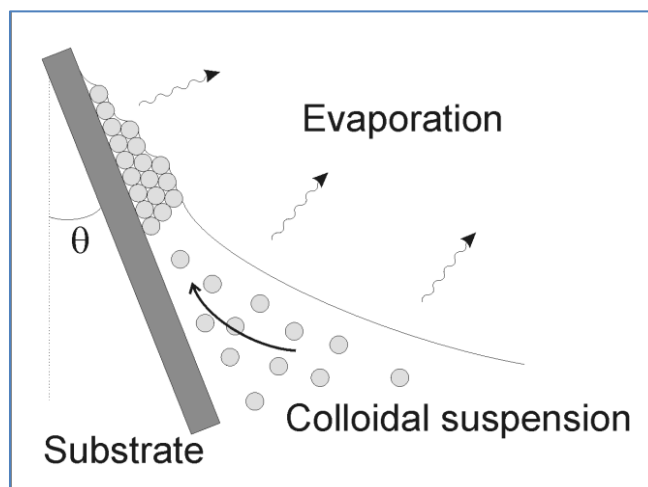


**Figure 2.3: Schematic of the vertical deposition method. A substrate is placed in a colloidal suspension which wets it. The substrate is inclined at an angle  $\theta$ . Ordering of the spheres takes place at the meniscus.**

Optimal conditions for the growth of a film with good crystalline order include an optimum evaporation rate which allows for the high quality ordering of the particles into a film. In this study an optimum temperature of 50°C was used for all ethanolic suspensions. However, when preparing films using mixed ethanol & water suspensions, higher temperatures, up to 60°C, were also found to produce high quality films. To provide a small convective flow within our systems, suspension containers were placed on the floor of the oven. A temperature difference of 2-5°C (depending on the depth of suspension) was measured between the suspension at the bottom of the container, and that at the suspension surface. Aluminium cylinders were placed in the oven to provide a heat sink, preventing temperature fluctuations within the oven, thus maintaining a stable

temperature during film growth. To reduce stick slip motions at the surface of the suspension (and therefore at the meniscus) the vessel walls were also made hydrophilic in the same manner as the substrates, reported earlier.

Initial experiments carried out by Jiang et al. [12] consisted of a solution of silica particles in ethanol, but were limited by the sphere size. For spheres with diameters above approximately 500nm, sedimentation decreased the sphere concentration and yielded poor quality samples. In this study, only silica spheres of diameter <500nm have been used. Bulk silica particle samples at 280nm (KEW30) were used in order to evaluate repeatability between samples in chapters, 6 & 7.

Glass microscope slides (37 x 12mm) were placed into 50mm x 24mm diameter vials with a 10ml suspension added, the substrate having an angle of 30° from vertical. Larger area films produced by controlled evaporation deposition were grown on a full microscope slide, 75mm x 25mm. To minimise the effects of increasing layers with length of growth, [16], slides were placed horizontally across a 500ml beaker, and near vertically in the y-direction (figure 2.4). By placing the slides horizontally, the growth length would be limited to a maximum of 25mm, thus minimising the increasing thickness effect seen using this method. At a growth rate at 50°C of approximately 0.6mm/hour, this method is still slow (approximately 40hrs to produce a 25mm film), however, relatively even films were produced along 25mm of film growth.

Initial trials with aqueous ethanol silica suspensions found that a ratio of 3:1 ethanol:water produced the highest quality films using KEW30 (280nm) silica particles (see Appendix A, figures 1 & 2 and table 1). Figure 2.4 shows a digital camera image of film fabrication using mixed solvents on a full glass slide. The glass substrate was placed centrally in a 500ml beaker containing the suspension. A 200ml suspension was sufficient to completely cover a 25mm depth of glass slide. A specific concentration, by volume percent, of silica colloid suspension was placed into the beaker, the slide was held in position near vertically with tweezers, and the film allowed to grow in an oven at 50°C (unless otherwise stated).



**Figure 2.4. Digital camera image of the experimental method.**

## 2.5 OPTICAL CHARACTERISATION

Optical characterisation was performed using a Mikropack halogen HL2000 white light source, with a focussed spot size at the sample of approximately 1.5mm diameter. The transmitted or reflected light was collected via an optical fibre to an Ocean Optics HR4000 detector for wavelengths in the UV-visible range (Figure 2.5). Spectral analysis was performed using Ocean Optics software SpectraSuite. Reflectance measurements were calibrated against a Thor Labs ME1-PO1 silver mirror. Transmission calibration was made with respect to air. For reflectance measurements, the sample, the 2<sup>nd</sup> focussing lens and detector lens were rotated around the axis of the sample to various reflectance angles from a minimum of 10° to a maximum of 80°, while for transmission measurements, only the sample itself was rotated. Angle-resolved transmission and reflection spectra of the films were acquired at different angles of incidence,  $\theta$ , with respect to the film normal.

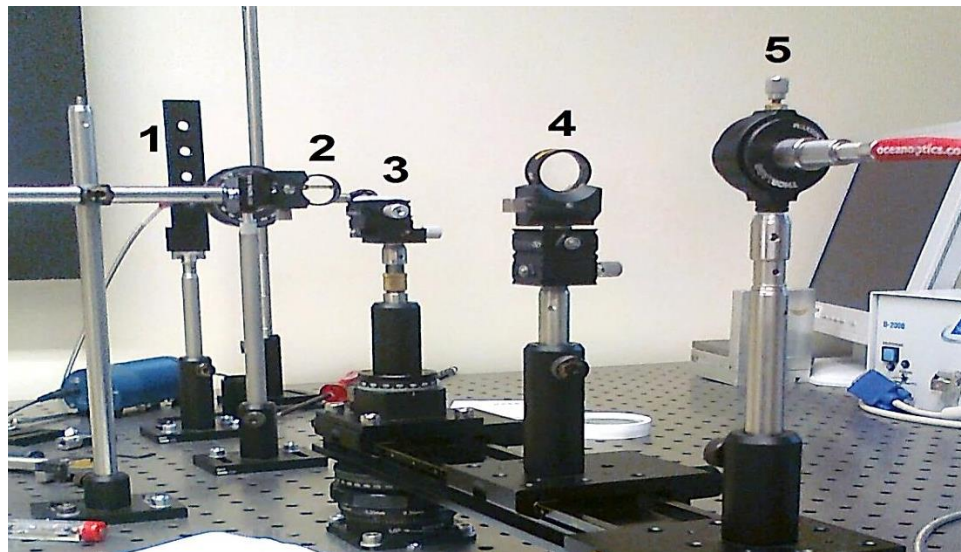


Figure 2.5. Showing the optical set up for determination of the spectral data; (1) light source, (2) focussing lens, (3) sample holder, (4) 2<sup>nd</sup> focussing lens, and (5) detector lens.

## **2.6 PHYSICAL CHARACTERISATION**

### **2.6.1 OPTICAL MICROSCOPY**

Optical Microscope images were taken using a Bruker Hyperion microscope, with a Lumenera Infinity 1 camera attached. Images were taken using Infinity Capture software.

### **2.6.2 SCANNING ELECTRON MICROSCOPY**

High magnification images were taken using a high resolution scanning electron microscope (HRSEM, Quanta FEG 650, FEI Company). During SEM investigations, samples were gold-sputtered prior to examination. Standardised conditions of beam voltage and spot size were used in all FFT quality images.

## REFERENCES:

1. Stober, W., A. Fink, and E. Bohn, *Controlled Growth Of Monodisperse Silica Spheres In Micron Size Range*. Journal of Colloid and Interface Science, 1968. **26**(1): p. 62-&.
2. [www.elotex.com](http://www.elotex.com)
3. Fudouzi, H., *Fabricating high-quality opal films with uniform structure over a large area*. Journal of Colloid and Interface Science, 2004. **275**(1): p. 277-283.
4. Fudouzi, H., *Novel coating method for artificial opal films and its process analysis*. Colloids and Surfaces a-Physicochemical and Engineering Aspects, 2007. **311**(1-3): p. 11-15.
5. Marlow, F., et al., *Opals: Status and Prospects*. Angewandte Chemie-International Edition, 2009. **48**(34): p. 6212-6233.
6. Jarai-Szabo, F., et al., *Shake-induced order in nanosphere systems*. European Physical Journal E, 2007. **23**(2): p. 153-159.
7. Sasaki, M. and K. Hane, *Ultrasonically facilitated two-dimensional crystallization of colloid particles*. Journal of Applied Physics, 1996. **80**(9): p. 5427-5431.
8. Li, Y.Z., T. Kunitake, and S. Fujikawa, *Efficient fabrication of large, robust films of 3D-ordered polystyrene latex*. Colloids and Surfaces a-Physicochemical and Engineering Aspects, 2006. **275**(1-3): p. 209-217.
9. Vickreva, O., O. Kalinina, and E. Kumacheva, *Colloid crystal growth under oscillatory shear*. Advanced Materials, 2000. **12**(2): p. 110-112.

10. Zhang, J., et al., *Fabrication of high-quality colloidal crystal films by vertical deposition method integrated with a piezoelectric actuator*. Thin Solid Films, 2010. **518**(18): p. 5204-5208.
11. Park, J. and J. Moon, *Control of colloidal particle deposit patterns within picoliter droplets ejected by ink-jet printing*. Langmuir, 2006. **22**(8): p. 3506-3513.
12. Jiang, P., et al., *Single-crystal colloidal multilayers of controlled thickness*. Chemistry of Materials, 1999. **11**(8): p. 2132-2140.
13. Denkov, N.D., et al., *Mechanism Of Formation Of 2-Dimensional Crystals From Latex-Particles On Substrates*. Langmuir, 1992. **8**(12): p. 3183-3190.
14. Norris, D.J., et al., *Opaline photonic crystals: How does self-assembly work?* Advanced Materials, 2004. **16**(16): p. 1393-1399.
15. Brewer, D.D., et al., *Mechanistic Principles of Colloidal Crystal Growth by Evaporation-Induced Convective Steering*. Langmuir, 2008. **24**(23): p. 13683-13693.
16. Hartsuiker, A. and W.L. Vos, *Structural properties of opals grown with vertical controlled drying*. Langmuir, 2008. **24**(9): p. 4670-4675.



# **CHAPTER 3.**

## **DEVELOPMENT OF AN IMPROVED METHOD FOR THE SYNTHESIS OF SILICA PARTICLES**

### **3.1 INTRODUCTION**

Traditionally the so-called Stöber synthesis [1] involves fixing the tetraethyl orthosilicate (TEOS) concentration and varying the water, ethanol and ammonia concentrations in order to achieve varying silica particle sizes. Via this method a wide range of silica sphere diameters can be obtained. However, many previous analyses of the relationship between water ammonia concentrations, and final sphere diameters do not show any simple correlation [2]. Indeed, usually the water and ammonia (or other) concentrations have to be varied in order to achieve a particular required silica particle size. By using a modified Stöber synthesis, without the inclusion of added water in the preparation, the size of the particles can be controlled simply by the addition of varying amounts of ammonium hydroxide, for diameters approximately 20 to 120nm [3, 4]. When the ammonia concentration is increased, both the rate of hydrolysis and condensation increase, and concentration of the intermediate  $(\text{Si}(\text{OC}_2\text{H}_5)_{4-x}(\text{OH})_x)$  rapidly increases due to the rapid hydrolysis reaction; however, as it reaches the supersaturation region, the rate of consumption of the intermediate through the

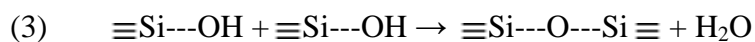
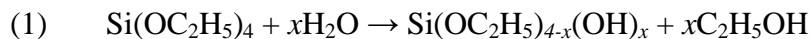
condensation reaction is also relatively high, which probably shortens the nucleation period. Thus, the total number of nuclei formed will be less, and the final particle size of the synthesized silica colloids will be larger [5]. Enomoto et al. [6] found they could improve silica particle monodispersity by ageing initial solutions of (1) an ethanolic solution with TEOS, and (2) an ethanolic solution with ammonia. Both solutions were aged at room temperature for several days before mixing.

In this work the particle sizes obtainable using this modified synthesis method have been extended up to approximately 600nm diameter in a single processing step. This is larger than that traditionally achieved from a one-pot methodology; to obtain silica particles of this diameter normally requires preparing them from smaller seed particles, and thus the work described here represents an advance in our understanding of colloidal silica synthesis, providing as it does a means of defining particle size over a large range of diameters. For the reasons described above, in the work presented here an ageing period was used. Although relatively short, a minimum of 2 hours ageing was selected.

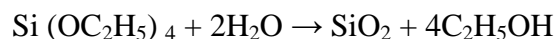
### **3.2 PARTICLE SYNTHESIS**

Silica particles were prepared by a modified Stöber synthesis [1] involving the hydrolysis of TEOS in the presence of ethanol and ammonium hydroxide as a catalyst. Each preparation was performed at room temperature under constant magnetic

stirring for 24 hours. In the Stöber synthesis many reactions can occur, but those of most importance are the hydrolysis and condensation reactions given below [7]:-



The overall reaction can then be depicted as follows:



In this modified method, solution (1), an ethanolic solution of TEOS was prepared from 50ml ethanol and 10ml TEOS. This solution was stirred in a sealed glass container for a minimum of 2 hours prior to introducing into the final mixture.

Solution (2), an ethanolic mixture of 200ml ethanol plus a given amount of ammonium hydroxide solution (dependent upon the required final particle size), was prepared and rapidly stirred in a sealed glass container for approximately 10 minutes. After which solution (1) was then added quickly into solution (2). The final solution was held under constant stirring for approximately 24 hours, in a sealed container. Final

particle solutions were “washed” by centrifuging and redispersion and by sonicating in an ultrasonic bath, in a 50:50 mixture of pure water and ethanol at least twice in order to remove residual ammonia hydroxide and TEOS, and then further “washed” in ethanol 6 times, before storage under pure ethanol ready for use. The suspensions in ethanol were thus concentrated and their final solid content was determined from the amount of residual solids in a given volume of suspension, after overnight drying at 60-65°C.

Via this method, spherical mono-disperse silica particles were formed having mono-dispersities generally in the range of 4-8%, as measured by SEM. The SEM images were then transferred to a software package, ImageJ, which allows measurement of over ca. 200 particles in order to give a statistically meaningful sample size for the mean diameters and standard deviations to be calculated [8]. Particles measured by both SEM and the ImageJ software gave a difference of <1% between the two measurements, allowing us to use the software as an accurate measurement tool.

In order to achieve high quality colloidal crystal films from these silica particles, a monodispersity of less than 5% is required, with smaller and larger particles removed. This was achieved by centrifugation and sedimentation similar to the method outlined in [9].

Larger particles (>600nm) were produced by using an initial batch of smaller (<600nm) particles as seeds for further growth; a trial of this technique was performed

using the experimental guidelines given in [10], the results from which are also presented below.

### **3.3 RESULTS AND DISCUSSION**

#### **3.3.1 SILICA SYNTHESIS**

The size of the particles was controlled by the addition of different amounts of ammonium hydroxide, for diameters from approximately 100 to 600nm. [3, 4]. By changing only one variable, (the volume of added  $\text{NH}_4\text{OH}$ ), a number of different batches were made, and their diameters versus ammonia volume added are plotted below, Figure 3.1. The volumes of ethanol (250ml) and TEOS (10ml) were kept constant during all experiments.

As can be seen in Figure 3.1, a power law curve fitted to these results allows the calculation of a specific volume of ammonium hydroxide to be used for the formulation of a specific size of particles. When taking into account the results achieved by Deak et al. [3, 4], we find that our power law fit also encompasses their results, along with these results. Therefore, particle sizes from below 100nm to approximately 600nm can easily be achieved by this method. When an excess of ammonia was used (40ml) the final average diameter was 613nm. When calculating the final diameter from the fitted power curve, at 40ml ammonia, particles of 1000nm would be expected. Therefore there is a

limit to the maximum particle sizes achieved by this method. The power law curve is a simple best fit using excel trendline options, and is not expected to be related to any particular reaction dynamics, at least not in an obvious way. The nature of this relationship was not examined further.

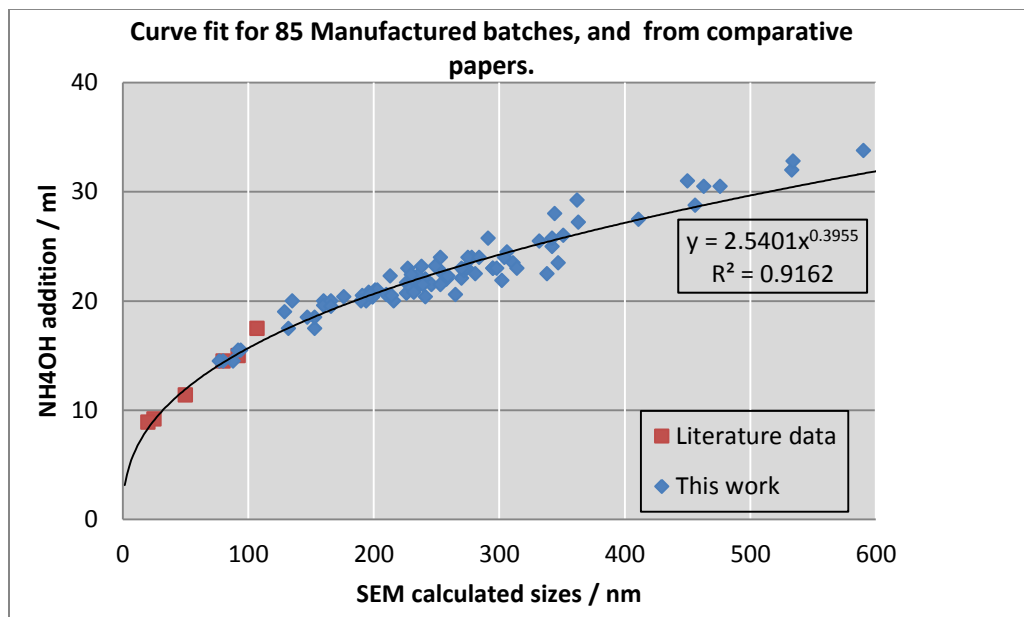


**Figure 3.1. Comparative graph of manufactured particle sizes versus addition volume of ammonium hydroxide, to those results recorded in the literature [3, 4]**

Costa et al. [11] were able to show that by using a greater addition volume of TEOS (doubled to 20ml in this case), into the equivalent proportions of ethanol and ammonia solution, the particle sizes decrease, most likely due to an increase in nucleation sites. Again, over a range of 20-120nm particle size, a power curve fits their results data, ( $R^2$  value of 98.9%), figure 3.2 (red curve).

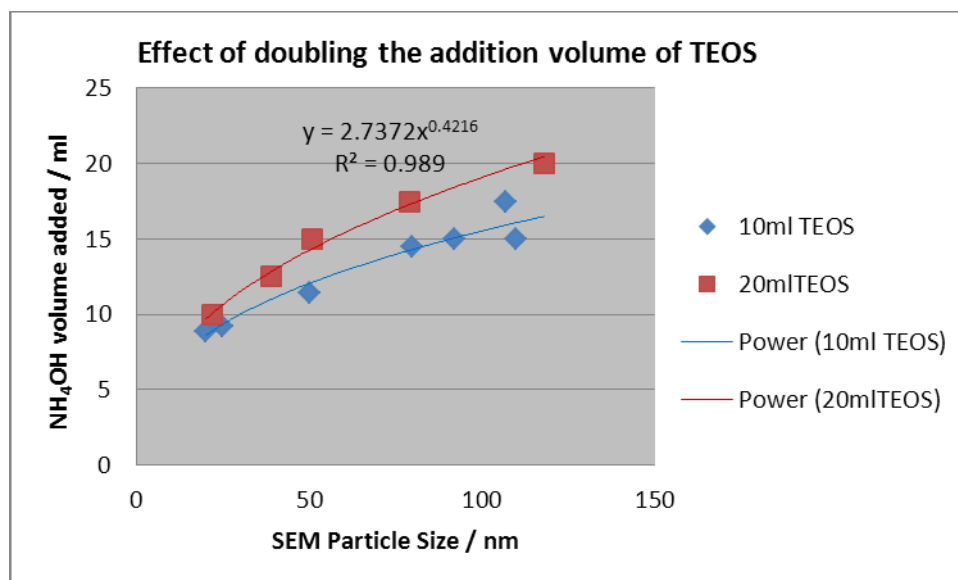


Figure 3.2. Comparative graph of particles manufactured by Deak et al. [3, 4] at 10ml addition of TEOS (blue), versus those manufactured by Costa et al. [11] at 20ml addition of TEOS (red).

### 3.3.2 SYNTHESIS OF LARGER PARTICLES (>600nm)

It was found that larger particles (>600nm) could be produced by using an initial batch of smaller (<600nm) particles as seeds for further growth, using the experimental guidelines in [10]. The formation of secondary particles during seed particle growth which could cause a multimodal distribution of particle size was suppressed using higher ammonia and water concentrations. In addition, a low feed rate of the TEOS, and rigorous fast stirring, significantly reduces secondary particle formation because they contribute to the slow generation of supersaturation and rapid seed particle growth, respectively [10].

An initial sample was prepared of approximately 600nm particles (with a dispersity of 7.4%), figure 3.3(a). A 20ml solution of this sample was added to 100ml

ethanol + 100ml purified water and an excess of  $\text{NH}_4\text{OH}$  (40ml), and stirred for 24 hours, solution (2). A dilute ethanolic TEOS solution, consisting of 10ml TEOS and 90ml ethanol, solution (1), was also stirred for 24 hours. Then 10ml per hour of solution (1) was added into solution (2) using a motorised syringe, over a period of 7 hours, (total volume addition of TEOS was 7ml), under rapid stirring. A SEM image of the resultant particles is shown in Figure 3.3(b). Although secondary particle growth is seen (secondary particle sizes are  $<200\text{nm}$ ) in these samples, these were easily removed by repeated centrifugation, (Figure 3.3(c)) followed by sedimentation (Figure 3.3(d)). The final particle size was 840nm, (3% dispersity).



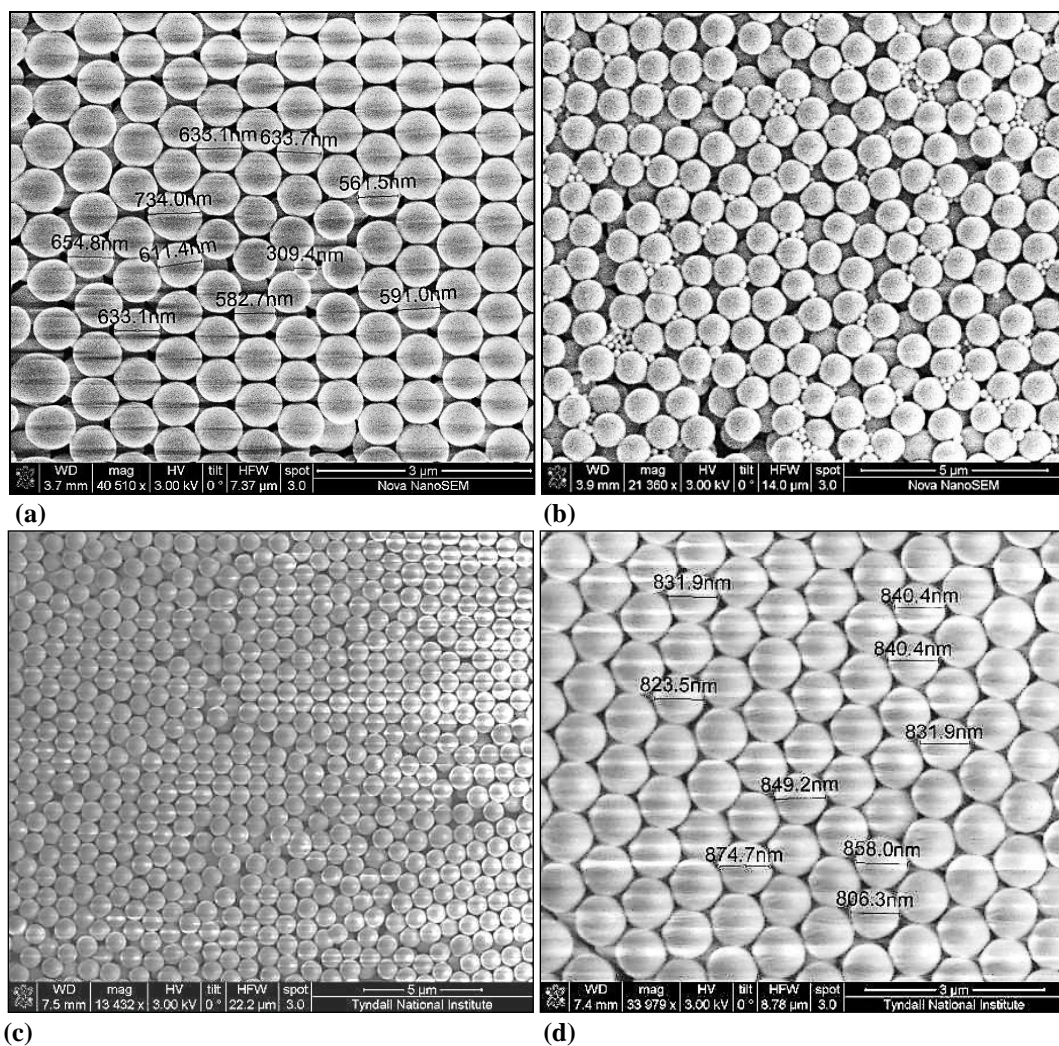


**Figure 3.3(a).** SEM image of particles used for further growth; (b) Particles >650 immediately after seed growth, showing smaller secondary particles; (c) secondary particles removed by centrifugation; (d) final particle batch after separation by sedimentation.

### 3.4 CONCLUSIONS & FURTHER WORK

- Following on from the work of Deak [3, 4], a simple yet completely monotonic method has been developed in order to produce silica particles in the range of 80 to 600nm.
- Particle monodispersities represented in the literature and as made here are generally in the region of 4-8%, but can be reduced by careful selection of centrifuge speeds to remove smaller particles, and sedimentation to remove larger particles and doublets.
- Faster stirring speeds during particle growth may produce improved monodispersities, and this should be investigated further.
- Other processing parameters may also be investigated to improve particle monodispersities, such as temperature, length of solution ageing, and length of the stirring times.
- Further work should also investigate the influence of changing the TEOS volume addition and its effects on monodispersity, before processing (centrifuging & sedimentation) steps are undertaken.
- Further work should also aim to produce particles, in a single step process, >600nm that would be useful for the production of colloidal photonic crystals

viable in the near infra-red region, i.e. telecommunications wavelengths (~1550nm).

## REFERENCES:

1. Stober, W., A. Fink, and E. Bohn, *Controlled Growth Of Monodisperse Silica Spheres In Micron Size Range*. Journal of Colloid and Interface Science, 1968. **26**(1): p. 62-&.
2. Razo, D.A.S., et al., *A version of Stober synthesis enabling the facile prediction of silica nanospheres size for the fabrication of opal photonic crystals*. Journal of Nanoparticle Research, 2008. **10**(7): p. 1225-1229.
3. Deak, A., et al., *Complex Langmuir-Blodgett films from silica nanoparticles: An optical spectroscopy study*. Colloids and Surfaces a-Physicochemical and Engineering Aspects, 2006. **278**(1-3): p. 10-16.
4. Deak, A., et al., *Nanostructured silica Langmuir-Blodgett films with antireflective properties prepared on glass substrates*. Thin Solid Films, 2005. **484**(1-2): p. 310-317.
5. Ismail A.M. Ibrahim, A.A.F. Zikry, Mohamed A. Sharaf, Preparation of spherical silica nanoparticles: Stober silica, Journal of American Science, 2010; **6** (11)
6. Enomoto, N., et al., *Novel processing for improving monodispersity of ceramic spheres and colloidal crystallinity*. Science and Technology of Advanced Materials, 2006. **7**(7): p. 662-666.
7. Bardosova, M., et al., *Synthetic opals made by the Langmuir-Blodgett method*. Thin Solid Films, 2003. **437**(1-2): p. 276-279.

8. Deng, T.S., et al., *One-step synthesis of highly monodisperse hybrid silica spheres in aqueous solution*. Journal of Colloid and Interface Science, 2009. **329**(2): p. 292-299.
9. Ni, P.G., et al., *Synthetic SiO<sub>2</sub> opals*. Advanced Materials, 2001. **13**(6): p. 437-441.
10. Chang, S.M., M. Lee, and W.S. Kim, *Preparation of large monodispersed spherical silica particles using seed particle growth*. Journal of Colloid and Interface Science, 2005. **286**(2): p. 536-542.
11. Costa, C.A.R., C.A.P. Leite, and F. Galembeck, *Size dependence of Stober silica nanoparticle microchemistry*. Journal of Physical Chemistry B, 2003. **107**(20): p. 4747-4755.

# **CHAPTER 4.**

## **IMPROVED SONICATION-ASSISTED FILM GROWTH**

It is important to control the thickness of a colloidal crystal film because it relates to its optical properties. Optical properties, such as the stop-band width, and reflectance peak are dependent on the film thickness [1]. A number of methods performed using a horizontal substrate claim to produce films with uniform thicknesses [2-7]. However, only the layer-by-layer methods such as the Langmuir-Blodgett method [8, 9] produce precise thicknesses over the entire area of the grown film. Horizontal self-assembly methods are able to make relatively flat (less than a few layers thickness difference) films over large areas, often in relatively short time periods [4, 6, 7]. Horizontal deposition methods enable rapid fabrication of films over large areas because of the formation of a relatively large area meniscus/contact line, and particle sedimentation is minimised due to the rapid deposition times.

Here we present an improved sonication-assisted colloidal photonic crystal film production method which has all the advantages of a horizontal substrate method, which is able to achieve high quality photonic crystals in a relatively short time, less than 1 hour to cover a glass substrate 75mm x 25mm. Potentially greater areas could be covered in similar short time periods.

## 4.1 EXPERIMENTAL

Silica colloidal particles (Seahostar KE-W30, Nippon Shokubai) 250nm diameter, were received dispersed in ultrapure water. These particles were obtained at approximately 20% by weight in water, and further reduced to a required concentration by diluting in ultrapure water (18.2M $\Omega$  cm). Ethanol 100, ammonium hydroxide (25%), hydrogen peroxide (30%), formamide and glycerol were purchased from Sigma-Aldrich, and used as received without further purification. Glass microscope slides were made hydrophilic by first rinsing with ethanol, sonicated in a 5:1:1 solution of H<sub>2</sub>O:NH<sub>4</sub>OH:H<sub>2</sub>O<sub>2</sub> for 30 minutes, prior to rinsing in pure water and dried under nitrogen.

Figure 2.2 (Chapter 2), shows a digital camera image of the set-up of the film fabrication method (image repeated below). After approximately 1 hour, a thin silica film with iridescent colours was formed on the glass substrate, figure 4.1. As controls a number of films were prepared under the same conditions without sonication.

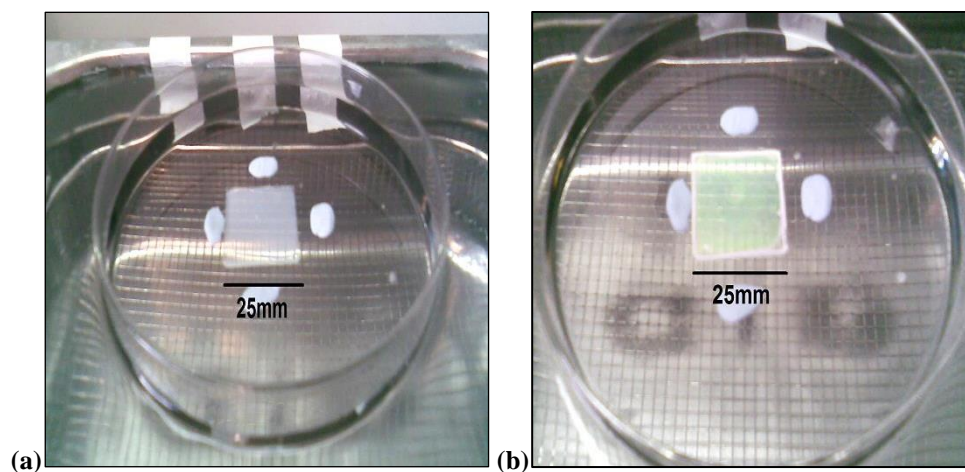


**Figure 4.1.** Film formation(a) before, and (b) after drying of a silica colloidal suspension by sonication.

## 4.2 RESULTS AND DISCUSSION

Comparison of films floated in the ultrasonic bath with and without sonication were initially undertaken. Figure 4.2 shows a comparison of the  $10^\circ$  reflectance spectra of films produced with and without sonication. The Bragg reflectance peak increases from 15% to 30% reflectance, indicating that higher quality ordering of the particles was achieved upon sonication. However, with the addition of a co-solvent, in this case +1% by volume of formamide, a 30% reflectance peak was also achieved without sonication (Figure 4.2, green curve), highlighting the importance of the solvent. All three films show Fabry-Perot fringes indicating uniformity of thicknesses.



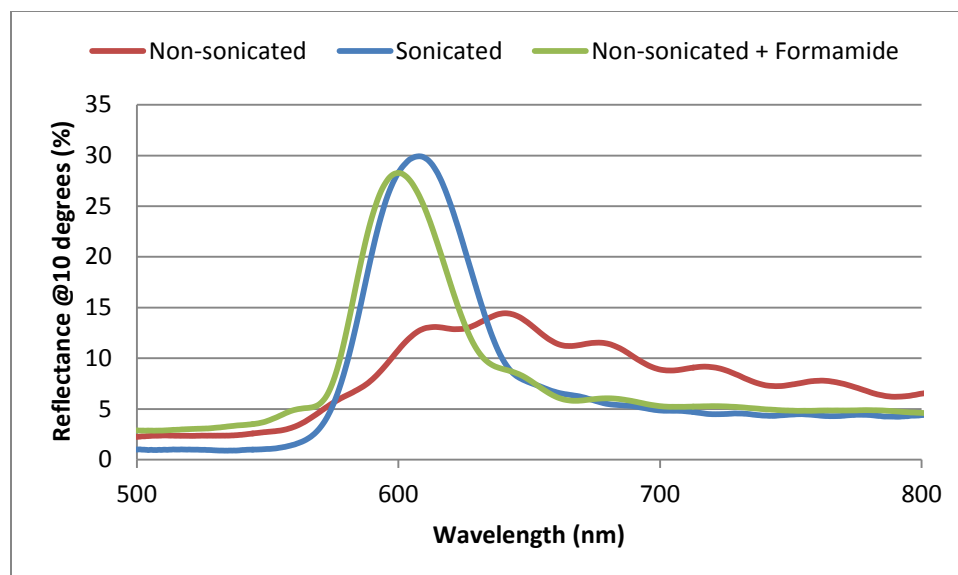


**Figure 4.2. Comparative reflectance spectra taken at 10° showing the difference in reflectance between non-sonicated (red) and sonicated (blue), and with added solvent (formamide) (green).**

Uniform films were not achieved in every case across the whole of the glass substrate by sonication, hence the addition of 2 co-solvents were assessed to achieve higher quality, uniform films. Park and Moon [10] used formamide to create a Marangoni or “tears of wine” effect within picolitre water droplets and were able to produce well-ordered 2D silica monolayers. Yoldi et al. [11] used glycerol to modify the drying conditions, to create larger domains, and hence reduce cracking within their colloidal films. When formamide was added to the system, at approximately 1% by volume (i.e. 0.005ml formamide in 0.5ml water/suspension droplet), the reflectance peak at 10° is strongly affected, increasing from approximately 30% (sonicated without formamide), to 60% upon sonicating with formamide, as shown in figure 4.3. This suggests that there is a much higher degree of inherent ordering in the film with formamide compared to without. This affect of the addition of formamide was also seen in the non-sonicated case above. However, in the case for adding glycerol to the suspension, at the same percentage by volume, no increase in the reflectance peak occurs

(figure 4.3). The Fabry-Perot fringes in the spectra of the film with added formamide indicate a even film thickness throughout the film.

The films with added solvents, both formamide and glycerol, fully cover the glass slides. Visually, the glycerol sample appeared to have a more uniform thickness, although it was less ‘opalescent’ overall, while the formamide sample appeared patchy and uneven. Figure 4.4 shows typical SEM images of the surfaces, and edge views, from each of these 3 films. The visually patchy nature of the fomamide film may be due to it being polycrystalline, with ordered domains seperated from each other by an irregular packing structure (domain boundary), i.e. each domain may be forming idependently, but the domains are not seperated by cracking, where ordering is usually repeated across the crack. (Figure 4.6(d) also gives the appearance of an uneven surface within the added formamide sample). It should be noted that because of the disorderd domain boundaries, distinct cracking is not seen within the films containing formamide.

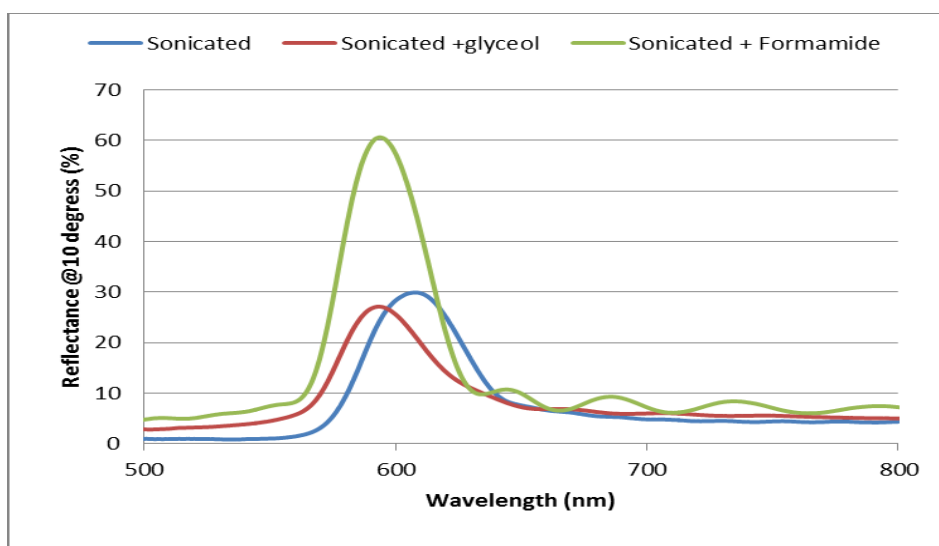
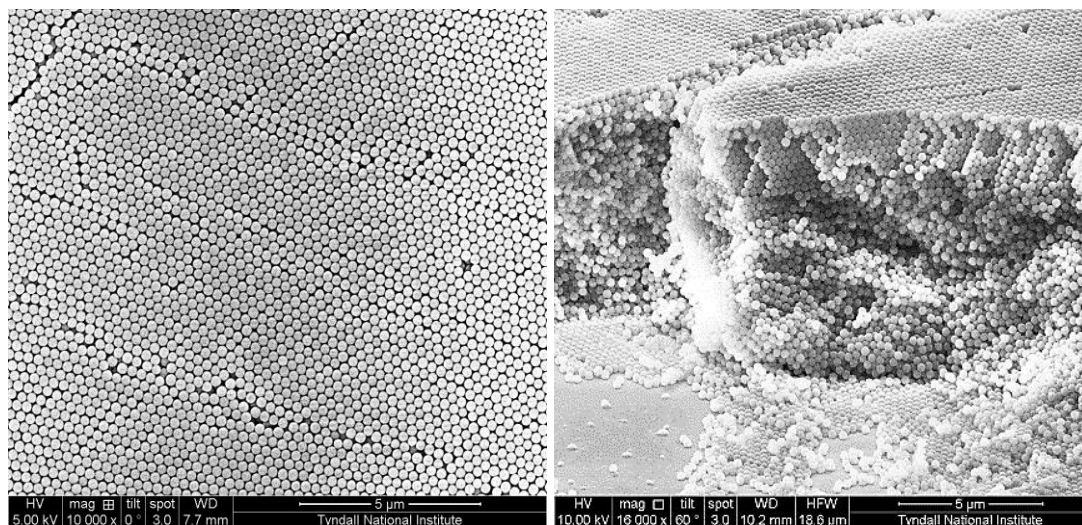
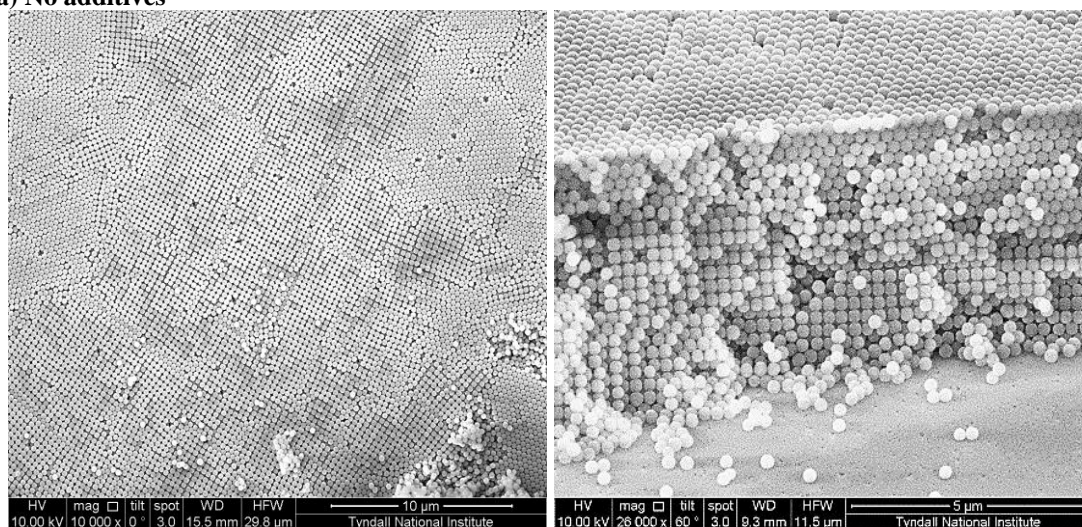


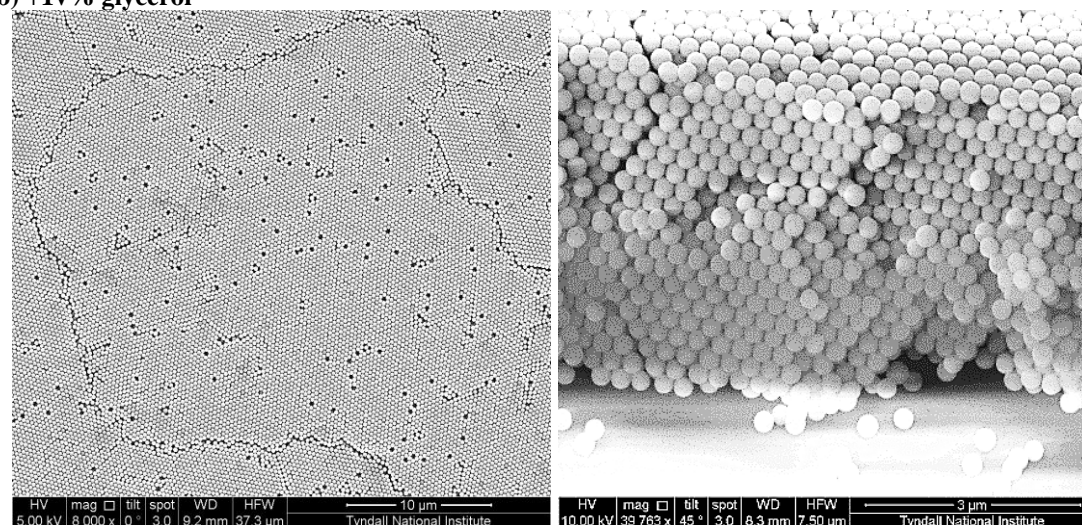
**Figure 4.3. Comparative spectra taken at 10° angle showing the comparative reflectance curves for sonicated (blue) with glycerol(red) and with formamide (green) films.**



**(a) No additives**



**(b) +1v% glycerol**



**(c) +1v% formamide**

**Figure 4.4. Comparison of surface (left) & edge (right) views from 3 sonication assisted films, (a) no additives, (b) + 1v% Glycerol, & (c) + 1v% Formamide**

It is clear the addition of formamide has a marked effect on the ordering of the particles within the sample. Without the addition of either solvent, the sample shows generally good surface ordering with domains surrounded by disordered drying fronts, (Figure 4.4a), similar to those seen by J rai-Szab  [12]. However, the cleaved edge view shows a generally disordered system, becoming more ordered towards the upper surface of the sample. Vickreva et al. [13] suggest that under oscillatory shear a trend towards “healing” of disordered particles can occur in the upper layers, and this appears to be the case here also.

With the addition of formamide, a Marangoni effect, coupled with sonication, gives a highly ordered film, which shows increased quality in the reflectance spectra. Here the surface ordering is again very good as seen from the SEM images (Figure 4.4c), however it does show a greater concentration of point defects in the form of missing particles in the lattice. The edge view from this sample shows a highly ordered fcc lattice (Figure 4.4c). The sample with added glycerol shows a different crystalline formation. In this case, both in the SEM surface and edge views (Figure 4.4b) mixed fcc lattice ordering appear, with (111) and (100) planes both prominent.

A sample with +1vol.% formamide addition was repeated on a full glass microscope slide, 75 x 25mm, with similar result to that previously described, which was also completely dried within 1 hour. Again a very high quality film was produced over the entire area of the glass slide, as seen in the digital camera image of the film and

the reflectance spectra, Figure 4.5(a&b). Note should again be taken of the pronounced Fabry-Perot fringes, which are indicative of uniform thickness within the film.

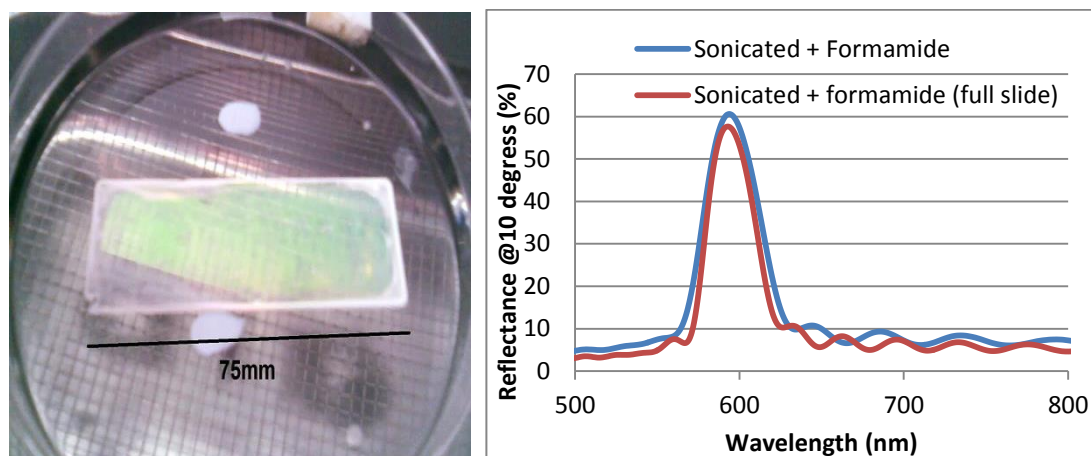


Figure 4.5. Digital camera image of large area film with +1v% Formamide (a) and comparative spectra versus smaller area film (b)

### 4.3 DISCUSSION

Sasaki and Hane [14] used ultrasonic radiation during the evaporation of a colloidal solution of PS particles, in order to improve the quality and ordering of monolayers of colloidal particles. They suggest that sonication induces forces which may overcome the relatively weak interactions of both particle to particle and particle to substrate, and therefore rearrange the particles in the film enlarging the ordered areas and reducing voids. J rai-Szab  et al. [12] used a computer model based on a spring-block stick-slip model to simulate a 2-D monolayer sonication-assisted colloidal film forming method, and confirmed that random shaking during the drying process would produce more ordered structures. They also found that increasing the intensity of

sonication, i.e. increasing the random force up to the limit of pinning (or friction) forces acting on the particles is beneficial to film formation and should eliminate most of the defects.

Li et al. [7] also used a sonicated-assisted method to form highly ordered 3D PS particle films, from various sphere sizes, up to 1053nm diameter. The thickness of their 3D films was adjusted by changing the initial concentration of the particles suspension. They concluded that unlike gravitational sedimentation and vertical deposition, there is no limit to the diameter of PS spheres for obtaining ordered films by this method, and hence the photonic stop band can be adjusted from the visible to near infra-red by adjusting the sphere size.

In this study using silica particles, while a film produced without sonication could produce opalescent colouring, it did not produce a uniform film of high quality as revealed by the reflectance spectra and SEM images (Figures 4.2 & 4.4). However, as the researchers noted above have observed, by introducing a random shaking from an ultrasonic bath, particle ordering was improved, and this was shown in the improvement in the intensity of the Bragg peak reflectance (Figure 4.2).

The generally accepted theory of crystalline growth is represented by 3 phases, (1) colloidal suspension, (2) intermediate stage, loosely packed crystalline “gel” as the solvent level approaches the diameter of particles, (3) close packed film. However, Marlow [15] states that during sonication-assisted film formation, the suspension is kept

homogeneous by application of the ultrasound, thus avoiding the formation of a lateral deposition front. The evaporation is now perpendicular to the film. Consequently, the opal formation front will also move perpendicular to the film; that is, over a very short distance, which means that the film can be formed much faster. He also notes that this method may enable large-area films to be produced in much faster timescales, and with reduced cracking, which was seen in this study, figure 4.4(a&c).

Park and Moon [10] used 700nm silica particles in their inkjet printing experiments, in conjunction with an appropriate combination of solvents for the successful printing of homogeneous ink jet films. When they used a mixed solvent approach by adding a drying control agent of high boiling point, the initial evaporation develops a concentration gradient along the droplet surface. Edge evaporation is slowed down, and a concentration gradient occurs within the droplet, and a Marangoni flow is established from regions with low surface tension, to regions with high surface tension. With the addition of formamide, a high boiling point solvent compared to water with a lower surface tension (58.22mN/m compared to 72.82mN/m), an edge to centre recirculation flow is induced, which may prevent the particles from concentrating at the contact line during the intermediate stage of drying, (2) above. Park and Moon were able to achieve near perfect monolayers of 700nm silica particles when formamide was used in their experiments. Cui et al. [16] used ethylene glycol (as a safer and more environmentally friendly alternative to formamide) in their ink jet printing experiments using PS core-PMMA/PAA shell particles (180-280nm diameter). They were able to print large area designs of high quality opaline films.

Both Vickreva [13] and Zhang [17] used piezoelectric devices to obtain an “oscillatory shear” across polystyrene particles, and found optimised or “resonance conditions” for particles to be manufactured into the highest quality film possible. For other systems, e.g. in our case silica, and for various sizes, and concentrations, the vibration conditions (vibratory amplitude and frequency) will also need to be optimised for “resonance” conditions to be achieved in each case.

Films produced without solvent revealed “random” crack patterns with some unconnected cracks (Figure 4.6 a&b). It appears that the cracks are prevented from joining together (as would be expected) due to some disorder in the lattice structure close to their end points. This disorder is therefore reducing the stresses causing the cracking in this region, and thus stop the crack fronts from growing (4.6b). With the addition of small amounts of cosolvent, glycerol or formamide, the overall structure appears to have reduced cracking (e.g. in figure 4.4(c)). These samples are polycrystalline, figure 4.6(c&d), which could account for their overall reduced cracking. The polycrystalline structure would have less residual stress between crystal-like domains, and therefore reduce the cracking in these films. This is particularly seen in the case of glycerol addition, where the surface structure tends towards an approximately equal mix of both the (111) and (100) fcc planes. Although the (100) plane is also seen in the formamide sample, it is much less dominant. Also because the boiling points of glycerol and formamide are much greater than the colloidal crystal forming temperature, then these solvents may be retained within the crystalline films, slowing down or avoiding complete drying. Hence the number of cracking defects could be reduced and



domain sizes increased. As seen from the use of these two co-solvents, solvents have the potential to control the lattice orientation, which may lead to possible applications.

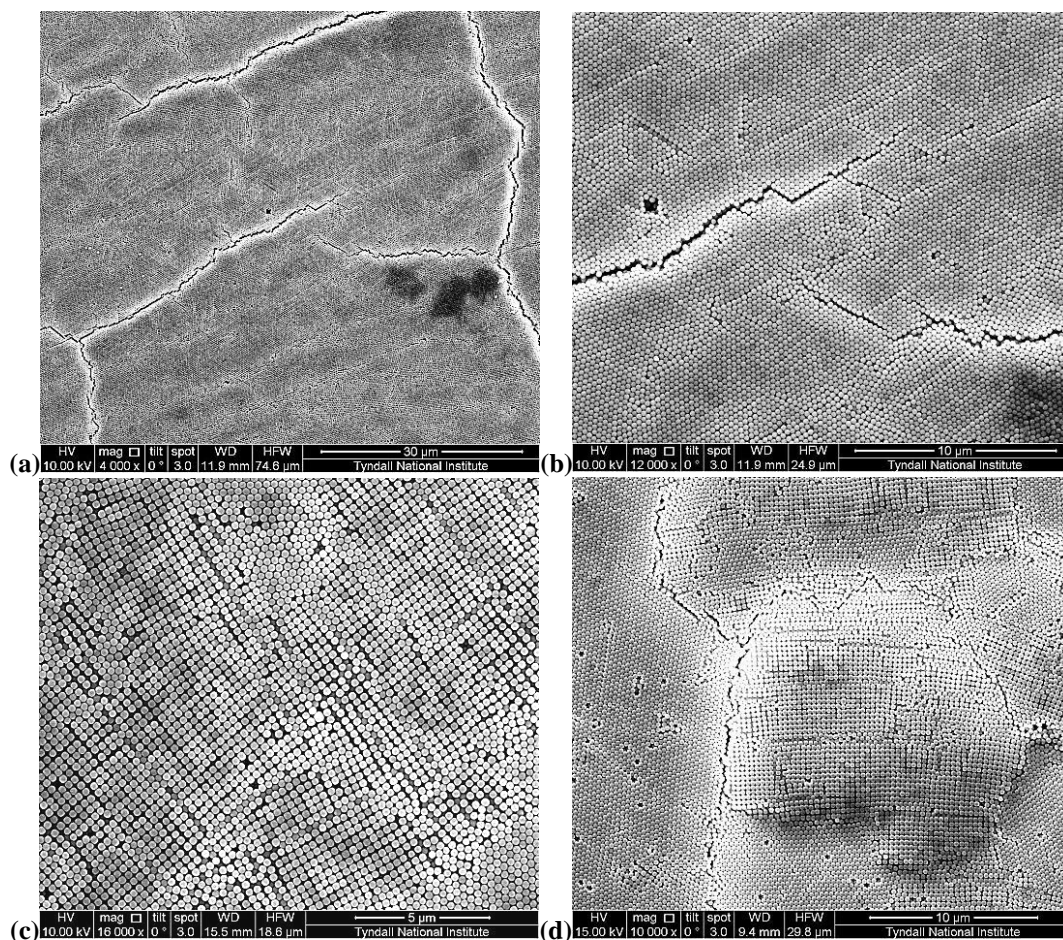


**Figure 4.6 Comparison of surface views from 3 sonicated films, (a & b) no additives, (c) + 1v% Glycerol, and (d) + 1v% Formamide**

#### **4.4 CONCLUSIONS & FURTHER WORK**

- Silica colloidal crystalline films have been made using a rapid production method, sonication, reducing production timescales to approximately 1 hour.
- Sonication can produce high quality films covering relatively large areas, (25mm x 75mm) in short timescales. (An equivalent area would normally take 2-3 days using either controlled evaporation or under oil crystallisation methods).
- The addition of small quantities of co-solvents, (approximately 1 vol.% additions), high quality films were able to be produced, with reflection peaks of >60%.
- With careful control over the sonication conditions (vibration “oscillatory shear”), optimised conditions may be reached for silica particles of all appropriate sizes (200 to 400nm) to be manufactured into a higher quality films on a 4 inch wafer.
- The addition of co-solvents in the sonication method has the potential to control lattice orientations at the surface. This should be further investigated, and may be useful in achieving alternative inverted opal structures.

## REFERENCES:

1. Bertone, J.F., et al., *Thickness dependence of the optical properties of ordered silica-air and air-polymer photonic crystals*. Physical Review Letters, 1999. **83**(2): p. 300-303.
2. Chung, Y.W., et al., *Fabrication of high-quality colloidal crystals by a capillary-enhanced method*. Applied Physics a-Materials Science & Processing, 2004. **79**(8): p. 2089-2092.
3. Chung, Y.W., et al., *Influence of humidity on the fabrication of high-quality colloidal crystals via a capillary-enhanced process*. Langmuir, 2006. **22**(14): p. 6454-6460.
4. Yan, Q.F., Z.C. Zhou, and X.S. Zhao, *Inward-growing self-assembly of colloidal crystal films on horizontal substrates*. Langmuir, 2005. **21**(7): p. 3158-3164.
5. Fudouzi, H., *Fabricating high-quality opal films with uniform structure over a large area*. Journal of Colloid and Interface Science, 2004. **275**(1): p. 277-283.
6. Wang, A., S.-L. Chen, and P. Dong, *Rapid fabrication of a large-area 3D silica colloidal crystal thin film by a room temperature floating self-assembly method*. Materials Letters, 2009. **63**(18-19): p. 1586-1589.
7. Li, Y.Z., T. Kunitake, and S. Fujikawa, *Efficient fabrication of large, robust films of 3D-ordered polystyrene latex*. Colloids and Surfaces a-Physicochemical and Engineering Aspects, 2006. **275**(1-3): p. 209-217.
8. Bardosova, M., et al., *Synthetic opals made by the Langmuir-Blodgett method*. Thin Solid Films, 2003. **437**(1-2): p. 276-279.

9. Bardosova, M., et al., *A new method of forming synthetic opals*. Acta Physica Slovaca, 2004. **54**(4): p. 409-415.
10. Park, J. and J. Moon, *Control of colloidal particle deposit patterns within picoliter droplets ejected by ink-jet printing*. Langmuir, 2006. **22**(8): p. 3506-3513.
11. Yoldi, M., et al., *On the parameters influencing the deposition of polystyrene colloidal crystals*. Materials Science & Engineering C-Biomimetic and Supramolecular Systems, 2008. **28**(7): p. 1038-1043.
12. Jarai-Szabo, F., et al., *Shake-induced order in nanosphere systems*. European Physical Journal E, 2007. **23**(2): p. 153-159.
13. Vickreva, O., O. Kalinina, and E. Kumacheva, *Colloid crystal growth under oscillatory shear*. Advanced Materials, 2000. **12**(2): p. 110-112.
14. Sasaki, M. and K. Hane, *Ultrasonically facilitated two-dimensional crystallization of colloid particles*. Journal of Applied Physics, 1996. **80**(9): p. 5427-5431.
15. Marlow, F., et al., *Opals: Status and Prospects*. Angewandte Chemie-International Edition, 2009. **48**(34): p. 6212-6233.
16. Cui, L., et al., *Fabrication of large-area patterned photonic crystals by ink-jet printing*. Journal of Materials Chemistry, 2009. **19**(31): p. 5499-5502.
17. Zhang, J., et al., *Fabrication of high-quality colloidal crystal films by vertical deposition method integrated with a piezoelectric actuator*. Thin Solid Films, 2010. **518**(18): p. 5204-5208.

# **CHAPTER 5.**

## **CRACK-FREE OPAL FILMS BY UNDER OIL** **CO-CRYSTALLISATION**

### **5.1 INTRODUCTION AND AIMS:**

During the course of this study the Advanced Materials and Surfaces Group (AMSG), Tyndall had a number of collaborative projects running with the National Institute of Materials Science (NIMS) Wave Optics Group, Tsukuba, Japan. An internship was undertaken at NIMS (from 1<sup>st</sup> February 2011 to 14<sup>th</sup> March 2011, for which a Certificate of NIMS Internship was awarded on completion of an internship report (Appendix B). As part of this collaborative work, the techniques for preparing large area colloidal photonic crystals by the under oil crystallization (UOC) method [1-4] developed at NIMS, were studied with the intention of applying these techniques to produce co-crystallised crack-free colloidal photonic crystals. Initially techniques for the fabrication of silica opal films on fluorinated rubber sheets, and then infiltrating them with an UV curable acrylate polymer ( $\eta=1.6$ ) were studied. (Note: when infilling polystyrene (PS) particle films, PDMS (Dow Corning Sylgard 184,  $\eta=1.4$ ) is used, on the same fluorinated rubber sheet). However the primary aim of the internship was to prepare mechanically strengthened opal films by co-crystallisation using the UOC method, with the intent to achieve large area crack-free films. Co-crystallisation was performed using

precursor TEOS based solutions, similar to those developed by Wang and Zhao [5] Hatton and Aizenberg [6], during their vertical evaporation deposition experiments.

Cracks typically divide the colloidal crystal films into areas of several tens of micrometers. The formation of cracks is mainly caused by the decrease in the distance between adjacent spheres during the drying stages. The hydrolysis of a precursor TEOS solution produces coarse silica species, which fill the voids between the silica spheres. Growth of the silica species connects the particles and counteracts the shrinkage of the colloidal crystals during drying. By adjusting the amount of the TEOS precursor solution, crack-free colloidal films can be obtained. Fabricated films are thus made up of non-close-packed silica spheres and a silica skeleton infilling the voids between the spheres.

During under oil crystallization, using polystyrene spheres, the average size of the grains (distances between cracks) is generally larger than 200 $\mu\text{m}$ , with some grains\* measuring up to 1mm in length [1]. During UOC, water, evaporated from the colloidal solution, is replaced by silicone oil, reducing the hydrostatic tension at the final stage of shrinking of the wet opal film. As a result, the grains grown in the UOC opal film are generally much larger than domain / grain sizes seen in evaporation deposition samples. Fudouzi [1] has used UOC to fabricate much larger area opal films, for instance on 4-inch silicon wafers having an area of 75cm<sup>2</sup>, suggesting that UOC can be scaled up to even greater areas. Using UOC one can make uniform flat opal films over large areas; however, the opal film is not a single crystal and is separated into many grains. Here work on the

under oil co-crystallisation focuses on the fabrication of opals with large grain size, free of cracks.

---

*\* grains are defined here as the areas between cracks (which can be single domains or domains separated by cracks)*

## **5.2 EXPERIMENTAL**

The production of flexible colloidal crystal films was undertaken using the under oil crystallization method, by the deposition of silica particles onto flexible substrates. A fluoride silicone rubber, 0.5mm thickness, was used as the flexible substrate, initially supported on a rigid surface; here a glass microscope slide acted as the support. Rubber substrates were ultrasonically cleaned for 5 minutes in a detergent solution, rinsed in pure water, and then sonicated again in pure water for 5 minutes. The glass support was cleaned with ethanol to provide a clean surface to bond the rubber to. A general purpose adhesive (mixed with pure water in a ratio of 1:5, adhesive:water) was spin coated onto the surface of the glass, and the rubber applied to the top surface. It was essential to achieve an air free bond between the rubber and the glass in order to maintain a perfectly flat upper surface of the rubber sheet. This was achieved through repeated vacuum and press/rolling cycles, designed to squeeze out excess adhesive and air bubbles. The adhesive was then allowed to cure before film fabrication began.

The edges of the rubber substrate were covered with an adhesive tape before being placed into an Ion Bombardment chamber (PRI-10) for 3 minutes. This resulted in

the formation of a hydrophobic edge to the rubber sheet, and an internal hydrophilic area for film coating. After removal of the edge tape, the substrate was placed into a flat-bottomed container. A known quantity of colloidal particles in pure water was added onto the hydrophilic surface of the rubber substrates, and the substrate and suspension was then covered with silicone oil (Toray-Dow Corning dimethylsiloxane, DMS T11, 10cSt) and allowed to stand until crystallization of the particle film was completed. This was normally achieved after 2-3 days at 60°C, or longer at room temperature.

Once crystallisation was completed, the silicone oil was removed using a pipette, and the film gently rinsed with volatile 0.65cSt silicone oil (Toray-Dow Corning dimethylsiloxane, DMS T00, 0.65cSt), leaving a dried film on the rubber surface.

Infiltration and binding the opaline film to the rubber substrate was performed in two stages. For silica particle films an UV curable acrylate polymer ( $\eta=1.6$ ) was used.

### **5.2.1 INFILLING SILICA PARTICLE FLEXIBLE FILMS**

Equal parts by weight of the UV curable acrylate polymer, World Rock XVL90A0, and xylene were stirred for 5 minutes, and then used to cover the silica film. After allowing a minimum of 8 hours for infiltration into the film and evaporation of the xylene, the film was placed under a 365nm UV lamp, under dry nitrogen for 30 minutes in order to cure the acrylate. Once cured, the sample was placed into a glass container



and covered with xylene. After approximately 1 hour the acrylate was swollen by the xylene, and the swollen acrylate could be peeled away from the surface of the film. This first infilling serves to open up the crystalline structure but preserves the nature of the film. A change in the colour of the film was observed at this point as compared to the original colour first viewed, at a particular angle.

The infilling method was repeated in order to fully infiltrate the crystalline film, and also bond the film to the rubber substrate. After the second infiltration and removal of excess acrylate by xylene swelling, the rubber could be removed from the glass support, leaving behind a flexible photonic crystal film.

### **5.2.2 INFILLING POLYSTYRENE PARTICLE FLEXIBLE FILMS**

PDMS (Sylgard 184) base, catalyst, and silicone oil (0.65cSt) were mixed in a ratio by weight of 10:1:5 respectively, covered and stirred for 5 minutes. A polystyrene opal film on a rubber substrate was placed in a flat container, and the film was completely covered with the PDMS mix and allowed to cure. Once cured, excess PDMS was removed from the opal film simply by peeling the thick PDMS layer away from the surface of the rubber substrate. Again this first infilling served to open up the crystalline lattice but preserved the structure of the film, and a change in the structural colour of the film was seen. Infilling was repeated with PDMS (Sylgard 184) base, catalyst, and silicone oil (0.65cSt) mixed in a ratio of 10:1:10 respectively. After the second

infiltration, and removal of excess PDMS, the flexible photonic opaline film could be removed from the glass support.

In both cases colour changes could be observed in the flexible films by applying pressure. Stretching and relaxing the film, expanded and contracted the crystalline lattice, thus changing the wavelength of the reflected Bragg peak, and hence the colour of the film (Figure 5.1).

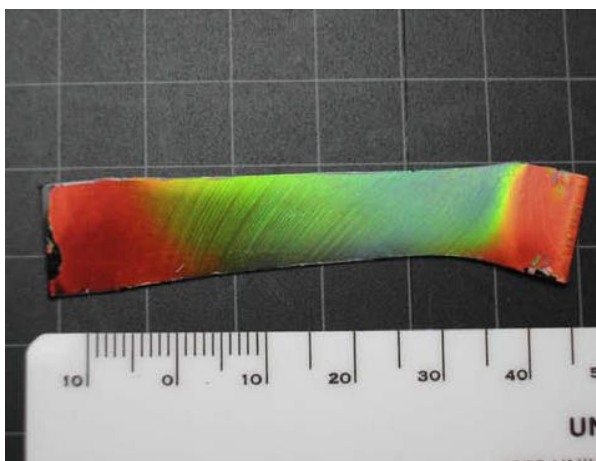


**Figure 5.1. Typical flexible opal film on rubber substrate. Plastic deformation is viewed as a change in structural colour [3].**

### **5.2.3 UNDER OIL CO-CRYSTALLISATION DEPOSITION**

Glass substrates were rendered hydrophilic by sonication in ethanol for 5 minutes, and allowed to dry. Glass surfaces were then ion bombarded as described previously. A silica precursor solution of tetraethyl orthosilicate (TEOS) and ethanol in a weight ratio of 1:1.5, was mixed for 1 hour. Various quantities of this precursor solution were added to a 280nm, 1wt% silica particle suspension (Nippon Shokubai Co.

Seahostar, KEW30) and stirred for 5 minutes. 0.5ml of suspension plus precursor solution were deposited onto a hydrophilic glass surface and covered with silicone oil, 10cSt, as described previously, and allowed to crystallize in an oven at 60°C.

Initially a precursor solution containing a catalyst, 0.1M hydrochloric acid was used, similar to the method described by Hatton and Aizenberg [6], but poorly structured films were achieved, probably due to the rate of formation of silica being faster than the rate of formation of the colloidal crystalline film. Hence, the acid catalyst was not employed subsequently.

Upon drying, the microstructure was examined using SEM, and optical properties assessed using Ocean Optics Spectra Suite software.

## **5.3 RESULTS**

### **5.3.1 UOC ON GLASS SUBSTRATES.**

Silica colloidal films on glass substrates, 25mm x 25mm, were prepared under oil and typically good quality, brightly coloured films were produced over large areas, particularly towards the sides and corners of the substrates. In some cases a central whitish area was seen, which was found to be an area of poor quality particle packing. Figure 5.2 shows SEM images of the particle packing and grain sizes within these films.

The grain sizes are similar to those recorded by Fudouzi [1], ~200 $\mu\text{m}$  length by ~30-50 $\mu\text{m}$  wide.

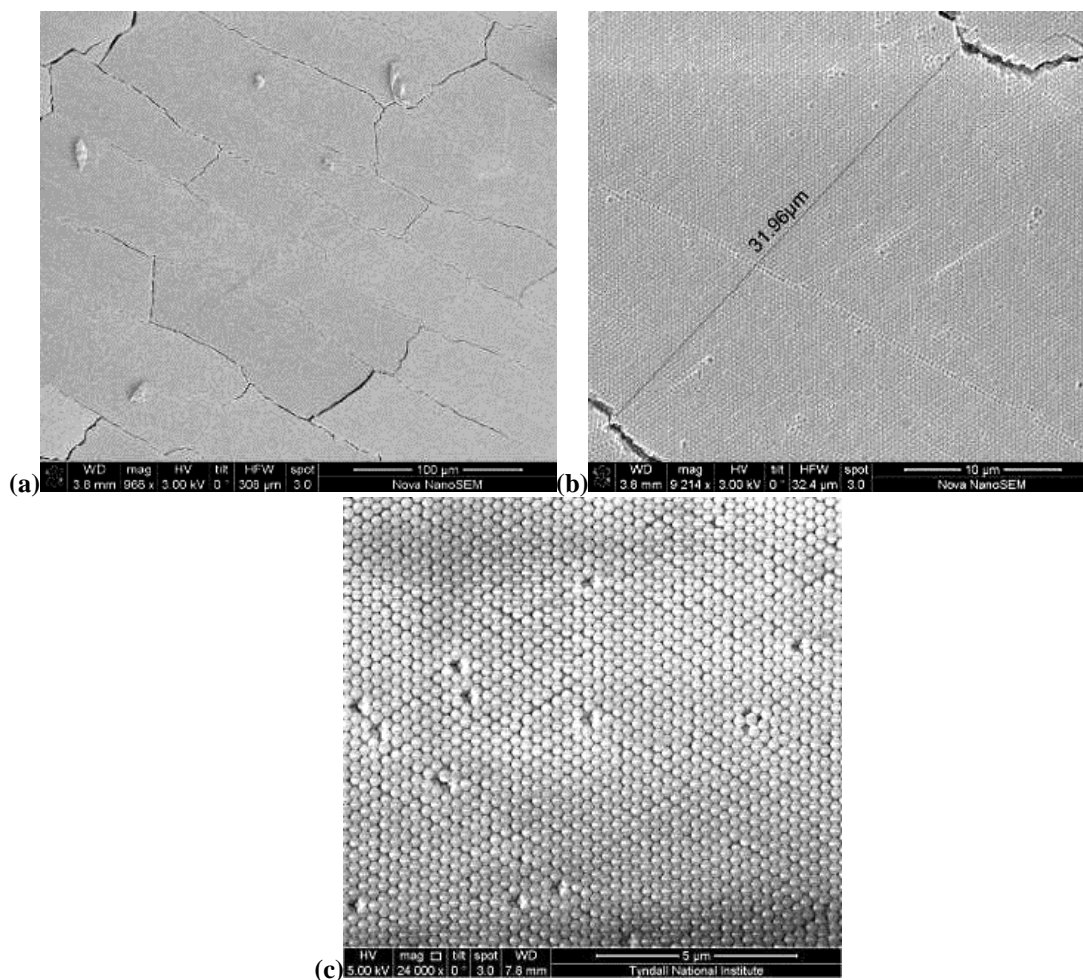


**Figure 5.2(a-c).** SEM images of the particle packing and grain sizes within UOC films of silica on glass substrates

The optical spectra of these films show sharp reflectance peaks and transmission dips, indicating high quality film formation. Figure 5.3 shows the optical properties from a film made from KEW30 (250nm) particles at 0° transmission and 10° reflectance.

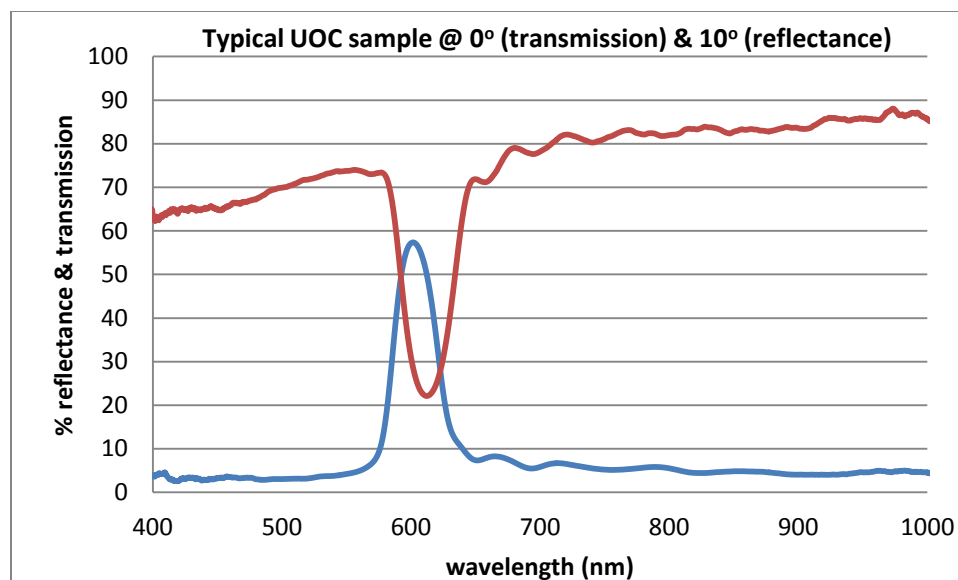
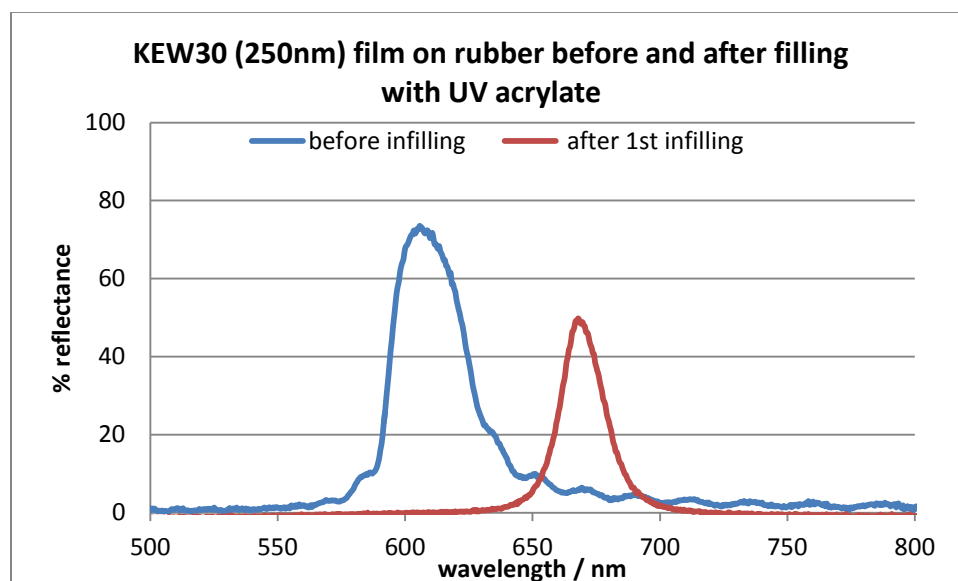


Figure 5.3. Typical optical spectra of a UOC film of KEW30 (250nm) silica on glass substrates

### 5.3.2 INFILLING OF SILICA PARTICLES ON RUBBER SUBSTRATES

A rubber substrate was bonded to a glass support as previously described in Section 5.2, and allowed to cure. The glass support was 50mm x 25mm, and the final rubber hydrophilic area after edge masking was approximately 40mm x 20mm (total area 800mm<sup>2</sup>). 1.0ml at 1.0wt%, 280nm particles, was added to the surface of the substrate and covered with 10cSt oil and placed in an oven at 60°C, until crystallisation was completed. In general good quality, brightly coloured films were produced, particularly around large proportions of the end and side areas, with a central ‘whitish’ thicker spot. This sample was infilled with the UV curable acrylate in two stages as previously described, and optical spectra were taken after each infilling.

As seen from the graph below (Figure 5.4), the film had a reflectance peak at  $0^\circ$  incidence of approximately 70% at about 600nm wavelength. After the first infilling, this peak was reduced to approximately 50% reflectance. The infilling process distorts the crystalline structure of the film, increasing the particle separation, and thus shifts the wavelength of the Bragg peak to higher wavelengths, i.e. from approximately 600nm to 660nm wavelength. There is also an increase in the effective refractive index of the infilled film, which would also shift the reflectance peak. The intensity of the reflectance peak is reduced due to a reduction in the refractive index contrast of the infilled film compared to the original, with air filled pores.



**Figure 5.4.** Optical spectra taken from a silica particle film infilled with a UV cured acrylate (before infilling, and after 1<sup>st</sup> infilling).

Upon removal of this sample from the supporting glass, it could be mechanically distorted. Shifts in viewed colours and Bragg peak could be seen with bending and stretching of the film.

### **5.3.3 RESULTS OF UNDER OIL CO-CRYSTALLISATION DEPOSITION**

The quantities of TEOS precursor solution required for each infilling were estimated from Hatton's optimum solution [6]. However, because the film production method employed here is different, a number of different TEOS precursor addition experiments were performed, in order to establish the optimum quantity required in order to produce large crack free areas by this under oil co-crystallisation method. Precursor quantities of 10, 15, 20, 30 and 40 $\mu$ l, were added to five individual droplets of 0.5ml at 1wt% and mixed as previously described, before placing onto 25mm x 25mm hydrophilic glass slides.

Good quality samples were not achieved over the whole area of each slide. The highest quality areas were visible towards the corner and edge areas of each film. SEM images show that central areas generally had poor packing of the particles, and no visible signs of silica binding between particles, Figure 5.5. The shell like appearance in the right hand image arises due to sputtering with gold to make the film conductive in the SEM.

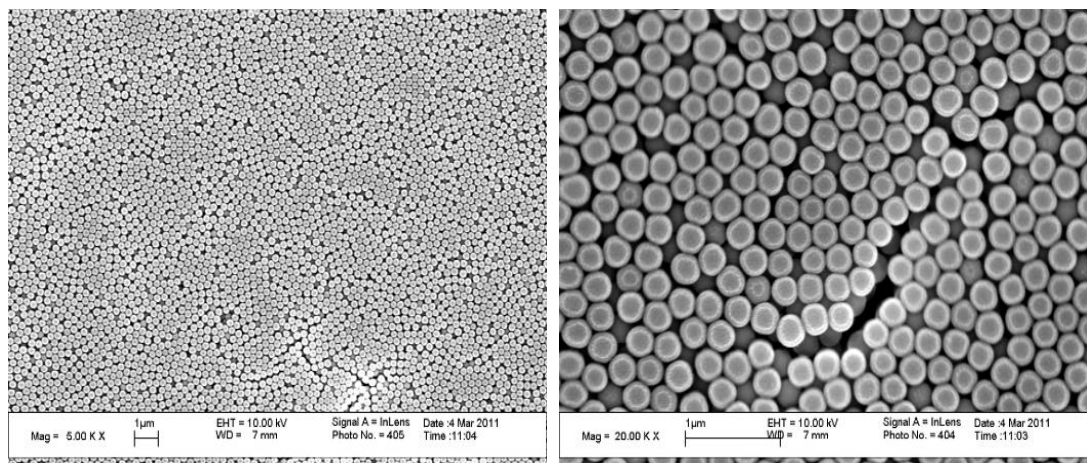


**Figure 5.5. Central area showing poor packing, with no visible signs of silica binding between particles.**

Figures 5.6 to 5.12 show SEM images of closely packed areas from 280nm silica co-crystallised under oil films at +10µl, +15µl, +20µl, +30µl, +40 µl TEOS precursor solutions respectively. Cracks and the areas immediately surrounding the cracks appear lighter in these images due to charging in the electron beam.



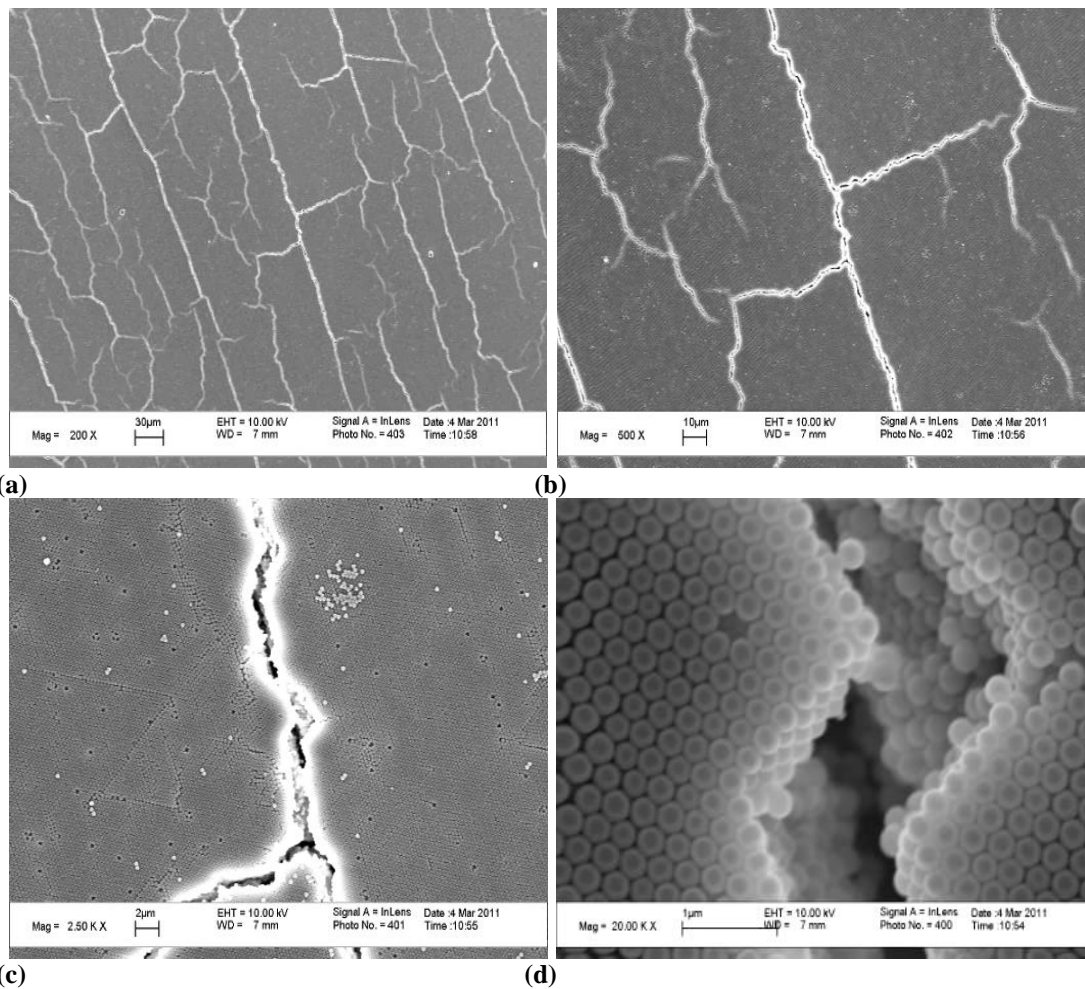


**Figure 5.6. + 10μl TEOS precursor. (a-d) Edge areas showing good particle packing, and some silica infilling. (b, c & d are magnified views from original area in (a)).**

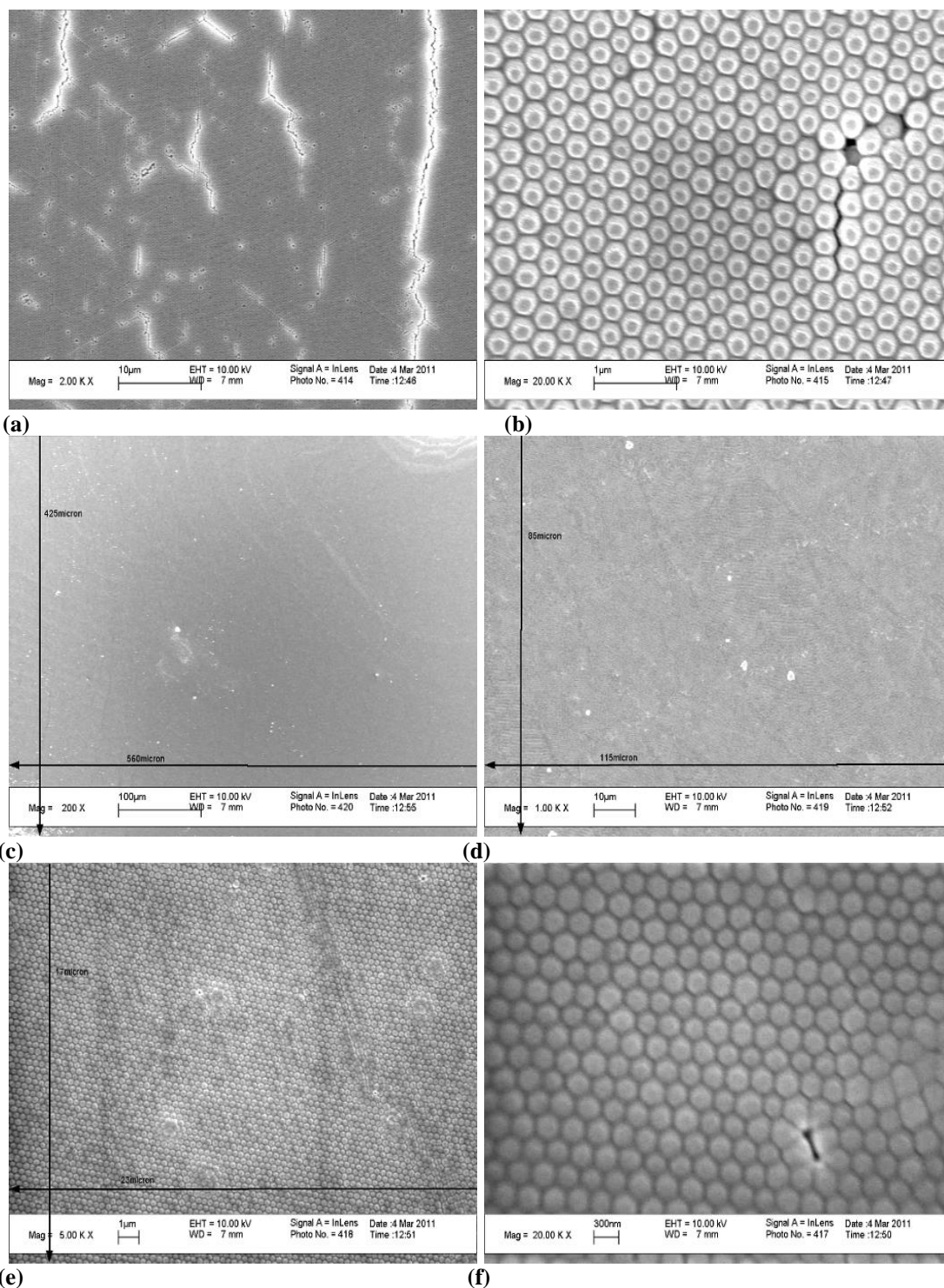
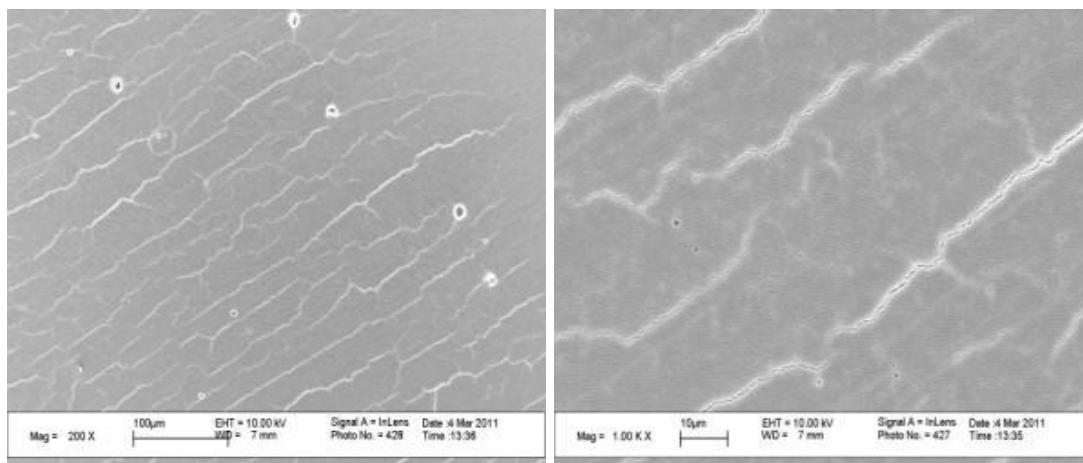
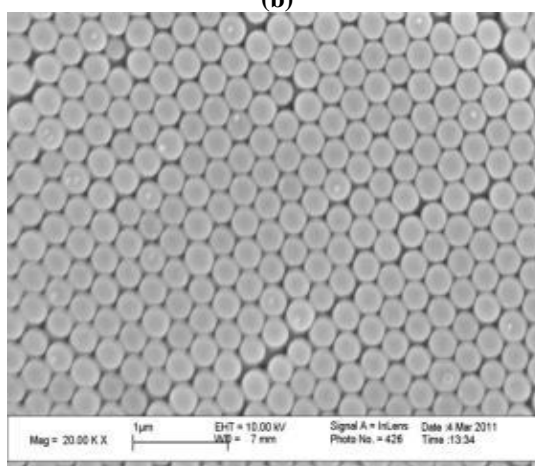


**Figure 5.7. + 15µl TEOS precursor. (a-b) Edge areas showing good particle packing, reduced cracking, and silica binding. (c-f) Corner areas showing no cracks and complete infilling with silica, (d, e & f are magnified views from original area in (c)).**

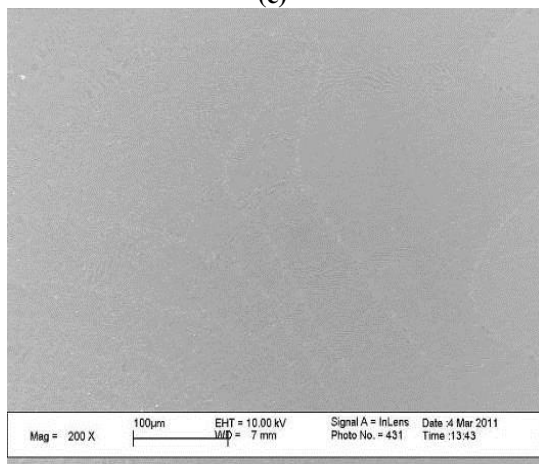


(a)

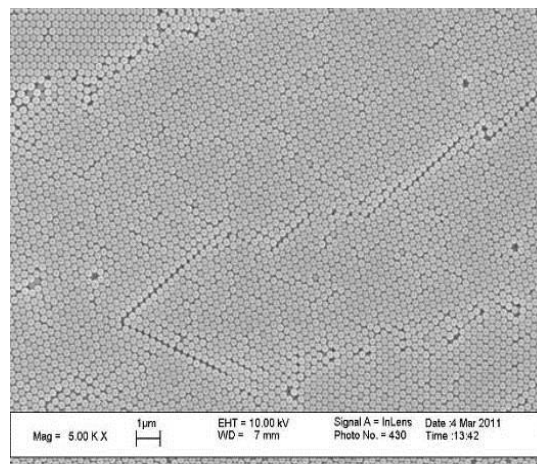
(b)



(c)



(d)



(e)

**Figure 5.8. + 20µl TEOS precursor. (a, b & c) Side areas showing good particle packing, but also cracks and no obvious silica infilling. (d & e) Corner areas showing good particle packing, with no cracks, but little visible evidence of silica infilling, (incomplete filling).**

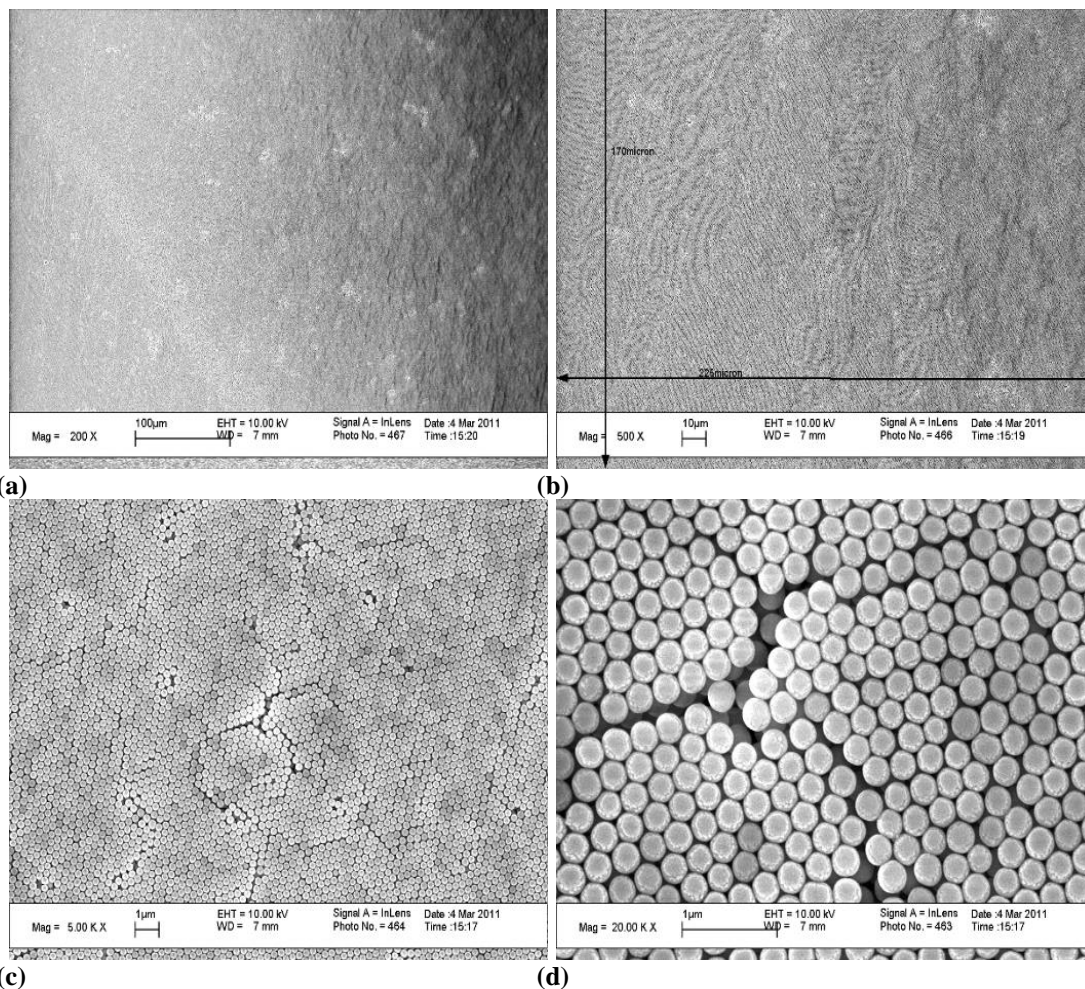


**Figure 5.9. + 30μl TEOS precursor. (a-d) Edge areas showing good particle packing and reduced cracking, although silica infilling is not obviously visible (b-d are magnified views from original area in (a)).**

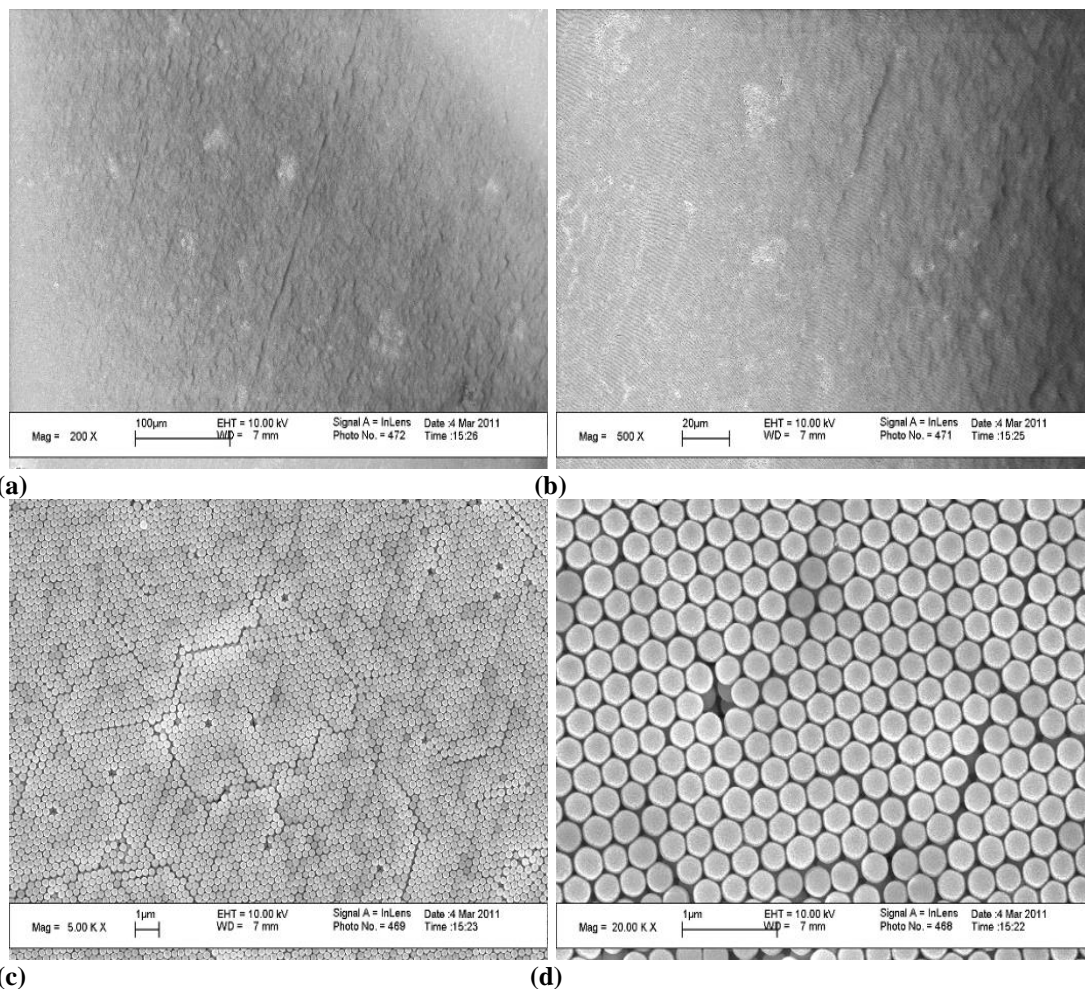
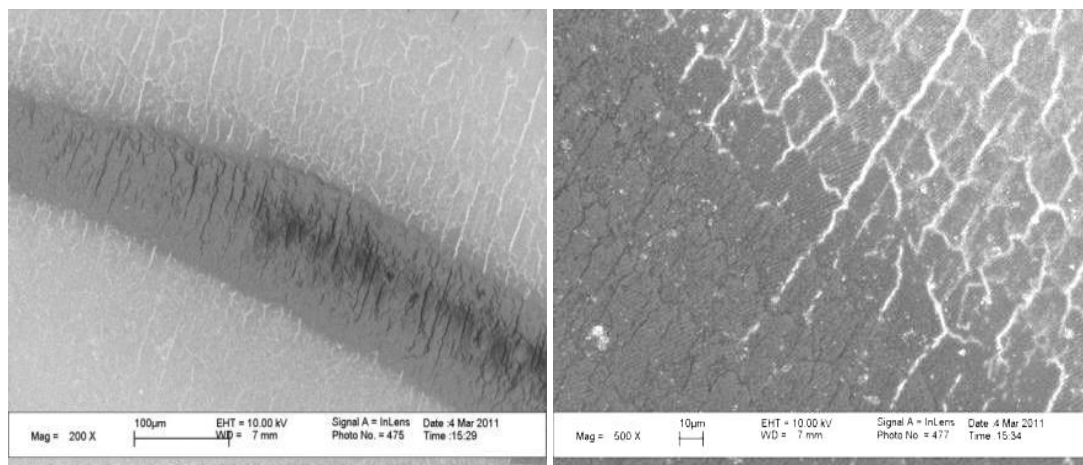
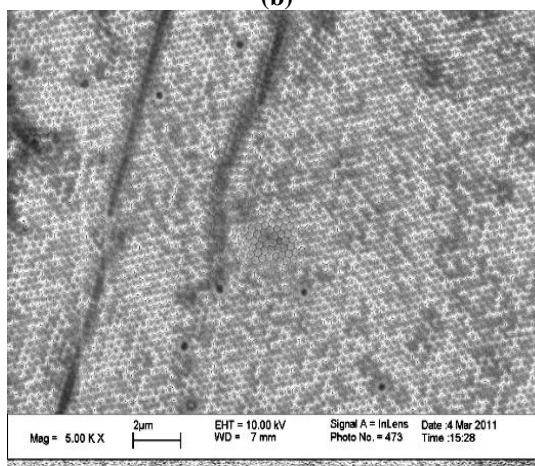


**Figure 5.10. + 30μl TEOS precursor. (a-d) Corner areas showing large areas with reduced cracking (although silica infilling is not obviously visible) (b-d are magnified views from original area in a)**



(a)

(b)



(c)

**Figure 5.11. + 30µl TEOS precursor. (a-c) Corner area showing a strip of a silica infilling. Cracks penetrate from the unfilled area into the filled area, and are closed/stopped inside the filled area (showing evidence of increased mechanical strength due to the infilling).**



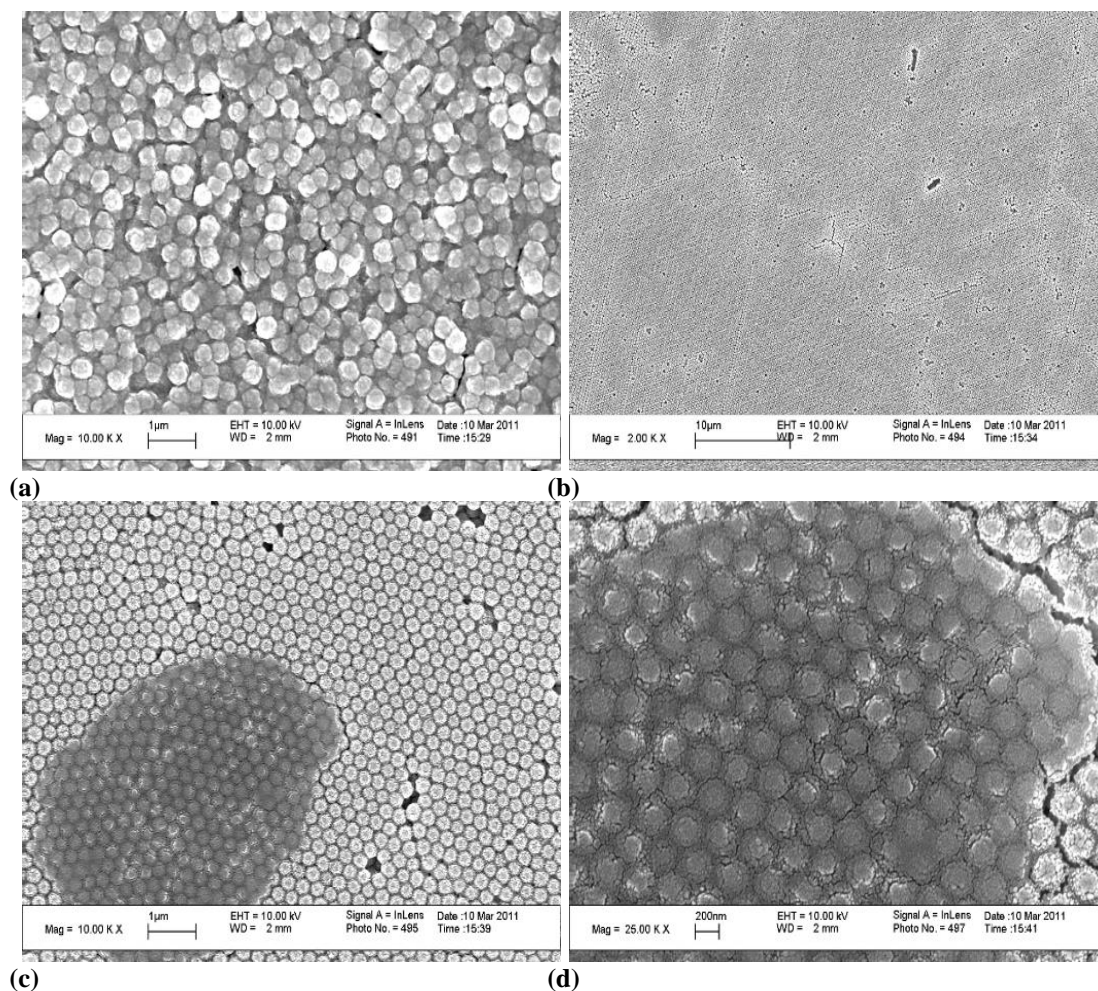


**Figure 5.12. + 40μl TEOS precursor. (a) Corner area showing excess silica giving rise to poor packing of the particles, (b) a second corner where the silica infilling is not obvious but ordered packing is visible, (c-d) central area with complete infilling.**

It can be seen from the SEM images in figures 5.6 to 5.12, that the typical cracking seen in UOC samples has, in general been reduced, by adding increasing amounts of the TEOS precursor solution. At +10μl addition, cracking still prevails in the high quality particle packing (fcc) areas, with distances between cracks of the order of 20-30μm. Clearly some cracking has been prevented by the silica infilling, (Figures 5.6 a & b).

Additions of +15, +20 and +30 $\mu$ l TEOS precursor solution to the colloidal particle suspension gave rise to much larger areas without cracks, (Figure 5.7(c) @ +15 $\mu$ l, 5.8(d) @ +20 $\mu$ l, and 5.9(a) & 5.10(a) @ +30 $\mu$ l). These images show crack free areas of 560 $\mu$ m x 425 $\mu$ m, although in some cases the silica binding is not obvious in the high magnification surface images from these areas, (Figures 5.8(e), 5.9(c&d), and 5.10(c&d) respectively).

Figures 5.11(a-d) and 5.12(c-d), show darker areas where complete silica infilling has occurred, but this process is clearly incomplete in the surrounding areas. Figure 5.11(a-d) with +30 $\mu$ l TEOS precursor shows a corner area with a stripe of complete silica infilling. In this area cracks penetrate from the unfilled area into the filled area, and are closed/stopped inside the infilled area, giving evidence of increased mechanical strength within the film due to the infilling. Figure 5.12(c-d), with +40 $\mu$ l TEOS precursor solution, also shows a central area with complete infilling.

Visible reflectance spectra were recorded from each corner of each sample. Spectra were taken at approximately 7mm diagonally from the corner of the sample, using Ocean Optics Spectra Suite software. Figure 5.13 shows the optical spectra taken from each of the TEOS precursor additions: (a) +10 $\mu$ l; (b) +15 $\mu$ l; (c) +20 $\mu$ l; (d) +30 $\mu$ l; and (e) +40 $\mu$ l. Spectra, labelled side 1-2 from the +40 $\mu$ l sample, figure 5.13(e), were taken from half way between corners 1 & 2, at approximately 5mm from the edge of the sample. Figure 5.13(f) shows a schematic of the positions on the slide where the spectra were taken.



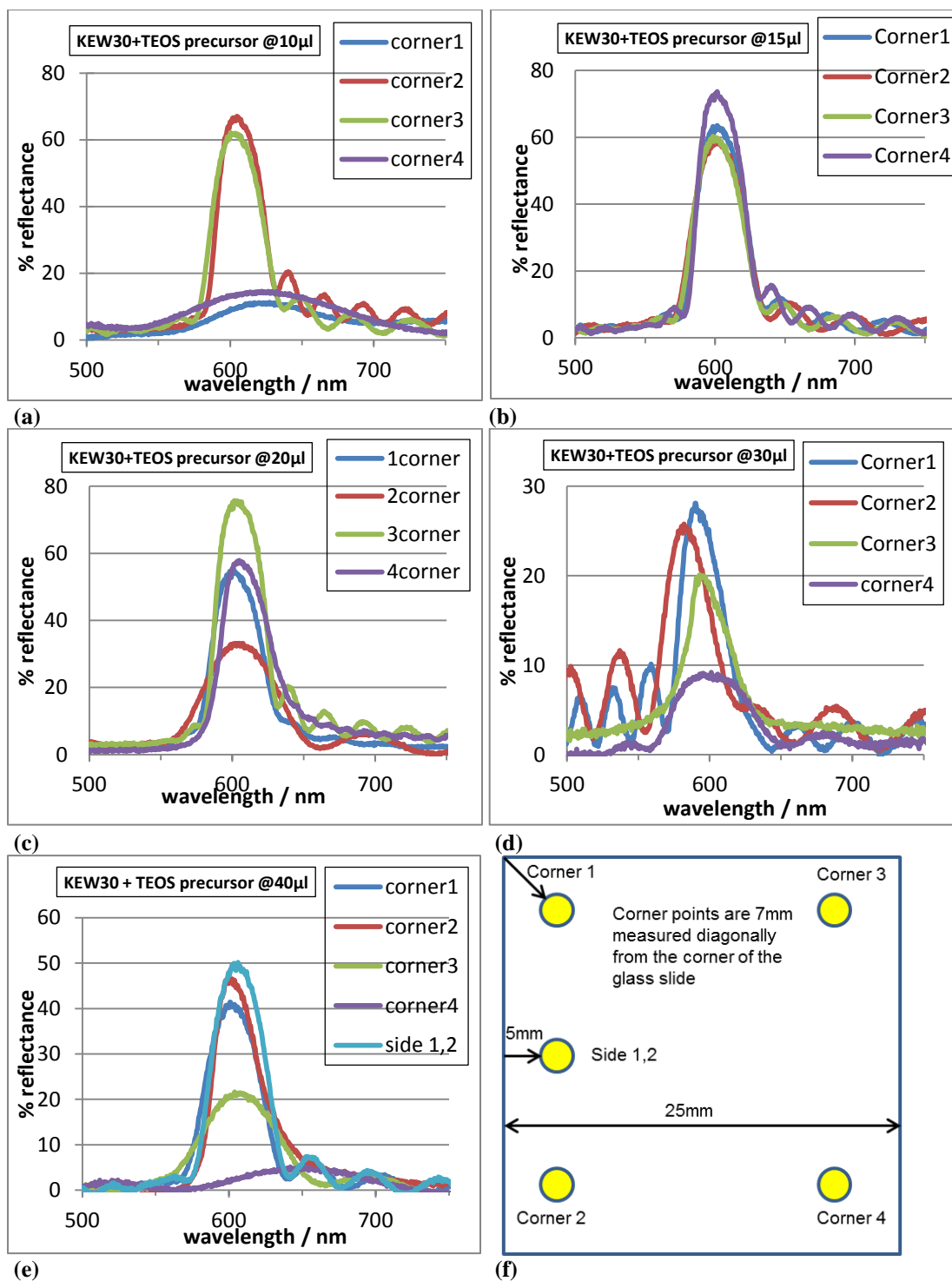


**Figure 5.13.** Optical spectra taken from each TEOS precursor additions: (a) +10 $\mu$ l; (b) +15 $\mu$ l; (c) +20 $\mu$ l; (d) +30 $\mu$ l; and (e) +40 $\mu$ l. (f) schematic of the positions where the spectra were taken.

The number of layers in each sample was calculated from the Fabry-Perot fringes in the optical reflectance spectra. These are given in Table 5.1, along with the height of

the reflectance peaks. The differences in the calculated thicknesses from each area of these films suggests inconsistent layering in the formation of the films, (this is in contrast to previous work [1, 2], which suggested that uniform film thicknesses are produced by this method). This discrepancy may arise as a result of a difference between using polystyrene and silica particle to make the films, or possibly as a result of the addition of the TEOS precursor solution, and the subsequent particle bonding during film formation. However, the sample with +15 $\mu$ l TEOS precursor addition gave the most consistent result in terms of uniform thickness of the film, and the most consistent reflectance peaks from all four corners of the sample.

Inconsistent infilling with silica from the TEOS solution is also highlighted in the +30 $\mu$ l sample, where a dark stripe is seen in the SEM images. This was an area of complete infilling, surrounded by areas of incomplete filling, and shows that cracks, developed in the incompletely filled areas, are closed and stopped from progressing in the infilled area. It should also be noted that the Bragg peak position at approximately 600nm is equivalent to that observed from an unfilled lattice (figure 5.3). With infilling it would be expected that the Bragg peak would be shifted to higher wavelengths. As this is not the case here, the suggestion is that large areas of the film may not be filled, and that the extent of complete silica binding / infilling is much less than might be expected from the SEM images, (figures 5.8(d&e), and figure 5.9(d)) where there is reduced cracking, but little indication of the silica binding in the higher magnification images.

**Table 5.1. Calculated number of layers from the Febry-Perot fringes, and peak % reflectance height at zero degrees reflectance taken from the various measurement positions.**

TEOS precursor addition		Corner 1	Corner 2	Corner 3	Corner 4	Side 1-2
+10 $\mu$ l	Layers	X	23	17	X	
	Peak %	12	70	65	18	
+15 $\mu$ l	Layers	16	14	16	21	
	Peak %	65	62	62	73	
+20 $\mu$ l	Layers	X	8	23	X	
	Peak %	55	33	78	60	
+30 $\mu$ l	Layers	16	11	X	X	
	Peak %	30	27	21	10	
+40 $\mu$ l	Layers	13	X	8	X	15
	Peak %	45	50	22	<10	52

**NOTES:** X = unable to calculate from reflectance curve. Zero degrees reflectance measured using a splitter optical fibre.

#### 5.3.4 OTHER UOC INFILTRATION METHODS

During UOC, the water evaporates and the silicone oil fills the voids in the film, such that it is possible that an oil-filled crack-free film could be achieved. If the oil could then be 'lifted', i.e. be removed from between the particles by the addition of water containing a soluble polymer, or other soluble material, which could bind the particles before re-drying the film, then a crack-free film may result. With this in mind a number of samples were prepared using PVA in the "lifting" solution. However, this method proved difficult to control, because the amount of polymer in the solution needed to refill the opal film, could not be easily controlled. Also, the entire area of the flat bottomed container needed to be covered in order to 'lift' the oil. Although the crack-free areas increased from ~200 $\mu$ m (length) by ~30-50 $\mu$ m (width), to ~350 $\mu$ m (length) by ~100 $\mu$ m (width), using this technique, film infiltration was patchy and

overfilled in certain areas, figure 5.14(a&b). Nevertheless the film retained the original fcc structure. A second drawback to this method for the production of large crack-free areas was the increased time required to achieve the final film. This includes 2-3 days for the infiltration and drying of the polymer solution, plus 2-3 days for the initial opal film crystallization.

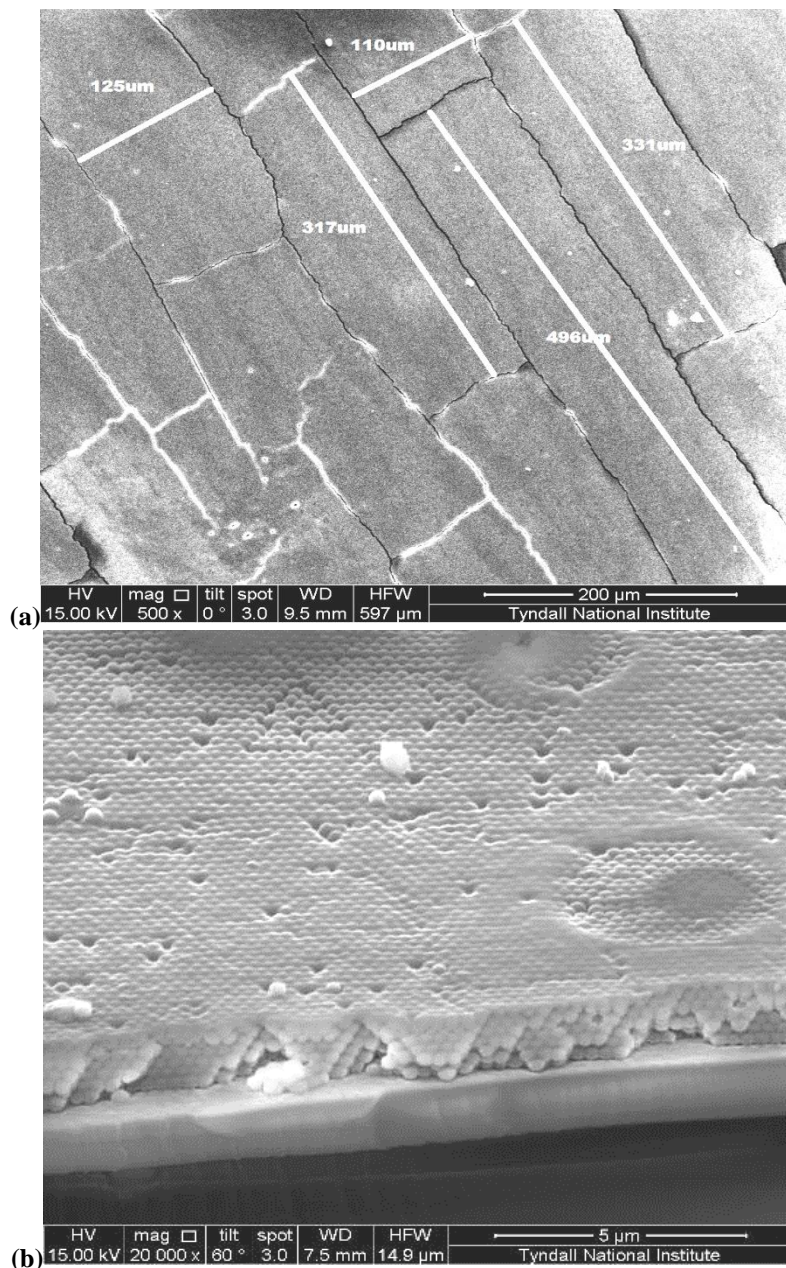
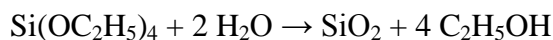


**Figure 5.14. SEM images, showing the increased crack-free areas (a), and patchy infilling with PVA (b), which also shows the fcc structure of the original film is retained.**

## 5.4 DISCUSSION.

### 5.4.1 SILICA INFILLING BY UNDER OIL CO-CRYSTALLISATION

Tetraethyl orthosilicate (TEOS) is easily converted into silicon dioxide. As discussed earlier (Chapter 3) this reaction occurs upon the addition of water:



This hydrolysis reaction is an example of a sol-gel process. The reaction proceeds converting the TEOS into solid silica. The reaction rate is sensitive to the presence of acids and bases, both of which serve as catalysts.

In this under oil co-crystallisation method, the formation of the silica infill from TEOS needs to develop at a slower rate than the formation of the crystalline film, otherwise disruption of the film will take place. This was seen when a precursor solution containing hydrochloric acid as a catalyst was used, in a method similar to that used by Hatton and Aizenberg [6]. As a consequence, the HCl catalyst was removed from further experiments.

Without the catalyst in the TEOS precursor solution, infilling of the voids with silica was achieved, and large crack-free areas could be produced. Additions of +15, +20 and +30 $\mu$ l TEOS precursor solution to the colloidal particle solution resulted in crack-

free areas of 560 x 425 $\mu$ m, (Figure 5.7(c) @ +15 $\mu$ l, 5.8(d) @ +20 $\mu$ l, and 5.9(a) & 5.10(a) @ +30 $\mu$ l), even though the silica infilling is not immediately obvious from the higher magnification images, (Figures 5.8(e), 5.9(c&d), and 5.10(c&d) respectively).

## **5.5 CONCLUSIONS AND FURTHER WORK**

- A large area opal production method, Under Oil Crystallisation (UOC) including the infiltration of UOC opals using two flexible backbones, PDMS (Sylgard 184) and acrylate polymer, (World Rock XVL90A0), was studied during an internship with the Wave Optics Group, NIMS, Tsukuba, Japan.
- Via the use of under oil co-crystallisation, using a TEOS precursor solution, we have shown that it is possible to strengthen and reduce cracking in UOC films, however the optimum quantities of precursor material still needs to be established.
- Inverse silica opals could be produced by under oil co-crystallisation prepared from polymeric particles (PS or PMMA). Removal of the particles by solvent or calcination can be easily achieved. The TEOS precursor solution (at +15 $\mu$ l addition) used here provides a useful guideline for the production of silica inverted opals.

- Inverse titania ( $\text{TiO}_2$ ) opal structures could be developed using under oil co-crystallisation, from the starting precursor solution of titanium (IV)- bis-lactato-bis-ammonium dihydroxide (TiBALDH) in a method similar to that described by Hatton and Aisenberg [6].
- Void filling while the opal film is still under oil, provided a method of increasing the distances between cracks in UOC opal films. However the mechanism and time scales involved reduce the effectiveness of this technique with regard to using it as a production technique.
- Void filling while under oil could be explored with regard to other materials, such as, silica (from TEOS precursor solutions), zinc oxide (from zinc nitrate solutions), and titania.

## REFERENCES:

1. Fudouzi, H., *Fabricating high-quality opal films with uniform structure over a large area*. Journal of Colloid and Interface Science, 2004. **275**(1): p. 277-283.
2. Fudouzi, H. *Novel coating method for artificial opal films and its process analysis*. in *14th International Seminar on Nisshin Engineering Particle Technology*. 2005. Hakone, JAPAN: Elsevier Science Bv.
3. Fudouzi, H., *Optical properties caused by periodical array structure with colloidal particles and their applications*. Advanced Powder Technology, 2009. **20**(5): p. 502-508.
4. Fudouzi, H. and Y.N. Xia, *Colloidal crystals with tunable colors and their use as photonic papers*. Langmuir, 2003. **19**(23): p. 9653-9660.
5. Wang, L.K. and X.S. Zhao, *Fabrication of crack-free colloidal crystals using a modified vertical deposition method*. Journal of Physical Chemistry C, 2007. **111**(24): p. 8538-8542.
6. Hatton, B., et al., *Assembly of large-area, highly ordered, crack-free inverse opal films*. Proceedings of the National Academy of Sciences of the United States of America, 2010. **107**(23): p. 10354-10359.



# **CHAPTER 6.**

## **POLYMER ADDITION DURING EVAPORATION DEPOSITION**

### **6.1 INTRODUCTION**

One approach designed to reduce the number of cracks in a colloidal crystal film is to use a polymeric adhesive to bind the particles together during film formation. The mechanical properties of a dried film can be improved by increasing the strength of the bond between individual particle pairs by the addition of a polymeric binder. Poly(vinyl alcohol) has been used to make crack-free films from the drying of aqueous alumina suspensions [1]. In the experiments described here, in order to maintain the optical properties of the films only small amounts of adhesive or polymer was added to the suspensions in each case, ranging from 1 to 5wt.%. These small concentrations should be able to bind the particles, but leave sufficient air voids so as the optical properties are not destroyed in the final films.

Several polymers were investigated, including a redispersible polymer (Elotex FX2700, a redispersible binder based on a copolymer of vinyl acetate and ethylene), poly vinyl alcohol (PVA), poly methyl methacrylate (PMMA) monomer (followed by

ultraviolet polymerisation), and a high refractive index ( $\eta=1.54$ ) adhesive, Norland Optical adhesive 68 (NOA68), which is a flexible UV curing photopolymer based on mercapto-ester (similar to that used in the under oil experiments). All polymers / adhesives were added to the colloidal suspension, pre dispersed in an ultrapure water solution at low concentrations, with the exception of NOA68 which was pre dissolved in an ethanol/hexane mix prior to adding to the silica suspensions.

## **6.2 EXPERIMENTAL**

Silica colloidal particles (produced at Tyndall National Institute) having an average diameter of approximately 275nm measured by SEM & ImageJ as outlined previously in Chapter 3, were used in the redispersible polymer experiments. Seahostar KEW30 (280nm) silica particles were used for all the other polymer / adhesive experiments. Glass microscope slides (37mm x 12mm) were made hydrophilic by first rinsing with ethanol, sonicated in a 5:1:1 solution of  $\text{H}_2\text{O}:\text{NH}_4\text{OH}:\text{H}_2\text{O}_2$  for 30 minutes, prior to rinsing in pure water and dring under nitrogen.

A pre-prepared solution of Elotex 2700 in ultrapure water was stirred for approximately 5 minutes, until all of the adhesive appeared dissolved. This solution was used to prepare, 1wt.% and 5wt.% addition of redispersible adhesive, to a 0.175vol.% silica suspensions with 90% water: 10% ethanol. Final suspensions were stirred for approximately 3 hours, and placed in a temperature controlled oven at 60°C for 18

hours. Samples were compared against a sample with 0% addition of redispersible adhesive.

Films prepared using NOA68, PMMA and PVA additions were made on 50mm x 25mm slides, hung vertically in a 0.45vol.% in 35ml suspension, at 60°C. This concentration was chosen to produce films of approximately 10 layers throughout the bulk of the film.

### **6.3 RESULTS - ADDITION OF A REDISPERSIBLE POLYMER**

Initial experiments included a redispersible polymer (Elotex FX2700), dispersed in a suspension with silica particles, 275nm diameter, in an ethanol water mix, and placed into an oven at 60°C overnight. When viewed under an optical microscope at 150x magnification (figure 6.1 (a-c) reflectance images), the images for the samples without any addition and with 1wt% addition of redispersible polymer show that the shape and size of the domains between cracks are roughly similar. However, with the addition of 5wt% redispersible polymer, the horizontal cracking is much reduced, with the vertical cracks dominating the image, (the 3 images shown are from a central position within each sample).

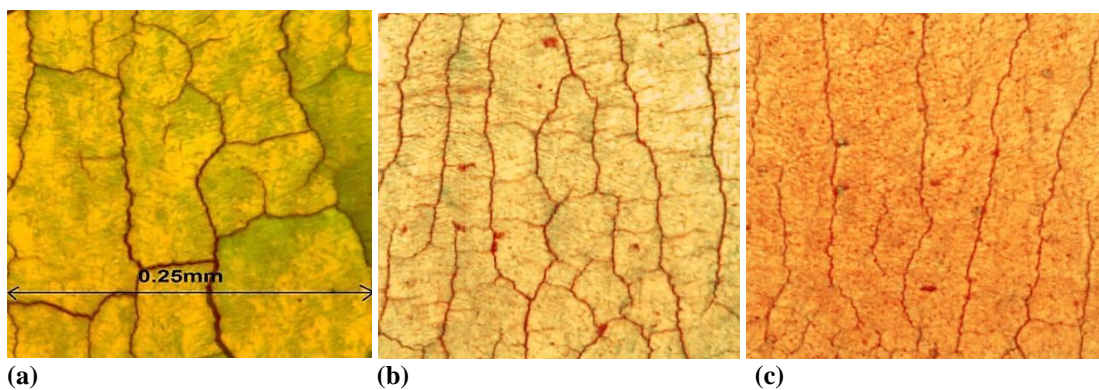


**Figure 6.1(a-c).** Optical microscope images, taken from a central position from each sample with (a) 0%, (b) 1wt% (c) 5wt%, addition of Elotex (all images are 150x magnification, 0.25mm across)

SEM images of the same samples are given in figure 6.2, 6.3 and 6.4, with 0%, 1wt%, and 5wt% addition of the redispersible polymer respectively. The area between cracks increases as polymer content increases, (from approximately  $250\mu\text{m} \times 60\mu\text{m}$  at 0% addition, to approximately  $300\mu\text{m} \times 120\mu\text{m}$  at 1% addition, and  $>400\mu\text{m} \times 120\mu\text{m}$  at 5% addition). However, at this relatively low level of polymer addition, cracks are still visible throughout the films, despite the polymer binding across the cracks. The SEM images show the polymer binds across the cracks by stringing, figures 6.3e and 6.4f. The additions of a small amount of polymer does not appear to affect the high quality ordering of the particles during film formation, as seen in Figure 6.4(d) with 5wt% addition. It should be noted that these films were relatively thick, approximately 30 layers.

The SEM images also show a number of other interesting features arising from the use of a redispesible polymer. Firstly, the number of missing particles in the crystalline structure increases with increasing polymer content, see table 6.1 below.

Sample	Number of missing particles	Total area $\mu\text{m}^2$	No. missing particles/ $\mu\text{m}^2$	Example images
<b>0% addition</b>	21	809	0.026	Figure 6.2d
<b>1% addition</b>	74	1090	0.068	Figure 6.3d
<b>5% addition</b>	170	1726	0.098	Figure 6.4d-f

**Table 6.1.** Comparison of the observed number of missing particles from SEM images, with respect to the quantity of redispersible polymer used in the suspension.

Secondly, areas of polymer concentrations show that the redispersible polymer is not evenly distributed throughout these films (despite the long stirring times, 3 hours), e.g. figure 6.3d is a typical magnified image of the large holes seen in figures 6.3c and 6.4b.

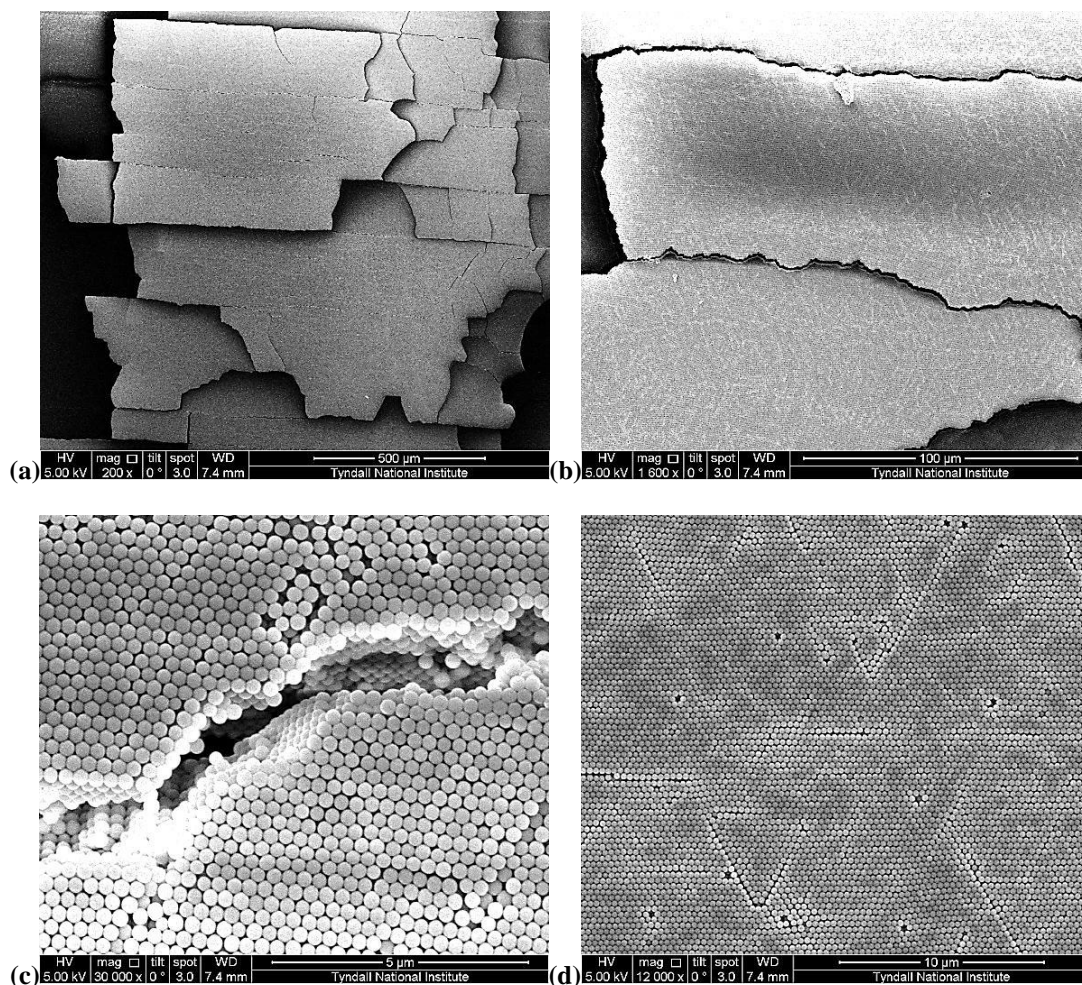


**Figure 6.2(a-d).** SEM images of a sample with no redispersible polymer additions, (a&b) showing areas of domain sizes between vertical cracks of up to 500microns, and distance between horizontal cracking approximately 50microns. (c) show a magnified area of cracking, and (d) shows high quality particle packing at the surface.

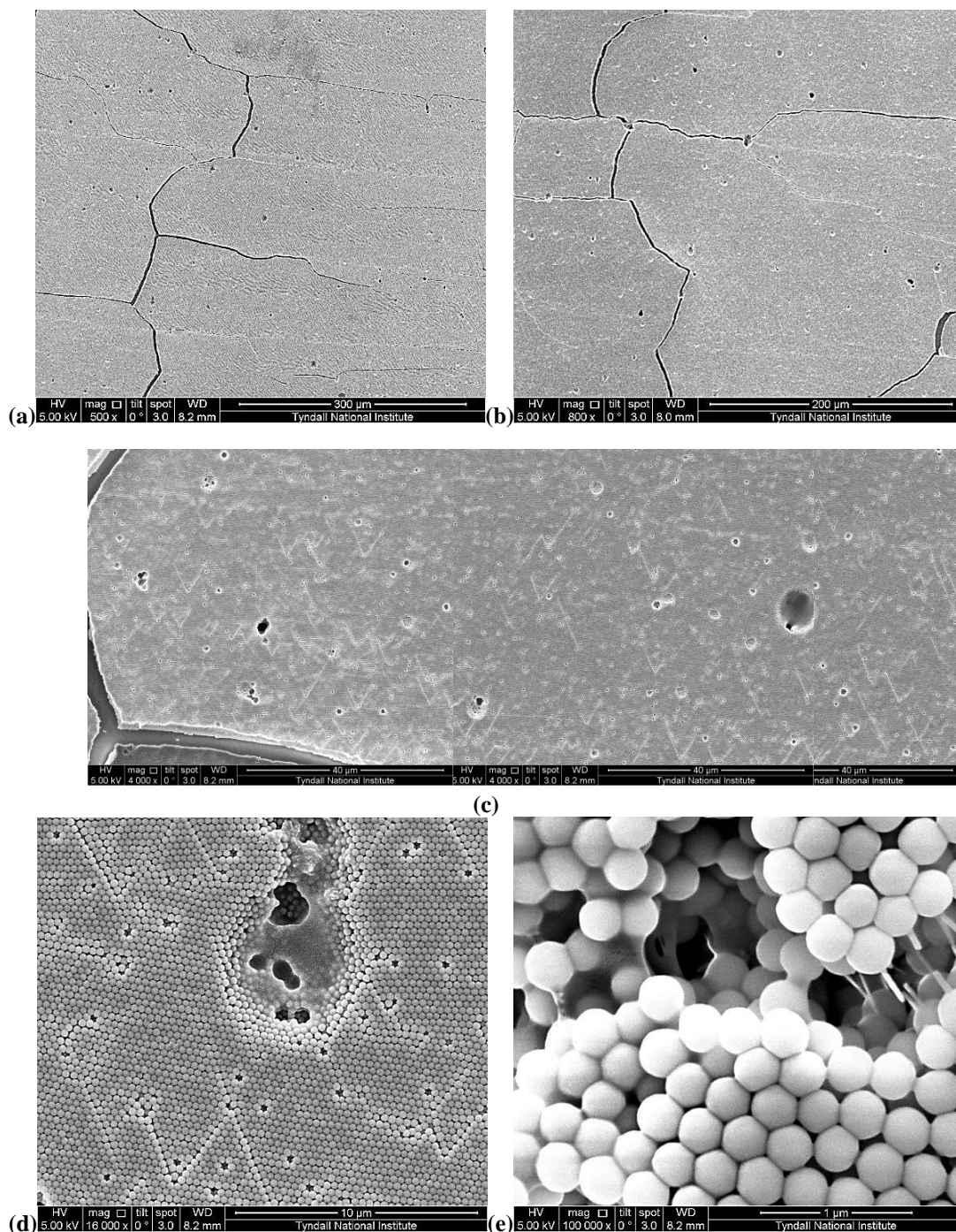


**Figure 6.3(a-e).** SEM images of a sample with 1% redispersible polymer addition; (a&b) show areas of domain sizes between vertical cracking of >400microns in many areas, and distance between horizontal cracking >200micron, (cracking is also shown to be more varied than the approximate straight-line cracks seen in the 0% sample above); (c) shows multiple images taken from (a) around the large central spot, (this spot is shown to be an area heavily filled with polymer showing the polymer is not evenly dispersed within the film); (d) shows high quality particle packing at the surface surrounding the polymer filled hole, and (e) is a cracked area revealing the stringing of the polymer across the crack width.



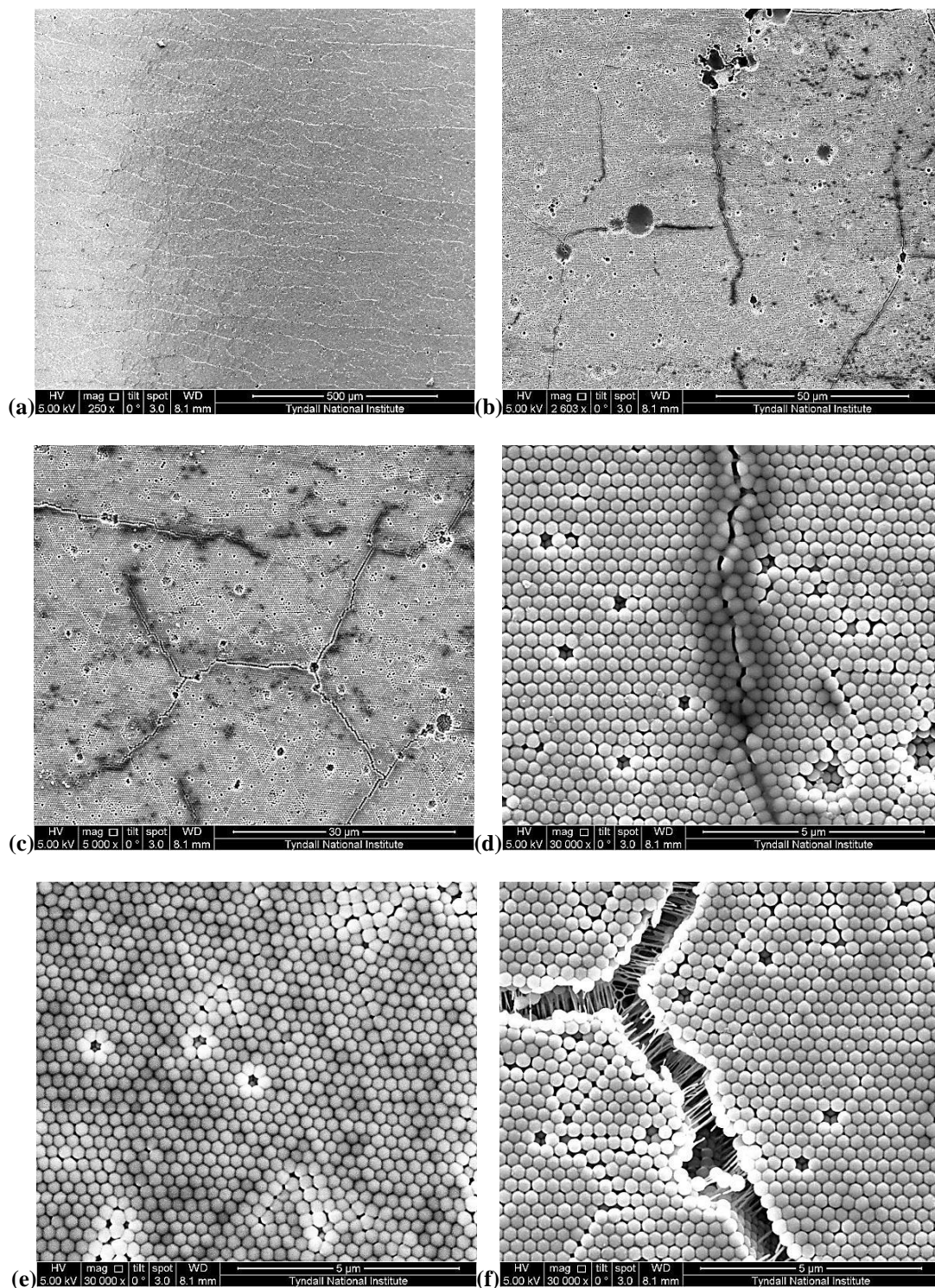


**Figure 6.4(a-f).** SEM images of a sample with 5% redispersible polymer addition; (a) large area image at 250x magnification, although cracking hasn't been avoided, the cracks are reduced (and compared to a similar magnification image, (Figure 2a) are less visible, suggesting they are narrower); some cracks do not join up to define a specific domain area, as shown in (b,c&d). (e) shows an area of polymer filling in an area of high quality packing, and (f) shows the polymer stringing across a crack.



Optical spectra (figure 6.5) from these 3 samples also reveal the reasonably high quality of the films, with Bragg reflectance peaks of 47% (at 620nm wavelength), and 27% (at 625nm), for the 1% and 5% samples respectively. Transmission dips are also deepest and narrowest for the 0% sample, the intensity of the dips reducing as polymer content increases, as would be expected. Figure 6.5b also shows that these films follow the Bragg-Snell law, in that the transmission dip shifts to lower wavelengths as the angle of incidence increases. The structural colour being tuned by the incident angle is a well-known phenomenon of these ordered colloidal photonic crystal films. This is expressed by the Bragg-Snell equation described in the introduction. This equation can be rearranged to give:

$$\sin^2\theta = n_{\text{eff}}^2 - (1/4D^2) \lambda^2. \quad (\text{Equation 6.1})$$

Where:

- $\lambda$  = the wavelength at the centre of the stop band at each angle of incidence
- $\theta$  = the angle of the incident light and the normal to the surface
- $D$  = the centre-to-centre distance of the nano-particles, or equivalent to the mean diameter of the particles.
- $n_{\text{eff}}$  = the effective refractive index

The relationship between the incident angle and the transmission dip position (or reflectance peak) is plotted graphically in figure 6.5c. A straight line fit has an intercept and gradient, corresponding to the average (effective) refractive index and interplane spacing for the fcc (111) lattice, respectively [2]. This observation allows one to

consider the diffraction of the light waves penetrating the bonded opal film on the same basis as that in a bare opal.

The mean or effective refractive index ( $n_{\text{eff}}$ ) of these films does not appear to change significantly with increasing polymer content, as shown in figure 6.5(d), (as may be expected from equation 5, Chapter 1). This is probably because of the small quantities of adhesive used, and the fact that the adhesive tends to agglomerate in certain areas, leaving each film relatively similarly filled, thus the  $n_{\text{eff}}$  does not change significantly between the films.

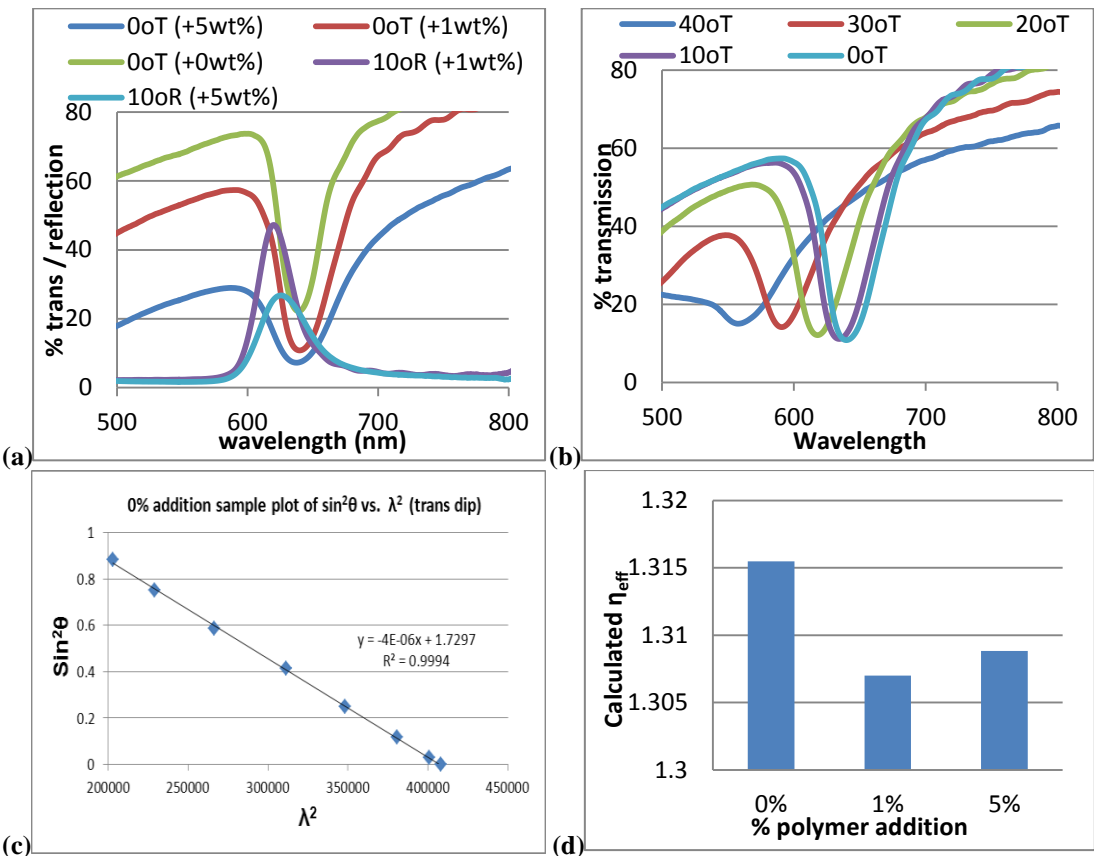


**Figure 6.5.** (a) Optical spectra of polymer bonded samples at 0, 1 & 5 weight percent additions, (reflectance @  $10^\circ$ , and transmission at  $0^\circ$ ); (b) Optical spectra of 1wt% polymer bonded sample @  $0^\circ$  to  $70^\circ$  transmission; (c) the relationship between the square of the incident angle and the square of the transmission dip position; and (d) effective refractive index plotted against polymer content.

## 6.4 DISCUSSION – REDISPERSIBLE POLYMER

The use of a polymeric binder to bond submicron silica particles together and reduce cracking in films has been demonstrated using a redispersible polymer. SEM images show stringing of the polymer (figures 6.3e and 6.4f) across the cracks. This redispersible polymer has particle sizes after dispersion of approximately 2-5 $\mu\text{m}$ . After mixing with water a dispersion is obtained, i.e. single polymer particles dispersed in the suspension medium (ethanol:water). After evaporation, a film is formed as shown schematically, figure 6.6. The sizes of the polymer particles were too large to be effectively dispersed evenly throughout the much smaller silica particles, and hence areas of polymer concentration are observed, (the large hole seen in figures 6.3d and 6.4b). However, using a polymeric binder has shown promise in reducing cracks in these colloidal photonic films, while retaining a high quality crystalline structure. As a consequence a number of other binder materials were investigated.

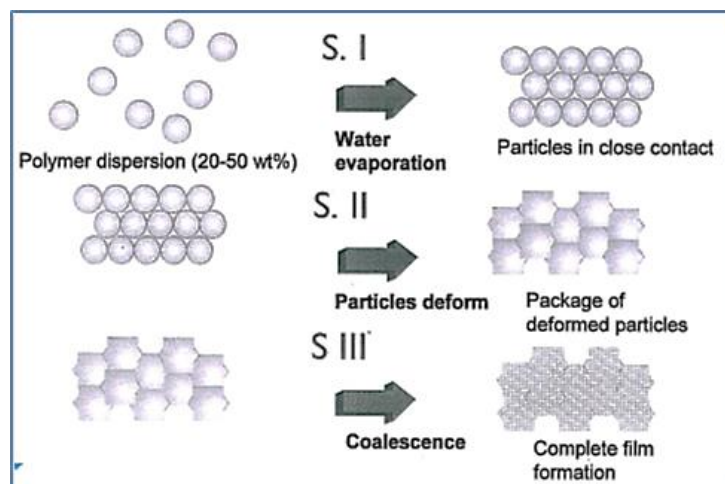
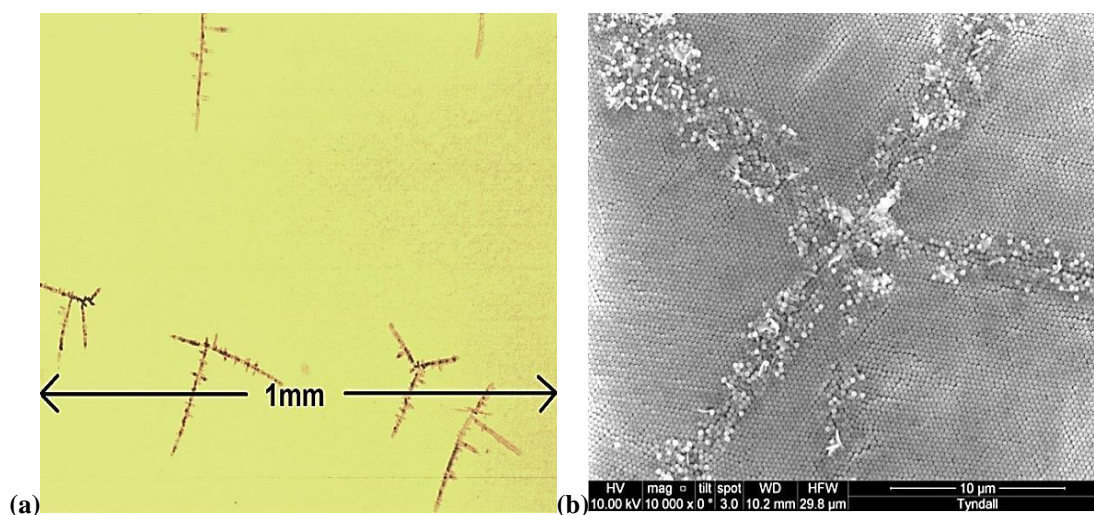


Figure 6.6. Schematic of polymer film formation from a redispersible polymer [3].

## 6.5 RESULTS – ADDITION OF UV CURING FLEXIBLE ADHESIVE

The second adhesive chosen for investigation was Norland Optical Adhesive 68 (NOA68) which is a flexible UV curing photopolymer based on mercapto ester (and is a similar adhesive to that used in the under oil crystallisation experiments described in Chapter 5). NOA68 was pre-dispersed in an ethanol/hexane mix and stirred rapidly for at least 10 minutes, before it was added to a suspension of silica particles (KEW30, 280nm diameter) in an ethanol water mix, and placed into an oven at 60°C overnight. A 2% by weight addition of NOA68 was added to the silica particle suspension and stirred again for a further 30 minutes.

When viewed under an optical microscope at 40x magnification (figure 6.7a) an area of approx 1mm x 1mm is shown, which shows no evidence of cracking. However there are areas of NOA68 adhesive deposition, which appears as dendritic like growth formations.



**Figure 6.7. (a) Optical microscope image +2wt% NOA68 at 40x (reflectance mode) & (b) SEM showing no obvious cracking due to the adhesive penetrating the film in this manner.**

Very well ordered particles are clearly shown in figure 6.7b, and across an area of approximately 300 $\mu$ m x 300 $\mu$ m Moiré fringes are visible throughout the picture (including around an area of dendritic-like adhesive deposition, figure 6.8). However, this sample was generally only 2-4 layers thick as shown in the SEM cleaved edge images, figure 6.9. Interestingly cleaving the film revealed (100) orientated particles in a NOA68 matrix, figure 6.9. This is probably due to the cleaving angle revealing this lattice orientation of the fcc structure at this position.

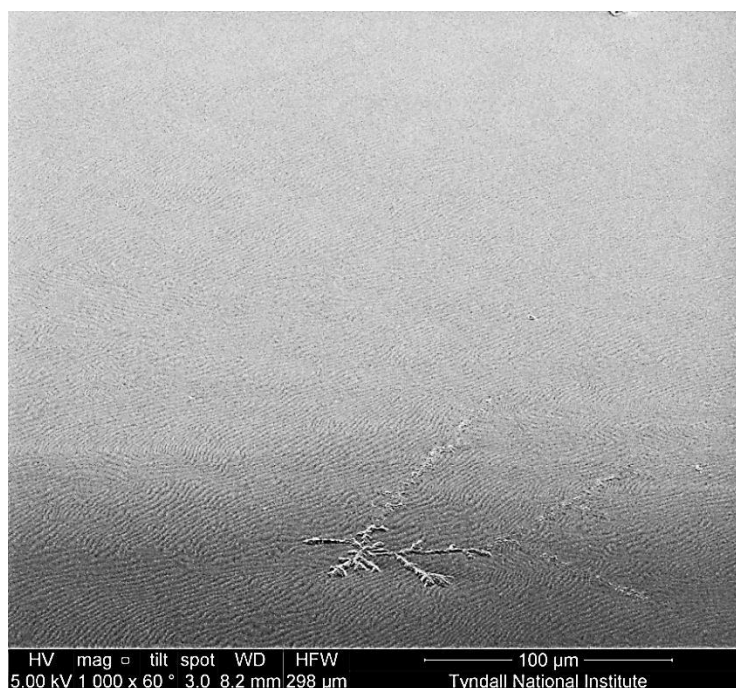


**Figure 6.8. 1000x mag SEM image, shows no cracking over and area of approximately 300micron x 300micron, including an area around dendritic-like adhesive deposition.**

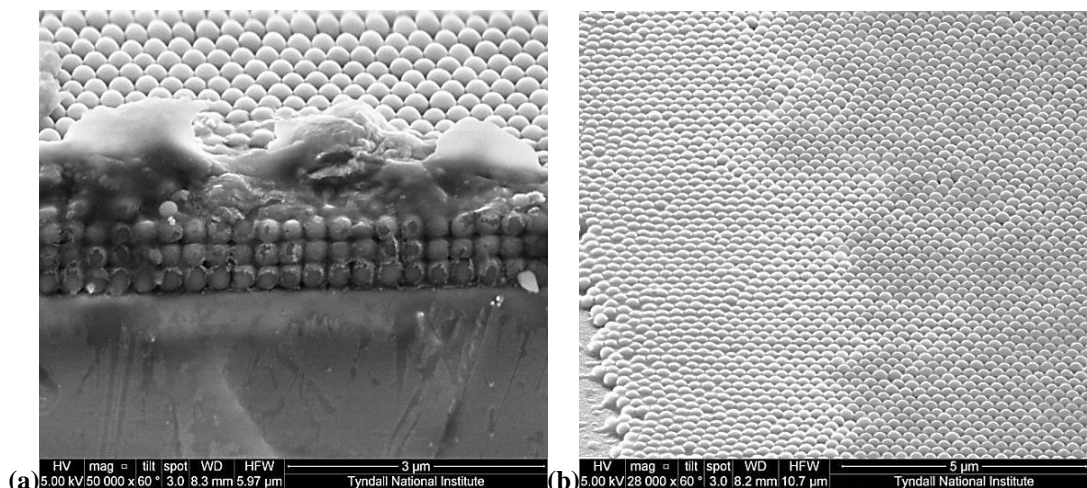
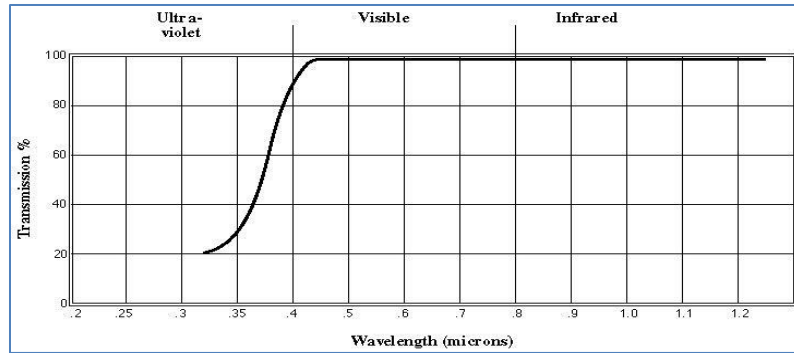


**Figure 6.9.** (a) SEM image of side view showing evidence that the NOA68 adhesive could be dispersed throughout the film binding the particles together, however (b) shows areas of film filled and unfilled with NOA68.

## 6.6 DISCUSSION – UV CURING FLEXIBLE ADHESIVE

NOA68 was chosen as an adhesive to investigate due to its very high transparency over most of the visible spectrum (figure 6.10). Small additions of NOA68 (2wt%) therefore should not significantly alter the optical properties of the photonic crystal films, and because NOA68 is flexible with good strength, it should be able to bind the particles together and reduce cracking in these films. To a certain degree this adhesive was successful in meeting the aims of this investigation; however there is still a need to disperse it more evenly throughout the suspension (in a suitable solvent), and therefore within the film. Because of NOA68's relatively high refractive index, 1.54, it may be possible to completely infill a film during controlled evaporation, and retain good optical properties, although the refractive index contrast between these particles,  $n = 1.41$ , (see below) and adhesive filled voids would be greatly reduced as compared to air voids.



Solids	100%
Viscosity at 25° C	5,000 cps
Refractive Index of Cured	1.54
Elongation at Failure	80%
Modulus of Elasticity (psi)	20,000
Tensile Strength (psi)	2,500
Hardness - Shore D	60

Figure 6.10. Shows the quoted Spectral Transmission of NOA68, and physical properties [4].

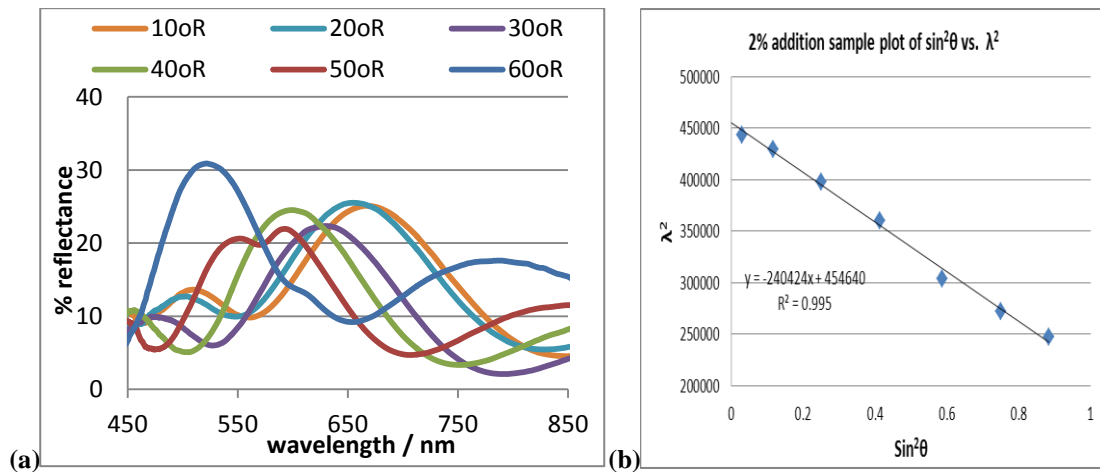
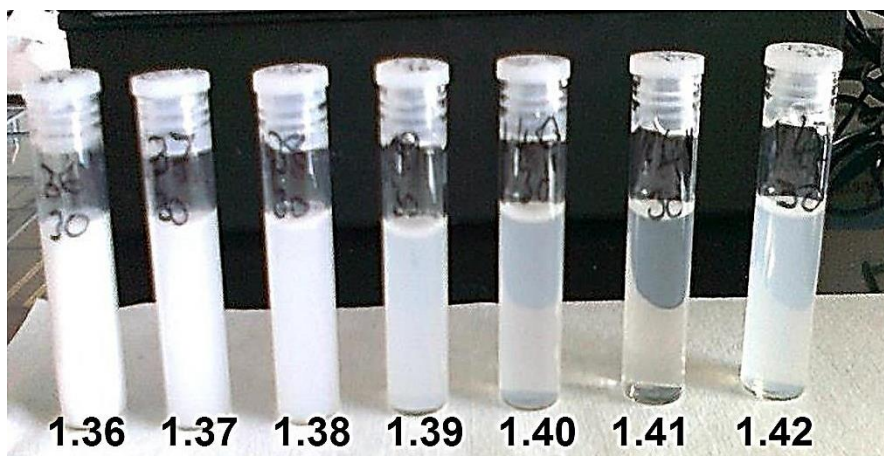


Figure 6.11. (a) Shows the visible reflectance spectra of 280nm silica particles + 2wt% NAO68; (b)  $\lambda^2$  vs.  $\sin^2\theta$ , and calculated slope and intercept values.

The optical properties of the NOA68 infiltrated film gave a calculated  $n_{\text{eff}}$  value (from the slope and intercept values (figure 6.11b)) of 1.375. This is greater than the

values above from the redispersible adhesive additions, above. NAO68 adhesive having a refractive index of 1.54 thus raises the overall effective refractive index of the film.

The refractive index of the 280nm silica particles purchased from Seahostar has been calculated from a number of samples, using equation 6.1, and back calculating the refractive index of the silica particles themselves, using equation 5 from Chapter 1: Introduction, (assuming a particle volume factor of 0.74). From 16 samples their average refractive index was approximately 1.41. This closely agrees with that indicated from dispersing the particles in a mixture of water and ethylene glycol (known as index matching) using the equation for refractive indices of aqueous ethylene glycol solutions at 25°C: refractive index =  $1.3325 + 0.000982x$  (where:  $x$  = weight % ethylene glycol) [5].



**Figure 6.12. Samples of silica particles in ethylene glycol:water mixes at (from left to right) 1.36, 1.37, 1.38, 1.39, 1.40, 1.41 & 1.42 refractive. Sample KEW30 (280nm Seahostar) matches the refractive index of the solution at approx. 1.41**

Hence a completely filled opaline film containing NOA68 would have a refractive index contrast of  $(1.54 - 1.41) = 0.13$ . This is above the minimum of 0.02 suggested as being necessary in order to maintain the *play-of-colour* of the opal [6].



## 6.7 RESULTS - ADDITION OF MMA MONOMER

The third polymeric addition studied was MMA monomer, (followed by UV curing of the manufactured film), dispersed in a suspension with silica particles (KEW30, 280nm diameter) in an 75% ethanol 25% water solution, and placed into an oven at 60°C overnight. When viewed under an optical microscope, 2 images at 40x magnification (figure 6.13 a & b) show vertical crack-like lines at an average of approximately 200µm (40x magnification optical images are approximately 1mm across), while no horizontal “cracks” are seen over a distance of 800µm in these images. Similarly in the images at 500x magnification using SEM, (figure 6.13c), there are no cracks in the vertical direction over a distance of 600µm, and the crack-like features are separated on average at 220µm. However, at higher magnifications, these crack-like features appear to be domain boundaries between domains of slightly differently orientated particle packing (figure 6.13d).

Indeed in the vertical direction there are no cracks at all over the full vertical length of this film, covering a distance of approximately 20mm. This particular film was made from 280nm particles at 1.0% by volume of particles in a 200ml solution of ethanol:water mixed at a ratio of 3:1, at 60°C over 3 days, with 5% by weight MMA monomer added.

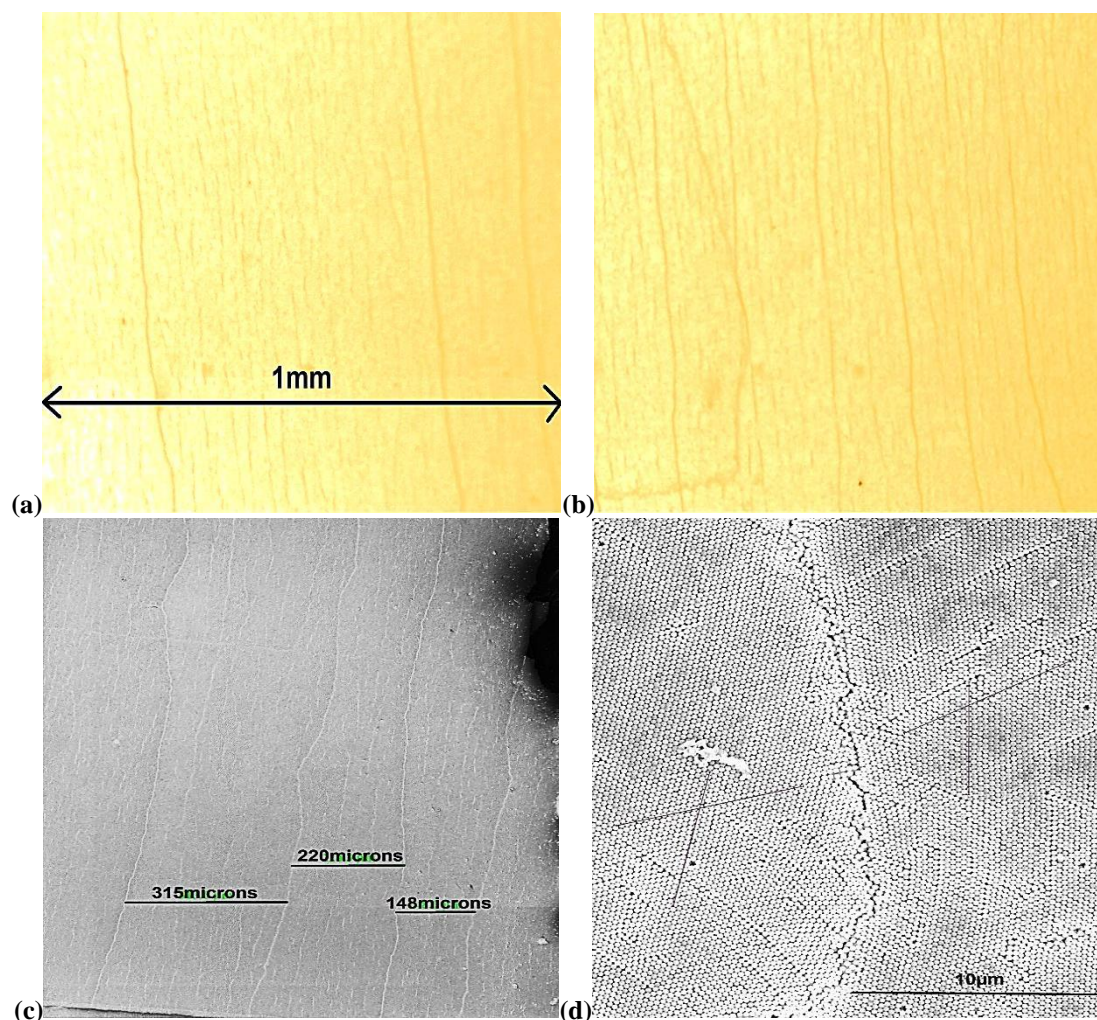


**Figure 6.13.** (a & b) are 2 optical microscope images at 40x magnification; (c) 500x mag of vertical “cracks” in a typical film. (average “crack” spacing is approx. 200µm); (d) 10,000x mag, shows that the vertical “cracks” are in fact domain boundaries between differently orientated packed domains.

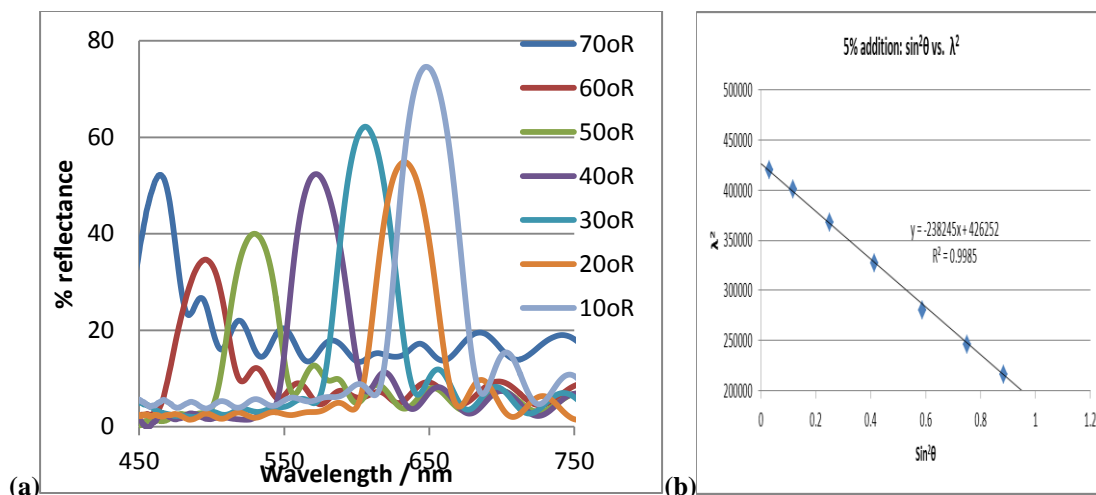


**Figure 6.14 (a) Shows the visible reflectance spectra of 280nm silica particles + 5wt% MMA monomer; (b)  $\lambda^2$  vs  $\sin^2\theta$ , and calculated slope and intercept values.**

The Fabry-Perot fringes in the optical spectra indicate approximately 15 particle layers, and SEM images show fcc packing over 17 layers (figure 6.15a) which corresponds well with the calculated value. The effective refractive index of the film is calculated as being 1.33. This corresponds well to that of an unfilled film. On closer inspection of these films there is a “white” area of film at the start of film deposition. Closer SEM inspection of this area shows that it is filled with cured PMMA, (figure 6.15b). Again, cleaving the film has revealed (100) orientated particles in a PMMA matrix, which is probably as a result of the cleaving angle revealing this lattice orientation of the fcc structure.

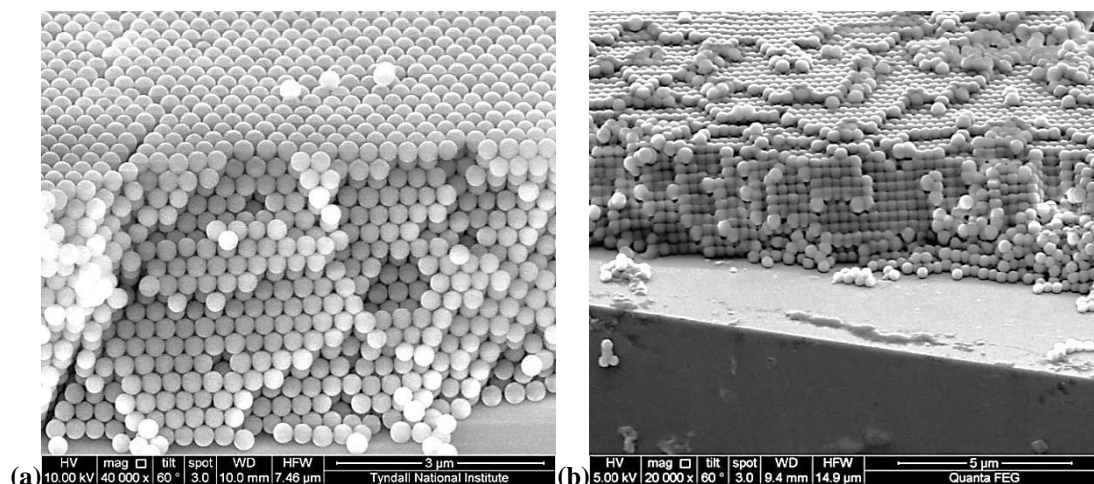


**Figure 6.15.** SEM images of (a) 17 layers “unfilled” film; and (b) MMA filled area in the upper area of the film.

## 6.8 DISCUSSION - ADDITION OF MMA MONOMER

The effective refractive index of the highly coloured area of the above film was calculated at 1.33, which (along with the SEM images from this area) suggests that there is very little or no MMA within this area of the film. The majority of the MMA monomer, being very volatile, has evaporated during early film development, and hence is mostly contained within the first few mm of the film. Transmission data from this area of the film is given in figure 6.16, the reduced transmission dips indicating a filled structure, which corresponds with the SEM image, figure 6.15b.

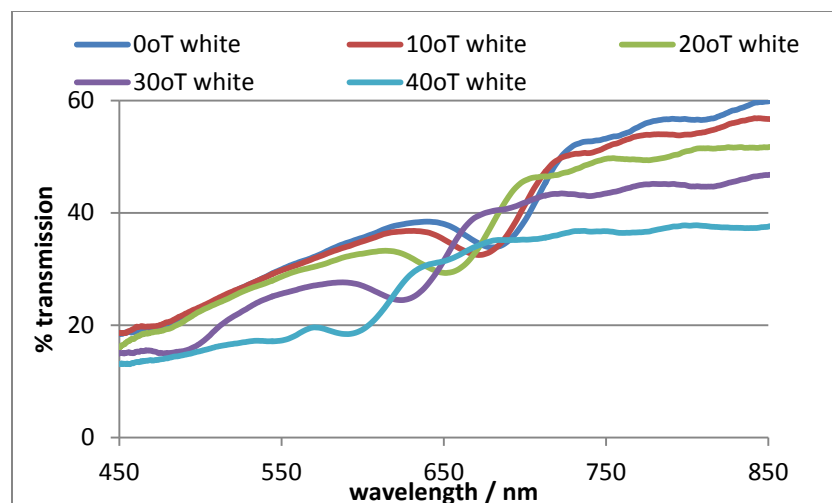


**Figure 6.16. Visible transmission spectra of 280nm silica particles + 5wt% MMA monomer (NOTE: White in the key indicates measurements taken from the MMA filled “white” area).**

To reduce the effect of the volatile MMA monomer evaporating too quickly, a lower evaporation temperature may be required to produce the film with MMA maintained throughout the film. However, this would obviously require longer production times.

## 6.9 RESULTS - ADDITION OF PVA WATER SOLUBLE ADHESIVE

The fourth polymer to be examined was poly vinyl alcohol (PVA) adhesive, which is readily soluble in water. PVA was dispersed in a suspension with silica particles (KEW30, 280nm diameter) in an 75% ethanol 25% water mix, and placed into an oven at 60°C overnight. These samples were all prepared using +2wt% addition of PVA predissolved in water, but with increasing volume percentages of particles, in order to achieve thicker films. When viewed under an optical microscope at 150x magnification

very fine vertical lines are seen within the film (Figure 6.17a), and new layer formations are visible in reflectance mode (Figure 6.17b). Generally during controlled evaporation film thickness increases occur as a film grows. Here we also see increasing layers, initiated around a point of agglomeration within the film, (seen in the left hand side of this image (b)), Here the shape of the meniscus has been altered, increasing its curvature around the point of agglomeration, thus providing the opportunity for more particles to be drawn into the meniscus region and increase the layers deposited within the film. Immediately surrounding this point defect at least 3 layers have developed. Figure 6.17(c) shows an increasing dip in the transmission curves with increasing film thickness, however no variation in the Bragg wavelength is seen compared to the sample made without any PVA addition. The red curve (+2%PVA-4 layers) corresponds to an area shown in figure 6.17(d). Although SEM images indicate that PVA within the film is not binding across a substantial number of particles, (Figure 6.17d), it does appear that a crack-free film has been produced.



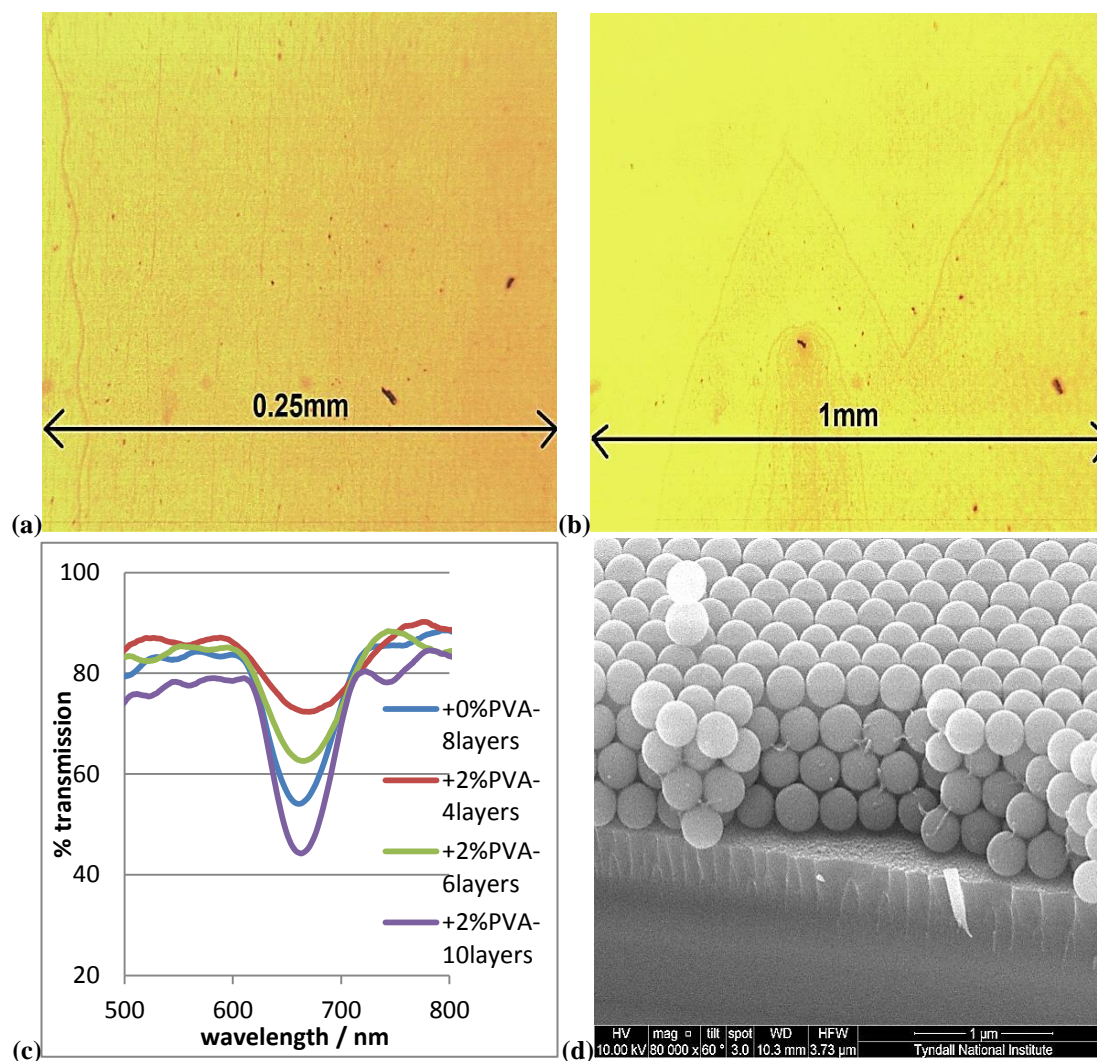


**Figure 6.17.** Optical microscope images (a) at 150x magnification showing similar crack free areas to that seen using MMA monomer (above); (b) 40x magnification of new layer formation; (c) transmission spectra showing increasing dip with increasing number of layers; & (d) SEM image showing limited PVA bonding.

## 6.10 DISCUSSION OF POLYMER ADDITIONS DURING EVAPORATION DEPOSITION.

Whilst all of these polymer additions appear to have produced crack-free films, where only the domain boundaries produce crack-like features in the optical and electron

microscopy, it must be noted that most of these films were relatively thin (<20 layers thick), and all were made using a single standard particle size (KEW30, 280nm). Also during these experiments, it was found that the best films (those showing the highest and sharpest Bragg reflection peaks) were made by producing films in a dispersion of ethanol and water in a ratio of ethanol:water = 3:1. When films are produced within these (mixed solvent and temperature) parameters, it is difficult to see any individual cracks by optical microscopy, or SEM imaging, until the films were sufficiently thick. This was the case on both silicon and glass substrates. With this in mind some of the very large crack-free areas seen using the above polymeric adhesives may not be due to the polymeric additions binding the particles, but be more to do with the thickness and production method used in making these films. During controlled evaporation deposition both sphere assembly and drying take place simultaneously. Li and Marlow state that the solvents do not influence the crack distribution inside the films qualitatively, but they influence the surface appearances of the final films and their fine structure [7]. Therefore the potential of the use of a mixed ethanol:water suspension is explored in Chapter 7.

Of the polymers chosen for examination, the redispersible polymer tended to increase the number of defects within the films, in particular the number of holes (missing particles); Norland Optical Adhesive NOA68 produced dendritic growth of adhesive within the films; the MMA monomer, being very volatile, tended to “congregate” in the upper areas of films produced by controlled evaporation deposition. Therefore, under these conditions, the water soluble PVA adhesive performed the most



reliably when using the evaporation deposition film formation method, although further work would be required to fully assess its contribution to the film formation.

## **6.11 CONCLUSIONS AND FURTHER WORK:**

- Norland Optical Adhesive (NOA68), having the greatest refractive index, (and therefore the greatest index contrast), high optical transparency, and good flexibility, should be explored further with regard to producing, not only crack-free films, but also the potential for producing flexible photonic crystal films.
- A suitable solvent needs to be established to make the use of NOA68 a viable process, as dissolving NOA68 in ethanol causes dendritic-like deposition of adhesive within the film.
- Higher quantities of adhesives should be explored to establish the maximum addition levels before quality film growth is disrupted, and particles become poorly ordered.
- Highly volatile adhesives / monomers (e.g. PMMA monomer) need low deposition temperatures, thus increasing production times.

## REFERENCES:

1. Xu, P., A.S. Mujumdar, and B. Yu, *Drying-Induced Cracks in Thin Film Fabricated from Colloidal Dispersions*. Drying Technology, 2009. **27**(5): p. 636-652.
2. Fudouzi, H., *Optical properties caused by periodical array structure with colloidal particles and their applications*. Advanced Powder Technology, 2009. **20**(5): p. 502-508.
3. (www.elotex.com - Elotex Technical Information).
4. <https://www.norlandprod.com/adhesives/noa%2068.html>
5. [http://www.meglobal.biz/media/product\\_guides/MEGlobal\\_MEG.pdf](http://www.meglobal.biz/media/product_guides/MEGlobal_MEG.pdf)
6. Filin S.V., Puzynin A.I., Samoilov V.N., *Some Aspects Of Precious Opal Synthesis*, The Australian Gemologist, Vol.21, No.7, 2002
7. Li, H.L. and F. Marlow, *Solvent effects in colloidal crystal deposition*. Chemistry of Materials, 2006. **18**(7): p. 1803-1810.

# **CHAPTER 7.**

## **CONTROLLED EVAPORATION DEPOSITION USING MIXED SOLVENTS**

### **7.1 INTRODUCTION.**

A number of authors have used mixed solvents during controlled evaporation deposition experiments in order to achieve improved quality in their colloidal films, usually achieving larger domain areas by this method. Wang et al. [1], using controlled evaporation, suggest that a small temperature gradient can be achieved by placing a vial or beaker directly onto the bottom of an oven (at 55°C in this case). Using a 10% ethanol by volume aqueous solution, they were able to deposit silica particles up to 600nm diameter with good quality and high thicknesses (>50 layers). They claim that their samples were also crack-free as a result of an appropriate drying rate.

Li and Marlow [2] explored the variations in controlled evaporation deposited films with varying ethanol and water concentrations. They suggested that the properties of the solvent; surface tension, viscosity, and volatility, can be tuned using a mixed solvent suspension. Here they used 260nm PS spheres at water to ethanol volume ratios of 100% water, 80% water: 20% ethanol, 66% water: 33% ethanol, and 100%

ethanol. The 100% ethanol sample showed very small domains, whereas the other samples exhibited larger grid-like cracks covering the films, and they observed that thicker opal films have larger, more perfect domains. The domain size is therefore related not only to the mixed solvent properties but also to the obtained thickness. Another effect seen in these experiments was that higher percentages of water in the original suspension resulted in thicker films at the same particle concentrations, and therefore the concentration of these samples had to be reduced in order to achieve the same film thicknesses as those produced at lower water percentage suspensions. SEM examinations of Li and Marlow's films revealed that the solvent mix can influence the packing quality of the particles, with the highest quality ordering seen in the 80% water: 20% ethanol, and the lowest quality ordering seen from 100% ethanol. This was reflected in the optical analysis of their samples, although they do state that direct optical comparison is difficult as the film thicknesses varied between samples at different solvent ratios. They conclude that during controlled evaporation, sphere assembly and drying take place simultaneously, and that the mixed solvents do not influence the crack distribution inside the films qualitatively, but do influence the surface appearances of the final films and their fine structure.

Yoldi et al. [3] used controlled evaporation to produce films of PS particles of 1.0, 1.4 and 2.8 $\mu$ m diameter, at 40-70°C, and noted that in water-only suspensions, average size of domains increased with particle concentration and also with temperature. This effect was also seen by McLachlan et al. [4]. In order to increase the rate of evaporation Yoldi et al. repeated their experiments with aqueous ethanol suspensions,

and found that the average domain size increased with the fraction of ethanol in volume until 0.5.

## **7.2 EXPERIMENTAL.**

Silica colloidal particles (Seahostar KE-W30, Nippon Shokubai) 280nm diameter, were received dispersed in ultrapure water. These particles were obtained at approximately 20% by weight in water and further reduced to a required concentration by diluting in ultrapure water (18.2 MΩ cm) and ethanol. Glass microscope slides (75mm x 25mm) were made hydrophilic by first rinsing with ethanol, sonicated in a 5:1:1 solution of H<sub>2</sub>O:NH<sub>4</sub>OH:H<sub>2</sub>O<sub>2</sub> for 30 minutes, prior to rinsing in pure water and dried under nitrogen.

In order to grow large area films by controlled evaporation deposition, it was decided initially to grow films on a full microscope slide (similar to the typical areas covered at Tyndall by L-B deposition, the areas achieved by the sonication method, and the UOC method). To minimise the effects of increasing layers with length of growth [5], glass microscope slides were placed horizontally across a 500ml beaker, and vertically in the y-direction (Chapter 2: figure 2.4). By placing the slides horizontally, the growth length was limited to a maximum of 25mm, to minimising the increasing thickness effect seen using this method, and relatively even films were produced across the entire area of the slide.

Since initial trials with aqueous ethanol silica suspensions found that a ratio of 3:1 ethanol:water produced the highest quality films this ratio was maintained in all the experiments in this chapter. Figure 2.4 (Chapter 2), shows a digital camera image of the experimental set up. A glass substrate was held centrally in a 500ml beaker containing the suspension of a specific concentration of silica particles, and the film was allowed to grow in an oven at 50°C (unless otherwise stated). A thin silica film with iridescent colours was formed on the glass substrate, Figure 7.1(a&b).

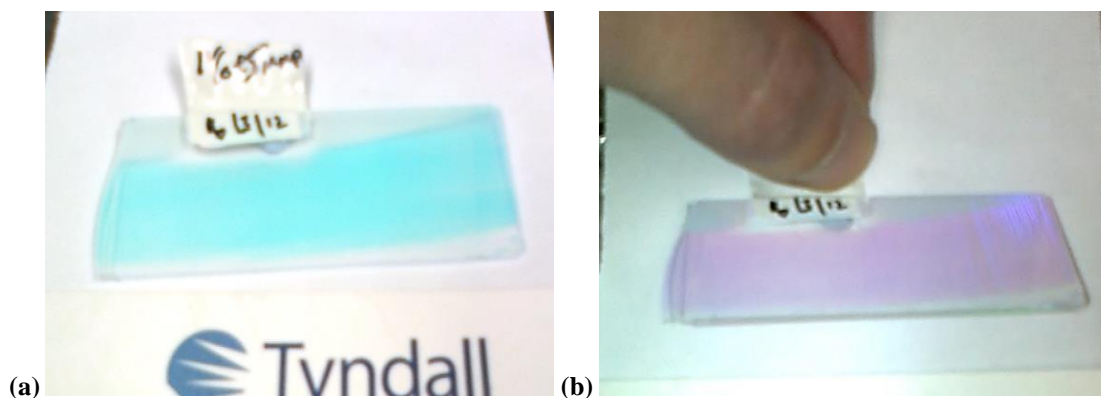
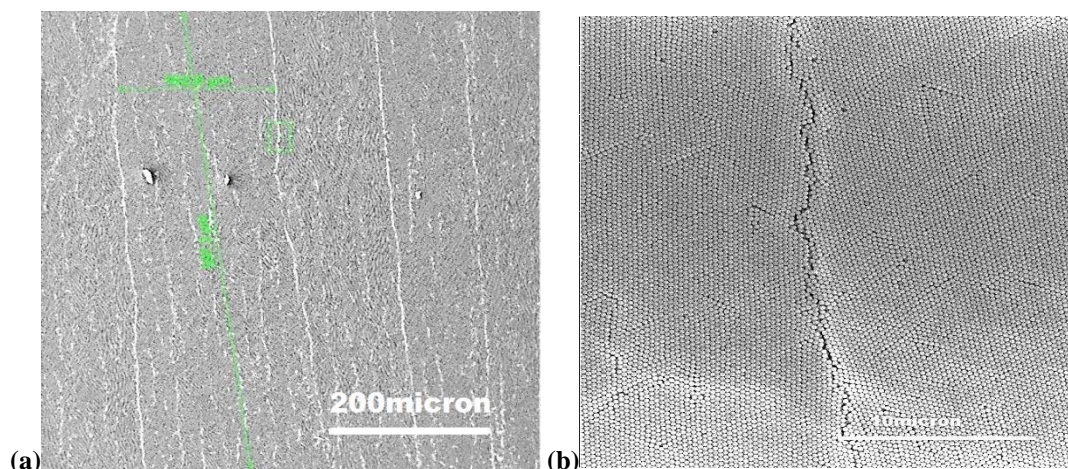


Figure 7.1(a&b). Digital camera images of a typical 75 x 25mm film taken at 2 different tilt angles.

### 7.3 RESULTS

On inspection, by electron microscopy (Figure 7.2a & b), of a number of films made in this manner using a variety of different concentrations, were found to be virtually crack-free. Apparent cracks in the film, seen as near vertical lines by optical microscopy, are shown to be domain boundaries in the SEM images. Also, in the

horizontal direction there were no cracks over the full vertical length of these film, covering a distance of up to 25mm.



**Figure 7.2. (a) SEM image of vertical lines seen in a typical film. (average spacing is approximately 200 $\mu$ m); (b) SEM image shows that the vertical lines are boundaries between differently orientated domains.**

Appendix A gives a detailed optical and electron microscopy analysis of the vertical lines seen in these films. The main observations here are that these domain boundaries are very narrow, nominally less than the diameter of the particles themselves, and join at a line of irregular packing between one domain orientation and another, unlike drying cracks which are generally quite broad ( $>$ particle diameters) and jigsaw-like. McLachlan [4] found vertical cracks to be nearly 5 $\mu$ m wide, and horizontal cracks were  $<1\ \mu$ m, whilst Wong, Kitaev and Ozin [6] state that typical micro-cracks range from a fraction of, to greater than a sphere diameter; with different crystal domains being irregularly shaped. Adjacent crystal domains often fit like pieces of a jigsaw puzzle, indicating that the cracks were formed after the spheres had ordered themselves. Cracks are therefore a result of stress during the drying of a crystal [5], and particle orientation across a drying crack would normally be the same. Assuming that these

samples are free from cracks, but that domains are only separated by very narrow disordered boundaries, their thicknesses were measured at various points in the y-direction (vertical) from the start of film growth, in order to establish a film thickness that could be produced whilst the film remains crack-free. Table 7.1 gives the thicknesses of the film produced in this manner. A colour coded key for the four criteria of **(1) no cracks / domain boundaries only;** **(2) cracks starting to develop;** and **(3) cracks visible;** is used to identify the differences in cracking across these films, examples of which are given in Appendix A, figure 8 (a-c).

**Table 7.1 HORIZONTAL HELD SAMPLES: KEW30 (280nm), concentration (as specified), temp (50°C unless specified), tilt (0° i.e. vertical), (200ml in 500ml beaker)**

SAMPLE	SEM (layers)	5mm	10mm	16mm
<b>By Volume %</b>				
<b>0.25v%</b>	7-9	(1) no cracks / domain boundaries only	(1)	(1)
<b>0.45v%</b>	4-6	(1)	(1)	(1)
<b>0.5v%</b>	12-13	(1)	(1)	(1)
<b>0.6v%</b>	9-15	(1)	(1)	(1)
<b>0.75v%</b>	11/12	(1)	(1)	(1)
<b>1.0v%</b>	12	(1)	(1)	(1)
<b>2.0v%</b>	22	(1)	(1)	(2) starting to develop
<b>By Temperature</b>				
<b>0.5v% / 50° (as above)</b>	12-13	(1)	(1)	(1)
<b>0.5v% / 55°</b>	3	(1)	(1)	(1)
<b>0.5 v% / 60°</b>	6-8	(1)	(1)	(1)
<b>0.5 v% / 65°</b>	5-11	(1)	(1)	(1)
<b>0.5 v% / 70°</b>	4-6	(1)	(1)	(1)
<b>OTHERS</b>				
<b>1.0v% / 70°</b>	(FP=6)*	(1)	(1)	(1)
<b>1.5 v% / 55°</b>	(FP=10)*	(1)	(1)	(1)
<b>1.0 v% / 60° +MMA</b>	15-18	(1)	(1)	(1)
<b>1.5 v% / 55° +MMA</b>	(FP=10)*	(1)	(1)	(1)

\*= Number of layers calculated from the F-P fringes on the optical spectra

Further films made in a similar manner were used to establish the thickness at which cracking occurs. These samples were made with increasing concentrations to produce



thicker films [5-9], and by increasing the tilt angles, to produce thicker films [10]. In each case the criteria given in Appendix A, figure 8 (a-c) was again used to establish the point of cracking. The results from which are given in tables 7.2 & 7.3, and graphically illustrated in Figures 7.3 & 7.4.

**Table 7.2. SAMPLES MADE WITH VARYING VOL% CONCENTRATION: at 55°C, 15° tilt, (100ml in 200ml beaker) except 0.6v%, (50°C, 15° tilt (300ml in 500ml beaker)).**

<b>SAMPLE Distance from start of film</b>	<b>0.2v% (no. layers / key code)</b>	<b>0.25v% (no. layers / key code)</b>	<b>0.3v% (no. layers / key code)</b>	<b>0.5v% (no. layers / key code)</b>	<b>0.6v% (no. layers / key code)</b>
<b>5mm</b>	7 layers = (1)	18 layers = (1)	16 layers = (1)	27 layers = (2)	50 layers = (2)
<b>10mm</b>	8 layers = (1)	22 layers = (1)	20 layers = (1)	45 layers = (3)	60 layers = (3)
<b>16mm</b>	10 layers = (1)	30 layers = (1)	35 layers = (2)	55 layers = (3)	88 layers = (3)
<b>26mm</b>		32 layers = (2)	43 layers = (3)	52 layers = (3)	73 layers = (3)
<b>32mm</b>		39 layers = (3)			

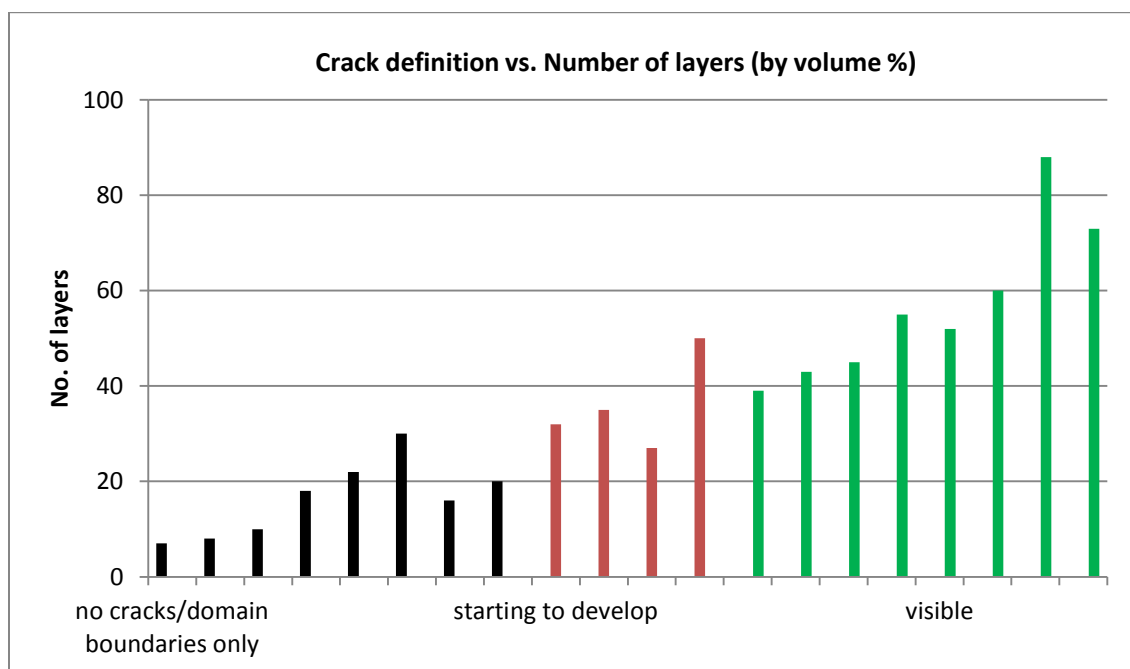


**Figure 7.3. Graphical representation of the crack definition vs. number of layers, of the samples in Table 7.2.**

**Table 7.3. TILT ANGLE SAMPLES: 0.6v%, 50°C (200ml in 500ml beaker)**

SAMPLE Distance from start of film	0° tilt (layers)	10° tilt (layers)	15° tilt (layers)	20° tilt (layers)
5mm	14 layers = (1)	16 layers = (1)	21 layers = (1)	50 layers = (3)
7mm			32 layers = (2)	
10mm	18 layers = (1)	22 layers = (1)	50 layers = (3)	70 layers = (3)
16mm	20 layers = (2)	26 layers = (2)	90 layers = (3)	90 layers = (3)

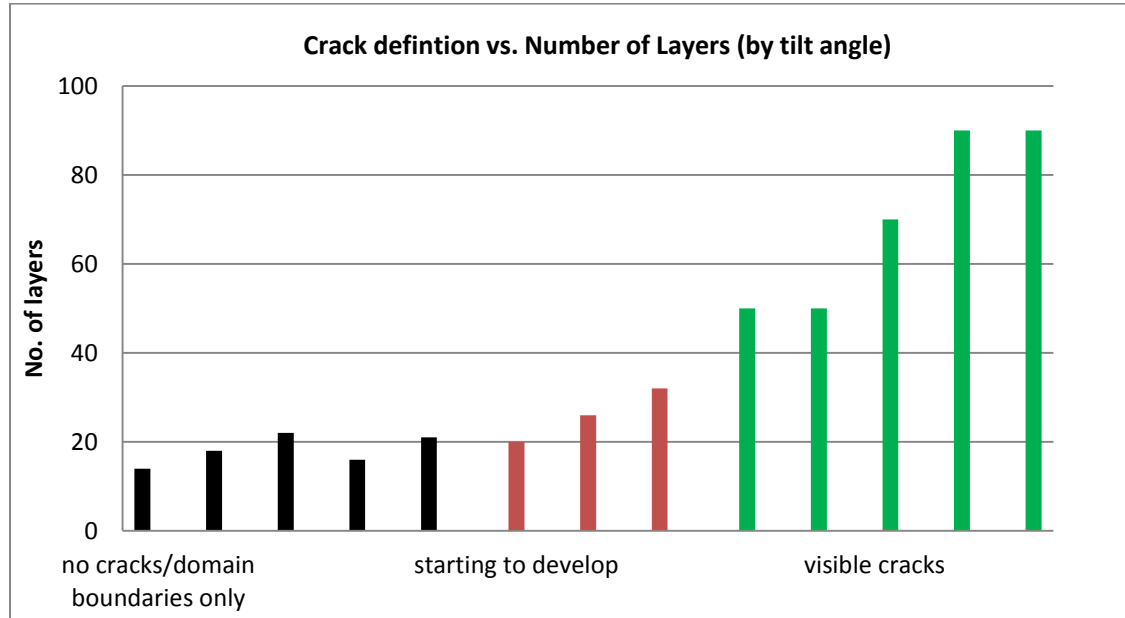


**Figure 7.4. Graphical representation of the crack definition vs number of layers, of the samples in Table 7.3.**

**Table 7.4. Summary of samples measured in tables 6.1, 6.2 & 6.3.**

	MIN-MAX NUMBER OF LAYERS			
	HORIZONTAL SAMPLES	BY VOL%	BY TILT ANGLE	ALL SAMPLES
NO CRACKS / DOMAIN BOUNDARIES ONLY	3-18	7-30	14-22	3-30
STARTING TO DEVELOP	22	27-50	26-32	22-50
VISIBLE		39-88	50-90	39-90

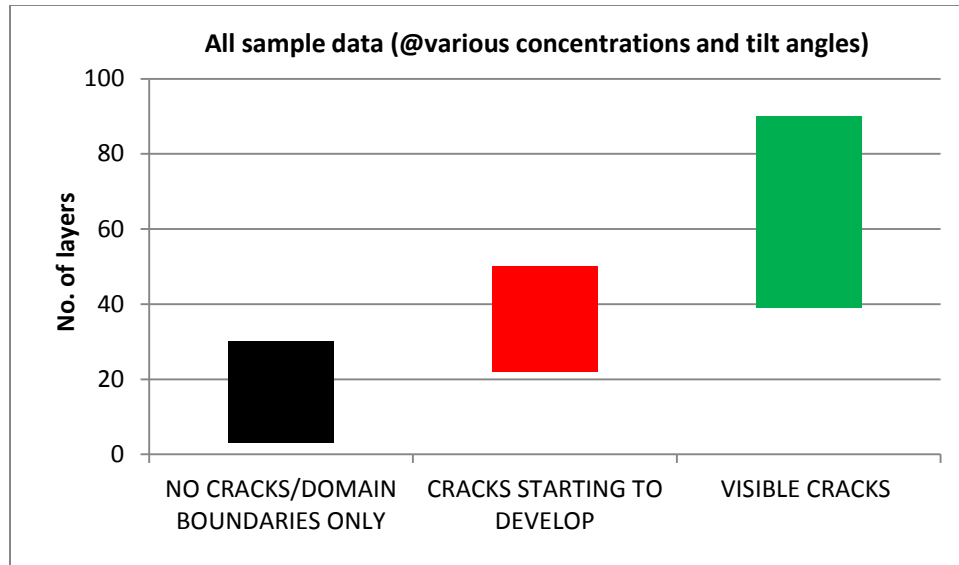


**Figure 7.5. Summary representation of the crack definition vs number of layers of the samples in Table 7.3.**

A number of other samples with different particle sizes (250, 360nm and 410nm) were made by the same method, at 50°C, slight tilt angle (<20°), 0.6v% in a 200ml suspension, in a 500ml beaker, with an ethanol to water ratio of 3:1. These show similar crack patterns to the 280nm films examined above, (Table 7.5). Optical microscopy and SEM analysis of the 360nm sample is also given in Appendix A (figures 9-11).

**Table 7.5. OTHER HORIZONTALLY POSITIONED SAMPLES: 0.6v%, 50°C (200ml in 500ml beaker).**

SAMPLE	250nm	360nm	410nm
5mm	14 layers = (1)	6 layers = (1)	11 layers = (1)
10mm	20 layers = (1)	6 layers = (1)	11 layers = (1)
16mm	32 layers = (2)	6 layers = (1)	14 layers = (1)
20mm	44 layers = (3)		

## 7.4 DISCUSSION

Shorlin et al. [11] and Hartsuiker and Vos [5] investigated the differences in domain shape during drying of colloidal films. They indicate that different drying mechanisms are occurring during film manufacture: irregularly shaped domains occurring during isotropic drying (usually seen at the start of film growth), whereas rectangular shaped domains (usually accompanied by large vertical cracks) are a sign of directional drying. Large rectangular shaped domains suggest that directional drying is occurring throughout the production of the above films, where large vertical domains are formed starting from the top of the sample (figure 7.6), progressing for up to 25mm in these cases. Chiu et al. [12] state that for films that are dried below their critical film thickness, a fracture front is absent and the film dries without cracking. Goehring, Clegg and Routh [13] describe four distinct drying fronts in directionally dried suspensions: an ordering front; an aggregation front; a fracture front; and a pore-emptying front. If drying films are able to be held within the region of aggregation, and are not grown beyond a critical thickness, then the film will remain crack free. This appears to be the case within the above films. However, when the thickness reaches approximately 20 layers then cracks do begin to develop. The disorganised domain boundaries may also provide a stress relieving zone also aiding the prevention of cracking in these films. Average distances between domain boundaries are typically approximately 100 $\mu\text{m}$ , but can be as much as 250 $\mu\text{m}$  and the areas separating domains are visible to the naked eye.

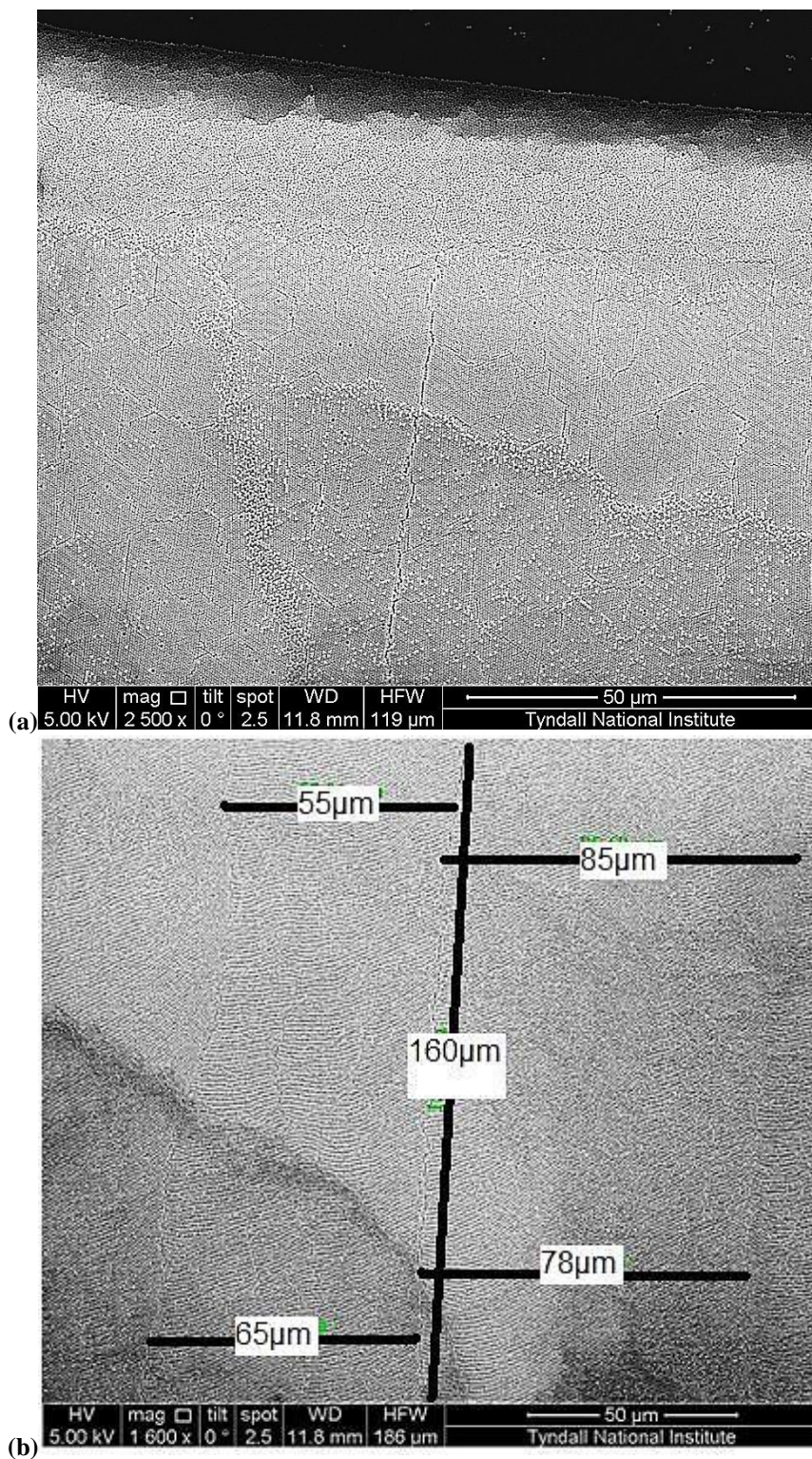
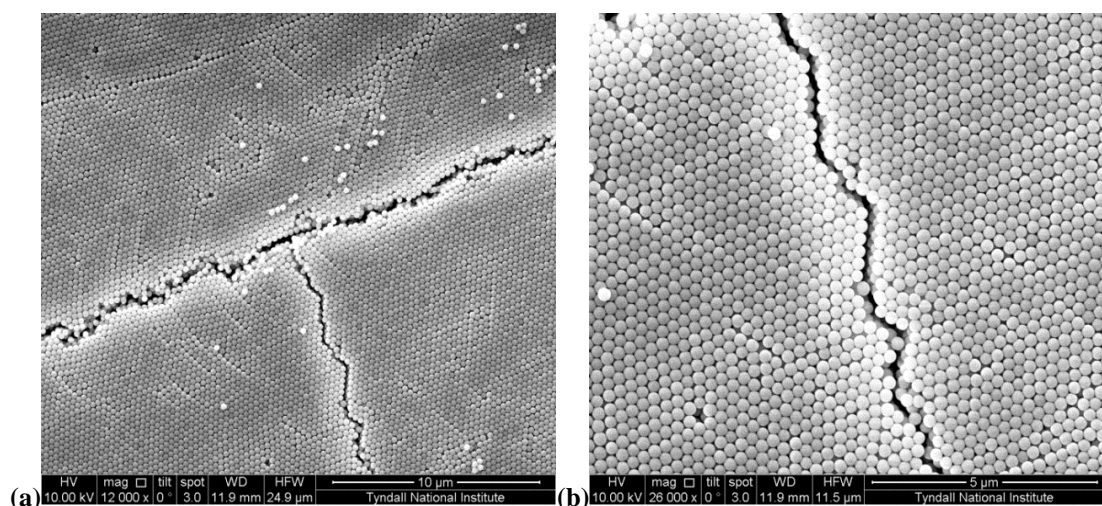


Figure 7.6. (a) Directional drying appears to occur right at the start of the film, and a domain boundary is established early in the film structure; (b) the domain boundary continues throughout the vertical length of the film, and separates areas of differing Moiré fringes, with domain widths generally 50-100 $\mu$ m across (in this case).

In some cases varied colours are seen in these films with the naked eye. In these cases it is often that the film exhibits different particle orientations either side of a domain boundary. This type of effect was most prominent in the larger particle films (e.g. 410nm film) and is explored in more detail in Appendix A (figure 13-14).

As can be seen from figures 7.1, 7.2, 7.6 and Appendix A (figures 3-6), within these films using 250 and 360nm silica particles, vertically orientated domain boundaries are observed, which develop right from the start of film growth, and progress for up to 25mm (provided the film thickness does not exceed a critical value of approximately 20 layers). These domain boundaries are quite different to the usual jigsaw-like crack features seen in colloidal crystalline films (figure 7.7) [5, 14, 15] and the distance across the domain boundaries are very small, (approaching zero nm in disordered boundaries), and usually less than the size of the particles in the films.



**Figure 7.7. Jigsaw-like cracks (a) and (b): distance between particles across the crack is approximately 250nm (approximately equal size of particles).**



These films also show Moiré fringes over very large areas. Appendix A, (figure 10) shows a typical area of Moiré fringes which is crack free over an area  $300\mu\text{m} \times 300\mu\text{m}$ . Li and co-workers [16] state that long range ordering is visible as Moiré patterns in low magnification SEM images, and this is clearly the case in these samples. It is difficult to show clear images of the full scale of particle ordering and the crack free dimensions in a single image; however these images showing Moiré fringe patterns over large areas are perhaps the best representation of the large scale ordering within these samples. However, the Moiré fringes are generally only visible in the SEM images at 500x to 1000x magnification range, and are therefore limited in revealing the full extent of the large areas under examination in this study.

High quality films were made by the method described above using a mixed solvent silica particle suspensions, (75% ethanol: 25% water). Figure 7.8 shows the quality that can be achieved. Here the maximum reflectance peak at  $\theta = 10^\circ$ , was 74.5% at 648nm, and the FWHM was 44.3nm. Therefore the fractional bandwidth,  $\Delta\lambda/\lambda_{\text{max}} = 0.068$ . This value closely matches the fractional bandwidth values achieved by Ko and Shin [17] using a dip coating method, and agrees with the theoretical minimum value calculated for a fcc structure. The well-defined Fabry-Pérot fringes in the spectra, on both sides of the stop band also give an indication of the high quality of crystalline film [9]. These fringes indicate the uniformity of the thickness and the similarity of orientation of the colloidal crystal film.

The high quality of this film is also demonstrated by the highly ordered stacking of the particles seen in the cleaved edge SEM image (figure 7.8b).

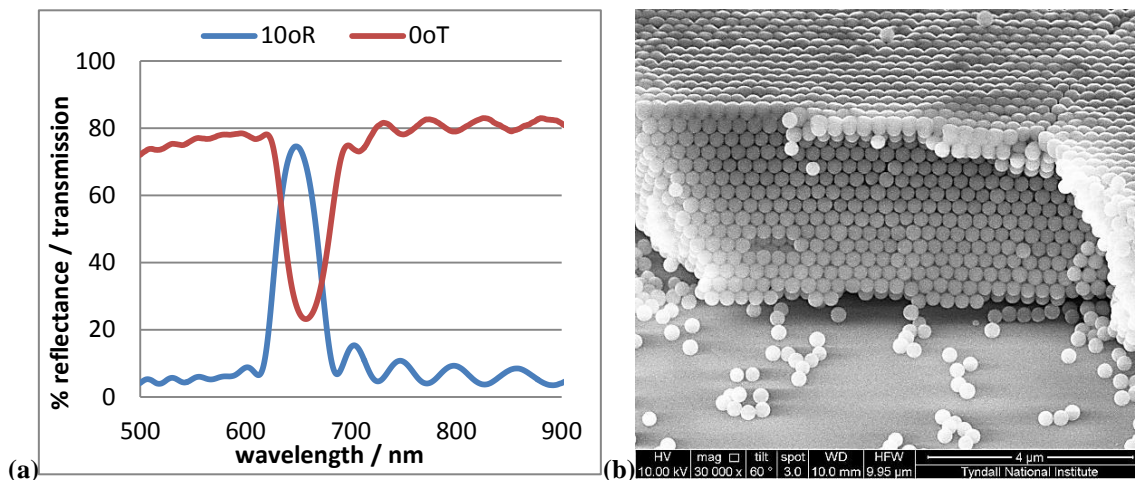


**Figure 7.8. (a) High quality visible spectra of a film made of approximately 16 layers (calculated from the F-P fringes) & (b) SEM image of cleaved edge showing 16 layers.**

The azeotropic point of an ethanol water mix is 95.6% ethanol [18]. When a 75%:25% mix of ethanol:water evaporates, more ethanol than water evaporates (progressing towards the azeotropic point). Therefore initially a greater concentration of water would remain behind in the drying area as the ethanol evaporates preferentially, i.e. more water remains in the pores of the growing film, which would slow down the rate of drying in this area.

A second effect could be the creation of a difference in the water and ethanol concentrations in the aggregation front, inducing a Marangoni (“tears of wine”) flow into this area [19, 20] with ethanol from the bulk suspension migrating into the drying region. This is observed visually, the growing film being nearly invisible to the naked



eye in this area, as the refractive indices of ethanol:water and the KEW30 particles are closely matched, approximately 1.36 and 1.41 respectively.

Therefore, not only is drying slowed down in the formed film, initially by residual water in the voids, but perhaps also by a “secondary drying” effect as ethanol is then being dragged into these areas again (keeping the film wet after initial formation). This “double drying” could reduce the stresses in the film during drying and therefore may be responsible for the very large crack free areas seen in these films, (up to a critical film thickness, of approximately 20 layers in this case (280nm particles)), which is more than enough for the complete photonic band structure to develop [21].

Stronger Marangoni effects are seen in samples at 60% ethanol 40% water producing irregular drying of the films in the initial stages, perhaps because the Marangoni effect is able to drag the particles up the surface of the slide (Appendix A: figure 2) and therefore this solvent mixture cannot be used to produce high quality crystalline films.

Films made from 360nm silica particles, made in the same manner as above, possess similar crack free results. In this case optical microscope and SEM images (Appendix A: figures 10-11) show a film of even thickness, 6 layers throughout the film.

Films made from 410nm silica particles show varied colours (usually 2 colours) to the naked eye within the film. These films exhibit different particle orientations either side of a domain boundary. Here, dislocations either side of domain boundaries, appear

to take on preferred orientations, i.e. slanting in a left-to-right \ orientation on left side, and slanting in a right-to-left / orientation on right side, in the SEM images (Appendix A: figure 13 a-c & e). This is more easily observed in the tilted SEM images (c & e). The slant direction changes either side of the next boundary (Appendix A: figure 13 d). Line dislocations seen within the domains tend to be broader in the 410nm film compared to films made from smaller particles, so these particle orientation effects become more visible.

Therefore different particle ordering orientations from one side of a domain boundary to the other produces a polycrystalline film, giving rise to the different observed colours from one side of the boundary to the other. This can also be observed in the optical spectra ( $0^\circ$  and  $20^\circ$  transmission curves are shown in Appendix A: figure 14 a & b). The  $0^\circ$  transmission curves are nearly identical (a single colour is observed by the naked eye across the sample at this angle), and the number of layers calculated from their F-P fringes indicate that the two areas are of the same thickness. However, at  $20^\circ$  transmission, secondary transmission dips in the “green” curve give rise to a different observed colour, even though the Bragg peak remains identical to that of the “blue” curve, (approximately 900nm at  $20^\circ$  transmission). Yoldi et al. [3] state that different colours can often be seen in optical transmission microscopy at low magnifications, even for the same number of layers. They propose that different structures may exist: ABCABC (face centred cubic) packing, ABABAB (hexagonal close packing) packing, or ABCBA (random hexagonal close packing) packing, which are not easy to distinguish between. Mishchenko et al. [22] using templated substrates were able to see

a single colour in their inverse opal structure, indicating that all domains in their crystal had a uniform orientation, whereas assembly of a direct opal gave multi-coloured optical images. However, here we see just two coloured domains (bi-crystalline), and therefore the use of a similar triangular template structure to that of Mishchenko et al. may aid in the production of a single, uniform domain, when using the mixed solvent approach here.

The growth of a film can be drawn schematically (Appendix A: figure 15). Each domain starts from a nucleation point, and domains then orientate themselves from this point downwards in the growth direction. Domain boundaries occur when two separately nucleated domains begin to overlap. If the orientation of adjacent domains is the same then the two domains may merge to create one wider domain, or a boundary may occur between them and they would appear different in colour at higher angles of observation.

## **7.5 CONCLUSIONS & FURTHER WORK**

- Controlled evaporation can be used as a method for growing large area crack-free films, 75mm x 25mm, by using a mixed solvent approach.
- Film thickness variations can be reduced with a shortened vertical dimension, and by maintaining a near vertical substrate during growth.

- Increasing the vertical dimension of films grown by controlled evaporation should be possible, but two factors will begin to compete with each other with the increased time requirements: those of increasing film thickness; and sedimentation over the longer periods. Further work should be undertaken to establish a limit to the vertical dimensions possible, but keeping the film within a specified thickness variation.
- Addition of a relatively small percent (25%) of water into an ethanolic silica particle suspension can increase the quality of the opal film, but only up to a certain point. Further additions results in decreasing film quality.
- In mixed solvent suspensions, Marangoni effects at the meniscus / solidification front may allow the opal film to dry more slowly, thus preventing cracking.
- A theoretical growth model has been constructed for these mixed solvent deposition films, which takes into account the contrasting particle orientations between adjacent growing domains, (Appendix A: figure 15).
- Further work should investigated the use of templates to form single uniform domain colloidal crystals by this mixed solvent approach over large areas, 75mm x 25mm and 4-inch wafers.

## REFERENCES:

1. Wang, J., C.W. Yuan, and F.Q. Tang, *Self-assembling three-dimensional colloidal photonic crystal multilayers from aqueous ethanol mixture solutions*. Chinese Physics, 2005. **14**(8): p. 1581-1584.
2. Li, H.L. and F. Marlow, *Solvent effects in colloidal crystal deposition*. Chemistry of Materials, 2006. **18**(7): p. 1803-1810.
3. Yoldi, M., et al., *On the parameters influencing the deposition of polystyrene colloidal crystals*. Materials Science & Engineering C-Biomimetic and Supramolecular Systems, 2008. **28**(7): p. 1038-1043.
4. McLachlan, M.A., et al., *Thin film photonic crystals: synthesis and characterisation*. Journal of Materials Chemistry, 2004. **14**(2): p. 144-150.
5. Hartsuiker, A. and W.L. Vos, *Structural properties of opals grown with vertical controlled drying*. Langmuir, 2008. **24**(9): p. 4670-4675.
6. Wong, S., V. Kitaev, and G.A. Ozin, *Colloidal crystal films: Advances in universality and perfection*. Journal of the American Chemical Society, 2003. **125**(50): p. 15589-15598.
7. Kuai, S.L., et al., *High-quality colloidal photonic crystals obtained by optimizing growth parameters in a vertical deposition technique*. Journal of Crystal Growth, 2004. **267**(1-2): p. 317-324.
8. Jiang, P., et al., *Single-crystal colloidal multilayers of controlled thickness*. Chemistry of Materials, 1999. **11**(8): p. 2132-2140.

9. Li, J.A. and Y.C. Han, *Optical intensity gradient by colloidal photonic crystals with a graded thickness distribution*. Langmuir, 2006. **22**(4): p. 1885-1890.
10. Im, S.H., M.H. Kim, and O.O. Park, *Thickness control of colloidal crystals with a substrate dipped at a tilted angle into a colloidal suspension*. Chemistry of Materials, 2003. **15**(9): p. 1797-1802.
11. Shorlin, K.A., et al., *Development and geometry of isotropic and directional shrinkage-crack patterns*. Physical Review E, 2000. **61**(6): p. 6950-6957.
12. Chiu, R.C., T.J. Garino, and M.J. Cima, *Drying of Granular Ceramic Films: I, Effect of Processing Variables on Cracking Behavior*. Journal of the American Ceramic Society, 1993. **76**(9): p. 2257-2264.
13. Goehring, L., W.J. Clegg, and A.F. Routh, *Solidification and Ordering during Directional Drying of a Colloidal Dispersion*. Langmuir, 2010. **26**(12): p. 9269-9275.
14. Galisteo-Lopez, J.F., et al., *Optical study of the pseudogap in thickness and orientation controlled artificial opals*. Physical Review B, 2003. **68**(11).
15. Teh, L.K., et al., *Growth imperfections in three-dimensional colloidal self-assembly*. Applied Physics a-Materials Science & Processing, 2005. **81**(7): p. 1399-1404.
16. Li, W., B. Yang, and D. Wang, *Fabrication of Colloidal Crystals with Defined and Complex Structures via Layer-by-Layer Transfer*. Langmuir, 2008. **24**(23): p. 13772-13775.

17. Ko, Y.G. and D.H. Shin, *Effects of liquid bridge between colloidal spheres and evaporation temperature on fabrication of colloidal multilayers*. Journal of Physical Chemistry B, 2007. **111**(7): p. 1545-1551.
18. <http://en.wikipedia.org/wiki/Ethanol>
19. Fournier, J.B. and A.M. Cazabat, *Tears Of Wine*. Europhysics Letters, 1992. **20**(6): p. 517-522.
20. Vuilleumier, R., et al., *Tears Of Wine - The Stationary State*. Langmuir, 1995. **11**(10): p. 4117-4121.
21. Bertone, J.F., et al., *Thickness dependence of the optical properties of ordered silica-air and air-polymer photonic crystals*. Physical Review Letters, 1999. **83**(2): p. 300-303.
22. Mishchenko, L., et al., *Patterning Hierarchy in Direct and Inverse Opal Crystals*. Small, 2012. **8**(12): p. 1904-1911.

# **CHAPTER 8.**

## **FAST FOURIER TRANSFORMS AND SURFACE** **QUALITY ASSESSMENT**

### **8.1 INTRODUCTION.**

The quality of the crystalline ordering in colloidal films is often shown by Fast Fourier Transform (FFT) images taken from an original SEM of ordered particles. The original SEM images usually show a relatively large area top surface image of particle ordering, and the dot patterns of the FFT images are described as “illustrating the long range order of the crystal” [1], or “these regular microstructures were also assessed by Fourier transform analysis of the corresponding SEM images and the sharp peaks confirm the presence of long-range crystalline order” [2].

Colvin et al. [3] assessed film ordering over long ranges, centimetres, by comparing SEM micrographs of  $40\mu\text{m}^2$  areas collected as a sequence over their samples. They suggested that if the FFT dot patterns were aligned between these images, this would show single domain structures over these lengths. Also FFT images could be used to confirm poor quality structures e.g. in 2 samples with differing size distributions, the sample with a narrower size distribution would show sharper peaks in the FFT image,



while the more disperse sample, would show weaker points, or even rings in the FFT image.

Khunsin and co-workers [4] characterized the ordering of spheres in the (111) lattice using the magnitudes of the harmonics in FFT patterns from SEM images, the FFT points representing harmonics of the periodic structure in the SEM image. They compared the magnitude of the 1st harmonic in order to estimate the regularity of the sphere spacing, and the rate of decrease in magnitude of the 2<sup>nd</sup> and 3<sup>rd</sup> harmonics, taken from a line drawn across the pattern points (Figure 8.1a). Thus by comparing the magnitudes of the 1<sup>st</sup>, 2<sup>nd</sup> and 3<sup>rd</sup> harmonics of different FFT patterns it was possible to judge which lattices were more ordered. They also noted that cracks in the opal film do not strongly affect the lattice spacing, but lead to a decrease in magnitude of the higher harmonics in the FFT pattern.

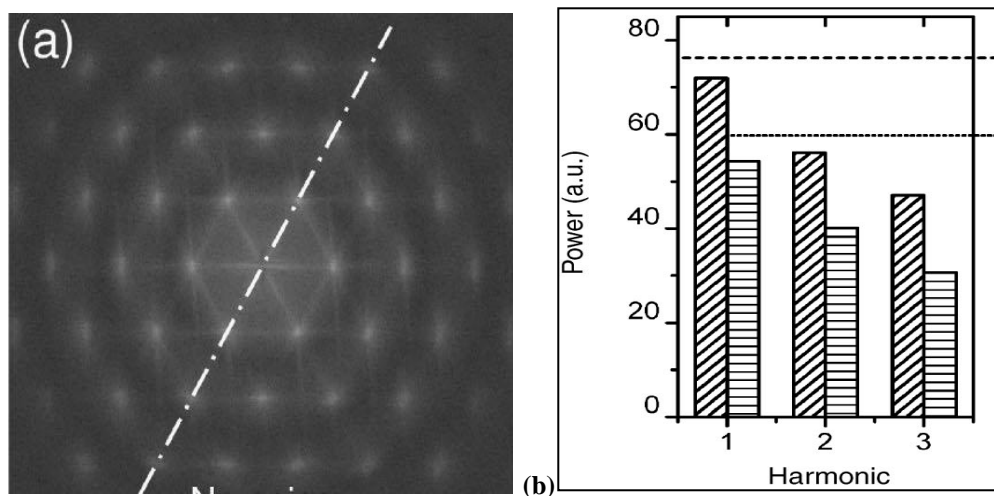


**Figure 8.1.** (a) Typical FFT pattern of an well-ordered film. (b) Shows the magnitudes of the first three harmonics in the FFT pattern shown in (a) (adapted from [4]).

In this study, a different approach has been taken, in that a number a widely spaced SEM images have been taken from each sample. The FFT images are then plotted as brightness against distance from central peak analysed using imageJ software. Comparisons were made between samples, at various temperatures, and from samples made by differing manufacture methods. The standardised method used in this study is given below:

1. 5 SEM images were taken 1mm apart, each at 20,000x magnification
2. Using imageJ software, 'Set Scale' to that of the SEM image scale bar
3. Select the full area of the image, equivalent to 14.5 $\mu$ m x 12.5 $\mu$ m (such that characterised areas contain an approximate equal number of particles)
4. Using imageJ take an FFT plot from this area
5. Adjust the Brightness & Contrast to standard settings (100 to 200)
6. Select the full area of the FFT image
7. Select 'Analyse', and 'Plot Profile'
8. Repeat for all 5 SEM images
9. Adjust the tabled values to align all central peaks when plotting data
10. Plot the 5 FFT profiles, and the average FFT profile
11. Record peak heights and distances of each side peak (-4 to +4) (Figure 8.2 below)

---

*NOTE 1: All SEM images must be taken using the same pixel imaging ratios otherwise direct comparison of results cannot be undertaken by this procedure.*

*NOTE 2: All SEM images must have approximately the same focussed clarity; otherwise direct comparison of results is compromised.*

*NOTE 3: All SEM images were taken from films using a single batch of silica particles, KEW30 (280nm) such that all films are standardised.*

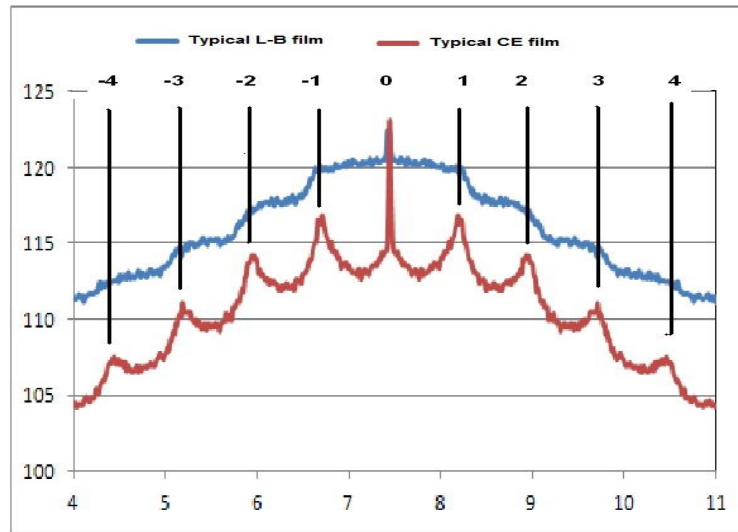


**Figure 8.2. Typical FFT profiles from SEM images of a Langmuir-Blodgett (L-B) film and a Controlled Evaporation deposition (CE) film.**

Record the position of each peak, and calculate the difference in distance between:

- (0-(-1)) and (1-0)
- (0-(-2)) and (2-0)
- (0-(-3)) and (3-0)
- (0-(-4)) and (4-0)

Calculate the average of the 4 “peak-to-peak distance” values for each of the five SEM images, (i.e. the average of 20 points).

Record the height of each peak, and calculate the difference in peak heights between:

- (0-(-1)) and (1-0)
- (0-(-2)) and (2-0)
- (0-(-3)) and (3-0)
- (0-(-4)) and (4-0)

Calculate the average of the 4 “peak height-to-peak height” values for each of the five SEM images, (i.e. the average of 20 points).

Therefore the symmetry of the FFT profile plots is calculated for each set of five SEM images with respect to the positions of the spacing between peaks, and the differences between peak heights, either side of the central peak. Highly symmetrical profiles give low calculated values, and indicate the highest quality particle ordering in the films.

## **8.2 RESULTS AND DISCUSSION.**

Khunsin and co-workers [4] presented a quantitative comparison of different samples, assuming the same brightness and contrast of the images and taking into account the areas contain an equal number of particles in the sampled area. They state that their analysis is therefore able to provide guidelines for experimental work on the optimization of crystallization conditions. Here the brightness and contrast of the FFT image are pre-selected prior to evaluation, and the sample areas are taken from the same size areas (x5 images), therefore the number of particles should be approximately equivalent throughout. Where this method differs from that of Khunsin et al. [4], is that rather than analysing a line drawn across the FFT pattern (Figure 8.1a), this method analyses all the points in the FFT image, and averages them out over a numbers of SEM images. An averaged grey scale intensity is then analysed for symmetry around the

central peak. A symmetrical FFT pattern, with regard to intensity of the pattern, would indicate lattices of greater order.

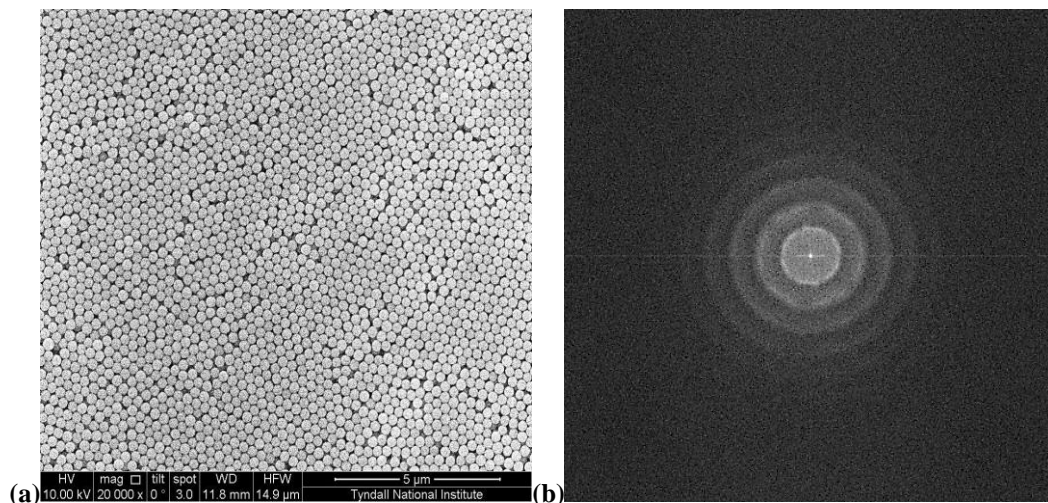


**Figure 8.3: Typical SEM of L-B sample (thickness of 5 layers) & its corresponding FFT image**

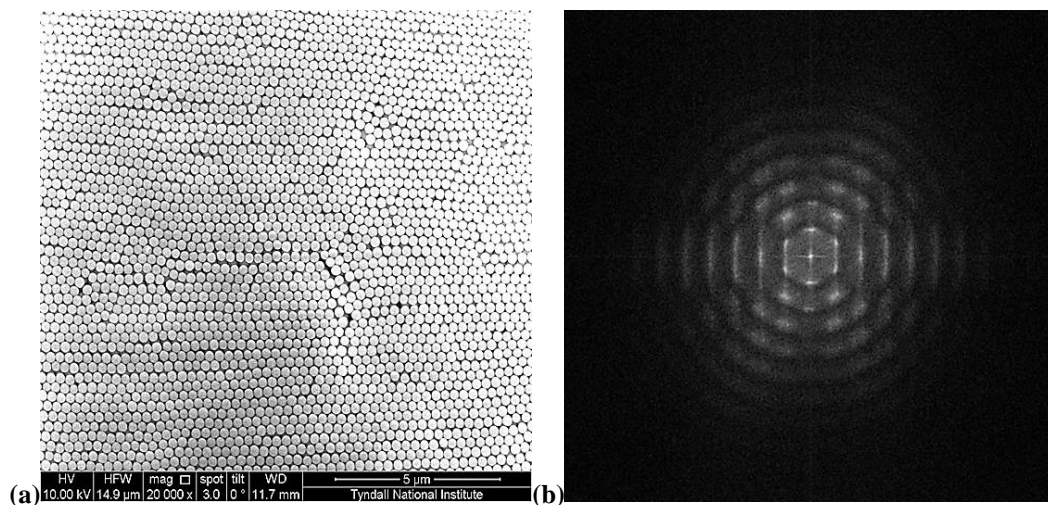


**Figure 8.4: Typical SEM of CE sample (0.5v% @ 60°C), from a sample having 5 layers at the image position, & (b) its corresponding FFT image**

Figures 8.3 and 8.4 give typical SEM images and FFT images taken from two samples; an L-B film surface, and a controlled evaporation (CE) film surface respectively. Visually it is easy to see the differences between the two surfaces, and between the two FFT images. However, when the images are not so different, is it

possible to ascertain which film has the highest degree of ordering of particles at the surface? The two graphs below (Figure 8.5a&b) are plotted from samples discussed in chapter 7 (and recorded in table 7.1), along with a number of samples made by the L-B method. These were used in the assessment of the quality of the surface ordering from these two types of organised films, with respect to the symmetrical uniformity of their FFT profiles, as calculated by the above method. Smaller values in the plots arise from highly symmetrical FFT patterns, indicating the highest ordered films.

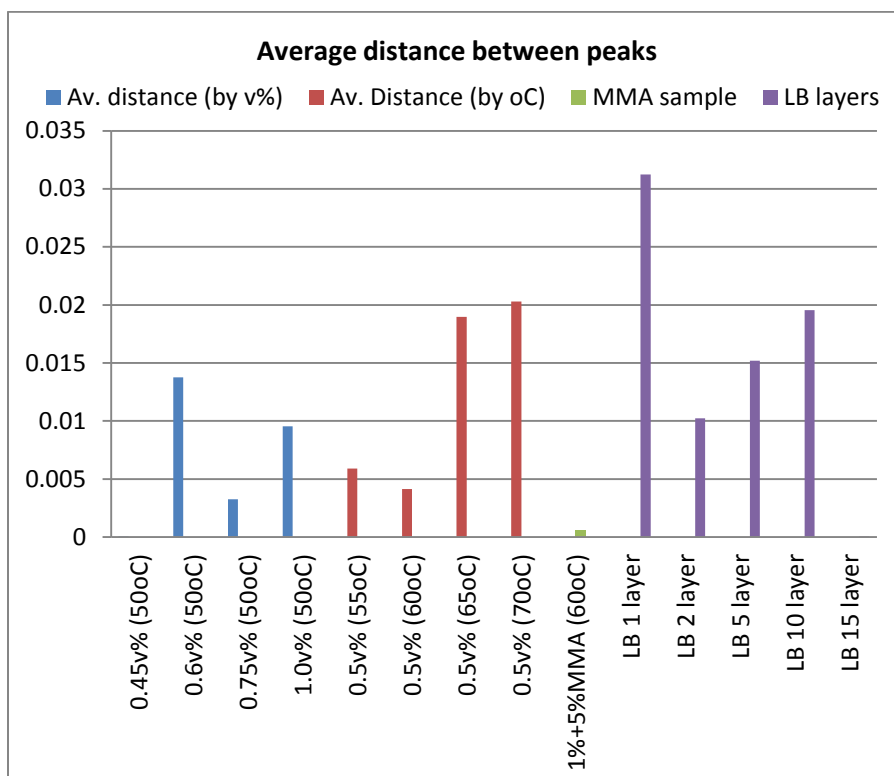
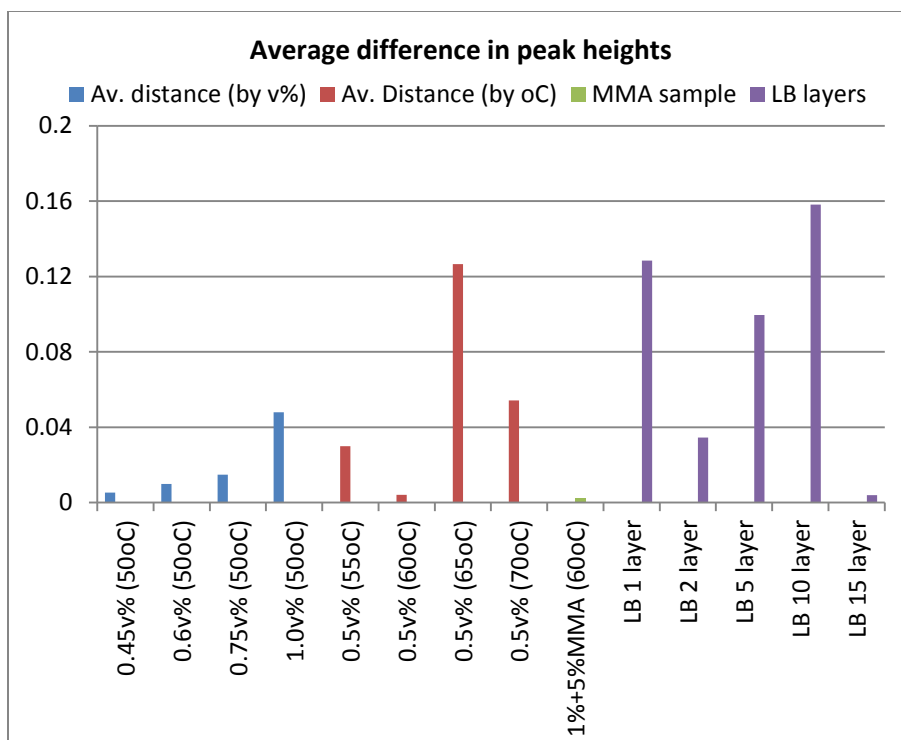


Figure 8.5(a) average difference between peaks



**Figure 8.5(b) average difference in peak heights.**

In general the two plots in figure 8.5 match relatively closely, with regard to the symmetry of FFT plots analysed by either the difference between the peaks, or by the difference in the peak heights, suggesting that the method gives an accurate assessment of the quality of surface ordering. In general, the Controlled Evaporation deposition films show greater quality of particle surface ordering than the L-B films, shown by the smaller calculated values. The degree of ordering decreases, in the CE films, as the temperature of evaporation is increased. This can also be seen from the original FFT profile plots versus temperature, shown in figure 8.6. While low temperatures promote slow assembly, they are costly in terms of time, and an optimised temperature needs to be established in terms of quality and production times. Above a critical temperature (approximately 60°C) the surface ordering of the Controlled Evaporation films reduces dramatically. This is because the particles have greater kinetic energy at higher

temperatures. Therefore the forces producing ordered structures at the meniscus are less significant than Brownian motion, and a poorly ordered film is obtained [5].

The growth rate of films produced from 3:1 ethanol : water solutions (from 200ml starting solutions in a 500ml beaker) was calculated at each temperature. At 50°C the growth rate was 0.3mm/hr, meaning a 25mm film required approximately 80 hours to complete growth, whereas at 60°C the growth rate was 0.55mm/hr, taking 45 hours to grow a 25mm film, i.e. nearly twice the speed of growth without loss of quality, making it a more viable production temperature.

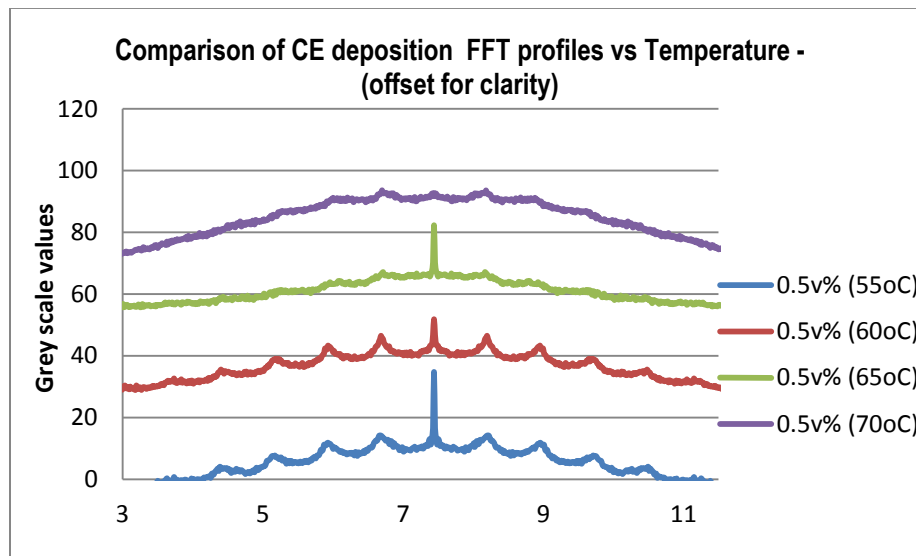


**Figure 8.6:** analysed data for Controlled Evaporation deposition films with increasing temperature (see also the data presented in Figure 8.5)

The very low values for the 15 layer L-B film indicating a highly ordered structure, is inconsistent with its SEM image (figure 8.7b). Visually the SEM image appears to have approximately similar ordering as the 10 layer L-B film (figure 8.7a), which gave a much higher value for both the difference between peaks, and heights



symmetry calculations (figures 8.5a & b). Here the spots in the FFT images are very diffuse, similar to those shown in figure 8.3b, and circular FFT patterns are observed. Picking out the “peak” or shoulder point in the profile curves is very difficult when FFT images are diffuse. In the case of the 15 layer L-B sample, the shoulders do not appear to be more symmetrical or distinctive than the 10 layer sample shown, figure 8.7c. In this method, for diffuse FFT “points” the identification of the shoulder position is operator dependant, (unless a peak is well defined), and therefore this raises questions as to the suitability of this method to establish the surface quality of L-B films.

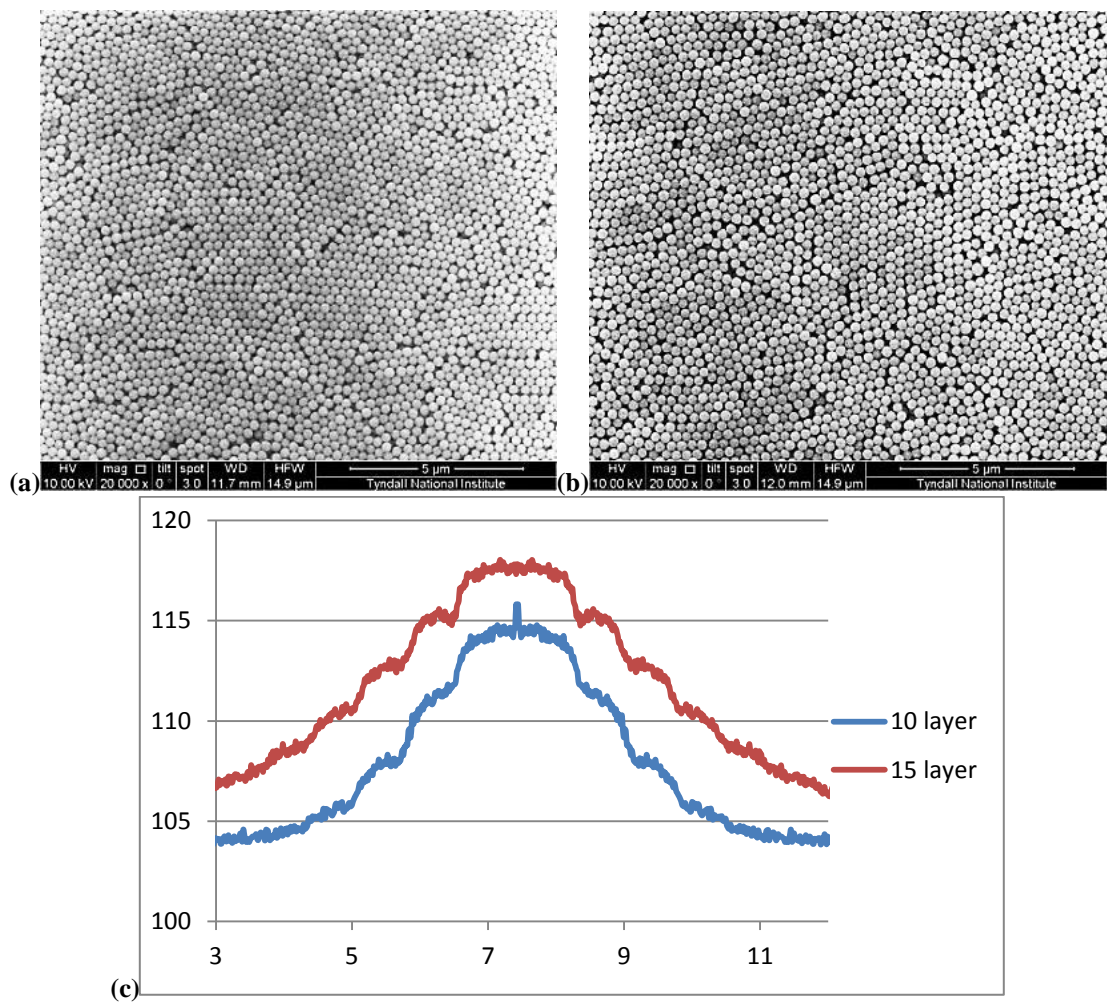


**Figure 8.7 (a) SEM image from a 10 layer L-B film, & (b) SEM image from a 15 layer L-B film & (c) FFT profile graph taken from the 15 layer L-B film.**

### 8.3 CONCLUSIONS

- An area method of grey scale symmetry, taken from the FFT spot intensities in FFT images, has been established to assess the surface particle ordering in opaline films.
- In general, the controlled evaporation films show higher quality surface ordering, than the L-B films, below a critical temperature (approximately 60°C).
- Increasing the temperature for controlled evaporation deposition increases particle energy, and leads to reduced ordering in the films. This is proven in these results.
- This quantitative method is not suitable for estimating the quality from diffuse FFT images, such as those established from L-B grown films.
- In the 3<sup>rd</sup> dimension (thickness) film quality cannot be assessed by this method; additional transmission and reflectance measurements, and FWHM calculations should be used for this purpose.

## REFERENCES:

1. Bertone, J.F., et al., *Thickness dependence of the optical properties of ordered silica-air and air-polymer photonic crystals*. Physical Review Letters, 1999. **83**(2): p. 300-303.
2. Cui, L., et al., *Fabrication of large-area patterned photonic crystals by ink-jet printing*. Journal of Materials Chemistry, 2009. **19**(31): p. 5499-5502.
3. Jiang, P., et al., *Single-crystal colloidal multilayers of controlled thickness*. Chemistry of Materials, 1999. **11**(8): p. 2132-2140.
4. Khunsin, W., et al., *Quantitative analysis of lattice ordering in thin film opal-based photonic crystals*. Advanced Functional Materials, 2008. **18**(17): p. 2471-2479.
5. Kuai, S.L., et al., *High-quality colloidal photonic crystals obtained by optimizing growth parameters in a vertical deposition technique*. Journal of Crystal Growth, 2004. **267**(1-2): p. 317-324.

# **CONCLUSIONS:**

A variety of self-assembly techniques have been investigated to produce large scale photonic crystal films from sub-micron particles. The work presented in this thesis assesses the long range order in these films and provides solutions to most of the issues involved in the fabrication of large area colloidal photonic crystal thin films on a scale equivalent to a 4-inch wafer. The ‘large-area’ methods developed include an improved sonication method, an under oil co-crystallization method and a controlled evaporation deposition method that employs co-deposition of adhesive binders using a mixed solvent approach. While each of the selected methods has their own advantages and disadvantages, all the methods were able to produce high quality large area, 75 x 25mm, films with reflection peaks >60%.

An improved sonication method was developed that exploits so-called Marangoni effects arising from the addition of small quantities of co-solvents during sonication are able to produce large area films rapidly (75 x 25mm in one hour). Whilst producing relatively uniform thickness films over the whole area, this method suffers from producing areas with different packing orientations.

Under oil crystallisation is known to produce large area films. This work has demonstrated that the addition of a silica binding agent facilitates the fabrication of more robust, ordered films. However, while this method is capable of forming films of

uniform thickness, the co-crystallisation method clearly needs further development in order to produce a uniform film over the entire areas required.

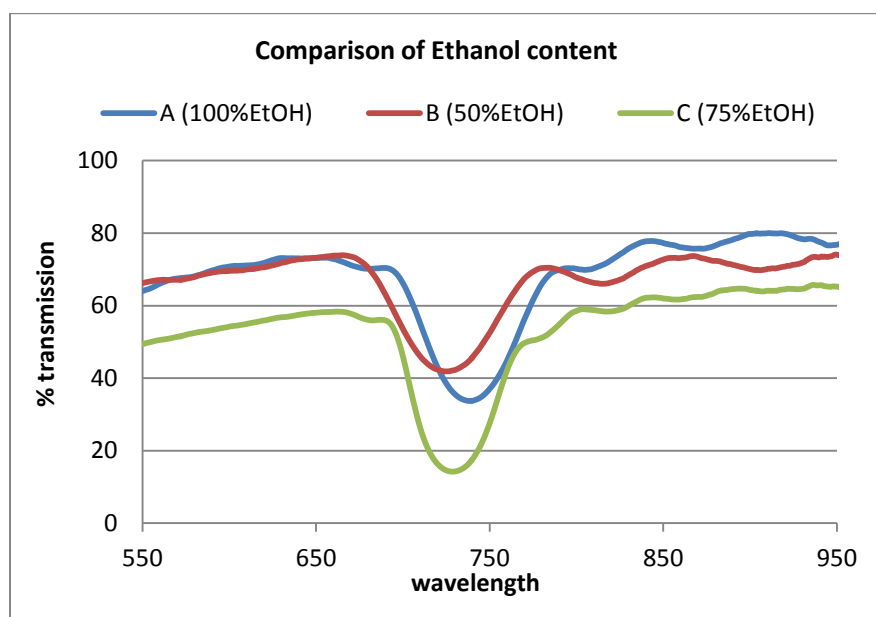
This work has demonstrated that controlled evaporation deposition using a mixed solvent suspension, presents the most promising method for the production of large area crack-free films. In this mixed solvent approach, film thickness variations are reduced with a shortened vertical dimension, and by maintaining a near vertical substrate during growth. Marangoni effects at the meniscus keep the film in the wet state longer, thus reducing the cracks that develop during the drying stage. These films are crack-free up to a critical thickness, and show very large domains. A theoretical growth model has been constructed for these mixed solvent deposition films, which takes into account contrasting particle orientations between adjacent domains. Colloidal photonic crystals produced by the mixed solvent approach, with added polymeric binders may be able produce flexible photonic films.

Using the fast Fourier transform (FFT) spot intensities an evaluation method has been developed to assess the surface particle ordering in colloidal films in a semi-quantitative manner. An area method of grey scale symmetry has been established to quantify the FFT profiles. Using this analytical method it has been shown that films made by controlled evaporation have higher surface ordering, than those made by the Langmuir-Blodgett method, and that high quality films can be produced up to a critical temperature (approximately 60°C), beyond which ordering is reduced because of higher particle energies.

Throughout this work, silica particles have been produced using a modified Stöber synthesis method. This modified method is a reliable method for the production of monodisperse particles, whereby particles can be produced to any required size, up to 600nm, using a simple one-step method.

# APPENDIX A.

## CRACK FREE ETHANOLIC FILMS BY CONTROLLED EVAPORATION



**APPENDIX A. Figure 1. Comparison of 0° transmission spectra of 320nm films made with varying ethanol:water ratios**

	100% Ethanol	50% Ethanol	75% Ethanol
$T_{\max}$	70.4	72.15	58.65
$T_{\min}$	33.7	41.9	14.2
$T_{\max}/T_{\min}$ [1, 2]	<b>2.089</b>	<b>1.722</b>	<b>4.130</b>
FWHM ( $\Delta\lambda$ )	54	59.3	51.3
Trans Dip ( $\lambda$ )	738.4	724.8	728.6
$(\Delta\lambda/\lambda)$ [3-5]	<b>0.073</b>	<b>0.082</b>	<b>0.070</b>

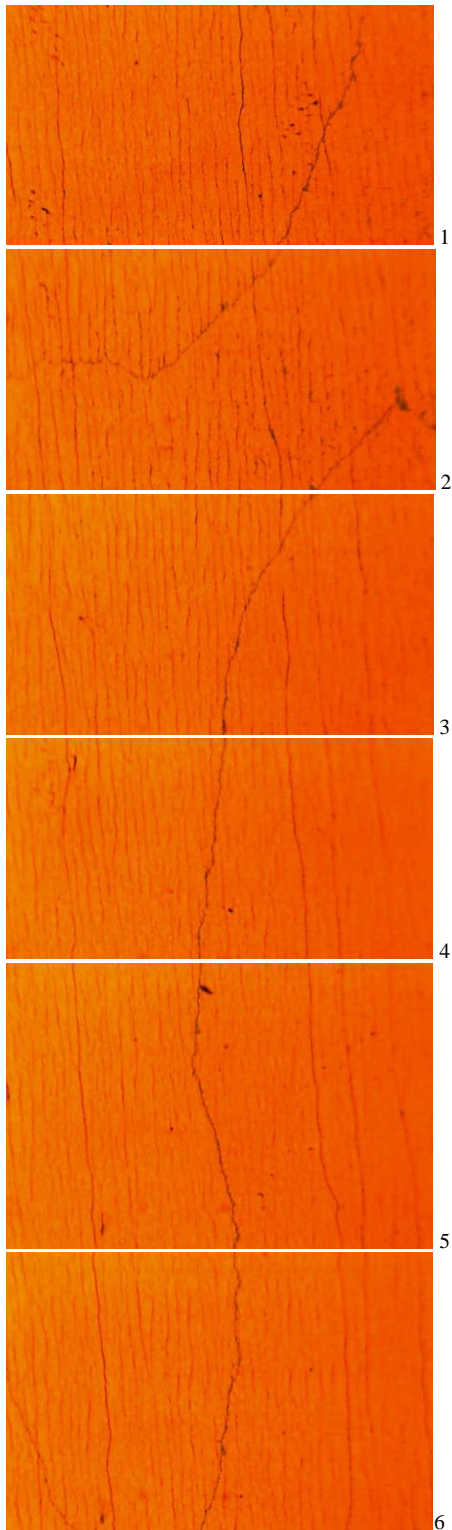
**APPENDIX A. Table 1. Quantitative quality comparison of films made with varying ethanol:water ratios**



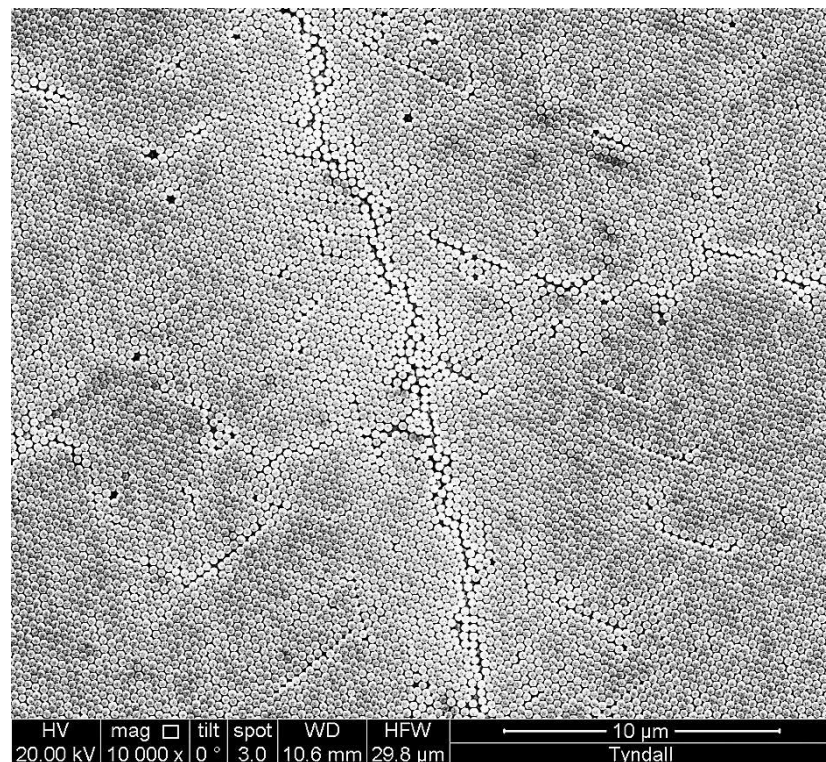
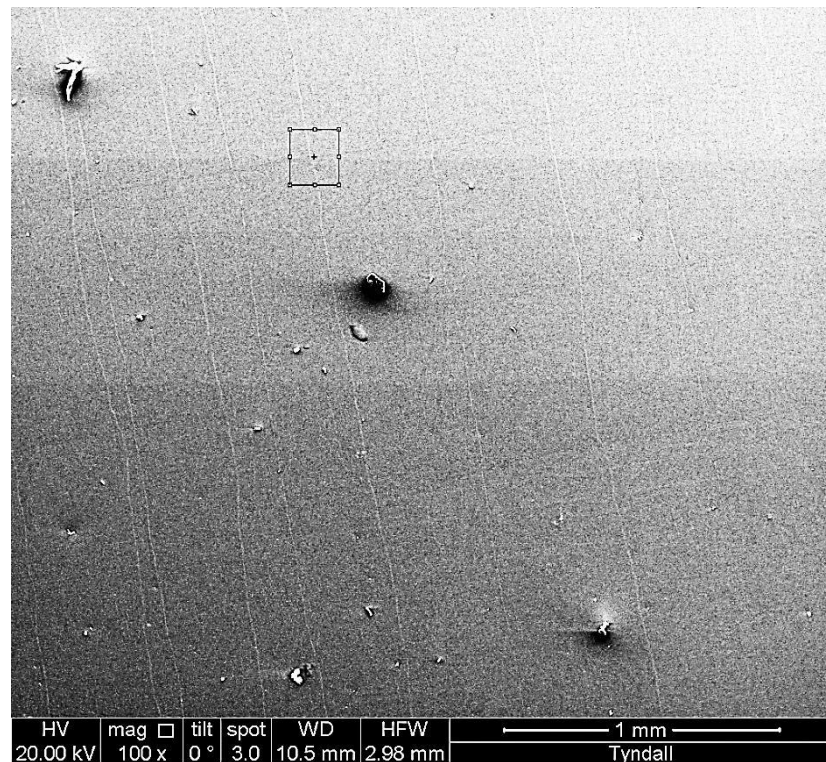


**APPENDIX A. Figure 2. Comparison of films made with 60:40 Ethanol:water ratio (left) and 72:25 ethanol:water ratio (right).**

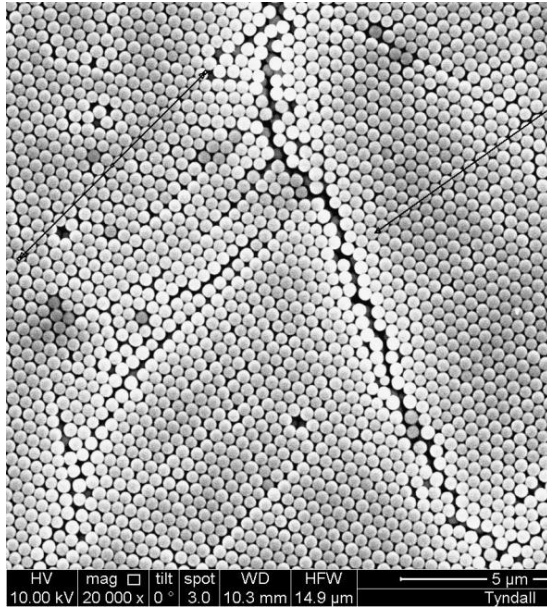
Films made with 60:40 ethanol water ratios suffer from an uneven start to the film deposition (Figure 2 above). This effect was also seen by Li and Marlow [6] during their experiments, and may be as a result of increased Marangoni effects at the meniscus with this ethanol water ratio.



**APPENDIX A. Figure 3. Sequential optical microscopy images (1-6), each showing approximately 0.5mm vertical growth length, (giving a total vertical length of 3.0mm), without cracks.**



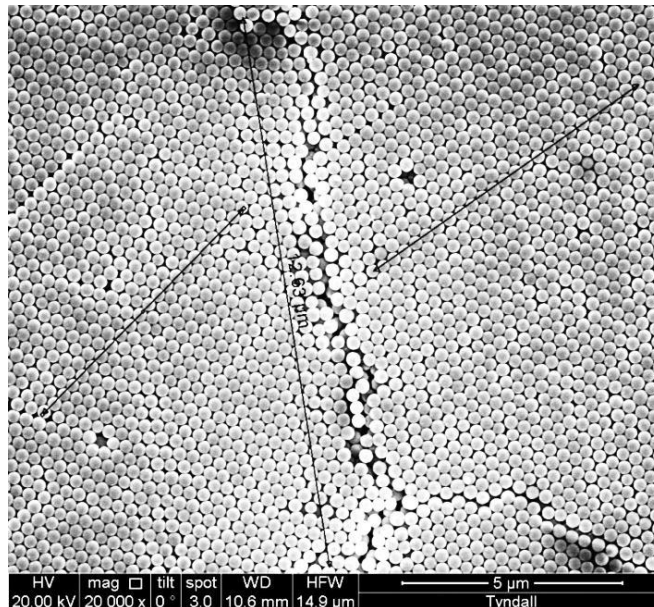
**Appendix A. Figure 4. Top: visible vertical lines suggest cracks in the film. Below: Increased magnification image of the highlighted rectangle area (at what appears to be a crack).**

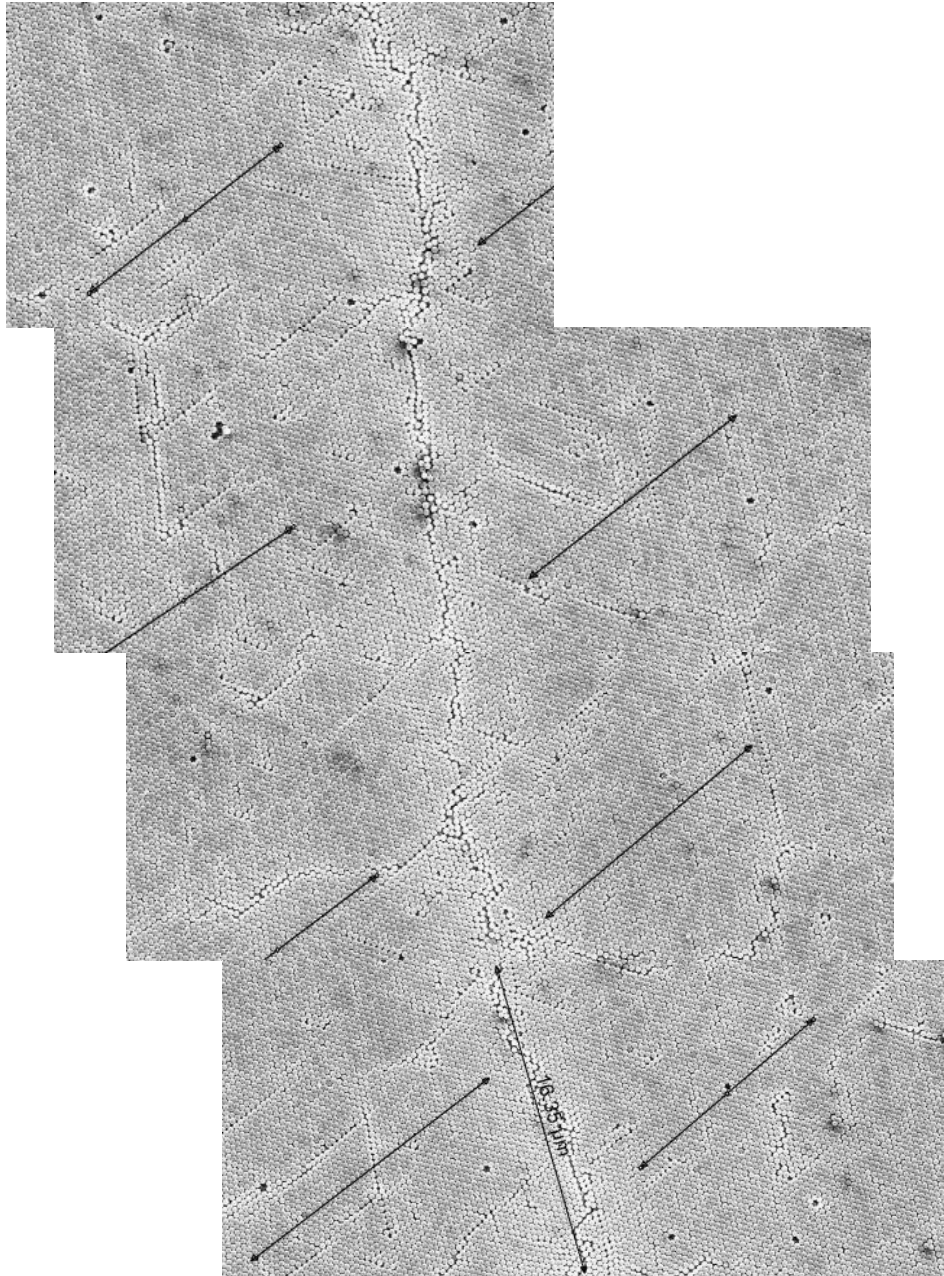


### Appendix A. Figure 5.

Two SEM images at 20,000x magnification (separated by approximately 1mm), showing the domain boundary, and the particle orientation either side of the domain boundary.

Although these two images are separated by 1mm, the orientation of particles on either side of the boundary is the same (despite some misalignments within either domain, e.g. below left side orientation arrow in the upper image).



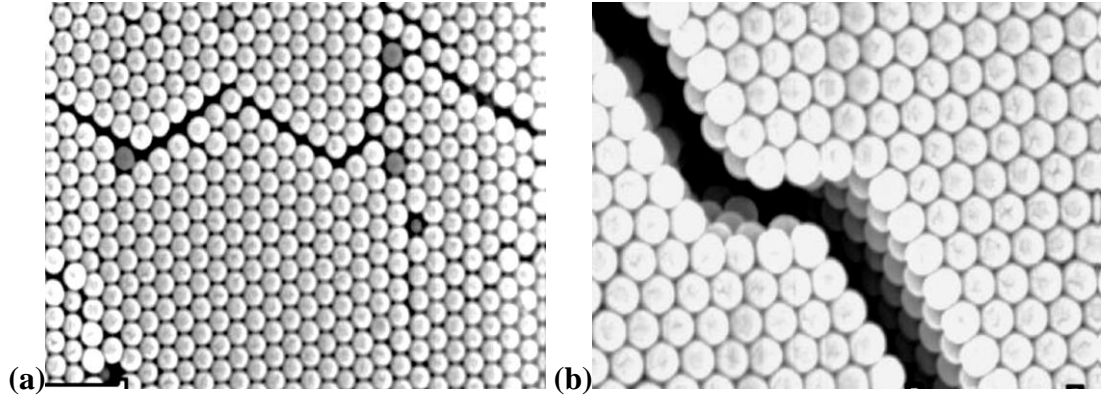


**Appendix A. Figure 6.**

Four overlapping SEM images, @ 8,000x magnification, showing the orientation of the particles either side of a domain boundary. Here particle orientation is approximately the same. (Each image is approximately 15μm in the vertical direction)

NOTE: These films were made from KEW30 (280nm Seahostar) silica particles, in a 3:1 Ethanol:Water suspension at 50°C, by evaporation deposition. The glass slide was held in a near vertical position, with the long edge across the surface of the suspension (200ml), in a 500ml beaker. The domain boundary images above (Figures

3-6) should be compared to standard images [7] of point defects and dislocations, and cracking shown below (figure 7).



**Appendix A. Figure 7. (a) Point defects and dislocations: & (b) crack separating two domains having the same orientation [7], (growth direction is from top to bottom in the images).**



**KEY TO CRACK PATTERNS IN CHAPTER 7: EVAPORATION  
DEPOSITION USING MIXED SOLVENTS:**

**Figure 8a. NONE / GRAIN BOUNDARY= BLACK**

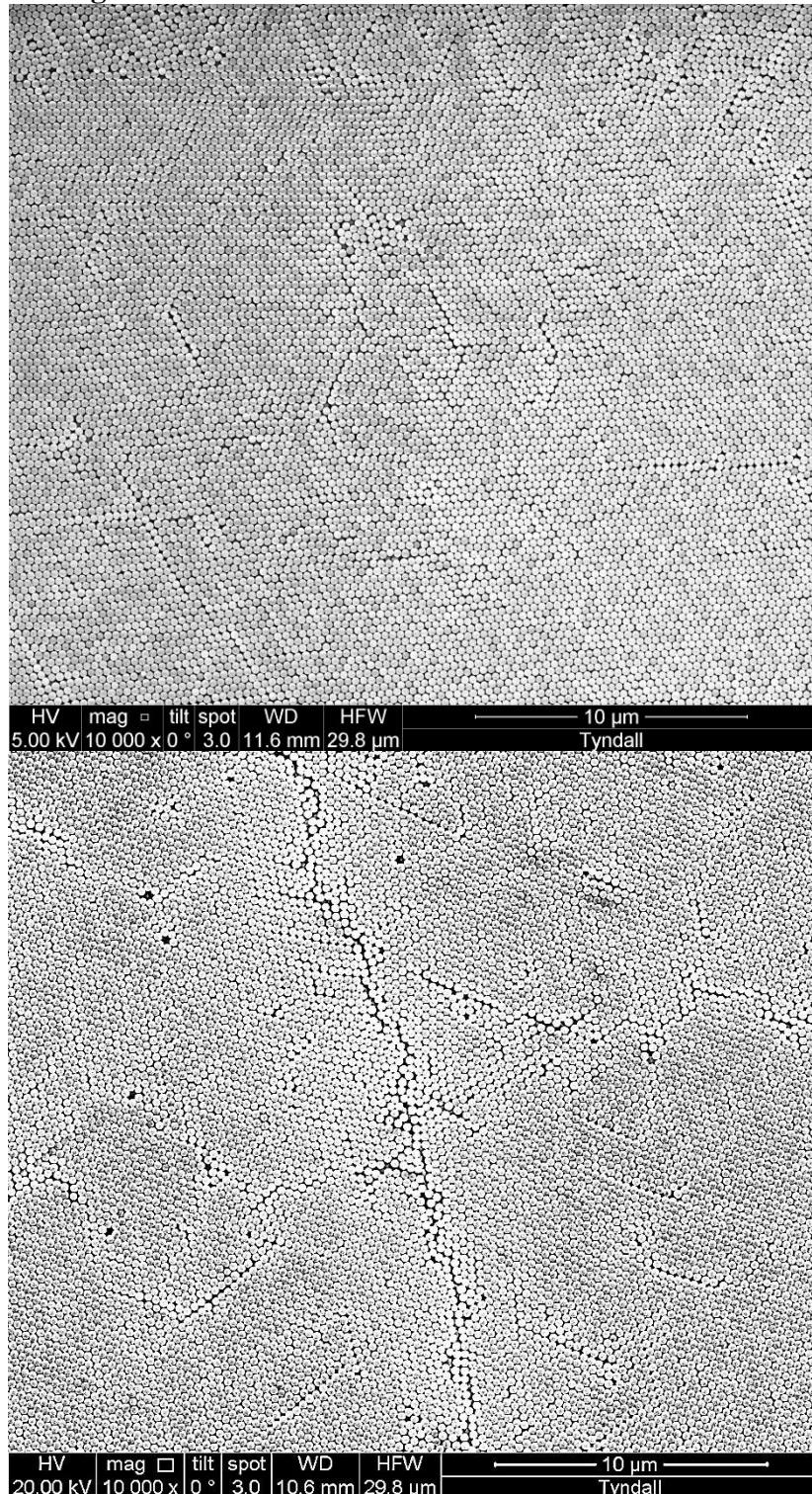


**Figure 8b. CRACKS STARTING TO DEVELOP = RED**

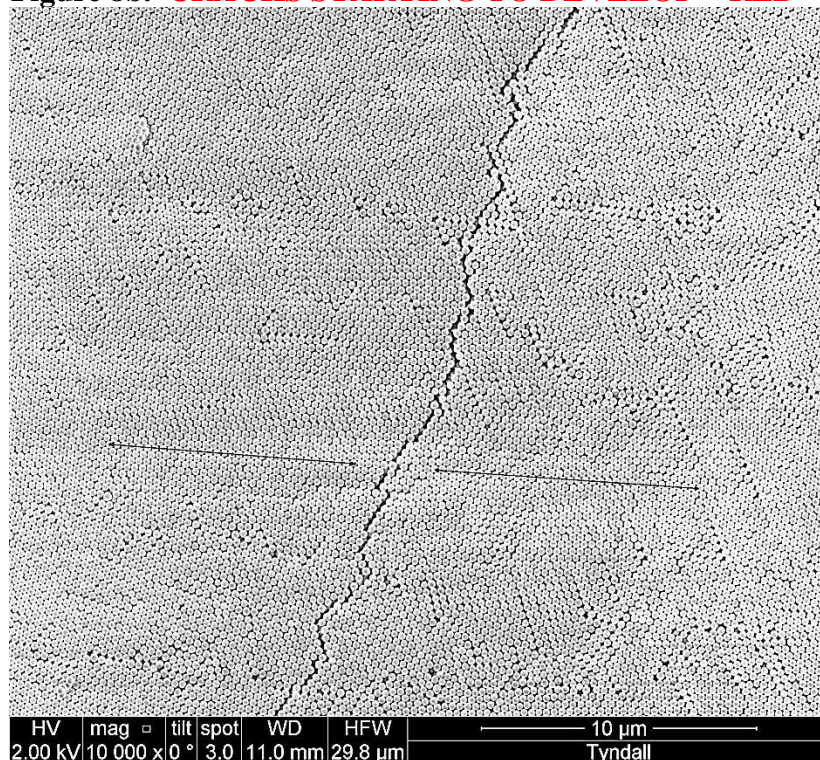
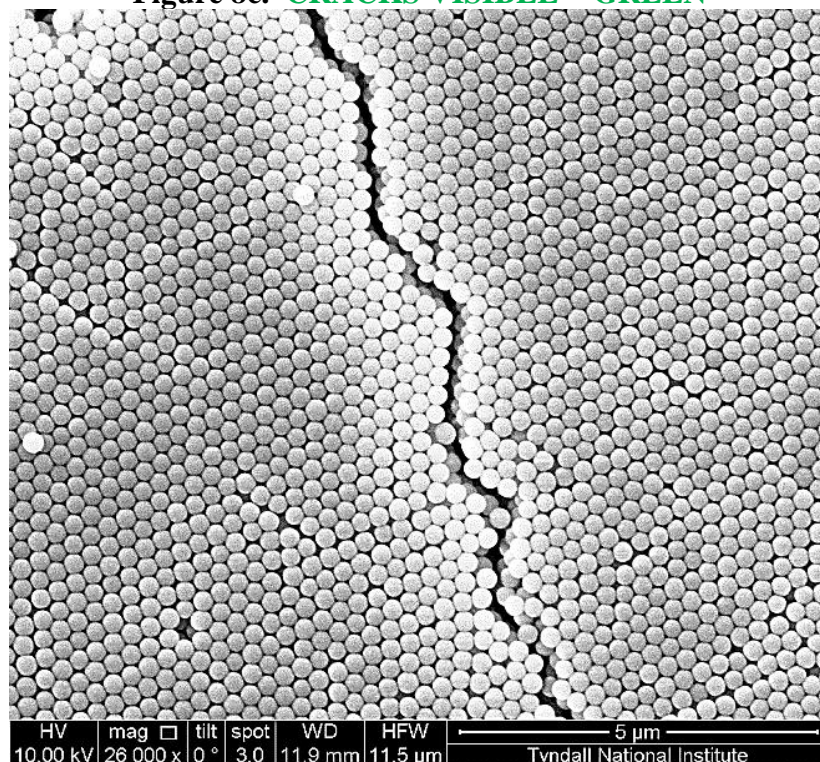


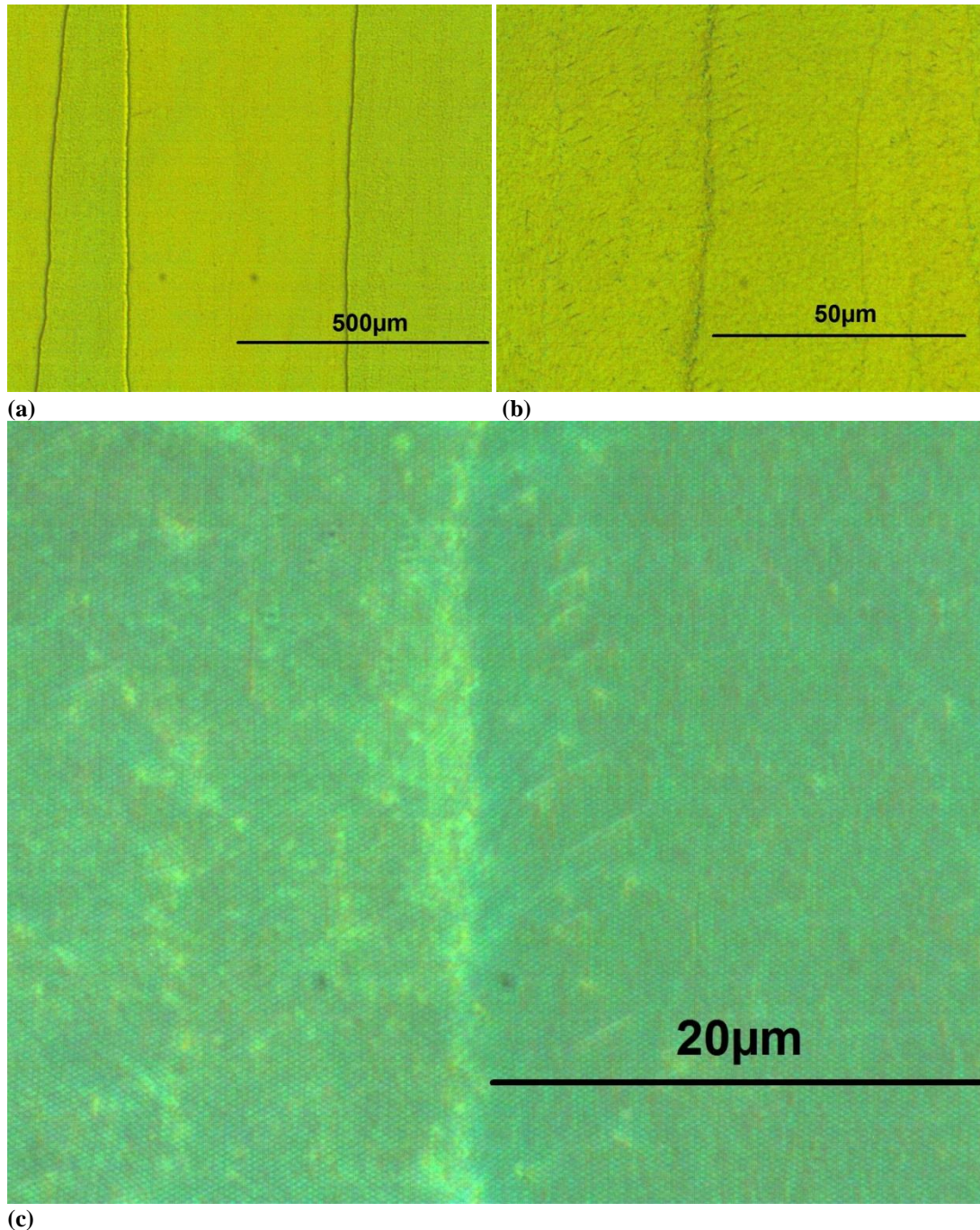
**Figure 8c. CRACKS VISIBLE = GREEN**



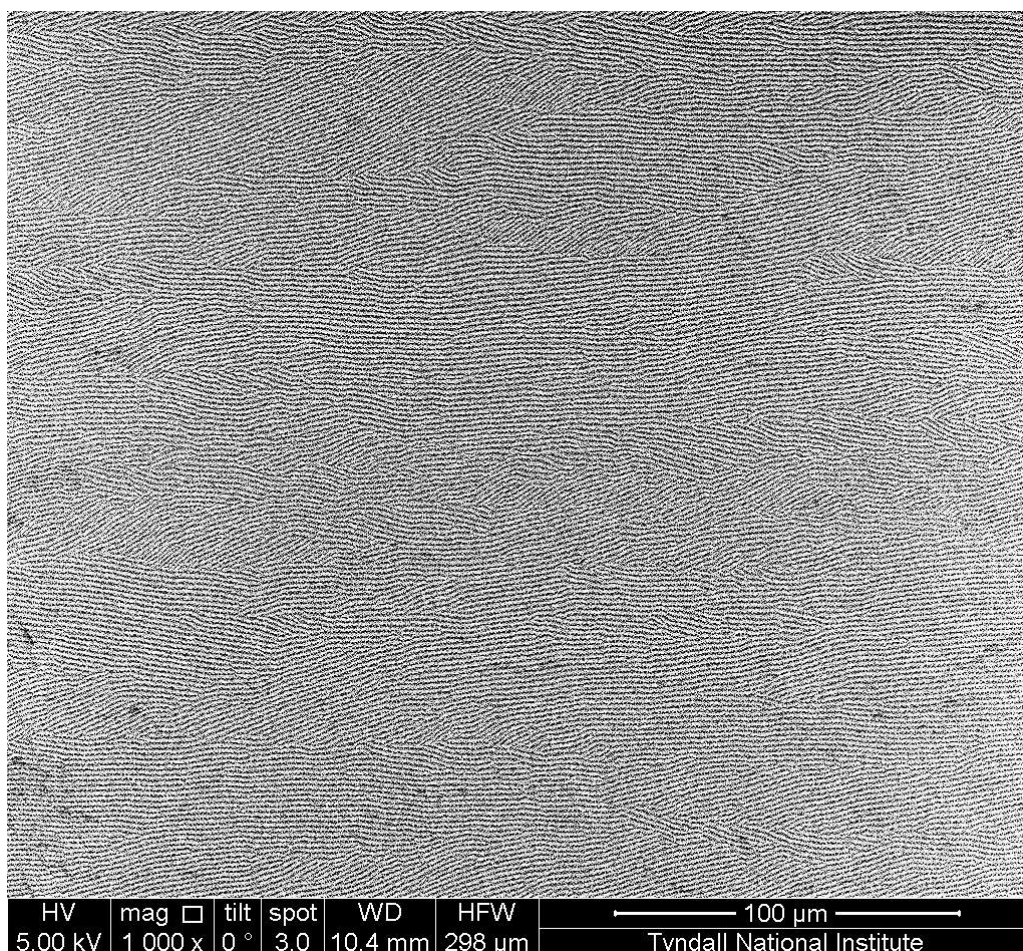
NOTE: In figures (8b) STARTING TO DEVELOP & (8c) VISIBLE images, the particle orientation is the same across the cracks, and the crack fronts are jigsaw-like. Whereas across the DOMAIN BOUNDARY the particle orientation is usually different.



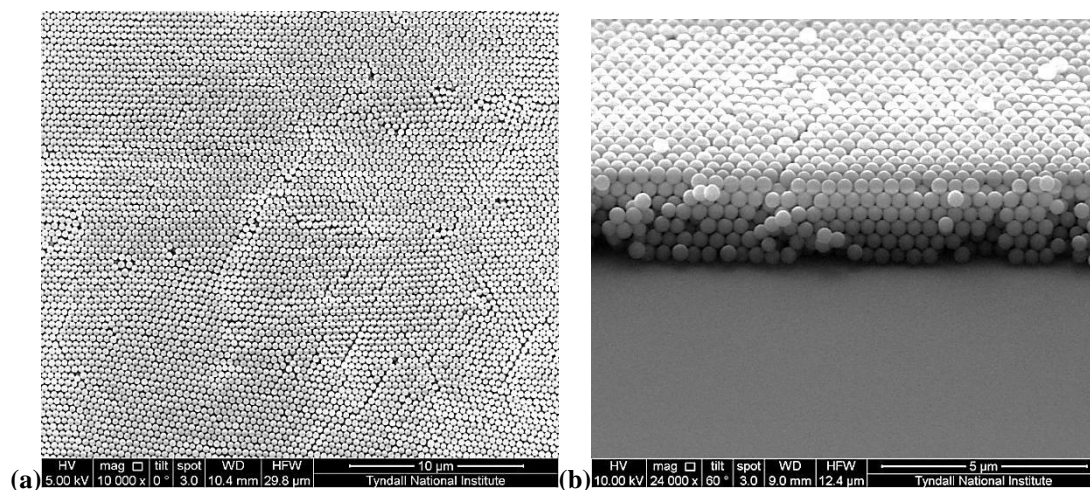
Films made from 360nm silica particles, made in the same manner as above, possess similar crack free results. In this case SEM images show a film of even thickness, 6 layers throughout the film.



(a) (b) (c)  
**Appendix A. Figure 9. Three optical microscope images of 360nm silica particle film, (a) apparent crack at 50x magnification; (b) at 500x mag, and (c) at 1000x mag.**

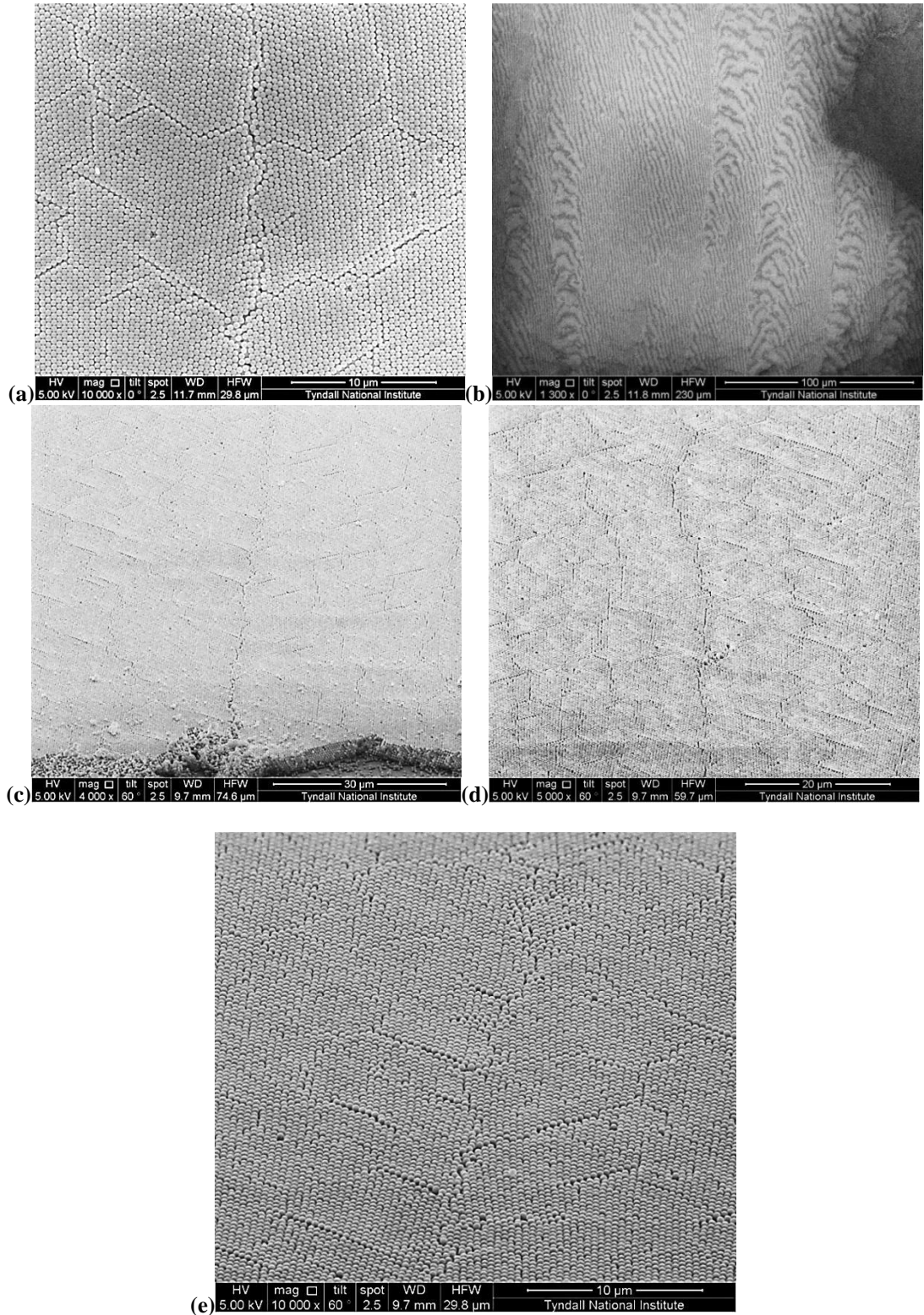


**Appendix A. Figure 10. SEM of 360nm film: typical area showing Moiré fringes (crack free over 300 x 300microns)**

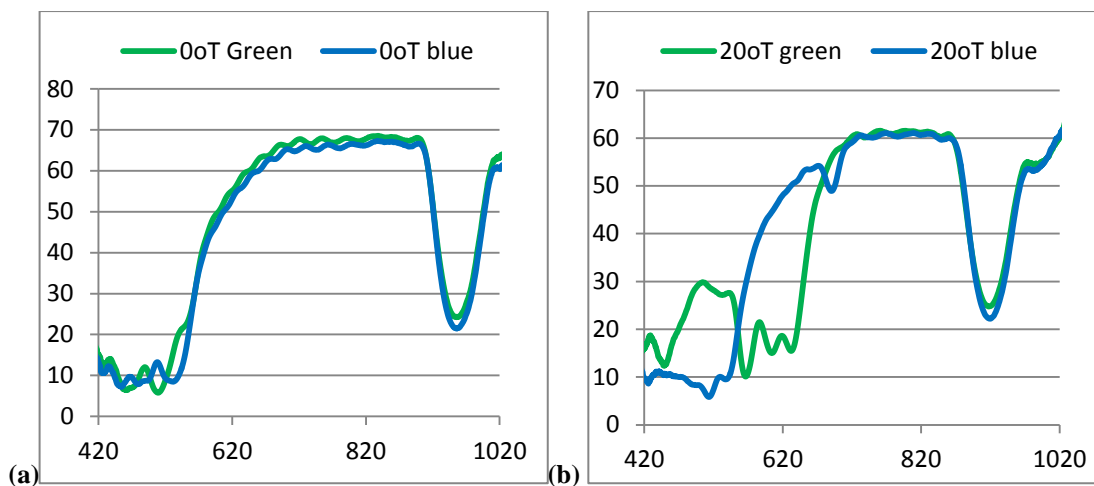


**Appendix A. Figure 11. (a) Magnified (10,000x) SEM of 360nm film showing typical (crack free) surface ordering; (b) cross section showing 6 layers.**

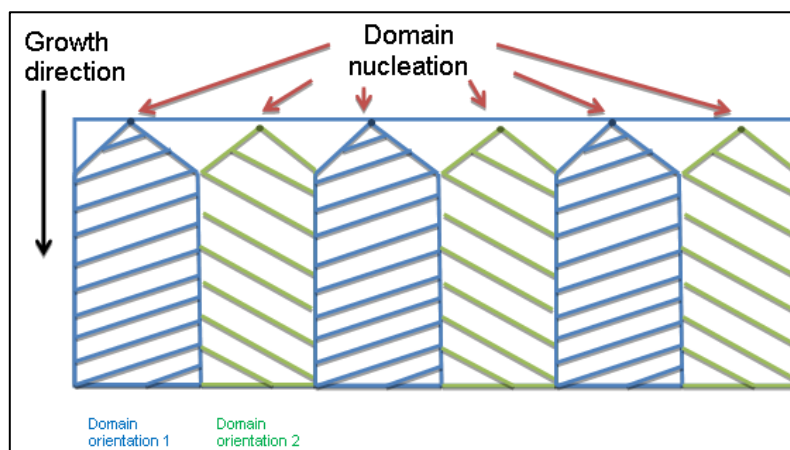




**Appendix A. Figure 13. (a) surface image across a domain boundary; (b) Moiré fringe patterns seen at low magnifications changing from one side of a boundary to another; (c & d) tilted images across adjacent boundaries; & (e) higher magnification image across the first boundary.**



**Appendix A. Figure 14 (a&b). Optical transmission curves at 0° (a) and 20° (b) from a 410nm silica particle sample.**



**Appendix A. Figure 15. Schematic of the growth of domain structures in a 410nm particle film, showing the different orientations giving rise to different visual colourings.**

## REFERENCES:

1. Li, Q.T., Y.F. Chen, and P. Dong, *Improvement of the quality of silica colloidal crystals by controlling drying*. Materials Letters, 2005. **59**(27): p. 3521-3524.
2. Li, Q.Y., et al., *Preparation of higher-quality SiO<sub>2</sub> opals using a new submicrospheres selection technique*. Colloids and Surfaces a-Physicochemical and Engineering Aspects, 2003. **216**(1-3): p. 123-128.
3. Enomoto, N., et al., *Novel processing for improving monodispersity of ceramic spheres and colloidal crystallinity*. Science and Technology of Advanced Materials, 2006. **7**(7): p. 662-666.
4. Piret, F. and B.L. Su, *High quality photonic opaline structure in one night and their optical reflectance*. Chemical Physics Letters, 2008. **454**(4-6): p. 318-322.
5. Ko, Y.G. and D.H. Shin, *Effects of liquid bridge between colloidal spheres and evaporation temperature on fabrication of colloidal multilayers*. Journal of Physical Chemistry B, 2007. **111**(7): p. 1545-1551.
6. Li, H.L. and F. Marlow, *Solvent effects in colloidal crystal deposition*. Chemistry of Materials, 2006. **18**(7): p. 1803-1810.
7. Galisteo-Lopez, J.F., et al., *Optical study of the pseudogap in thickness and orientation controlled artificial opals*. Physical Review B, 2003. **68**(11).

## APPENDIX B

### *Certificate for NIMS Internship*



*This is to certify that*  
**Mr. Joseph McGrath**  
*has completed*  
**NIMS Internship Program**  
*from February 1, 2011*  
*to March 14, 2011.*

April 20th, 2011



**President Prof. Sukekatsu Ushioda**



**NATIONAL INSTITUTE  
FOR MATERIALS SCIENCE**

# **APPENDIX C**

## **PAPERS:**

**‘A facile method for the synthesis of highly monodisperse silica@gold@silica core-shell-shell particles and their use in the fabrication of three-dimensional metallodielectric photonic crystals’.** S.C Padmanabhan, J McGrath, M Bardosova and M E. Pemble., Journal of Materials Chemistry, 2012. **22**(24): p. 11978-11987

**‘Electrochemical properties of opal-V6O13 composites’.** D. Vernardou, M, Apostolopoulou, D. Louloudakis, E. Spanakis, N. Katsarakis, E. Koudoumas, J. McGrath, M E. Pemble., Journal of Alloys and Compounds, 586, (2014), 621-626

**‘Colloidal Crystallisation of Photonic Crystals: self-assembly, manufacture and film quality’** Paper in progress (taken from Chapter 1)

**‘Large area Crack-free Colloidal Crystallisation of Photonic Crystals by a Mixed Solvent Controlled Evaporation Deposition Method’** Paper in progress (taken from Chapter 7)

## **TALKS:**

Joe McGrath, M. Bardosova, M E. Pemble, J. Kinsella, **‘Development of large scale Colloidal Crystallisation Methods for Photonic Crystals’** Materials Ireland, Tyndall National Institute, Cork, Ireland (2009).

Joe McGrath, **‘Development of large scale Colloidal Crystallisation Methods for Photonic Crystals’** Nanomaterials and Nanoarchitectures, FP7 “PhANTASY” ASI NATO, Cork, Ireland (2013).

## **POSTERS:**

Joe McGrath, M. Bardosova, H. Fudouzi, T. Kohoutek, M E. Pemble, **‘Chalcogenide As-S Glass Infilled Colloidal Photonic Crystals’** Trends in Nanotechnology (TNT) Conference, Braga, Portugal, 6-10<sup>th</sup> Sept. 2010.

S. Kassim, Joe McGrath, S C. Padmanabhan, M E. Pemble, **‘Polymer and Metallodielectric based Photonic Crystals’** Materials Ireland conference, December 2010

Joe McGrath, G. Kocher-Oberlehner, M. Bardosova, M E. Pemble, B S. Richards, **‘Planar Colloidal Photonic Crystal Concentrators for Building-integrated photovoltaics’** Photonics Ireland Conference, Malahide, Dublin, 7-9<sup>th</sup> Sept. 2011.